Universidade do Minho
Escola de Engenharia

Susana Maria Trindade Moreira

Seismic retrofit of masonry-to-timber connections in historical constructions

Julho de 2015

Universidade do Minho
Escola de Engenharia

Susana Maria Trindade Moreira

Seismic retrofit of masonry-to-timber connections in historical constructions

Tese de Doutoramento
Engenharia Civil

Trabalho efectuado sob a orientação do
Professor Doutor Luís F. Ramos
Professor Doutor Daniel V. Oliveira

julho de 2015

DECLARAÇÃO

Nome Susana Maria Trindade Moreira

Endereço electrónico: su.moreira.pt@gmail.com Telefone: 253510200

Número do Bilhete de Identidade: 12715330

Título da tese:

Seismic retrofit of masonry-to-timber connections in historical constructions

Orientador(es):

Professor Doutor Luís F. Ramos, Universidade do Minho

Professor Doutor Daniel V. Oliveira, Universidade do Minho

Ano de conclusão: 2015

Designação do Doutoramento: Doutoramento em Engenharia Civil

Universidade do Minho, ___/___/_____

Assinatura: _____

STATEMENT OF INTEGRITY

I hereby declare having conducted my thesis with integrity. I confirm that I have not used plagiarism or any form of falsification of results in the process of the thesis elaboration.

I further declare that I have fully acknowledged the Code of Ethical Conduct of the University of Minho.

University of Minho, _____

Full name: Susana Maria Trindade Moreira

Signature: _____

"If you would not be forgotten, as soon as you are dead and rotten, either write things worth reading, or do things worth the writing."

B. Franklin

Acknowledgments

This thesis was carried out under the supervision of Prof. Luís F. Ramos and Prof. Daniel V. Oliveira, to whom I am sincerely grateful for all the suggestions and guidance, important technical discussions and constant support, which made this work possible.

I would also like to acknowledge the company Monumenta Lda. for collaborating in the construction of the specimens and installation of the strengthening solutions, availability to answer to any difficulties, and constant interest on the work being developed, in particular Eng. Vitor Cóias, Eng. Luís Mateus, and Eng. Raquel Paula. I take also this opportunity to thank to Cintec® for the installation of the injection anchors and all the information provided.

I would like to thank to University of Trás-os-Montes e Alto Douro (UTAD) for borrowing the actuator and the hydraulic group used during the early stages of the experimental campaign.

A special thanks to the technicians of the laboratories of Civil Engineering, for the technical support given during the experimental campaign, in particular Marco Jorge and António Matos, technicians in the Structures Laboratory (LEST), whose constant interest and technical help were truly essential and exceptional. I also would like to acknowledge the help of the master students Pedro Basto, Tristan Charles, and Zehra Teker in the preparation of the tests. Thank you to all, who directly or indirectly contributed for the work carried out.

Thank you, to my colleagues and friends for their constant support, pep talks, and technical discussions (You are all truly great!).

Finally, I would like to acknowledge and to dedicate this thesis to my family. Their care, support, understanding, and love were essential on bringing this work to fruition (*Obrigada por me terem apoiado sempre e por me mostrarem o valor do trabalho e da perseverança).*

This work was partially funded by project FP7-ENV-2009-1-244123-NIKER of the 7th Framework Program of the European Commission, which is gratefully acknowledged.

Abstract

Proper structural connections play an important role in ensuring seismic loads distribution and developing global damage mechanisms of structures. In unreinforced masonry buildings, effective connections between masonry walls and timber floors or walls through the use of anchors can prevent the occurrence of out-of-plane mechanisms and promote "box-like" behavior. This thesis aimed at studying and developing seismic retrofit solutions for connections between masonry walls and timber structural elements, such as floors and timber framed walls, for historical unreinforced masonry buildings built in Lisbon, from the late 19th century to the beginning of the 20th century. However, similarities concerning constructive details of connections found on unreinforced masonry buildings across different countries, bring the possibility of expanding the solutions under study to other contexts. The tasks carried out focused on characterizing the tensile response of the connections, through an experimental campaign followed by analytical development of the results.

Quasi-static monotonic and cyclic tests were carried out on pairs of injection anchors, to be applied on masonry-to-timber elements connections, and on wall-to-floor connections retrofitted with a system of steel tie rod with anchor plate. The pairs of injection anchors failed by combined cone-bond failure, with strength capacity and shape of the envelopes being highly influenced by the boundary conditions of the masonry wall. Hysteretic loops' shape is mainly influenced by bond slip at the grout/masonry interface, causing strength and stiffness degradation, and pinching. Unstrengthened wall-to-floor specimens' failure mechanism was nails pullout, while for the strengthened ones was failure of the bolted connection between steel angle and timber joist. The hysteretic behavior of the latter shared similarities with the one of the injection anchors, but it was controlled by slip at the bolted connection. There were considerable increases in maximum pullout force and dissipated energy, from unstrengthened to strengthened wall-to-floor connections, and ductility was kept high as well.

From the experimental results, strength prediction formulae were studied and adapted to better fit the results obtained and idealized curves were developed based on force-displacement backbone curves. Existing behavior models provided good approximations to the experimental results but further validation needs to be implemented. The trilinear curves provided better approximations to the backbone curves, and ASCE/SEI 41-06 approach revealed to be very conservative. Retrofit design and acceptance criteria regarding displacements, forces and behavior factors were proposed.

Resumo

Ligações estruturais eficientes assumem um papel crítico na transmissão de solicitações sísmicas e no desenvolvimento de mecanismos globais de colapso, em detrimento de modos de rotura locais como derrubamento parcial ou total de paredes para fora do plano. Estes mecanismos para fora do plano das paredes são particularmente recorrentes e nefastos em edifícios antigos de alvenaria não armada, sendo necessário o desenvolvimento de soluções de reforço sísmico de ligações capazes de promover um comportamento de "caixa" de todo o edifício. Esta tese teve como objetivo principal colmatar esta necessidade e, para tal, focou-se em ligações entre paredes de alvenaria e pavimentos e paredes de madeira, existentes em edifícios contruídos em Lisboa, depois do terramoto de 1755 até ao início do século XX.

Ensaios de arrancamento quase-estáticos monotónicos e cíclicos foram realizados em provetes constituídos por paredes de alvenaria e mangas injetadas e em provetes representativos de ligações piso-paredes, sem reforço e reforçados com tirantes e placas de ancoragem. Os pares de mangas injetadas romperam por combinação de cone de alvenaria com corte na interface alvenaria/grout, mas com diferentes contribuições dos mesmos, conforme a sua localização na parede. As forças de arrancamento e a forma das envolventes foram muito influenciadas pelas condições fronteiras da parede. No entanto, em todos os ensaios os ciclos histeréticos foram governados por escorregamento na interface alvenaria/grout, sendo caracterizados por perdas de força e rigidez entre ciclos, assim como mudanças de rigidez em carga e descarga. O mesmo se verificou para os ensaios realizados nos provetes piso-parede, sendo no entanto, o escorregamento na ligação aparafusada entre cantoneira e viga de madeira o responsável pelo comportamento histerético observado. O mecanismo de rotura verificado nos provetes piso-parede não reforçados foi o arrancamento dos pregos, enquanto nos provetes reforçados foi a rotura da ligação aparafusada. Houve um aumento da capacidade em força e da energia dissipada nos reforçados, sendo possível manter uma ductilidade elevada na ligação.

Modelos de comportamento e respetivas expressões para a estimativa de forças máximas foram aplicados aos resultados experimentais, assim como foram desenvolvidas curvas idealizadas com base nas envolventes força-deslocamento. As expressões existentes permitem boas aproximações às forças obtidas experimentalmente, mas necessitam ser melhoradas. As envolventes ASCE/SEI 41-06 são bastante conservativas e as curvas trilineares constituem melhores aproximações às envolventes experimentais. Foram também propostos critérios de aceitação com base em deslocamentos e forças, assim como fatores de comportamento.

Contents

List of Figures

List of Tables

List of Symbols

A_{ap}	Area of the anchor plate
A_{bil}	Area below the bilinear curve
A_{env}	Area of the experimental envelope curve (backbone curve)
A_{env}^{post}	Area below the experimental envelope, post-peak
A_{env}^{pre}	Area below the experimental envelope, pre-peak
A_n	Net area of the masonry wallet
A_{Nc}	Area of the projected cone failure
A_{Nc0}	Area of the projected cone failure of one single anchor
A_{pt}	Projected area
A_s	Nominal cross-section of a steel bar
A_{tri}^{post}	Area below the trilinear curve, post-peak
A_{tri}^{pre}	Area below the trilinear curve, pre-peak
b	Side of the anchor plate
c_a	Minor edge distance of an anchor or group of anchors
C_c	Coefficient relative to critical edge distance
C_{cr}	Reduction factor to estimate the crack limit force
C_s	Coefficient relative to distance between anchors
C_{sd}	Strength degradation factor
d	Diameter of a steel bar
d_0	Diameter of the hole
$d_{ap\text{-}bw}$	Displacement between the anchor plate and the back of the wall
d_{cone}	Difference between $s_{j\text{-}bw}$ and $s_{j\text{-}fw}$
d_{cr}	Crack limit displacement
d_e	Idealized elastic limit displacement
d_{Fmax}	Displacement at the maximum force
d_{max}	Maximum displacement
d_{res}	Residual displacement
d_u	Ultimate displacement
d_y	Yield displacement
e_d	Error in diameter
E	Elastic modulus
$E_{0,mean}$	Mean modulus of elasticity parallel to grain
$E_{90,mean}$	Mean modulus of elasticity perpendicular to grain
f_c'	Compressive strength of concrete in cylinders
$f_{c,0,k}$	Characteristic compression strength parallel to grain
$f_{c,90,k}$	Characteristic compression strength perpendicular to grain

f_{cc200}	Compressive strength of 200 x 200 cubes of concrete
f_{cm}	Mean compressive strength of mortar
f_{m}	Mean compressive strength of masonry
$f_{b,k}$	Characteristic bending strength of timber
f_{mk}	Characteristic compressive strength of masonry
$f_{t,0,k}$	Characteristic tensile strength parallel to grain
$f_{t,90,k}$	Characteristic tensile strength perpendicular to grain
f_{tk}	Characteristic tensile strength of masonry
f_{u}	Ultimate tensile strength
$f_{v,k}$	Characteristic shear strength
f_{y}	Yielding strength
F_{ax}	Withdrawal force
F_{cr}	Crack limit force
F_{det}	Detachment force
F_{dmax}	Force at the maximum displacement
F_{e}	Idealized elastic limit force
F_{lev}	"Lever" effect force
F_{max}	Maximum force
F_{res}	Residual force
F_{u}	Ultimate force
F_{v}	Shear connection capacity
h_{c}	Cone depth
h_{ef}	Effective embedment length
k_0	Initial stiffness
k_c, k_1, k	Calibration parameters for masonry cone breakout failure
k_{e}	Effective stiffness
L_0	Original bar length
L_{cg}	Original clip-gauge length
L_{u}	Final bar length after fracture
M_{y}	Plastic moment
n	Number of anchors
n_{ef}	Number of effective anchors
N_{exp}^{Bot}	Experimental pullout capacity of anchors at the bottom
N_{cap}	Nominal strength associated with crushing of mortar under the anchor plate
N_{cb}	Nominal tensile load for combined cone-bond failure
N_{cg}	Nominal tensile capacity associated with cone failure
N_{sa}	Tensile capacity of the steel angle

N_{sa}	Nominal tensile strength by steel failure
N_{exp}^{Top}	Experimental pullout capacity of anchors at the top
P	Applied force
q	Behavior factor
q^0	Basic behavior factor
R_m	Tensile strength
$R_{p0.2}$	Proof strength
s	Distance between anchors
$s_{j\text{-}bw}$	Slip of the joist relative to the back wall
$s_{j\text{-}fw}$	Slip of the joist relative to the front wall
$s_{j\text{-}wp}$	Slip of the joist relative to the wall-plate
s_L	Slip related to the interface grout/masonry
s_T	Total slip
$s_{wp\text{-}fw}$	Slip of the wall-plate relative to the front wall
S_0	Nominal cross-section area
S_s	Shear strength according to ASTM E519
t_w	Thickness of the wall

α	Coefficient regarding the stiffness of the second branch of a trilinear curve
β	Coefficient regarding the stiffness of the third branch of a trilinear curve
Δ_{CP}	Displacement at Collapse Prevention limit state
Δ_{DL}	Displacement at Damage Limitation limit state
Δ_{IO}	Displacement at Immediate Occupancy limit state
Δ_{LS}	Displacement at Life Safety limit state
Δ_{NC}	Displacement at Near Collapse limit state
Δ_{SD}	Displacement at Significant Damage limit state
ε_m	Measured strain
ε_e	Estimated strain
ε_u	Percentage of elongation after fracture
θ	Cone angle
μ	Displacement ductility
ρ	Density
σ_I	Principal stress I
σ_{II}	Principal stress II
τ	Shear stress of the masonry wall panel
τ'	Bond strength at the interface steel tie/grout

τ_0'	Bond strength at the interface grout/masonry
ϕ	Strength reduction factor
$\psi_{s,N}$	Factor considering stress distribution
$\psi_{ec,N}$	Factor considering load eccentricity
Ψ_c	Coefficient relative to the influence of the concrete strength

List of Acronyms

ASCE/SEI	American Society of Civil Engineers/ Structural Engineering Institute
BSO	Basic Safety Objective
CCD	Concrete Capacity Design
CIP	Cast-in-Place
CoV	Coefficient of Variation
CP	Collapse Prevention
DL	Damage Limitation
EC 5	Eurocode 5
EC 8	Eurocode 8
EC 3	Eurocode 3
FM	Failure Mode
GFRP	Glass Fiber Reinforced Polymer
IO	Immediate Occupancy
LEFM	Linear Elastic Fracture Mechanics
LEST	Laboratory of Structural Engineering of University of Minho
LS	Life Safety
LVDT	Linear Variable Displacement Transducer
NC	Near Collapse
SD	Significant Damage
URM	Unreinforced Masonry
VAC	Variable Angle Cone Method

Chapter 1. Introduction

1.1 MOTIVATION

Out-of-plane failure mechanisms observed in historical unreinforced masonry (URM) buildings, subjected to seismic action, are often a direct result of poor connections between structural elements. During a seismic event, these weak connections become incapable of assuring proper load transmission, which can lead to local instabilities, instead of global structural seismic response. Post-earthquake surveys of recent events — e.g. Azores (Portugal) 1998, Bhuj (India) 2001, L'Aquila (Italy) 2009, and Christchurch (New Zealand) 2011 — show that failure mechanisms related with the out-of-plane response of masonry walls is the most common in historical masonry buildings (Costa et al., 2011; Bothara & Brzev, 2011; Senaldi et al., 2012). Although being a local mechanism, it can cause irreparable damage to culturally significant buildings or even compromise the overall stability of a structure. Papanicolaou et al. (2007) citing Coburn (2002) stated that URM buildings were responsible for 60 % of the fatalities caused by earthquakes in the second half of the 20th century and Bothara & Brzev (2011) mentioned that 74 000 people died, in the 2005 Kashmir earthquake, most buried under the rubble of traditional stone houses. The absence of appropriate structural connections is known to be one of the main factors contributing to the activation of this type of failure mechanism (Bruneau, 1994; Dizhur et al., 2011), as shown in Figure 1.1a. Therefore, the need to prevent these phenomena goes hand in hand with the critical effort to understand the behavior of masonry-to-timber connections and to develop effective retrofit solutions.

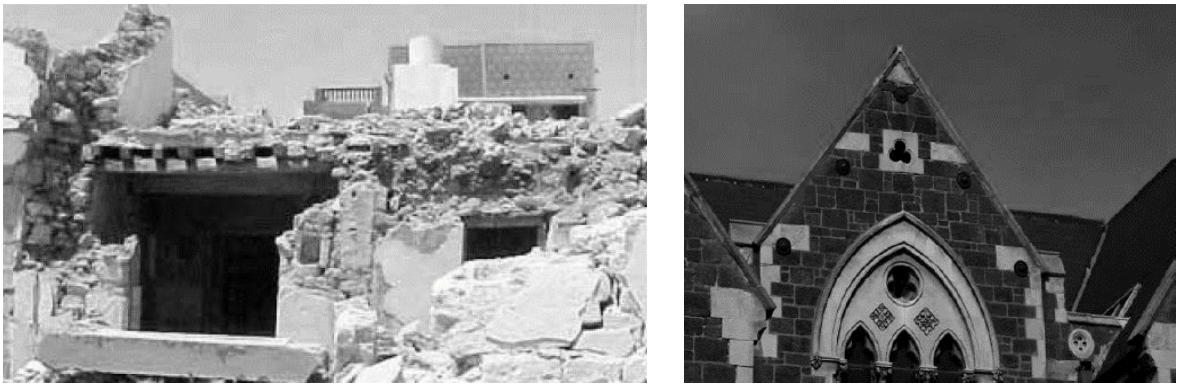

(a) (b)

Figure 1.1 URM seismic performance: (a) Inadequacy of wall-to-floor connections leading to wall collapse (Bothara & Brzev, 2011); and (b) successful case of wall-to-floor anchorage (Dizhur et al., 2011).

In Christchurch 2011 earthquake, as in other earthquake scenarios, it was observed that strengthened wall-to-floor connections prevented effectively out-of-plane collapses (see Figure 1.1b), allowing the development of a global response of the structure (Bruneau, 1994; Dizhur et al., 2011). However, little research has been carried out in the past

decades to characterize the behavior of connections between masonry walls and timber walls or floors (Peralta et al., 2004; Lin & LaFave, 2012; Dizhur et al. 2013). Research has been mostly directed towards the study of the seismic behavior and the development of retrofit solutions for the building as a whole and for its two primary structural elements, the loadbearing masonry walls and the flexible timber diaphragms (Magenes & Calvi, 1997; Tomaževič, 1999; Yi et al.,2006; Parisi et al., 2008).

The most recent report on Housing and Building Rehabilitation of 2011 (INE, 2012), regarding Lisbon Region, Portugal, points out that until 1945, approximately 50% of the total of constructed buildings were in masonry with timber floors (with and without metallic beams), being the remaining 50% distributed by masonry with a concrete slab, reinforced concrete buildings and others. Until 2011, buildings of masonry with timber floors (with and without metallic beams) represented 10.7 % of the total constructed buildings, from which 60.5 % were constructed previously to 1945. For the Municipality of Lisbon, this last value is considered to be much higher, reaching 50 % (including pre-*Pombalino* buildings) of the existing buildings (Cóias e Silva, 2001). Summing up, there is still a considerable amount of URM buildings with timber floors that are historical and in need of retrofit.

Focusing on the buildings constructed, after the 1755 earthquake, in downtown Lisbon, until the beginning of the 20th century, one has the *Pombalino* buildings, which are considered to be highly efficient in response to seismic demands, and the *Pombalino Tardio* and the *Gaioleiro* buildings, which have increased seismic vulnerability, especially the latter, mostly due to the degradation of construction techniques and quality of materials. *Pombalino* typology of buildings was a seismic engineering breakthrough at the time, and most of its buildings were build right after the earthquake. They were, and still are, shelter of key governmental institutions, museums, schools, banks, stores, as well as, housing, being part of the Portuguese built heritage. However, some concern has been raised regarding out-of-plane mechanisms of masonry facade walls, especially in elevated floors, and the need to improve their connection to inner half-timbered walls (Ramos & Lourenço, 2004; Cardoso et al., 2005). *Pombalino Tardio* style belong to the transition period between *Pombalino* and *Gaioleiro* buildings, leading to great variety of architectural and structural details, nonetheless many of these buildings have similar uses to the *Pombalino* buildings. *Gaioleiro* buildings have housing as a more common use, which partially justifies why their quality is inferior, and misguided alterations are more common (Cardoso, 2003; Ramos, 2000). Either to conservation of built heritage or protection of human lives, there is the need to decrease the seismic vulnerability of these buildings.

Existent literature, as well as, a brief survey on plans and descriptive construction reports of the typologies mentioned carried out on the Municipal Archive of Lisbon, confirms that it was common practice to place the timber floor joists perpendicularly to the facades of the buildings. By present standards, inner walls are considered to be nonstructural, but at the time most of them were taken as loadbearing, since they could carry vertical static loads. Therefore, the general rule of placing the timber floor joists in the direction of the smallest span would be accomplished by considering the inner walls. Having timber elements, from the floors and inner walls, placed perpendicularly to the masonry walls, facilitates the application of retrofit solutions, to improve their connections, and consequently promote a "box-like" behavior of the entire structure.

All these factors, support the necessity of studying masonry-to-timber connections and the development of engineered retrofit solutions. The objectives and associated tasks established for the thesis are part of this effort, and intend to push forward this field of study.

1.2 OBJECTIVES OF THE THESIS

The research developed focused on understanding the local pull out response of retrofitted masonry-to-timber connections, when subjected to cyclic demands on the horizontal direction. Considering the small amount of existing information – experimental, analytical or numerical – about masonry-to-timber connections and proper retrofit solutions, a systematic approach is needed, thus one established the following objectives to be achieved by the work carried out:

1. Compile information regarding the typologies of historical connections (configuration and materials) and possible retrofit solutions, in order to understand the extent of their variety and which variables are determinant for their seismic response;
2. Add new experimental data to the existent database, regarding the pullout behavior of masonry-to-timber connections (unstrengthened and strengthened). It is essential that the cyclic response is captured and parameters like tensile capacity, ductility, and energy dissipation are determined. A fully functional pullout test setup should be proposed;
3. Develop an analytical approach to the experimental data that can be applied on further tests and can be the foundation of adequate design procedures. This should focus on defining the idealized behavioral curves and respective hysteretic rules based on the data acquired experimentally, for each connection and primary failure

mode. From a point of view of performance-based design, performance criteria (force and/or displacement) should be established to be applied on linear and nonlinear procedures;

4. Propose design approaches and recommendations regarding the retrofit solutions under study.

1.3 RESEARCH FOCUS AND BACKGROUND

Considering the motivation and objectives established previously, and the fact that the work developed has a great experimental component, one chose to focus the research on masonry-to-timber connections found in buildings built in downtown Lisbon, after the 1755 earthquake. Two different types of connections were analyzed: wall-to-timber framed wall and wall-to-floor connections. The first is commonly found in *Pombalino* and *Pombalino Tardio* buildings, while the second is typical of the latter and *Gaioleiro* buildings. The research carried out on this thesis relied on the extensive existing literature regarding historical, architectural, and structural features, materials, and construction techniques, found in the works of Mascarenhas (2004), Appleton (2005), Appleton & Domingos (2009), and Pinho (2008). Regarding the seismic performance of these types of buildings, one relied on previous works of Ramos & Lourenço (2004), Cardoso et al. (2005), and Candeias (2008). Further background is provided in Chapter 2.

A different retrofit solution was studied for each typology of connection, following the proposals of Cóias e Silva (2007) to improve the response of masonry-to-timber connections found in the architectonic styles of buildings aforementioned (see Figure 1.2). However their application is interchangeable, if proper conditions are met. A configuration of each type of connections (one of wall-to-timber framed wall and one of wall-to-floor connections) was chosen as base of the experimental campaign and following analysis, to be carried out under the European program NIKER (New integrated Knowledge based approaches to the protection of cultural heritage from Earthquake-induced Risk), with the objective of studying masonry-to-timber connections and effective "engineered strengthening solutions". This research was carried out in collaboration with the contractor Monumenta Ltd., which provided the prototypes of the retrofit solutions. These strengthening solutions try to respect principles as minimum intervention and reversibility, required for historical interventions, stated by The Venice Charter (ICOMOS, 1965) and the ICOMOS Charter for structural restoration (ICOMOS, 2003).

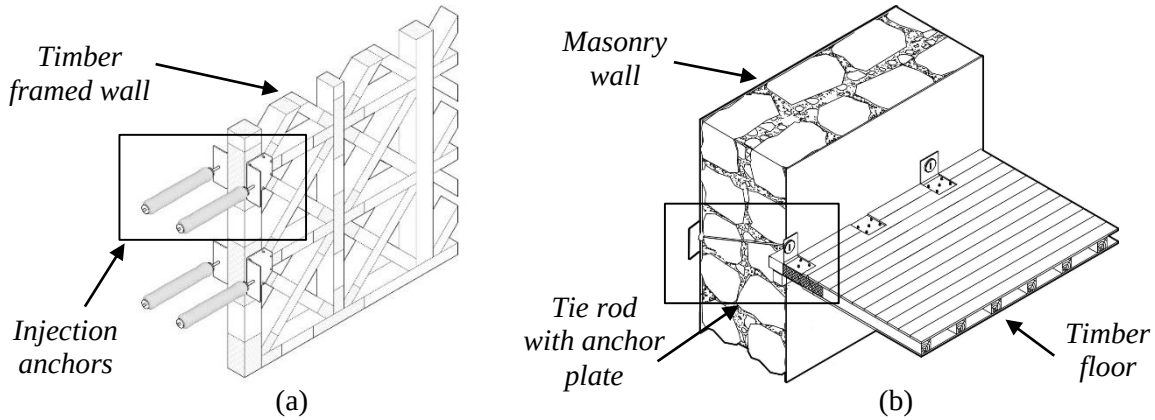

Figure 1.2 Sketches of the adopted connections and strengthening solutions (Cóias e Silva, 2007): (a) wall-to-timber framed wall; and (b) wall-to-floor.

For the wall-to-timber framed wall connection, the strengthening solution consists of a pair of injection anchors placed in pre-cored holes in the masonry wall. The timber framed wall goes between the parallel injection anchors so that a symmetrical behavior can be explored (see Figure 1.2a). The injection anchor itself is a steel rod inside a woven polyester based tubular sleeve, provided by the company Cintec®. It is placed in a pre-drilled hole and injected, under low pressure, with a cementitious grout. The sleeve can expand to suit the diameter of the borehole, which can vary according to the steel bar diameter, and control the flow of grout into voids. The distance between anchors can vary according to the thickness of the timber framed wall and the steel gusset plates. These plates are bolted to both sides of the timber framed wall, usually at the intersection of the different timber elements of the cross (vertical, horizontal and diagonal), so that they work as a double shear connection. Although focus is given here to the connection between timber framed walls and masonry walls, the strengthening solution analyzed can also be extended to other types of connections found in masonry constructions, namely timber floors to masonry walls.

The type of wall-to-floor connection adopted consists of a timber floor joist end nailed to a timber wall-plate, embedded in the masonry wall. The strengthening solution is an evolution of the metal straps being applied for centuries. It consists of a stainless steel angle bolted to the timber floor joist and anchored to the masonry wall, by means of a tie rod with an anchor plate on the exterior face of the wall (see Figure 1.2b). Instead of nailing a metal strap to the timber floor joist, the stainless steel angle is bolted to the joist, improving the single shear connection with timber. Historically, metal straps were usually nailed laterally on the joist but to facilitate power drilling of the pre-drilled hole of the bolts, the stainless steel angle needs to be applied on the top or bottom face of the joist. In this case, it was preferable to position the stainless steel

angle on the top face of the floor joist, not to damage the timber wall-plate, while drilling the hole for the tie rod.

1.4 METHODOLOGY AND OUTLINE OF THE THESIS

The thesis applies a quantitative approach to the development of an experimental campaign, and analysis and exploitation of the results. The tasks carried out are reflected on seven chapters (see Figure 1.3). Each one of them comprises the highlights (except for Chapter 1 and Chapter 7), the body of text, and the conclusions. The chapters are the following:

- **Chapter 1 – Introduction**: presents the motivation and the main objectives associated with the research developed, as well as, a brief description of the background, research focus, and outline of the thesis;
- **Chapter 2 – The role of structural connections**: expands the background and research focus already introduced in the present chapter, presenting the state-of-the art about historical context, the various typologies of structural connections and appropriate retrofit solutions. It also discusses the role of connections on the seismic response of unreinforced masonry buildings, especially on the out-of-plane behavior of walls;
- **Chapter 3 – Material characterization**: focuses on the description of the mechanical properties of the materials used on the specimens. Timber, grout, and certain metallic components had their typical mechanical properties presented, rather than being tested experimentally. The experimental characterization concentrated on: tensile tests of stainless steel bars, compression tests of mortar, stone and masonry, as well as, diagonal compression tests of masonry wallets. The compression tests of mortar were used to choose a mortar proportion that could approximate its mechanical properties to the ones of the historical mortar described in Chapter 1;
- **Chapter 4 – Injection anchors applied to connections**: presents the quasi-static monotonic and cyclic pullout tests carried out on pairs in injections anchors, acting simultaneously. It encompasses all the steps to be carried out when defining an experimental work (descriptions of the specimens, the test setup, including instrumentation, and test procedure), an extensive description of the hysteretic behavior, the damage observed, seismic parameters, and finally a discussion of the results obtained;
- **Chapter 5 – Wall-to-floor connections**: presents the quasi-static monotonic and cyclic pullout tests carried out on unstrengthened and strengthened wall-to-floor connections.

It follows similar organization to the one presented in Chapter 4 for the injection anchors;

- **Chapter 6 – Analytical development**: focuses on analyzing the results obtained from the experimental campaigns described in Chapters 4 and 5, and on developing analytical tools that can be applied to design of retrofit solutions. Existing behavioral models, regarding different types of failure modes, were adapted to the damage observed experimentally on the retrofitted connections, resulting on strength prediction formulas. The hysteretic response of the connections was idealized to facilitate analytical and numerical implementation, by constructing bilinear and trilinear curves from the experimental backbone curves. From the idealized curves, performance criteria to be used on seismic retrofitted design were proposed. Finally, flow charts of the design of the two types of strengthening solution under study were also proposed;
- **Chapter 7 – Conclusions and Future work**: presents the main conclusions taken from the research developed in the previous chapters and suggests topics that need further development.

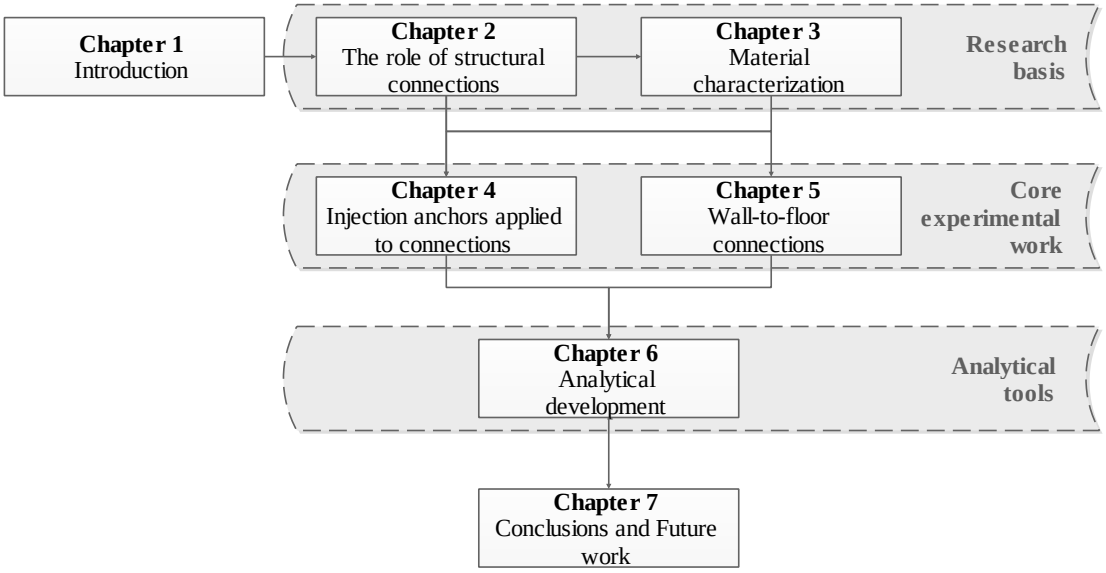

Figure 1.3 Outline of the thesis

Chapter 2. The role of structural connections

Highlights:

- Buildings built after the 1755 Lisbon earthquake until the 1930s, fitting the architectural styles of *Pombalino Tardio* and *Gaioleiro* are under scope;
- Out-of-plane collapse of masonry walls is one of the most observed failures in recent earthquakes;
- Inexistence or lack of proper connections is largely associated with out-of-plane collapse of masonry walls;
- Wall-to-timber framed wall and wall-to-floor connections present great variety but are common to unreinforced masonry buildings across the world;
- Different kinds of strengthening were developed over the years, but metallic straps is the most common one.

2.1 INTRODUCTION

This thesis is focused on the development of appropriate retrofit solutions for connections found in *Pombalino*, *Pombalino Tardio* and *Gaioleiro* buildings. As a result, this particular chapter starts by summarizing the historical background and structural systems of these buildings. Types of materials, dimensions of structural elements, and structural and architectural configuration of buildings was determined through literature review and a survey performed on the existing archive information of twenty buildings in Lisbon. The compounds of buildings chosen were located in areas where *Pombalino* or *Gaioleiro* buildings can be found, where the company Monumenta Lda. had photographic records of their interventions and there was the possibility of visiting the site. So, the buildings belong to compounds facing: Elias Garcia Av., Barbosa du Bocage Av., Liberdade Av., Conceição da Glória St., Glória St., and Fanqueiros St. The documents were obtained in the Archive of the Municipality of Lisbon (AML), which has records of alterations of existing buildings and construction of new buildings.

Due to the relationship between out-of-plane mechanisms of walls and structural connections' efficiency, this subject is also addressed in this chapter, accompanied by a comprehensive state-of-the art on existing types of connections and possible retrofit solutions.

2.2 HISTORICAL BUILDINGS BACKGROUND

2.2.1 Historical context

In November 1st of 1755 Lisbon, Portugal, was struck by one of the most devastating earthquakes ever, with an estimated magnitude of 9 and intensity of X in the Mercalli scale. After the earthquake, fires all over the city destroyed what it was left. According to Pereira de Sousa (1928), only 30% of the buildings were spared from this catastrophe, being 10% completely destroyed and the remaining 60% severely damaged. He also points out that high rise buildings and buildings located in alluvial areas suffered more damaged compared with the rest. It is not easy to quantify exactly how many people died, but official reports stated between 6000 to 8000 people. These large numbers were justified with three reasons: inadequacy of the structures to seismic actions, especially in tall buildings, disorganized urban tissue and finally panic. To sum up, Lisbon was not prepared to face this type of natural challenges, earthquakes (Ramos, 2000).

The 'Nova Lisboa' (New Lisbon) was born from the ideas of Manuel da Maia, Eugénio dos Santos and Carlos Mardel, following the illuminist ideals of Marquês the Pombal. The result

was a complex but structured urban net, with eight vertical main streets and nine horizontal ones, delimiting compounds (blocks) of buildings with symmetrical plans and limited height. One of the crucial parts of the plan was 'Terreiro do Paço', which would welcome everyone to this new city. This layout was able to solve the problem of disorganized urban tissue, which difficult the rescue of survivors.

Besides the urban chaos prevailing before the 1755 earthquake, there was the necessity to improve the structural response to earthquakes and fires as well as ensure fast reconstruction of the Portuguese capital. So, engineers and decision makers at the time thought about a series of rules that buildings should obey in order to account for this accidental actions. The buildings that respected standards regarding this configuration and general quality were called *Pombalinos*. With time, memories of the terrible earthquake started to fade and as reconstruction works were taking more time than predicted, construction techniques and quality of the materials started deteriorating. The so-called *Pombalino Tardio* and *Gaioleiro* buildings are products of this degradation, but they still maintain masonry walls and timber diaphragms as their main structural components. After them, came the advent of concrete changing forever the structural and architectural configuration of buildings (see Table 2.1). *Placa* typology of buildings got its name from the thin concrete slabs that substituted the timber floors, but it maintained the masonry walls.

Table 2.1 Chronology of buildings in Lisbon [adapted from Cóias e Silva & Soares (1997)]

Type of Building	Main structural materials	Period of Construction
Pre-Pombalino	Stone masonry	<1755
Pombalino and *Pombalino Tardio*	Stone and solid clay brick masonry and timber framed walls (*gaiola*)	1755 - 1870
Gaioleiro	Stone and hollow clay brick masonry with some structural timber elements	1870 - 1930
Placa	Masonry with some structural elements in concrete	1930 - 1940
Reinforced concrete frame structure and brick masonry	Reinforced concrete and brick masonry	1940 - 1960
Reinforced concrete	Reinforced concrete	>1960

2.2.2 Types of buildings

During 175 years, buildings evolved from *Pombalino* to *Gaioleiro* style, changing at the architectural and structural levels (see Figure 2.1). *Pombalino* buildings are inserted in blocks,

usually of seven buildings, constructed side by side around a central courtyard. So many aspects regarding structural and fire safety were taken into account that these buildings can really be considered truly innovative for that time. Going from the foundations to the roof everything contributes to the overall behavior and distinguishes them from other types of buildings. They are recognizable mainly for these distinguishable features: composition of the façade, 5 storeys at most, usually symmetrical plans, constant height from the 2nd to the 4th floor and of course, the three dimensional timber frame the so-called *gaiola* (see Figure 2.1a).

The *gaiola* is a three-dimensional timber frame (oak, holm-oak) constituted by a set of horizontal (*travessanhos*), vertical (*prumos*) and diagonal elements, which would provide resistance to horizontal loading and capacity to dissipate energy. Internal walls, above the ground floor, are structural shear walls composed by vertical and horizontal timber elements, braced by diagonals, forming St. Andrews crosses, with brick or rubble masonry infill (half-timbered walls). Examples of common cross-sections of these elements were: diagonals with 0.10×0.08 m^2, *travessanhos* with 0.10×0.10 m^2 and *prumos* with 0.14×0.10 m^2. The ground floor was built entirely in masonry, being used dry stone masonry for barrel vaults or clay brick masonry for crossed vaults. The remaining structural elements (walls, arches and columns), which supported these vaults were in dry stone masonry. Wreckages of the buildings destroyed by the earthquake were 'recycled' and used as infill for the vaults (Ramos & Lourenço, 2004). This floor was mainly used as a retail area, which required open spaces and large openings in the façade. To prevent the occurrence of a soft-storey collapse and to stop fire propagation to the rest of the building, the ground floor was solely built with masonry.

The external and party walls are rubble masonry walls with constant thickness through the height, usually 0.60 m and 0.50 m, respectively. Elements of the timber frame were embedded in the interior face of the masonry walls, approximately 0.05 m from the face, and connection between them and the wall was improved by means of timber connectors called hands (*mãos*) (Mascarenhas, 2004; Ramos, 2000).

The timber diaphragms were constituted by timber joists with a quadrangular section and spaced within the range of 0.3 m to 0.5 m. They were usually placed perpendicularly to the façade and would go into the wall between 0.2 m to 0.3 m. At the connection with the wall, the timber floor joist would be pinned between lower and upper timber wall-plates embedded in the wall.

The staircase was next to the main façade, providing natural light and easy access in case of rescue. One of the most common configurations was two straight flights of stairs per floor with a stair landing in between, being the first flight in the ground floor in masonry and the remaining

in timber. The stairs supported in three parallel walls, which was the fastest way to build them, and also prevented smoke propagation between floors.

Roofs were very well connected to the timber frame, mainly to prevent a pounding effect on the façade, which could cause overturning. They were composed by traditional timber trusses, with reinforced carpentry joints.

The facade follows strict architectural principles and shows regularity in height and length, not only for each building but also for the entire block. Decoration is rigid and poor, stonework is standardized and carefully designed to better resist vertical loads, usually 2nd floor has windows with balconies, 3rd and 4th floors have regular windows and the 5th floor has dormer windows (see Figure 2.1a). Usually the fireplace is located in the kitchen, thrown to the back of the building, leaning on a party wall (Mascarenhas, 2004).

Downtown Lisbon is characterized by its very soft and alluvial soil, which could had cause amplification of seismic waves and consequently more damage during the earthquake. There is also the problem of the high groundwater level. At the time of reconstruction, the wreckage resultant from the collapsed buildings, were used to do an embankment for the foundations of the new buildings. Timber piles were used as the preferable structural system, which was already used by some pre-*Pombalino* buildings. Foundations could be executed by means of masonry arches or masonry platforms supported by a timber grid, with elements of approximately 0.15m and connected by wrought iron dowels, directly supporting on timber piles, 1.5m long and with a diameter of 0.15m to 0.18m (Mascarenhas, 2004; Ramos, 2000).

As pointed out by Bento et al. (2005b) and Ramos (2000), the timber piles were very short and didn't reach solid rock, so their purpose was to stiffen the alluvial soil and to create a rigid platform above the water level. The evolution of *Pombalino* to *Gaioleiro* buildings was gradual and different characteristics took different shapes over the years, until their final configuration. In certain way, this justifies the variability found for both styles and the type of buildings in between (Mascarenhas, 2004). distinguishes three phases of the *Pombalino* buildings, the first concerns the original buildings as described previously, the second one regards some changes in the configuration of the plan and structural elements, *Pombalino Tardio*, and the last one can be considered a completely different style, the *Gaioleiro* (see Figure 2.1b).

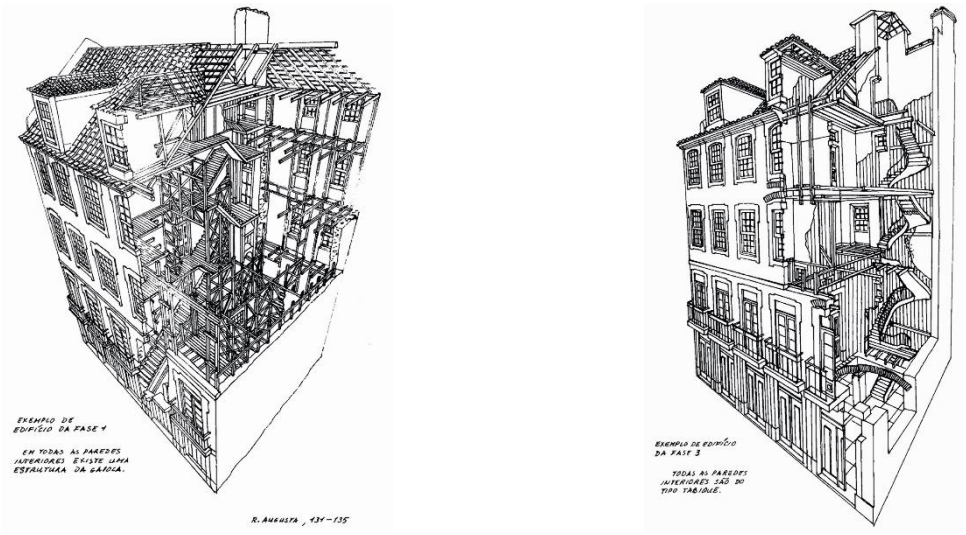

(a) (b)

Figure 2.1 Typologies of buildings: (a) *Pombalino* building and (b) *Gaioleiro* building [in Mascarenhas (2004)].

Regarding the non-structural changes, several buildings do not respect the strict decoration of the façades and its configuration. Windows vary in type, shape and disposition at the same floor level or in alternate floors. The stonework is more elaborated and less standardized. Three areas can be distinguished on the façade (the so-called *soco*, an intermediate zone and the parapet wall) due to the excessive decoration.

As said before, the original plans had the staircase right behind the façade, which restrained the layout of the building. In time the staircase migrated to the back, near the external wall, and then to the interior of the building, starting the use of skylights and light-shafts. Since the apartments were narrowing, these sources of natural light and ventilation became a necessity, as well as a longitudinal corridor across the apartment. The appearance of the *marquise*, which basically resulted from covering the balconies on the back of the building, was also one away of increasing usable space.

At the structural level, these types of buildings represent a degradation of the quality present in *Pombalino* buildings, by disregarding material quality, structural connections and mainly the importance of the timber frame. The second phase buildings, the *Pombalino Tardio*, just kept the timber framed interior walls (St. Andrews cross) in the North-South direction (the direction of the earthquake) while in the other direction walls were no longer structural (Mascarenhas, 2004). The last ones were built using the lath and plaster process. For third phase *Gaioleiro* buildings, partition walls lost completely their seismic structural function. These walls were made of timber elements (vertical and horizontal) with perforated brick infill or they were built using lath and plaster technique. The second ones were thinner and usually were perpendicular

to the façade. Since the idea of the timber frame was lost, there was no need to keep the timber elements embedded in the masonry walls (see Figure 2.2).

For *Gaioleiro* buildings, the thickness of the masonry external walls decreased with height, making more difficult to assure a good connection with the pavement beams. They also had five to seven floors, increasing the dead load of the structure and vulnerability to horizontal actions. *Pombalino Tardio* buildings are the transition between *Pombalino* and *Gaioleiro*, which allow these buildings to have characteristics of both.

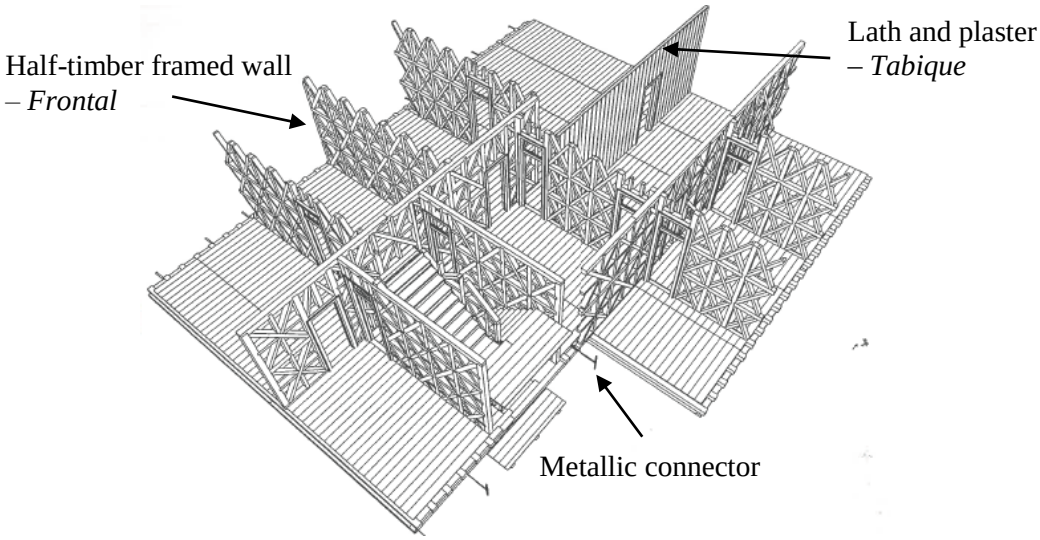

Figure 2.2 Interior of a *Pombalino Tardio* building (adapted from Cóias e Silva, 2007).

Besides the buildings which initially belong to a different style, there are a lot of changes performed in original *Pombalino* and Late *Pombalino* buildings, which also diminish their seismic response. The most common alterations are substitution of the dormer windows in the last floor for mansard roofs and increase the number of floors, creating additional habitable space. Since most of these buildings are in downtown Lisbon, they were adapted to fit commercial and office purposes. To apply the concept of open space, timber framed walls and masonry columns were demolished, creating the opportunity of soft-storey failure in case of seismic activity. Besides taking away entire walls, sometimes the timber frame is corrupted by cutting the diagonal elements to place plumbing inside the walls (Cardoso, 2003). Other important and severe alteration concerns the substitution of timber and masonry structural elements for similar elements in concrete and steel. An estimate provided by Ramos (2000) citing Silva (1999) determined that 80% of the *Pombalino* buildings still have their original structure. When analyzing a particular compound of buildings (Martinho da Arcada, near Comércio Square), Ramos (2002) verified that it was profoundly modified, being far away from the percentage suggested before. He observed that more than 50% (in average) of the structural

system had been deeply changed, with substitution of existent structural elements for slabs and walls of new materials. Only 20% of the block presented its initial structural configuration and the remaining showed some minor alterations (removal of one to two walls or incorporation of new elements, without changing the structural system). Some of the buildings of this compound are part of the survey presented in this thesis.

2.2.3 Materials

The importance of timber in construction decreased from *Pombalino* to *Gaioleiro* buildings, being its structural use reduced exclusively to the floor joists. The type of timber used at the time is much better characterized than the masonry, because it was the main material of the seismic resistant structure. The timber structural elements of *Pombalino* buildings were commonly made out of oak (*quercus faginea*), while the ones from *Gaioleiro* buildings were commonly made out of maritime pine or scots pine (Appleton, 2005).

Masonry is a composite material, depending on the type of mortar, units and assembly to define its properties and behavior. Stone masonry was mainly used in the confining walls of each building (external, separation and light shaft walls), but it could also work as infill of the timber framed walls. As shown in Figure 2.3, the rubble masonry is composed by irregular limestone units, of different sizes, bound together by a poor mortar, forming an unorganized mixture. These walls are built stone by stone, arranging them in the best possible way and feeling the voids with mortar. The mortar resulted from the mixture of air lime and sand, usually in the proportion of 1:2, but could take other ratios like 1:2.5, 3:5 or 5:9. Existing material descriptions specify that the sand should be of good quality, without clay and from a specific place of pine trees, probably referring to Leiria. They also prescribed that the stone should be a soft stone, like limestone, of good quality and should come from Monsanto or Sacavém.

Brick masonry was also used in vaults and arches on the ground-floor but also in some walls of *Gaioleiro* buildings. This type of masonry was much more regular and performed with solid clay bricks (or perforated bricks for ‘Gaioleiros’) and mortar of 1:2, as described previously. A regular assembly, with well-defined units and courses, leads the structural element to present more of an in-plane orthotropic behavior than an irregular assembly, which has no specific orientation of properties and can be assumed isotropic.

How to choose a proper constitutive law for the materials is a true challenge that has profound consequences in results. Besides the initial material properties, one has also to consider evolution over time and its impact on results. Silva & Soares (1997) citing Lopes & Azevedo (1996) refer intervals from 0.8 MPa to 1.5 MPa for the compressive strength of a

Pombalino building and they also state an interval from 700MPa to 900MPa for the modulus of elasticity of a *Gaioleiro* building. Pinho, (2008) citing Segurado (1908) suggests values between 0.5 MPa and 1.0 MPa to the compressive strength of an irregular masonry with a poor mortar of 1:3 (air lime: sand), which has close characteristics to the ones described previously.

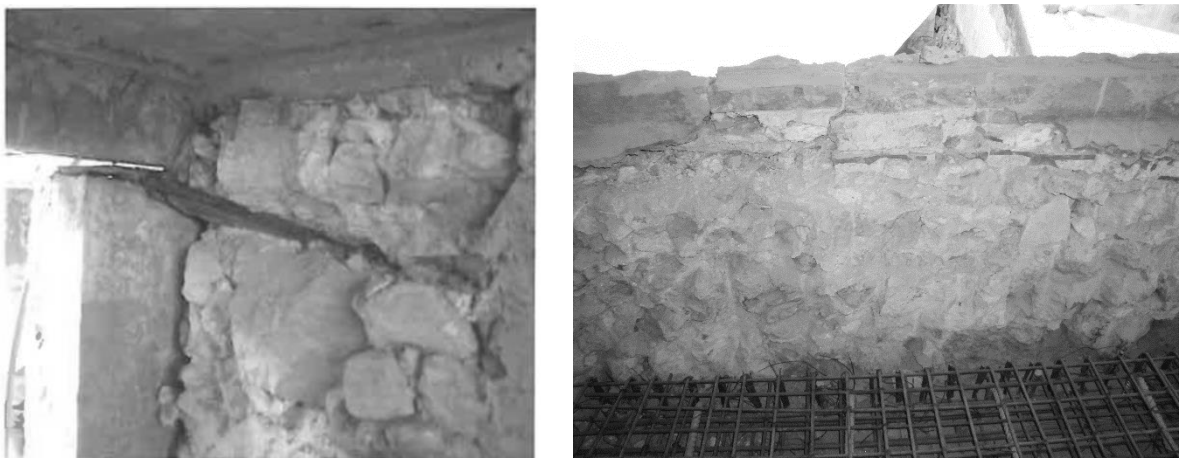

(a) (b)

Figure 2.3 Cross-section of peripheral masonry walls of *Pombalino* building: (a) in Appleton (2009); and (b) taken in Liberdade Av.

The National Laboratory of Civil Engineering (LNEC) performed tests on structural walls (masonry panels and half-timbered walls) retrieved from a *Pombalino* building. The masonry specimens are mainly composed by limestone and fragments of brick with mortar (proportion is not mentioned) and they were removed from a wall that separates buildings. Monotonic tests were performed on the 3 specimens, with dimensions around 0.72 × 0.79 × 1.00 m^3, taking them to failure. Compressive strength reached approximately 0.85 MPa and the modulus of elasticity was estimated in 1000 MPa (tangent value taken at 0.3 of the maximum compressive strength of the force-displacement curve), which agree with the estimated intervals presented previously.

The three half-timbered walls were approximately 0.20 m thick, 2.50 m long and 3.50 m tall, had 6 St. Andrews crosses each and had rubble masonry infill, similar in composition to the masonry panels. Since they are shear walls, besides the constant vertical load, a cyclic horizontal load was applied at the top of the specimens to obtain the hysteretic behavior. Measured shear strength was around 0.12 MPa and the modulus of elasticity was approximately 50 MPa (Ramos, 2000).

2.3 OUT-OF-PLANE SEISMIC BEHAVIOR OF URM BUILDINGS

Before concrete and steel, masonry alone or combined with wood was the material most used in construction. Nowadays, the use of those buildings goes from housing or offices to key

infrastructures like schools, hospitals and government facilities. One must not forget that most of the really cherished monuments and world heritage or historic city centers mainly consist of masonry structures, more specifically unreinforced masonry (URM) structures. Typical URM buildings are constituted by loadbearing masonry walls and flexible timber diaphragms (Magenes & Calvi, 1997). Unfortunately, this type of construction is considered one of the most seismically vulnerable types (Bruneau, 1994; Tomaževič, 1999). Considering that unreinforced masonry stopped being a primordial structural material by the 50s, the collapsed buildings causing economical and human loses are old, and probably need to be retrofitted.

Information regarding structural connections involving masonry walls is scarce and descriptions have great variability, mainly because their observation requires demolishing parts of the walls, and there are many aspects that can change for each building.

In this thesis, the designation masonry-to-timber connections refers to the connections between masonry walls and timber floors (wall-to-floor connections) and masonry walls with timber framed walls (wall-to-timber framed wall connections). Connections with timber roofs are not within the scope of this research, but some constructive details and strengthening solutions are similar to the ones performed for wall-to-floor connections.

Under the light of several surveys conducted over the last 30 years, URM buildings have shown similar damage patterns, in spite of location, material or structural layout, as pointed out by Tomaževič (1999). Bruneau (1994) giving more attention to the cause of failure established six categories, which are intrinsically related between them and with the typical damage patterns described by Tomaževič (1999), which are presented in Table 2.2.

Damage patterns related with cracks between walls and floors, cracks at the corners and at wall intersections, and out-of-plane collapse of peripheral walls result from out-of-plane bending of the walls. On the other hand, cracks in spandrel beams and diagonal cracks in structural walls clearly reflect the in-plane behavior of walls, when shear and flexure capacities are mobilized (see Figure 2.4). Either behaviors or their combination can be responsible for partial or total disintegration or collapse.

The in-plane behavior of walls is controlled by the geometry and the quality of the material of piers, spandrels, and openings. In-plane failure modes display in general high to moderate ductility, which makes them desirable to control the behavior of URM buildings. New design codes explore the in-plane capacity of walls, by preventing the occurrence of out-of-plane mechanisms, yet this behavior is a major concern when addressing old URM buildings. Figure 2.5 gives a general overview of the in-plane mechanisms in URM buildings. Commonly

observed and well documented in-situ failure modes are: pier rocking/toe crushing, bed joint sliding, diagonal tension, and foundation rocking (ATC-43 Project, 1998).

Table 2.2 Seismic damage patters and causes of failure.

Cause (Bruneau, 1994)	**Damage** (Tomaževič, 1999)
Lack of anchorage;	Cracks between walls and floors;
Anchor failure;	Cracks at the corners and at wall intersections
In-plane failure;	Out-of-plane collapse of peripheral walls
Out-of-plane failure;	Cracks in spandrel beams and/or parapets
Combined in-plane and out-of-plane effects;	Diagonal cracks in structural walls
Diaphragm-related failures.	Partial disintegration or collapse of structural walls
	Partial or complete collapse of the buildings

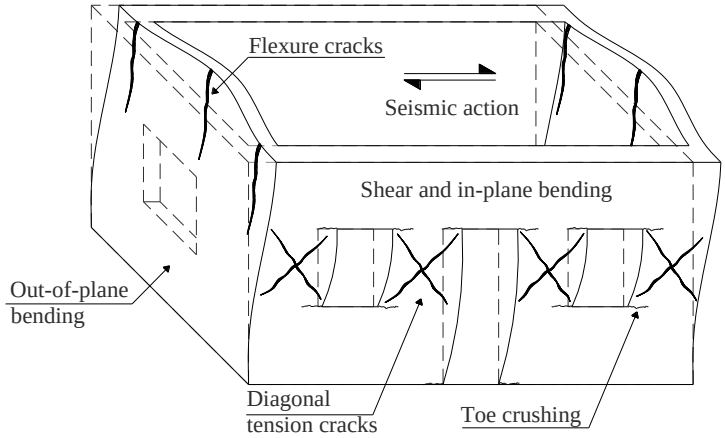

Figure 2.4 Damage on URM buildings due to seismic action [adapted from (Tomaževič, 1999)]

Anchors tying opposite parallel walls or walls to floors are the oldest and most common solution when it comes to strengthened buildings against seismic action. In many URM buildings, joists are simply supported on a pocket hole in the wall, relying only on friction to sustain the seismic demand. Although it can be enough to low dynamic excitation, for higher demands it can lead to slippage of the joists ends from the support, causing complete collapse of floors. When no positive anchorage exists between floors and walls, the walls have no horizontal restrain, and consequently behave like cantilevers over the total height of the building. This behavior can lead to appearance of vertical cracks on walls intersections or to complete overturn of the peripheral walls, as listed in Table 2.2.

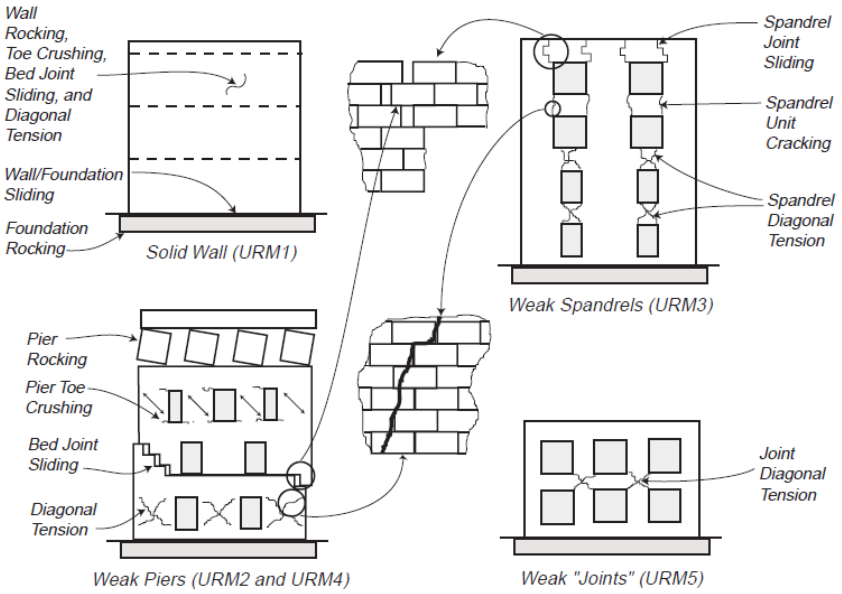

Figure 2.5 In-plane failure mechanisms [in FEMA 306 (ATC-43 Project, 1998)].

Anchor failure can occur by yielding of the iron/steel anchor, by cone shear breakout of the masonry, or by crushing of the masonry under the anchor plate. These failure modes depend on the anchor being used, on the quality of masonry, and ultimately, if they exist in sufficient amount and how they are distributed. By failing, these anchors will not provide the desired box-behavior, which can lead to out-of-plane failure of the walls. When the connection between walls and floors is efficient, by means of constructive details or efficient wall-to-floor anchors, the out-of-plane failure of walls is restricted to the height spanning between positive connections, instead of the total height of the building (see Figure 2.6a).

Non-structural components like parapets or other small and thin components like gables are extremely vulnerable to out-of-plane collapse because of the amplification of the seismic ground motion at the top of buildings. Usually, these partial collapses do not compromise the global stability of the buildings but constitute great danger to the surroundings of the building. In multiple leaf, cavity, and veneer masonry walls can occur separation of their layers, which usually causes collapse of the outer layer (see Figure 2.6b). In Figure 2.6c, d depict the cases where overturning rips part of the corner of the in-plane wall and where there is a good connection at the top of the building leading to formation of a hinge on the discontinuity.

Corner damage usually appears at the intersection of the roof and walls, due to a combined effect of in-plane and out-of-plane behaviors of the walls, in moderate dynamic excitations. The combined causes can be: lack of shear anchorage capable of transfer the in-plane deformation of the flexible diaphragms to the reaction walls, lack of connection restraining the horizontal

span of the wall, and excessive tensile demands on the head and bed joints at the pier/spandrel intersection near the corner (ATC-43 Project, 1998).

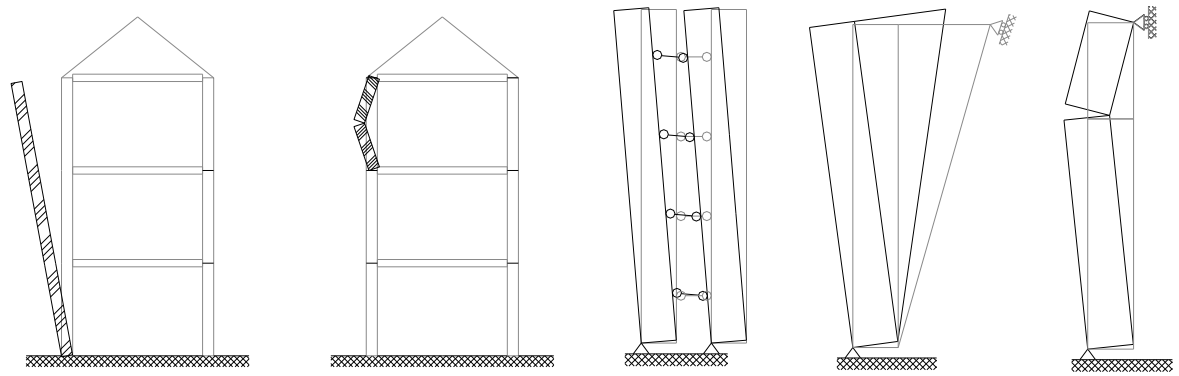

Figure 2.6 Different types of overturning of a façade (adapted from Binda & Saisi, 2005)

Past and recent post-earthquake surveys have shown that in spite of the high vulnerability of URM buildings, some buildings are able to sustain moderate to severe seismic excitation without walls' overturning. Many of the URM buildings that "survived" to high seismic demand are demolished instead of being rehabilitated, because they do not comply with the requirements imposed by existing assessment codes. The fact is that during post-cracking behavior, the wall is governed by stability mechanisms and can achieve large displacements trough rocking, which are not considered in most of the analysis procedures. Recently this ability has been recognized and doors have been open to displacement-based approaches applied to out-of-plane performance of walls (Doherty et al, 2002; Griffith & Ferrata, 2003).

Better quality of masonry and timber, combined with efficient connections between walls and floors can prevent early out-of-plane collapse of walls and exploit in full, the in-plane capacity of walls. Steel ties connecting perpendicular walls is another strengthening solution capable of inducing box-behavior of the URM building and activating global failure mechanisms.

2.4 MASONRY-TO-TIMBER CONNECTIONS

Masonry walls can be found extensively described in literature, according to their different configurations (e.g. rubble, ashlar and coursed) and materials (e.g. stone, brick and adobe) (Pinho, 2008; Oliveira, 2003).The same applies to timber floors and walls, whose configurations are also well known (Cestari & Lucchio, 2001; Parisi et al., 2009). As primary structural components, their structural behavior to static and dynamic actions, as well as possible retrofitting techniques have been source of study, both experimental and numeric, over the past 40 years (Yi et al., 2006; Paquette & Bruneau, 2006; Brignola et al., 2008).

The same cannot be said about connections between both elements. Even if their importance has been recognized for a long time as one of the main causes of out-of-plane collapse and other damages, the topic has been "neglected" over time. It is difficult to collect information about masonry-to-timber connections because usually they are not at sight on the finished building and drawings of old URM are not available. On post-earthquake surveys, due to safety issues, assessment is conducted from outside the URM buildings, so no information is retrieved about the conditions of the connections and the timber diaphragm (Bruneau, 1994).

Considering the above reasons, a brief description of some of the most common wall-to-timber framed walls and wall-to-floor connections is presented next.

2.4.1 Wall-to-timber framed walls

Dating back to the Romans, timber-laced masonry construction has been used all over the world, showing different particularities depending on location but also sharing common principles. It can be divided into two main categories: timber-frame with infill masonry and horizontal timber-laced bearing wall masonry. The first category, as the name states, encompasses the walls constituted by a timber frame, composed by a combination of vertical, horizontal and diagonal members, with and a non-structural infill of masonry (rubble, coursed brick. As part of this group are the *dhajji-dewari* in India, the *colombage* in France, the *fachwerk* in Germany, the *himis* in Turkey, the *half-timber* in the UK, the *entramados* in Spain, the *Casa baraccata* in Italy, and the *frontal Pombalino* in Portugal (see Figure 2.7). These last two types of half-timber walls were developed as anti-seismic solutions, after the occurrence of two major earthquakes, the 1755 one in Lisbon and the 1783 one in Calabria and Sicily (Langenbach, 2007).

The second category corresponds to load bearing masonry walls, usually peripheral walls, that incorporate horizontal timber ties (embedded), working as reinforcement in the wall. It has been mainly been observed in India and Greece (Langenbach, 2007). Timber horizontal ties in masonry can have different arrangements within the thickness of the wall, which can go from a single longitudinal element located at mid cross-section to a timber elements with width equal to the thickness of the wall, in extreme cases. It is also suggested that timber wall-plates placed longitudinally on the masonry wall, not only distribute vertical loads from the timber joists as they increase the deformability of the masonry (Vintzileou, 2008).

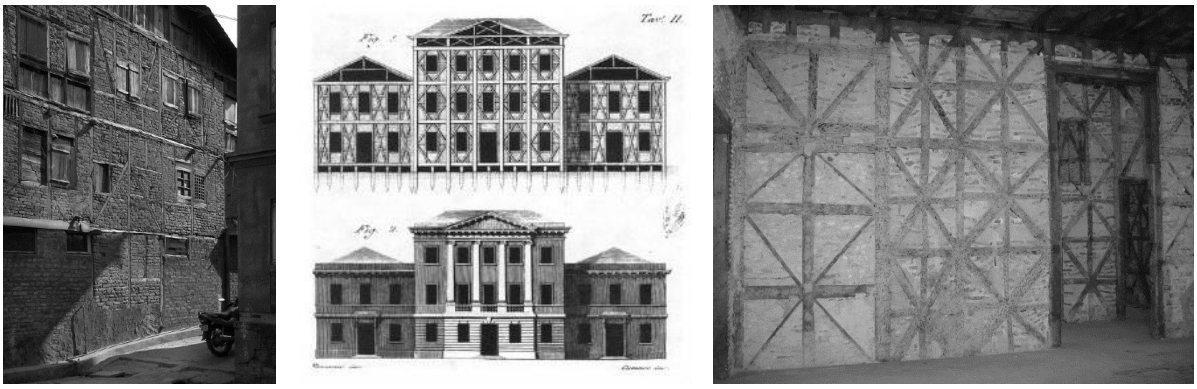

(a) (b) (c)

Figure 2.7 Timber-framed construction: (a) *dhajji-dewari* in India (Langenbach, 2007); (b) *Casa baraccata* in Italy (Vivenzio (1783) in www. architetturaecosostenibile.it); and *frontal Pombalino* (by Monumenta Lda.).

As already mentioned, *Pombalino* buildings were the engineering answer to the destruction of downtown Lisbon, by the 1755 earthquake. The solution consisted of a mixed construction of masonry and timber, where a three-dimensional timber frame (*gaiola*) was incased by external masonry walls. The main elements of this timber "cage" were the half-timbered shear walls, with a frame composed by St. Andrews crosses with masonry infill that could be rubble stone or solid brick (Ramos & Lourenço, 2004). Horizontal ties and vertical struts were present in the inner face of *Pombalino* buildings, ensuring connections to timber floors and half-timbered walls, and possibly improving the behavior of the URM walls. Half-timbered walls connecting perpendicularly to loadbearing masonry walls can be found in *Pombalino* and *Pombalino Tardio* buildings, as well as in some buildings in the north and center of Portugal (Pinho, 2008). Figure 2.8 shows some of the possible connections found in previous researches, which all have at least the intermediate horizontal timber element penetrating the wall (C1 to C5), with exception of configuration C6. In this case the only connection is ensured by the timber floor joists that connect the half-timbered wall at the top and bottom (Cardoso, 2003).

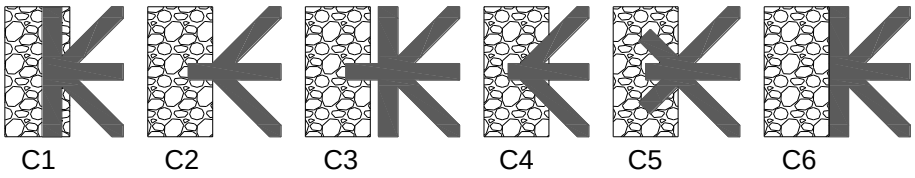

Figure 2.8 Possible connections between the masonry wall and the timber frame wall (adapted from Cardoso, 2003).

The configurations of the connections presented in Figure 2.8 lead to different behaviors and account for different variables, when subjected to horizontal actions. As seen, the geometry and the anchorage length of the timber elements inside the wall play a major role on determining the behavior of the different setups. Connections type C2 and C3 rely mainly on friction

between timber and masonry, while the remaining ones can also consider the shear contribution of the masonry wall, especially connection type C5. From a site visit performed to a *Pombalino* building in Liberdade Avenue, in Lisbon, it was possible to observe a C1 connection type, where the timber strut was embedded 5 cm from the face of the wall (see Figure 2.9a). In Figure 2.9b, is presented a *frontal à galega*, similar to a configuration called *franceza* in the center of Portugal, where one can see four points of connections with the masonry wall: two by the timber floor joists and other two of the type C4 (Pinho, 2008).

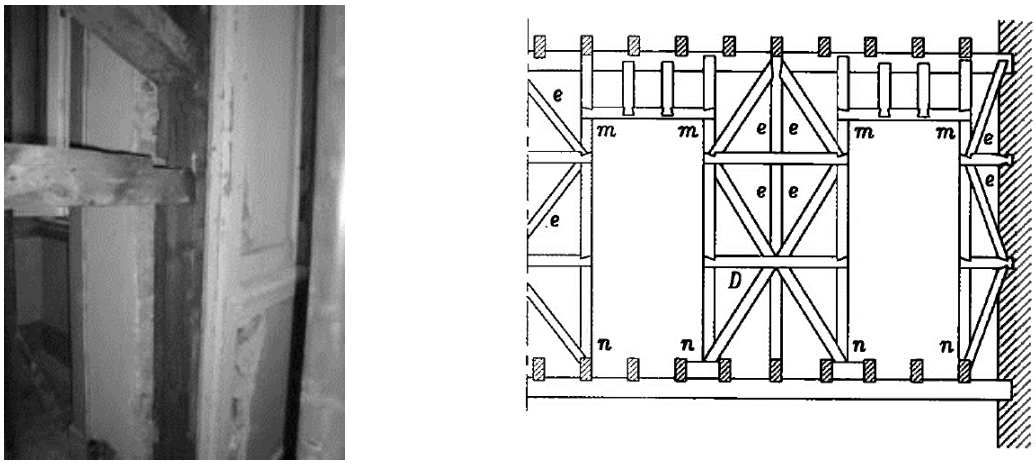

(a) (b)

Figure 2.9 Wall-to-timber framed wall connections of a *Pombalino* buildings: (a) photograph of type C1; and (b) sketch of type C4 (in Pinho, 2008).

Cóias e Silva, (2007) describes some *in situ* pullout tests carried out on connections from type C1 to C5 in a *Pombalino* building. No information is provided about anchorage length, the story where the connection was found, or any other significant details. However, the pullout horizontal forces obtained in the tests ranged from 1.5 kN to 6 kN. Such a limited capacity contrasts with the resistant capacity of the masonry and half-timbered walls, suggesting the necessity of strengthening solutions to improve load transfer between both structural elements. This is critical since this type of connection connects elements with very different stiffnesses, strengths, and therefore behaviors. The masonry wall, with a much larger stiffness and mass, dictates the out-of-plane behavior. Thus, it is necessary to anchor the flexible timber frame to the masonry in order to expect effective resistance to out-of-plane failures during a seismic event (Bento et al., 2005b).

2.4.2 Wall-to-floor connections

Commonly in URM buildings, wood diaphragms and masonry walls are the main structural members that resist vertical and lateral loads. Therefore, it is crucial to ensure proper load

transmission between these two elements, as discussed in section 2.3. There is a great variety of wall-to-floor connections, but most are common to URM buildings all over the world.

Some of the oldest considerations on how to perform appropriate connections between timber floor joists and masonry walls are summarized in Cestari & Lucchio (2001). Bearing the timber floor joist on a stone corbel connected to masonry by means of cramps, copper clasps or iron cramps is one of the oldest recommendations, proposed by Alberti (1485) and Milizia (1785). The recommended depth of a joist bearing directly on the wall varied from author to author, but in general it was recommended that the fixing depth should be between 0.25 and 0.30 m, depending on the thickness of the wall. Other recommendations contemplated fixing the joist to a depth equal to half or the entire thickness of the wall, depending if it was thick or thin, respectively (Scamozzi and Valadier, 1831), or anchoring the joist 0.32 to 0.35 m for a masonry thicker than 0.50 m or with timber sections of considerable dimensions (Cestari & Lucchio (2001) citing Emy (1856)). For floor joists supporting on timber wall-plates, it was recommended that they were connected by a mortise and tenon joint type and that dimensions of the wall-plate sections should be between 0.12 and 0.15 m. In 1880, it was suggested by Emy (1856) that the wall plate should rest on 3/4 of the entire thickness of the walls or on stone corbels similar to was is depicted in Figure 2.10a. Stone corbels are common in connections found in constructions of higher quality (e.g. palaces and castles) like the ones seen in the Abbey of Santa Maria la Real de Las Huelgas, in Spain (see Figure 2.10b) or in other structures of high cultural significance.

As already explained for the wall-to-timber framed walls, connections of *Pombalino* buildings were more elaborate than in other types of construction of the same period (1755-1870). The timber floor joist would be connected to a top and bottom timber wall-plates embedded in the masonry wall (see Figure 2.11a), through carefully done cross-lap joints and the use of 8 cm to 30 cm nails (Mascarenhas, 2004; Appleton & Domingos, 2009). It was common practice the use of metal straps nailed to the timber joists and going through or into the wall. These iron straps were placed on joists both perpendicular and parallel to the wall, as seen in Figure 2.11b. Mascarenhas (2004) states that in most cases the timber floor joists were perpendicular to the façade, and contrary to what one might think the iron straps would go deeper into the party walls than the façades.

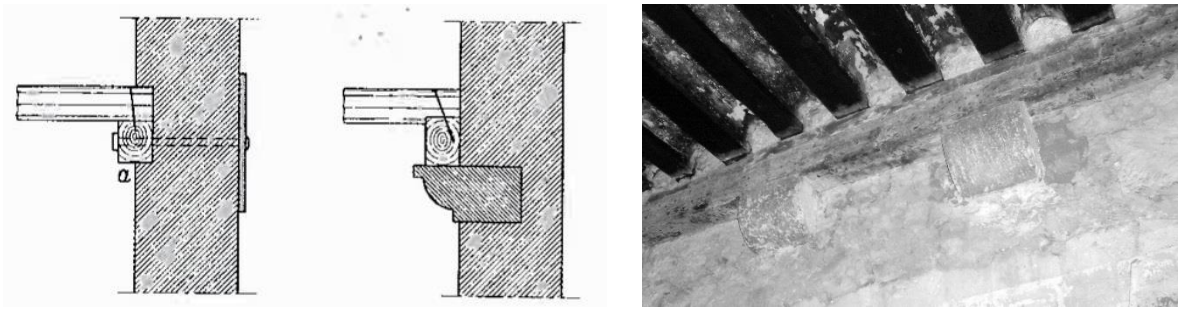

(a) (b)

Figure 2.10 Wall-to-floor connections found in: (a) URM walls without embedded timber elements (in Pinho, 2008); and (b) Ducal Palace in Guimarães, Portugal.

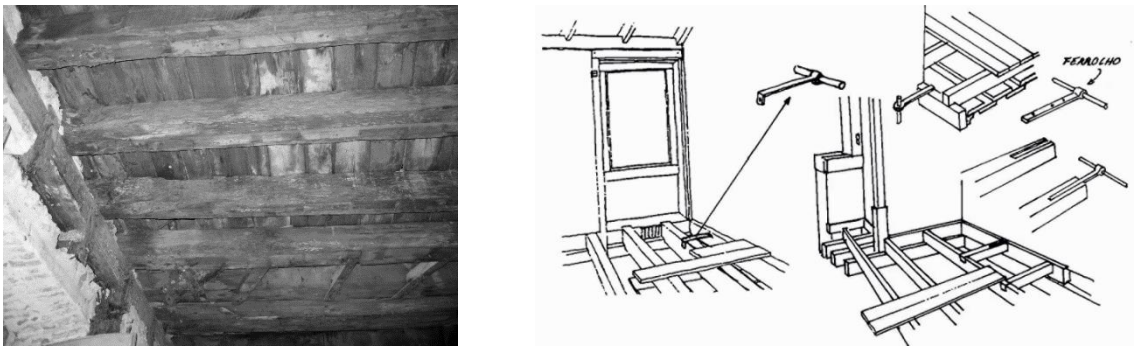

(a) (b)

Figure 2.11 Wall-to-floor connection found in *Pombalino* buildings: (a) in Comércio st.; and (b) sketch in Mascarenhas (2004).

In Lisbon, towards the end of the 19th century and beginning of the 20th century, connections and general quality of the buildings started decreasing. There is not a lot of information regarding connections of *Pombalino Tardio* buildings but as transition buildings, connections must reflect this aspect. Construction details were found in the survey performed in AML and it was possible to confirm the transition theory regarding connections. This connection no longer displays the double timber wall-plate pinning the floor joist, as found in *Pombalino* buildings, but still maintains the carpentry joint with the bottom wall-plate (see Figure 2.12a). This carpentry joint is absent in connections of *Gaioleiro* buildings as shown in Figure 2.12b. From the survey, it was also possible to observe that in most cases the timber joists were placed perpendicularly to the facades.

In Figure 2.13 are presented some of the typologies of connections that exist in *Gaioleiro* buildings. The first solutions contemplate the timber joist supporting directly on the masonry pocket hole, the previous configuration with a timber tie improving anchorage, and the timber joist nailed to a timber wall-plate along the masonry wall (see Figure 2.13a). For better quality buildings, a cross-lap joint was executed between timber elements. Usually this wall-plate is embedded 5 cm relatively to the interior face of the wall. Later configurations, executed at the beginning of the 20th century, already included wrought iron/steel ties and corbels, as the ones

presented in Figure 2.13b (Appleton, 2005). These configurations had to adapt to the decrease of thickness of the walls over the height of the building, since the pocket hole in the masonry wall was not possible anymore.

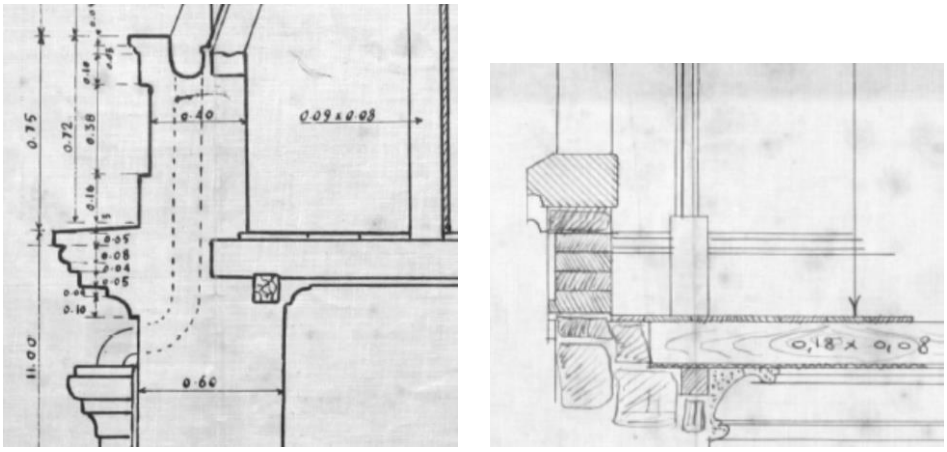

(a) (b)

Figure 2.12 Details of a wall-to-floor connections found in the survey: (a) in a *Pombalino Tardio* building; and (b) in a *Gaioleiro* building.

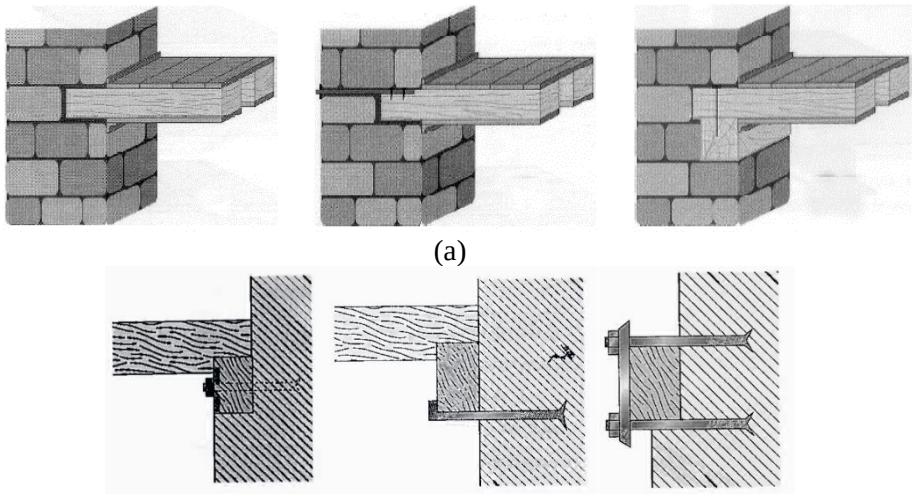

(a)

(b)

Figure 2.13 Typologies of wall-to-floor connections of *Gaioleiro* buildings: in the end of the 19th century; and (b) beginning of the 20th century (Appleton, 2005).

In one of the simplest and oldest typologies of wall-to-floor connections, the timber floor joist rests on a pocket hole in the masonry wall, leaving a gap between the joist's end and the end of the pocket hole. This type of connection is found in buildings built until the beginning of the 20th century, in Portugal (Pinho, 2008), in Italy (Cestari & Lucchio, 2001), in the United Kingdom (University of the West of England, 2009), in the US (Peralta et al., 2004) and in New Zealand (Wilson, Quenneville, & Ingham, 2011), as shown from Figure 2.13 to Figure 2.15.

As seen in Figure 2.14, connections in the UK are very similar to the ones adopted in countries like Portugal or Italy, but mainly applied to brick masonry. Recent solutions that rely

on steel joist hangers to ensure the connection are spread out across the world and are seen in reinforcement masonry buildings.

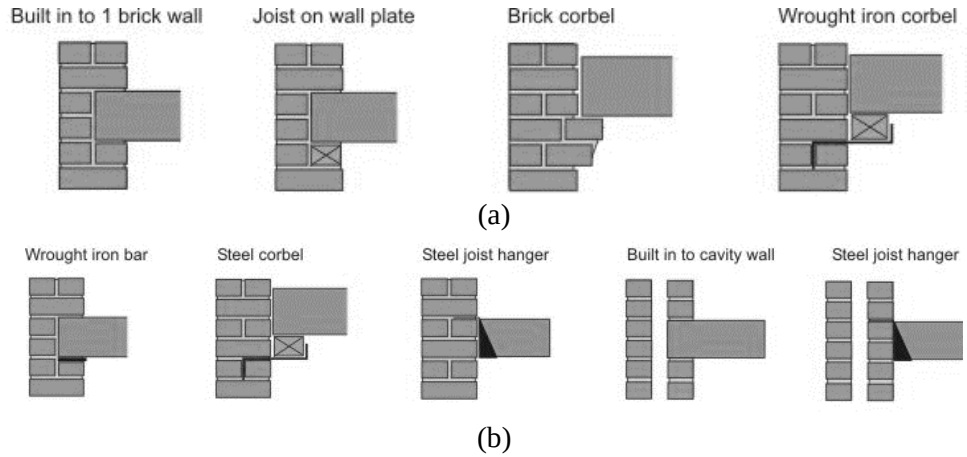

Figure 2.14 Drawings of wall-to-floor connections found on masonry buildings in the UK: (a) late 19th century; (b) in the 1930s (University of the West of England, 2009).

Lin & LaFave (2012) and Peralta et al. (2004) studied this type of connections in typical pre-1950s brick buildings, in the United States, where the joists ends were cut diagonally (firecut) and rested in pocket holes, in the masonry wall (see Figure 2.15). With a small bearing length of approximately 76 mm at the support, the joists were anchored at every fourth joist with iron straps. These were common for joists perpendicular to the wall but not for parallel ones. In Figure 2.15a is visible the brick corbel, similar to the one constructed in the UK, in the late 19th century. Figure 2.15b provides details of a perpendicular and parallel to the wall connection of the floor joists, where is possible to see details of the wall through anchors, the floor sheathing and the diagonal bridging.

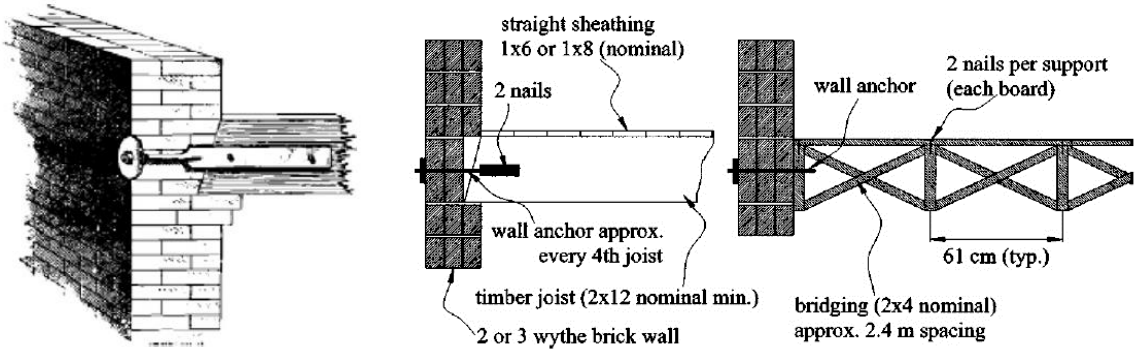

Figure 2.15 Drawings of wall-to-floor connections from pre-50s buildings in the US (Lin & LaFave, 2012; Peralta et al., 2004).

2.4.3 Types of retrofit for connections

Retrofitting of buildings can be addressed from the point of view of reducing seismic demand or improving the resistant capacity of the building. Typical URM buildings, especially

the ones in stone masonry, are rigid structures with low periods of vibration. In theory, reducing the weight of the structure would make the period decrease even more and consequently, reduce seismic demand. On the other hand, mass has a stabilizing effect, when walls are subjected to overturning mechanisms. Thus, removing upper stories or non-structural components (e.g. parapets), or replacing timber floors with heavier concrete floors are solutions that must be carefully analyzed for each structure. Increasing the capacity of a structure can be done by enhancing strength and/or ductility of the existing materials (e.g. reinforcing masonry or grouting, adding extra floor sheathing), substituting them or developing composite solutions with greater strength and/or stiffness (e.g. concrete layer on existing floors or walls, ring concrete beams) and improving overall behavior (e.g. steel ties, wall-to-floor connections, steel diagonal bracing) (Tomaževič, 1999; Public Works and Government Services Canada, 2002; Senaldi et al., 2014).

Efficient seismic retrofit design results from balancing the elastic response (elastic energy) of the structure with the non-linear one (dissipated energy). Energy dissipation can be obtained by increasing the viscous damping coefficient or the hysteretic energy through plastic deformation. Base isolation and viscous dampers address the first kind of energy dissipation, but are not within the scope of this thesis since no appropriate solutions are developed for connections (Fajfar & Krawinkler, 2005).

Retrofitting connections has the main purpose of assuring continuity between the different structural elements being connected. Most of the solutions presented show wall-to-floor connections, but they can be extended to wall-to-timber framed wall connections as well.

Anchor systems are composed by two main parts: anchorage to the wall and connection to the timber joist. First solutions contemplated the iron strap as anchor, which could be into or throughout the wall, anchoring on the exterior face, and it would be nailed to the timber joist, as seen in Figure 2.15 and Figure 2.16. For anchors going through the wall, the anchor plate could have several shapes, being the more common ones: a simple iron bar, squared or circular plates, and in the US, star shaped plates.

With time, nailed solutions gave place to bolted solutions since they provide better shear and pullout behavior. Tomaževič (1999) proposes a strengthening solution with double steel anchors aligned with the longitudinal axis of the floor joist, which decreases the possibility of eccentric behavior to tensile and shear forces (see Figure 2.17a). Strengthening applications on the top or bottom of the joist do not take advantage of the symmetrical behavior of the connection, but are more cost-effective solutions, as the one displayed in Figure 2.17b. FEMA 547 (2006) suggests some constructive details to anchor perpendicular and parallel joists

to the wall like the use of high grade stainless steel anchors, anchor plates in stainless steel, galvanized or painted with a protective coating, and rotary drilling without percussion for brick or coring with diamond tipped blade for hard stone. Another possible anchor system to the wall is injection anchors, which have been applied in masonry since the 1920s in Germany (Gigla, 2004; CEB, 1994). The installation of injection anchors is advantageous in comparison to tie rods and anchor plates since injection anchors require access from only one side of a wall, which facilitates interventions on façade and party walls. Since the grout injection is contained by the woven sleeve, there is greater control over the amount of grout injected. The solution of Cóias e Silva (2007) presented in Figure 2.18a incorporates the use of injection anchors and the connection to the floor joist is ensured by a bolted steel angle. Strengthening solutions presented in Figure 2.18 were developed specifically to *Pombalino* and similar buildings but can be adopted to many other connections. Figure 2.18b presents a system to retrofit wall-timber framed wall connections that consists of tie rods with anchor plates, alternating between sides of the wall and reinforced with GFRP layers on the timber joints.

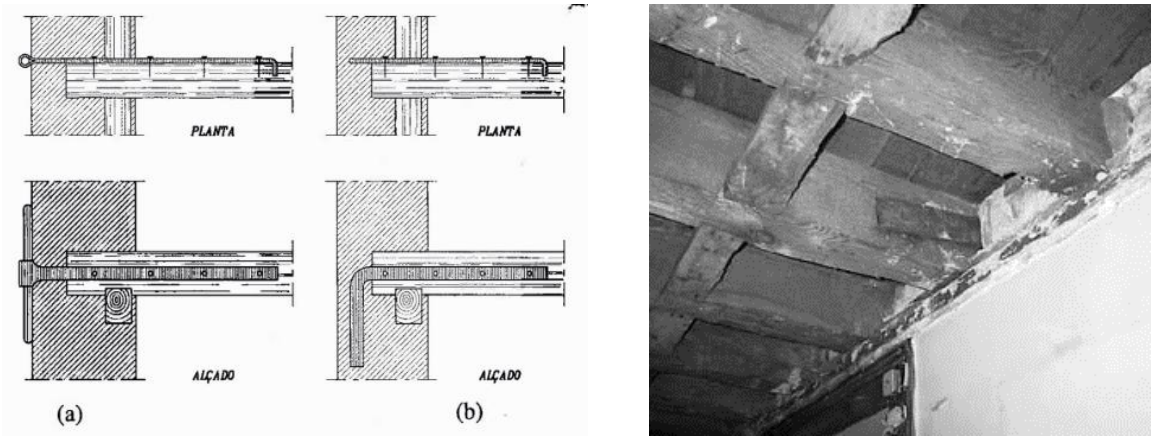

(a) (b)

Figure 2.16 Wrought iron straps (a) in Pinho (2008); and (b) in Cóias e Silva (2007).

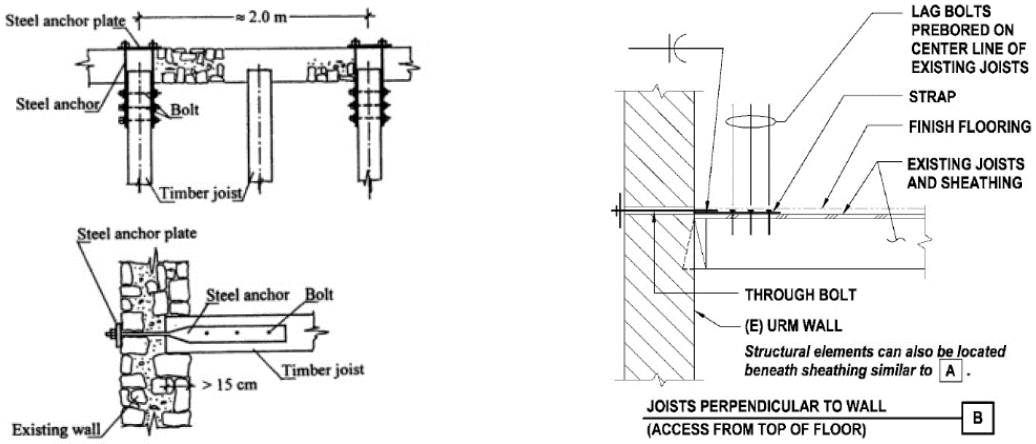

(a) (b)

Figure 2.17 Strengthening solutions: (a) in Tomaževič (1999); and (b) in FEMA 547 (2006).

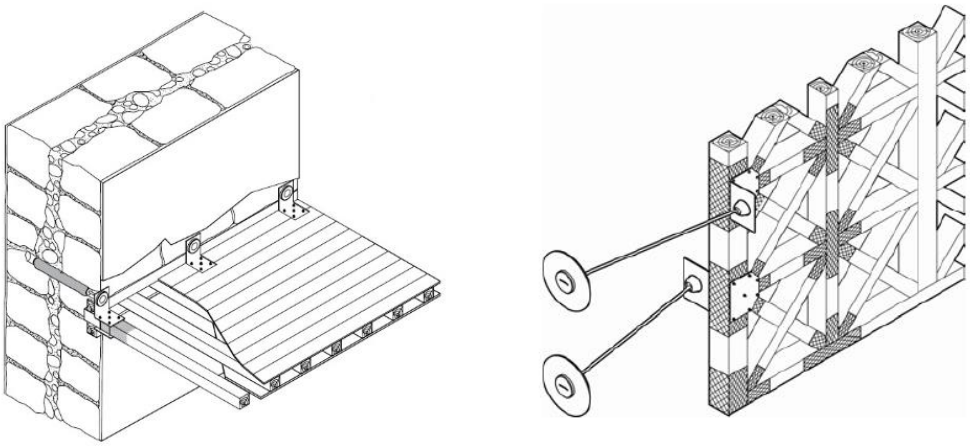

(a) (b)

Figure 2.18 Strengthening solutions proposed for *Pombalino* and similar buildings (Cóias e Silva, 2007): (a) injection anchors; and (b) parallel tie rods with anchor plates.

2.5 CONCLUSIONS

URM buildings have been the core of many studies, since they are present all over the world and their seismic vulnerability is well documented and recognized. Their inability to sustain large deformations without severe strength loss and damage, raises concerns regarding life safety, economic loss or even irrecoverable architectural and cultural damage. Nonetheless, in recent seismic events has been observed that URM buildings perform better than predicted, being able to sustain damage much after their maximum strength capacity is reached. In-plane mechanisms of walls, like rocking, are displacement-controlled which impose more of a ductile and more desirable behavior to the structure. In order to take advantage of the in-plane capacity of the masonry walls, it is necessary to safeguard the out-of-plane mechanisms of walls. In spite of being local mechanisms, out-of-plane damage culminating in partial or complete collapse of walls can compromise the stability of the entire structure. Several studies reported poor connections between structural members, like the masonry walls and timber wood diaphragms, as being one of the main causes of walls' overturning and collapse of floors.

Different types of wall-to-timber framed wall and wall-to-floor connections were presented and in general, connections reflect the quality of the building itself. Good connections can be found in *Pombalino* buildings, but over the years these connections got deteriorated and increased the seismic vulnerability of the later buildings. Nonetheless, even structural connections in *Pombalino* buildings can be improved to comply with recent design codes.

The most ancient strengthening solution for connections is the metal strap nailed to the timber floor joist and anchored into or through the wall, with an anchor plate. Recent solutions, like the ones motivating this research, explore a bolted connection to the timber floor joist and

anchoring systems with injection anchors (wall-to-timber elements) and tie rods with anchor plates (wall-to-floor).

Chapter 3. Material characterization

Highlights:

- Timber and metallic components of the wall-to-floor strengthening were provided according to specifications, thus were not characterized experimentally;
- Steel bars from the injection anchors were tested, and were according to specifications;
- Definition of mortar compressive strength was essential to establish adequate masonry mechanical properties;
- Mortar is very poor in contrast with the high strength limestone;
- Cracks on masonry occurred on the mortar or on the mortar/stone interface;
- Masonry reproduced in laboratory is a good approximation of the historical masonry under study, when it comes to mechanical properties.

3.1 INTRODUCTION

The unstrengthened and strengthened connections are designed to dissipate energy through hysteresis, which relies on plastic deformation of the structural members involved. Consequently, material properties and behavioral models, together with structural configuration and type of loading are responsible for the connection's behavior. Material characterization assumes critical importance when transposing these buildings to experimental or numerical levels. The objective of this chapter is to properly characterize the materials that constitute the different structural components of the pullout specimens, relying on literature review and experimental tests. These materials are: timber, stone, mortar, masonry, steel (different kinds) and cementitious grout.

Since the timber elements, the steel components for the wall-to-floor specimens (nails, angle, tie rod, and anchor plate) and the grout for the injection anchors were provided according to specifications, with standard properties, no material characterization tests were carried out. Some of their main properties are provided next.

The stone, the mortar and the arrangement of the masonry were chosen in a way that would represent the historical masonry described in subsection 2.2.3. Experimental characterization of their properties enabled a better understanding of the behavior of the tested connections, the possibility of comparison of the results with force predicting formula, and future application on numerical models. The following tests were carried out to determine mechanical material properties, and they are better described ahead in this section: compression of mortar samples, compression tests of limestone cores, compression tests of masonry prisms, and diagonal compression tests of masonry wallets.

3.2 STANDARD PROPERTIES

In this section, are provided the standard properties of materials used in the specimens but not characterized experimentally: timber, steel used in the wall-to-floor connections specimens, and cementitious grout.

The species of the timber used in the wall-to-floor specimens was chosen according to the characteristics previously described in subsection 2.5.3, and with the fact that this species is found worldwide (Macdonald et al., 2010). The species of timber used on the specimens was the Scots Pine (*Casquinha Vermelha*) from Portugal, which according to M4 report (LNEC, 1997) has a mean density, ρ_{mean}, of 530 kg/m^3 and a bending strength, f_m, of 98 MPa, for a relative humidity of 12%. Depending on its general quality (knots, distortion, resin

pockets, etc.), its strength class can vary, and consequently its mechanical properties. For structural purposes, a common used grade is C22, which main mechanical properties (characteristic values) are presented in Table 3.1.

Table 3.1 Mechanical properties of C22 Scots Pine EN 338 (CEN/TC B/525, 2003)

Strength properties (N/mm²)		
Bending	$f_{b,k}$	22.0
Tension parallel to grain //	$f_{t,0,k}$	13.0
Tension perpendicular to grain ⊥	$f_{t,90,k}$	0.3
Compression parallel to grain //	$f_{c,0,k}$	20.0
Compression perpendicular to grain ⊥	$f_{c,90,k}$	5.1
Shear	$f_{v,k}$	2.4
Stiffness properties (N/mm²)		
Mean value of modulus of elasticity parallel to grain	$E_{0,mean}$	9.0
Mean value of modulus of elasticity perpendicular to grain	$E_{90,mean}$	0.3
Density in kg/m3		
Density	ρ_k	340

From all the metallic components used in the specimens, only the tie rods part of the injection anchors were tested for tensile strength, but this test and other types of tests should be extended to all components. The steel angle and anchor plate of the strengthening solution developed with the company Monumenta Lda. for the wall-to-floor connections were of stainless steel AISI 304 (ultimate tensile strength (f_u) of 700 MPa and yield strength (f_y) of 450 MPa). The tie rods, and respective nuts belonged to the class 8.8 (higher strength class), thus f_u was 800 MPa and f_y was 640 MPa. For the nails, was admitted a tensile strength of 600 MPa.

Cintec's Presstec™ grout is part of their standard anchoring solution, and is provided directly by the company. It presents 4.5 MPa for tensile strength and 51.5 MPa for compressive strength, both at 28 days (values provided by Cintec®). The installation of the anchors in the specimens was carried out by Cintec's technicians, stressing the fact that all procedures were taken to obtain their standard properties.

3.3 TENSILE TESTS OF STEEL BARS (INJECTION ANCHORS)

To prevent yielding of the tie rods before the occurrence of other failure modes, the tie rods from the injection anchors provided by Cintec® were in a high grade of steel, in this particular case, a stainless steel AISI 304 class 80 (Ultimate tensile strength, f_u = 800 MPa and Yield strength, f_y = 600 MPa). Since extra injection anchors were provided, tensile tests were carried

out on three ϕ16 mm steel ties. The tubular sleeve was removed from the anchors and the end with the welded washer was cut, so that the tie rod could be perfectly adjusted to the clamps, as seen in Figure 3.1a.

The test setup and procedure applied were according to EN 10002-1 (CEN ISE/NFE/4, 2001), and a clip-gauge was placed at the center of the specimen, in order to determine the modulus of elasticity, E, and the proof strength $R_{p0.2}$. Before failure the clip-gauge was removed, to prevent its damage. Stress-strain curves of the three specimens (obtained with the clip-gauge) are presented in Figure 3.1b.

The original cross-sectional area of the parallel length, S_0, of the bars was 157 mm^2 for all bars, and the original clip-gauge length, L_{cg}, was 116 mm (see Table 3.2). The following parameters resulted from the tensile tests performed on the steel ties and are presented in Table 3.2:

- Original bar length (L_0) – bar length measured before application of the force;
- Final bar length after fracture (L_u) – bar length measured after rupture of the specimen;
- Maximum force (F_m) - maximum value of force measured during the test;
- Permanent elongation after fracture – difference between the final and original bar length ($L_u - L_0$);
- Percentage of elongation after fracture (ε_u) – permanent elongation after fracture expressed as a percentage of the original length (L_0);
- Tensile strength (R_m) – stress corresponding to the maximum force;
- Proof strength ($R_{p0.2}$) – stress at which a non-proportional extension is equal to 0.2 % of the deformation of the clip-gauge;
- Elastic modulus (E) – slope of the linear range of the stress-strain curve.

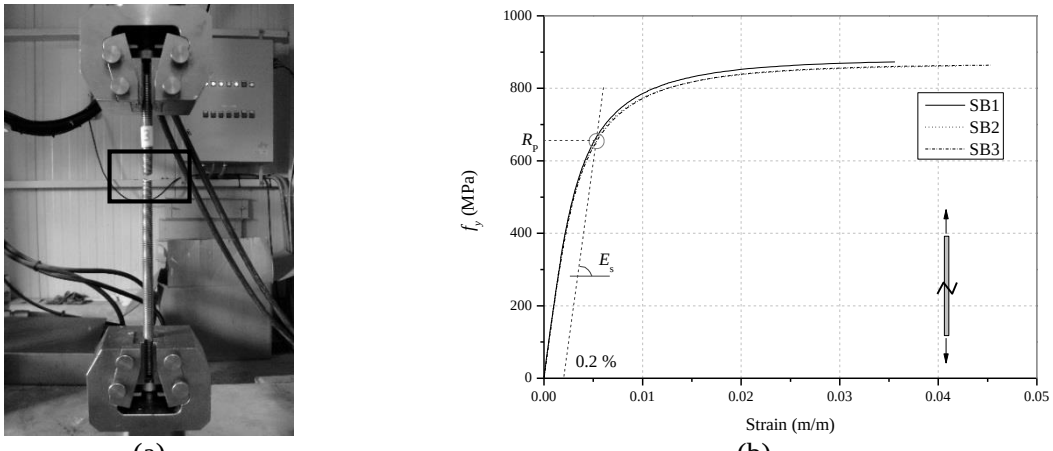

(a) (b)

Figure 3.1 Tensile tests of steel rods: (a) typical failure mode; and (b) stress-strain curves.

Table 3.2 Properties of the tested steel bars

Specimen	L_0	L_u	F_m (kN)	(L_u-L_0) (mm)	ε_u (%)	R_m (N/mm^2)	$R_{p0.2}$ (N/mm^2)	E (GPa)
SB1	351	393	138	42.0	12.0	879	671	193
SB2	352	389	136	37.0	10.5	865	661	199
SB3	352	394	136	42.0	12.0	867	653	198
Média	352	392	137	40.3	11.5	870	662	197
CoV (%)	0.16	0.67	0.84	7.16	7.53	0.84	1.36	1.63

As expected, the Coefficients of Variation (CoV) are low. The tensile tests confirmed that the steel ties provided were according to the mechanical specifications of an AISI 304 class 80. The nominal values adopted for further study of the anchors are: $f_y = R_{p0.2} = 662$ MPa and $f_u = R_m = 870$ MPa. The average E, 197 GPa, is within 195 GPa and 200 GPa, which are the design values proposed by EC3-Part 4 (CEN/TC250, 2006) for austenitic grades.

3.4 COMPRESSION TESTS OF MORTAR SAMPLES

For the type of masonry described in subsection 2.5.3, mortar plays a very important role defining the behavior and mechanical properties of the masonry itself. As presented before, the historical mortar was an air-lime mortar, but to ensure fast setting time and approximately the same strength, hydraulic lime and cement were chosen as binders of the composition to be included in the masonry specimens. Arandigoyen & Alvarez (2007) and Pereira, Camões, & Lourenço (2010) present the influence of different cement/lime (C/L) and binder/aggregate (B/Ag) ratios on the compressive strength, elastic modulus and other properties, which helped on the definition of four different cement/lime/river sand/clay-rich sand compositions (by mass): 1:3:10:6 (T1), 1:3:13:7 (T2), 1:3:8:4 (T3), and 1:2:10:5 (T4). All the compositions have a 1:3 C/L ratio, with exception of T4 which has a 1:2 ratio. On the other hand, the B/Ag ratio is 1:3 for T3, 1:4 to T1 and 1:5 to T2 and T4 (see Table 3.3).

According to Arandigoyen & Alvarez (2007), after 28 days there is a slight increase in strength and over a year the variation is very small for compositions with cement percentage ranges from 0% to 40%, which applies to all except for T4. Therefore, compressive tests were carried out on 36 cylindrical specimens, of ϕ75×150 mm^3, at the ages of 7, 14 and 28 days, enabling a fast decision regarding the mortar composition.

Previously to testing, all the specimens were capped with a 3 mm layer of self-leveling mortar to assure smooth surfaces, parallel to the longitudinal axis of the cylinder. The diameter was determined from the average of three measurements at mid height, top and bottom, while

the average height was obtained from three measurements only. The tests were carried out under displacement control, with a loading rate of 10 μm/s. Compressive strength was calculated by dividing the compressive force by the area calculated from the average diameter.

Concerning the B/Ag and C/L ratios, the first one has bigger influence on the compressive strength of the different compositions, clearly distancing the composition T3 from the remaining ones, since it has the highest B/Ag ratio (see Table 3.3 and Figure 3.2a). As expected T2 composition constitutes the lower boundary of the compressive strength, since it is the combination of the lowest B/Ag and C/L ratios. The composition chosen was T1, since is tending to 1.5 MPa (see Figure 3.2a), which will enable a compressive strength of masonry slightly higher than the values reviewed in the literature. This decision will push further the boundaries of the failure modes related with the masonry wall, enabling the observation of other failure modes during the pullout test without compromising the stability of the wall.

Table 3.3 Characteristics of the mortar ratios.

Chosen ratios (volume)		**binder/ aggregate**	**cement/ lime**	**f_{cm} (MPa)**			**Evolution (%)**	
				7 days	**14 days**	**28 days**	**7→14**	**14→28**
T1	1:3:10:6	1:4	1:3	0.65	1.16	1.43	79	23
T2	1:3:13:7	1:5	1:3	0.45	0.69	0.92	55	34
T3	1:3:8:4	1:3	1:3	1.63	2.44	3.05	50	25
T4	1:2:10:5	1:5	1:2	0.58	0.97	0.89	68	-8

Cylindrical mortar samples were collected during the construction of the specimens and tested at the ages of 28 days (to compare with a study performed initially) and at the time of testing. At curing age of 28 days, the average compressive strength, f_{cm}, is approximately 1.3 MPa, which is lower than the reference value for T1, 1.4 MPa, probably a reflection of different conditions of preparation and higher percentage of water in the mixes. It should be stressed that the reference value was determined from mortar mixes prepared in the laboratory, following standard procedures, while these mortar samples were prepared by professional masons using a large scale mixer. At time of testing, around 400 days, the average compressive strength was approximately 1.3 MPa, the same value determined at 28 days, showing that the compressive strength is hardly affected by the testing age, as predicted, thus allowing the testing of specimens at different ages without major consequences in terms of mortar hardening. In Figure 3.2b is presented the average stress-strain curve of the mortar samples collected.

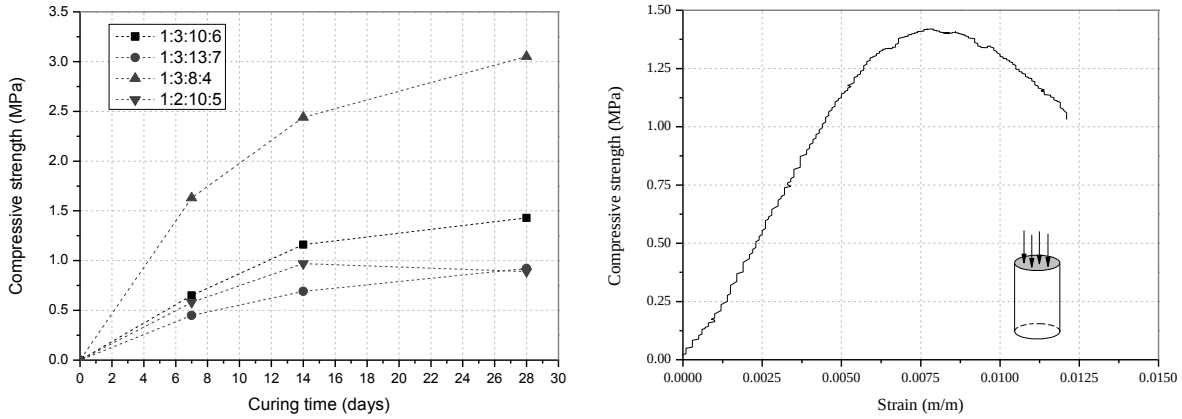

(a) (b)

Figure 3.2 Compression tests of mortar samples: (a) compressive strength vs. curing time; and (b) average stress-strain curve.

3.5 COMPRESSION TESTS OF LIMESTONE CORES

In order to characterize the compressive strength and the elastic modulus, compression tests were performed on five limestone cores, extracted from the same type of stones used on the masonry walls. The limestone came from a quarry in the surrounding area of Lisbon, Monsanto, which is one of the areas that supplied the construction of *Pombalino* and *Gaioleiro* buildings. As recommended by ASTM D7012-10 (2010) and by the authors Hudson & Harrison (1998), Vasconcelos & Lourenço (2009) and Oliveira (2003), the most desirable length to diameter ratio is 2, since for the above mentioned ratio the compressive strength is independent of the size and a uniform uniaxial stress state can be established in the central zone of the specimen. Therefore, the limestone specimens have an average diameter of 55 mm and an average length of 110 mm, establishing a length to diameter ratio of 2. The specimens' ends were machined flat. Until the time of testing, the specimens were kept under the same moisture conditions as the masonry walls, since it can have a significant effect upon the deformation of the rock.

After an initial minimum pre-load of 0.3 kN, the test was carried out under displacement control, at a constant loading rate of 2 μm/s, producing failures between 2 and 15 min, as suggested by the ASTM D7012-10 (ASTM International, 2010a). The axial deformation was continuously recorded by three LVDTs placed 120° apart between the lower and upper steel plates (see Figure 3.3a), which average value was used to determine the axial strain. The compressive strength is the ratio between the applied load and the original cross-section. After computing these parameters, the stress-strain curves were defined as presented in Figure 3.3b. Even with a small loading rate, the post-peak branch was only recorded for two of the four specimens (LSC4 and LSC5). Specimen LSC3 presents a slower adjustment at the beginning

of the test, probably due to small imperfections on the contact surface with the platens, which did not compromise its results.

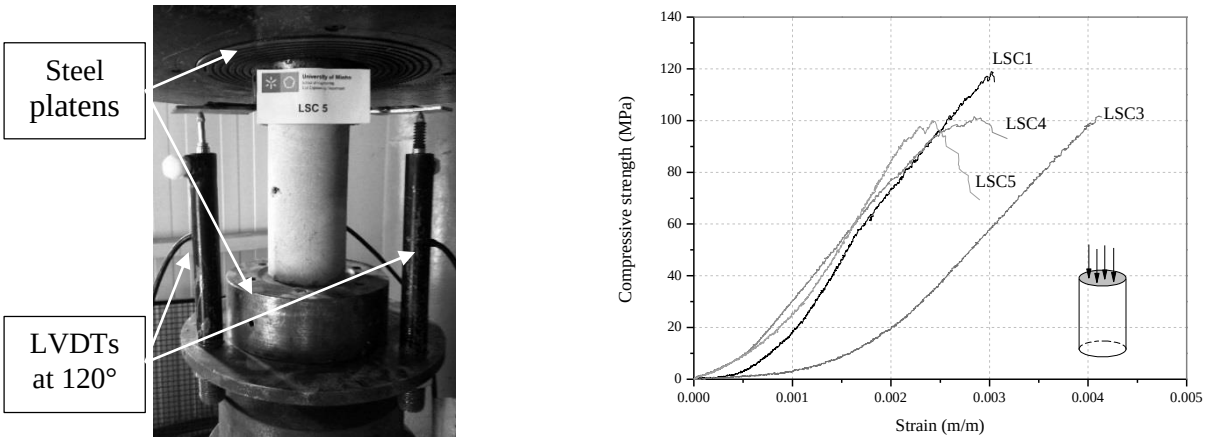

(a) (b)

Figure 3.3 Compression tests of limestone cores: (a) test apparatus; and (b) stress-strain curves.

All specimens with exception of LSC2 presented an hourglass shape failure, which is consistent with uniform uniaxial stress state and low confinement at the bases (see Figure 3.4). Specimen LSC2 proved to be an outlier, statistically and by presenting an inadmissible failure mode, thus excluded from the determination of compressive strength and elastic modulus. From the stress-strain curves, it was possible to calculate the elastic modulus, *E*, by making a linear least squares fit to the stress-strain data in the straight-line portion of the curve (method 10.4.2 of ASTM D7012-10 (ASTM International, 2010a)). The average compressive strength obtained was 106.7 MPa and the average *E* was 51466 MPa (see Table 3.4).

Figure 3.4 Limestone specimens after failure.

Table 3.4 Mechanical properties of the tested limestone specimens

Specimen	f_c **(MPa)**	***E*** **(MPa)**
LSC1	119.9	58445
LSC3	102.3	40814
LSC4	102.3	47355
LSC5	102.1	59251
Average	106.7	51466
CoV (%)	8.3	17.4

3.6 COMPRESSION TESTS OF MASONRY PRISMS

Five masonry prisms were constructed at the same time of the specimens using materials from the same batch. Following the recommendations of EN 1052-1 (CEN/TC 125, 1999) and considering 0.20 m as the maximum unit dimension, the dimensions established for the masonry prisms were 0.40×0.50×0.80 m3. The specimens were hand built, without the use of any formwork, being the stones fitted together as randomly as possible. The mortar joints were at most 0.05 m thick (see Figure 3.5a). The specimens contained some imperfections like leaning, vertical joints continuous throughout the height of the prism, or thin horizontal joints allowing contact between stone units. Although accidental, these imperfections do represent common aspects found in real masonry walls (see Figure 3.5b).

(a) (b)

Figure 3.5 Construction of the masonry prisms: (a) halfway construction; and (b) complete prism.

The compression tests were carried out on a metallic frame, as the one depicted in Figure 3.6a., equipped with a hydraulic actuator with a capacity of 500 kN, in compression, where the specimen rested directly on a concrete base. The load was properly distributed by a set of metallic rigid plates placed on top of each other (see Figure 3.6), whose weight was recorded, to be accounted for on the compressive strength (f_m) calculations.

In order to measure vertical deformation, each specimen was instrumented with four LVDTs, as described in EN 1052-1 (CEN/TC 125, 1999). An effort was made to place the LVDT measuring points at the central third of the specimens' height, despite the random distribution of stones (see Figure 3.6b).

Taking into consideration both EN 1052-1 (CEN/TC 125, 1999) and Vasconcelos & Lourenço (2009), one monotonic and four cyclic compressive tests were performed. Initially, the monotonic test enabled the determination of the value of the maximum compressive strength, which was then used to define the procedure for the cyclic tests. For the determination

of the modulus of elasticity, *E*, the vertical displacement of the specimen was stabilized during the pre-peak phase by the means of steps with constant load or loading-unloading cycles. The cyclic procedure included two loading-unloading cycles at 25% and 50% of the maximum compressive strength (obtained from the monotonic test) carried out under force control. After their completion a constant displacement rate was applied, ranging from 5 μm/s to 10 μm/s. The failure occurred between 15 min to 30 min. The low value adopted for loading rate prevented abrupt failures and allowed stable failure processes capable of capturing the softening behavior of masonry.

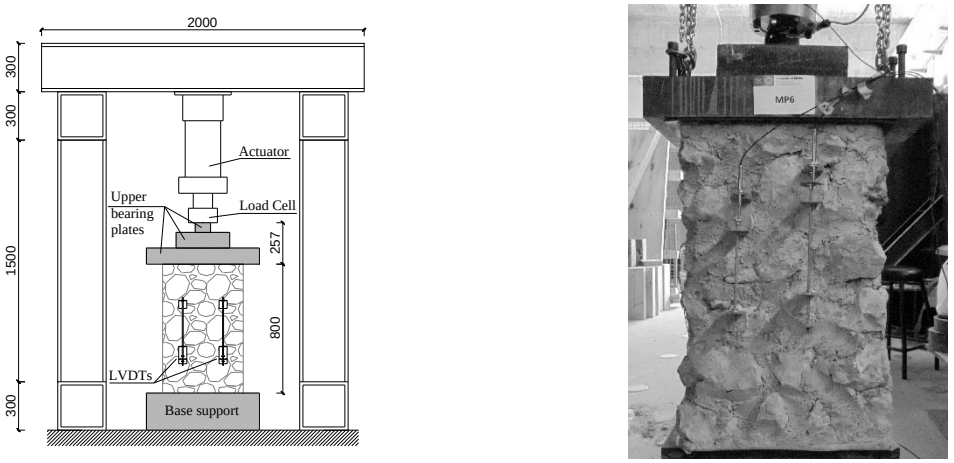

(a) (b)

Figure 3.6 Compression test set-up for masonry prisms: (a) sketch of the entire set; and (b) instrumentation of the specimen.

The mechanical properties were calculated based on the stress-strain curves of each specimen, as presented in Figure 3.7a. The modulus of elasticity was determined using linear regression in the interval from 30% to 60% of the ascending branch of the stress-strain curve, which was constructed using the average of the vertical strains of the four LVDTs placed on each specimen (Vasconcelos & Lourenço, 2009). The two first tests, MP1 and MP2, were tested at 90 days (one monotonic test and one cyclic test), while the remaining four were tested at 400 days (around 13 months). Crack patterns formed initially in the central part of the specimen and then spread throughout. This indicated a good application of the load and, consequently, a uniform stress state at mid height (see Figure 3.7b).

Compressive strength and elastic modulus of all specimens are presented in Table 3.5. The average f_m of the first two specimens was 1.7 MPa, while for the remaining was 1.8 MPa. This slight variation was consistent with what was observed for the mortar, giving more freedom in terms of time to test. As previously discussed, values found in literature range between 0.50 MPa and 1.50 MPa, thus placing the tested specimens slightly above the interval and directly correlating to the higher compressive strength chosen for the mortar. The *E* had an average

value of 1015 MPa, at 400 days, which was very close to the value found in literature (Ramos, 2000). Specimen MP2 did not contribute to the determination of *E*, due to a malfunction of the LVDTs' acquisition system.

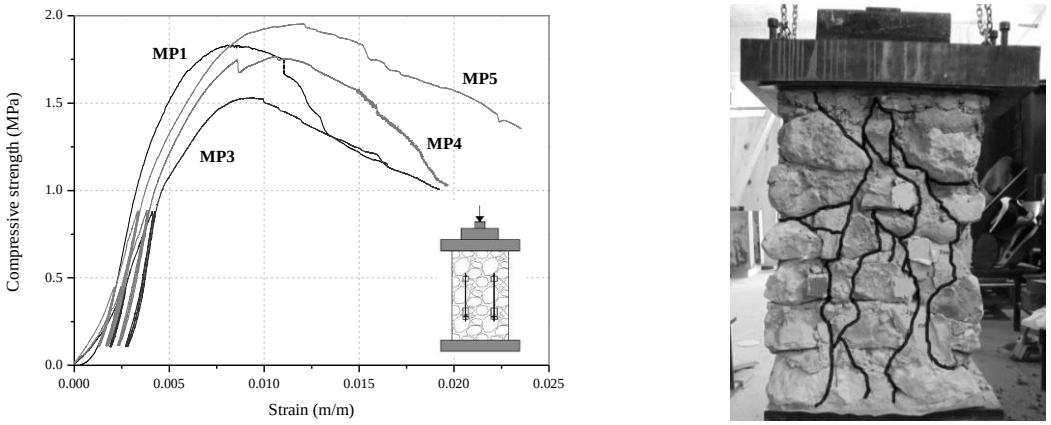

(a) (b)

Figure 3.7 Compression tests of masonry prisms: (a) stress-strain curves; and (b) typical crack pattern.

Table 3.5 Determined mechanical properties of the masonry prisms

Specimens	f_c (MPa)	E (MPa)
MP1	1.84	1095
MP2	1.59	-
MP3	1.53	1105
MP4	1.77	1701
MP5	1.96	846
Average (MPa)	1.7	1187
CoV (%)	10	31

3.7 DIAGONAL COMPRESSION TESTS OF MASONRY WALLETS

The diagonal compression tests were carried out in three masonry wallets, at the age of 124 days (4 months). This test aimed at estimating tensile and shear strengths, which can be used later on force prediction expressions for the injection anchors. The specimens were constructed as usual, being later rotated 45°. The same method of construction of the masonry prisms subjected to compression test was applied to these masonry wallets, therefore the same kind of imperfections was observed. Three specimens were built with the same type of mortar, stone units and workmanship (see Figure 3.8a). Although ASTM E519 (ASTM International, 2010b) suggests 1.2 m square specimens with the thickness that best describes the masonry under study, this study opted instead by a 0.8 m square wallet with 0.3 m thickness. This decision took into consideration the heavy weight of the final assemblage with relation to the low strength mortar and the need to transport and rotate the specimens to their final position. Nonetheless RILEM

TC76 (Committee, 1994) does not specify any specific dimensions of the specimens as long as they are representative of the finished masonry.

Each specimen was placed in a bed of fast curing mortar in the lower loading shoe. The same type of capping was carried out in the upper loading shoe. The specimen was then centered and plumbed. To measure the shortening of the vertical diagonal and the lengthening of the horizontal one, two LVDTs were placed on each direction per face of the wallet, from which the shear strains were calculated. A total of 4 LVDTs was used per test (see Figure 3.8b). The tests were carried out under displacement control, with a uniform displacement rate ranging of 150 μm/s.

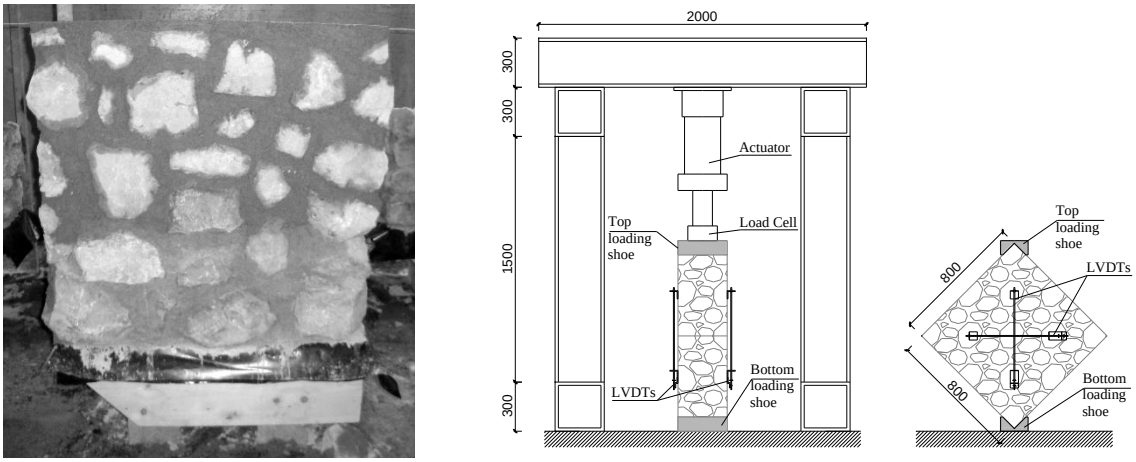

(a) (b)

Figure 3.8 Diagonal compression test: (a) masonry wallet; and (b) test set-up.

The horizontal and vertical shear strains were plotted versus the principal stresses (see Figure 3.9a), which were calculated according to Frocht (1931) theoretical approach (see Eqs. (3.1) and (3.2)). This approach is already adopted by RILEM TC76 (Committee, 1994). Contrary to the ASTM E519 (ASTM International, 2010b), which considers that a pure shear stress state develops in the specimen due to the diagonal compression (see Eq.(3.4)), Frocht (1931) demonstrated, and Brignola et al. (2008) and Calderini et al. (2010) confirmed that the elastic isotropic solution is more reliable to estimate masonry properties. Therefore, the following expressions were considered to determine the principal stresses, σ_{I} and σ_{II}, tensile strength, f_{t}, and the shear strength, τ, presented in Table 3.6:

$$f_t = \sigma_I \simeq 0.5\frac{P}{A_n} \tag{3.1}$$

$$\sigma_{II} \simeq -1.62\frac{P}{A_n} \tag{3.2}$$

$$\tau = 1.05\frac{P}{A_n} \tag{3.3}$$

$$S_S = \frac{0.707P}{A_n} \tag{3.4}$$

where P is the maximum applied load and A_n is the net area of the specimen. The average values obtained for the tensile and shear strengths were 0.14 MPa and 0.29 MPa, respectively. From diagonal compression tests of masonry wallets with similar arrangement and materials, Milosevic et al. (2013) obtained experimentally values of 0.22 MPa and 0.18 MPa for the tensile strength. Other authors that estimated the tensile strength from diagonal compression tests on random rubble stone masonry with air lime mortar reported the following ranges of values: 0.06-0.16 MPa (Chiostrini et al., 2000) and 0.02-0.04 MPa (Brignola et al., 2008).

Table 3.6 Mechanical properties of the tested masonry wallets

Specimen	P (kN)	A_n (mm^2)	$f_t = \sigma_I$ (MPa)	σ_{II} (MPa)	τ (MPa)	S_s
DCW1	80.8	260677	0.15	-0.50	0.33	0.22
DCW2	58.2	264056	0.11	-0.36	0.23	0.16
DCW3	78.6	256615	0.15	-0.50	0.32	0.22
Average	72.5	260449	0.14	-0.45	0.29	0.20
CoV (%)	14.0	1.2	14.8	14.8	14.8	14.8

The typical crack pattern consisted of cracks along the vertical diagonal, opening at first in the center of the specimen and propagating to the extremities, as presented in Figure 3.9b. The cracks occurred in the mortar and especially at the interface mortar-stone, due to the high difference in capacity of the two materials.

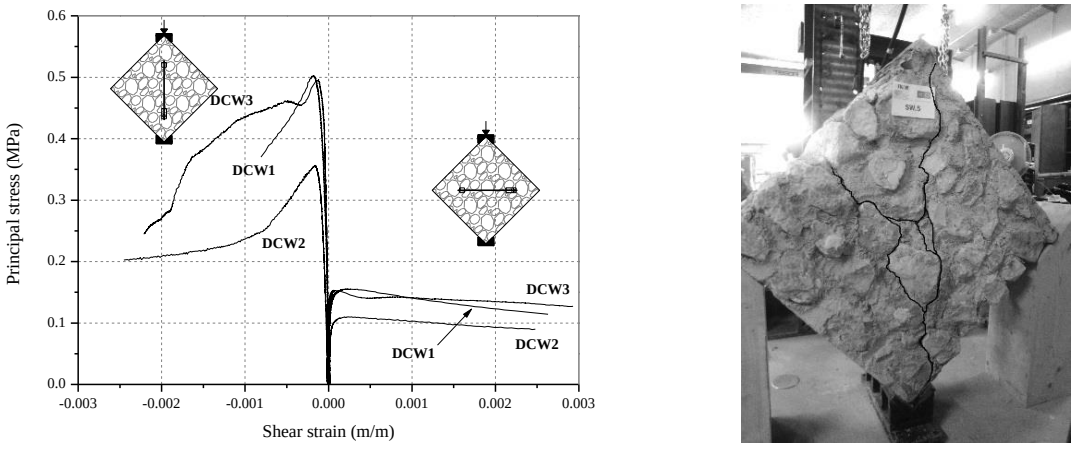

(a) (b)

Figure 3.9 Diagonal compression test of masonry wallets: (a) stress-strain curves; (b) typical crack pattern.

3.8 CONCLUSIONS

All the materials that are part of structural components were characterize, either by literature review or actual testing. In Table 3.7 are summarized the mechanical properties determined experimentally for mortar, stone and masonry.

The ratio between the compressive strengths of stone and mortar (f_b/f_c) plays an important role on the behavior of the masonry itself, which in this case is approximately 82. This very high value is reflected on the masonry failure modes, where cracking mainly occurs on mortar or on the mortar/stone interface. In this kind of irregular stone masonry, the role of mortar is more related to accommodating the randomly distributed stones than actually effectively distributing the stresses.

Table 3.7 Nominal mechanical properties determined experimentally

Materials	Compressive strength (MPa)	Tensile strength (MPa)	Shear strength (MPa)	Elastic modulus (MPa)
Stainless steel	-	870	-	197000
Mortar	1.3	-	-	-
Stone	106.7	-	-	51500
Masonry	1.8	0.14	0.29	1015

On the construction of the specimens and choice of materials, there was always an attempt to represent the most accurately possible the historical characteristics described in subsection 2.2.3. As result, the mechanical properties of the masonry and its behavior are very similar to what was intended.

The obtained results can be used to predict the capacity of the retrofitted connections, using force prediction formula, and in future numerical models depicting the connections studied experimentally.

Chapter 4. Injection anchors applied to connections

Highlights:

- Four failure modes were hypothesized;
- Combined cone-bond failure was common to all tests;
- Boundary conditions of the specimens greatly affected maximum pullout force and dissipated energy;
- Bottom wall tests presented higher pullout forces and higher contribution of bond;
- Top wall tests' failure displayed higher contribution of masonry cone breakout;
- The pair of injection anchors showed high ductility.

4.1 INTRODUCTION

This chapter focuses on the experimental campaign carried out on injection anchors to be applied on wall-to-timber framed wall connections, in the Laboratory of Structures of University of Minho (LEST). The performed testes concerned the pullout behavior of pairs of injection anchors, with the objectives of developing a full functioning test apparatus for this particular type of tests, studying failure modes and quantifying parameters as: maximum pullout force, stiffness and force degradation, displacement ductility, and energy dissipation.

Following sections describe all the steps from the hypothesized behavior, passing through test set-up development, and closing with the discussion of the results.

4.1 EXPERIMENTAL BACKGROUND AND HYPOTHESIZED BEHAVIOR

The application of injection anchors has been widely researched in concrete, but only recently the interest was extended to masonry. Contrary to concrete, the clear distinction of material components (units and mortar) and their arrangement plays an important role on the technique application (CEB, 1994). For irregular or double-leaf masonry, with a rubble core with an unknown amount of voids, special care is required when grout injections are needed. As a consequence, masonry applications of injection anchors usually include some kind of expandable sleeve, polymeric fabric or steel case, surrounding the steel tie, to control the flow of grout into the voids. Nonetheless, there are some experimental research campaigns that study the behavior of injection anchors without any sleeve, applied to regular brick masonry (Gigla, 2004, Arifovic & Nielsen, 2004). Load transfer mechanisms for these particular anchors can involve mechanical interlocking between injection anchor and masonry substrate, local mechanical interlocking between injection mortar and voids, and bond and friction between sleeve-grout and surface of the drilled hole. Therefore, tests discussed in this research used an expandable sleeve and the walls were in constant compression for the installation and testing of the anchors, to best represent *in situ* conditions.

Considering the mechanisms involved, the existing literature discussing failure modes on bonded anchors (Algeri et al., 2010; Zamora et al., 2003; Eligehause et al., 2006), and assuming that the test would develop as a direct pullout test, the following isolated failure modes were defined as possible (see Figure 4.1):

1. Masonry cone breakout (FM1): cracking of the masonry following a conical interface, due to the exceedance of the resistant tensile strength. The angle of the

cone is assumed to be at 45º with the longitudinal axis of the anchor, according to the existent literature. This hypothesis was to be confirmed by the tests;

2. Yielding of the steel tie (FM2): exceedance of the tensile capacity of the steel tie;
3. Failure of the interface masonry/grout (FM3): sliding at the interface between the masonry pre-drilled hole and the sleeve with injected grout. Since it is a cementitious grout, no chemical phenomena occur in the interface, relying only on adhesion, friction and mechanical interlocking;
4. Failure of the interface grout/steel tie (FM4): sliding at the interface between the injected grout and the steel tie. In these particular anchors, the probability of occurrence of this failure mechanism is very low, due to the presence of a washer at the free end of the anchor (opposing to the loaded end) encompassing most of the mortar plug.

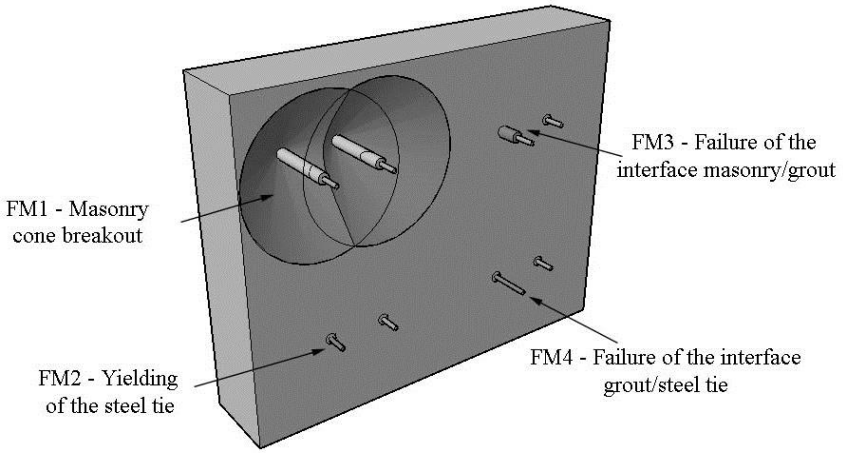

Figure 4.1 Failure modes predicted for the pullout tests of injection anchors.

Literature concerning adhesive anchors (Cook et al., 1998) contemplates the occurrence of a combined cone-bond (grout/steel tie interface) failure, for longer embedment lengths. Since FM4 is prevented by the presence of the washer on the free end of the steel tie, the combined cone-bond failure can occur with the contribution of the grout/masonry interface (FM1+FM3).

The pullout tests carried out had the objective of assessing the tensile capacity of the anchors, failure modes, and parameters related with cyclic loading, like energy dissipation, strength and stiffness degradation, and ductility. To do so, one can choose between different test setups taking into consideration available equipment, location (*in situ* or laboratory), time span, and level of detail to extract from the tests. In order to allow all failure modes to occur, especially the masonry cone breakout, the test setup should be unconfined. The test setup recommended by the ETAG 001 (EOTA, 2008) for unconfined tests of bonded tests in concrete

is represented in Figure 4.2a, where the clear distance from the anchor should be higher than $2h_{ef}$, where h_{ef} is the effective embedment length. This particular distance is very conservative, and for higher anchorage lengths leads to heavy testing rigs, in order to assure stability and negligible deformation from the test setup. Consequently, authors estimate the angle defining the masonry cone surface, commonly 45º, and define a test perimeter higher than the predicted projection area (see Figure 4.2b, c and d) (Arifovic & Nielsen, 2004; Algeri et al., 2010; Dizhur et al., 2013)

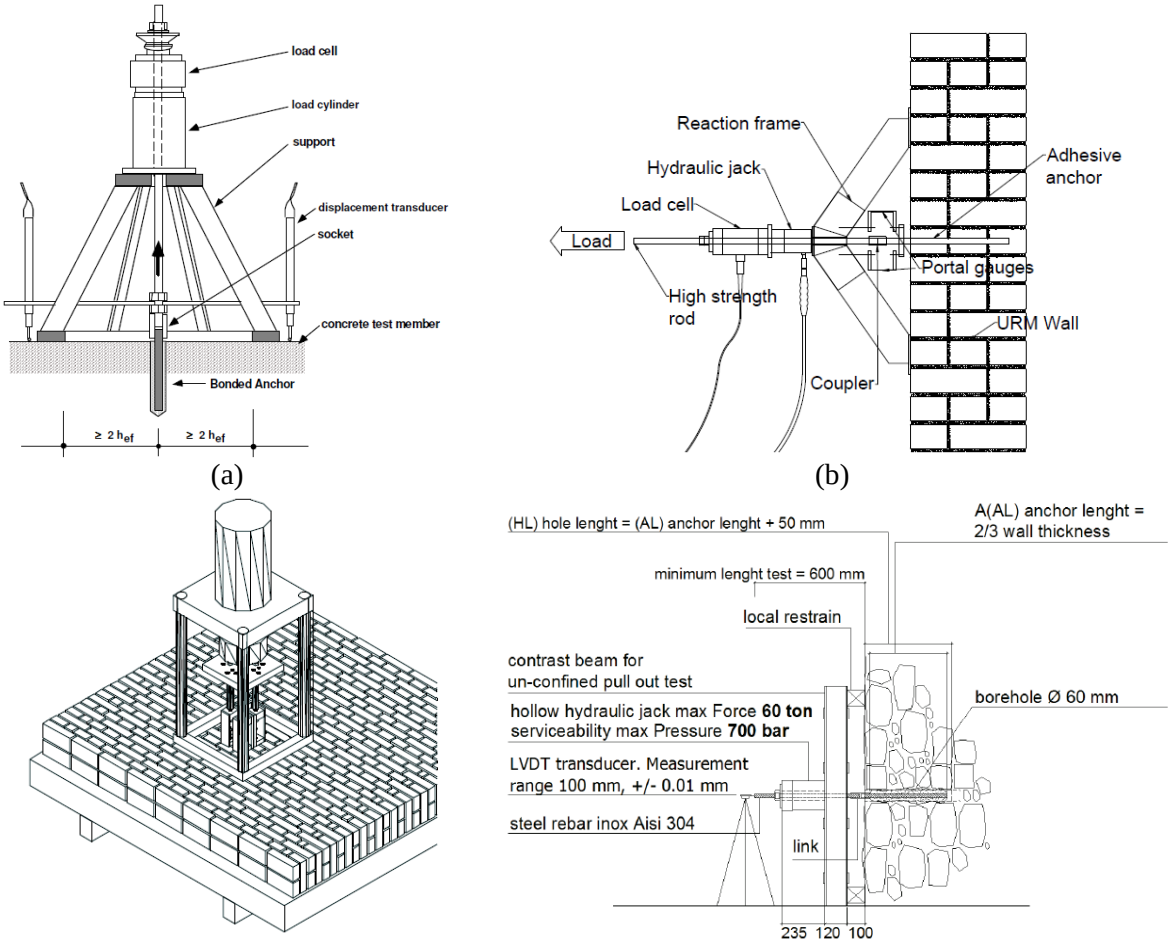

Figure 4.2 Different test set-ups for bonded anchors: (a) in ETAG 001 (EOTA, 2008); (b) by Dizhur et al. (2013); (c) by Arifovic & Nielsen (2004); and (d) Algeri et al. (2010).

Depending on the position of the masonry wall, the anchor can be pulled out horizontally (see Figure 4.2b, d) or vertically (see Figure 4.2a, c). For grouted anchors, it is very important to study their behavior in the position that possibly they will assume in reality, because the setting of the grout influences the bond behavior of the interfaces. Plus allows to study the feasibility of the installation process of the anchors. Particularly for low strength masonry, with irregular arrangement, it is not advisable to turn or move the wall, since it can cause micro-cracking, therefore being preferable to keep the walls vertical. The pullout test on horizontal

walls has the advantage of the test setup supporting on the wall, while for vertical walls the test setup requires a vertical support.

4.2 SPECIMENS

Two masonry walls with a rectangular shape and dimensions of 2.0×0.4×1.6 m^3 were hand built by professional masons, without the use of any formwork. The irregular stone masonry walls were built with lime stones of different dimensions, ranging from a minimum unit dimension of 0.1 m to a maximum of 0.2 m, with joints of maximum dimension of 0.05 m (see Figure 4.3). Further detail on the construction is given ahead.

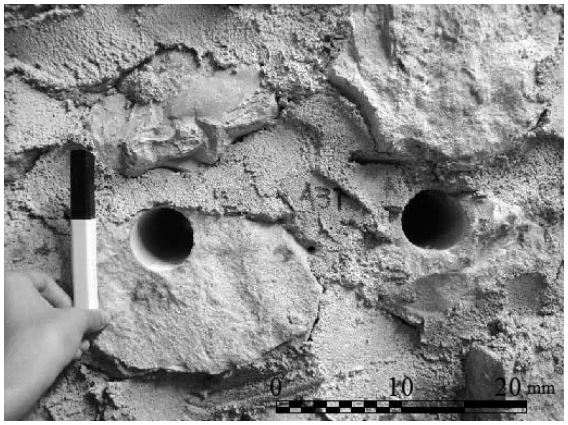

Figure 4.3 Masonry typology.

Geometry, constructive details, and expected failure modes of the anchor system were established through the consideration of existent literature (Algeri et al., 2010; Arifovic & Nielsen, 2004). Other aspects like laboratory conditions and availability of resources also were taken into consideration. As presented previously, the connection where the timber leans against the wall being solely connected by the timber floor joists can be considered the most unfavorable connection because the lack of timber elements embedded in the masonry wall does not allow it to take advantage of friction (see subsection 2.4.1). Considering this, and the fact that the double shear connection between steel gusset plates and timber elements can be properly designed using for instance EC5 (CEN/TC 250/SC5, 2004), it was decided that the specimens would include only the masonry wall and the anchor system, as shown in Figure 4.4. The denomination used was WT.40.I.1 and WT.40.I.2, where "WT" stands for wall-to-timber framed wall, "40" represents the thickness of the wall in cm, I refers to the injection anchors, and "1" or "2" is a reference to the wall number. Four pairs of injection anchors were installed in each wall, allowing four tests on each wall sample. The specimens were referenced

using letters: “A” and “B” to the bottom of the wall, “C” and “D” to the top of the wall (see Figure 4.4).

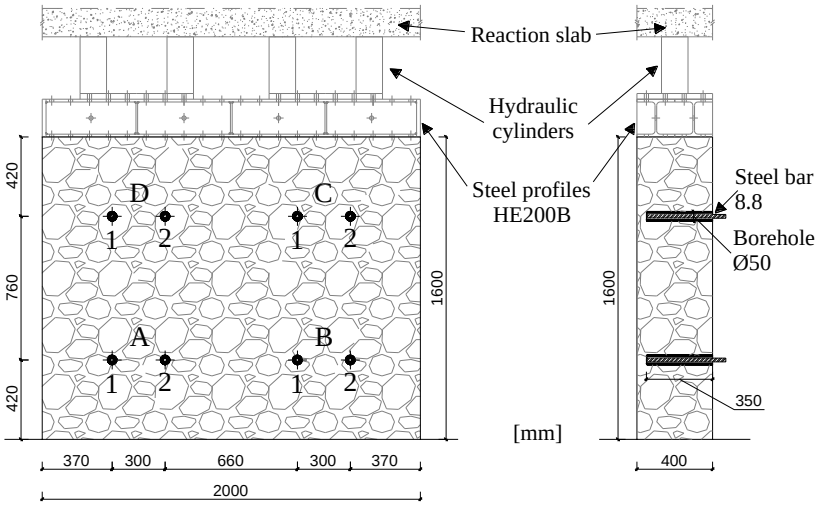

Figure 4.4 Disposition of the pullout test specimens.

The diameter of the steel ties in each wall was different: for the WT.40.I.1 a ϕ20 mm tie was used and for the WT.40.I.2 a ϕ16 mm tie was used. Despite the different tie diameter, the boreholes were uniformly drilled with a ϕ50 mm diameter. By keeping the same borehole diameter for two different tie’s diameter, one may conclude on the influence of the latter on the results.

Both walls were built with a thickness of 0.40 m. This wall thickness is representative of a 4th floor of a *Gaioleiro* building, as described in subsection 2.2.2 and Annex 1. Wall thickness had impact on the embedment length of the anchor, and consequently, on the force necessary to form the masonry cone failure. Therefore, by choosing a smaller wall thickness a conservative approach could be assumed. Interference between tests had to be avoided, so length and height of the wall, 2.0 m and 1.6 m respectively, were established considering a 90° opening angle at the end of each anchor and an embedment length of 0.35 m. This embedment length corresponds to the thickness of the wall minus 0.05 m, in order to allow some geometrical tolerance in real case study applications. Coring of the anchor’s holes was made throughout the entire thickness of the wall, to facilitate the instrumentation of the free end of the anchors. The distance between parallel injection anchors was calculated considering a 0.12 m thick timber framed wall in between plus the dimensions of the steel gusset, giving approximately a total of 0.30 m (see Figure 1.2).

After 28 days, following construction, the walls were loaded with a vertical compressive stress of 0.2 MPa to simulate the quasi-permanent stress state of a 4th floor wall. The anchoring system was installed only after the walls were vertically loaded. This consideration was critical

in properly representing the installation of these anchors in the field. The permanent compression of real walls has a direct impact on the stress state of the anchors when they are installed and on the structural behavior. The loads considered for the quasi-permanent combination were self-weights of various architectural details, balconies, floors, roof components, and other imposed loads for residential areas as recommended in EC1 (CEN/TC 250/SC1, 2002).

Figure 4.5 shows different stages of the construction of the specimens, from construction of the wall to the installation of the injection anchors. Particularly in Figure 4.5a one can observe that no formwork was used during construction of the walls, as mentioned in construction descriptions of existing buildings, found in the Municipal Archive of Lisbon. The holes were cored with a diamond tipped blade, at room temperature of 20°C ± 5°C, and afterwards were cleaned with compressed air and a nylon bristle brush (see Figure 4.5b, c). Then, the boreholes are ready for anchor installation. Previous to installation, the injection anchors were wet and during injection, the anchors were kept centered in the borehole, with the tube for the grout insertion in the sleeve on top of the steel tie rod. After injection, the plastic tube is bent to prevent leaks, as shown in Figure 4.5d.

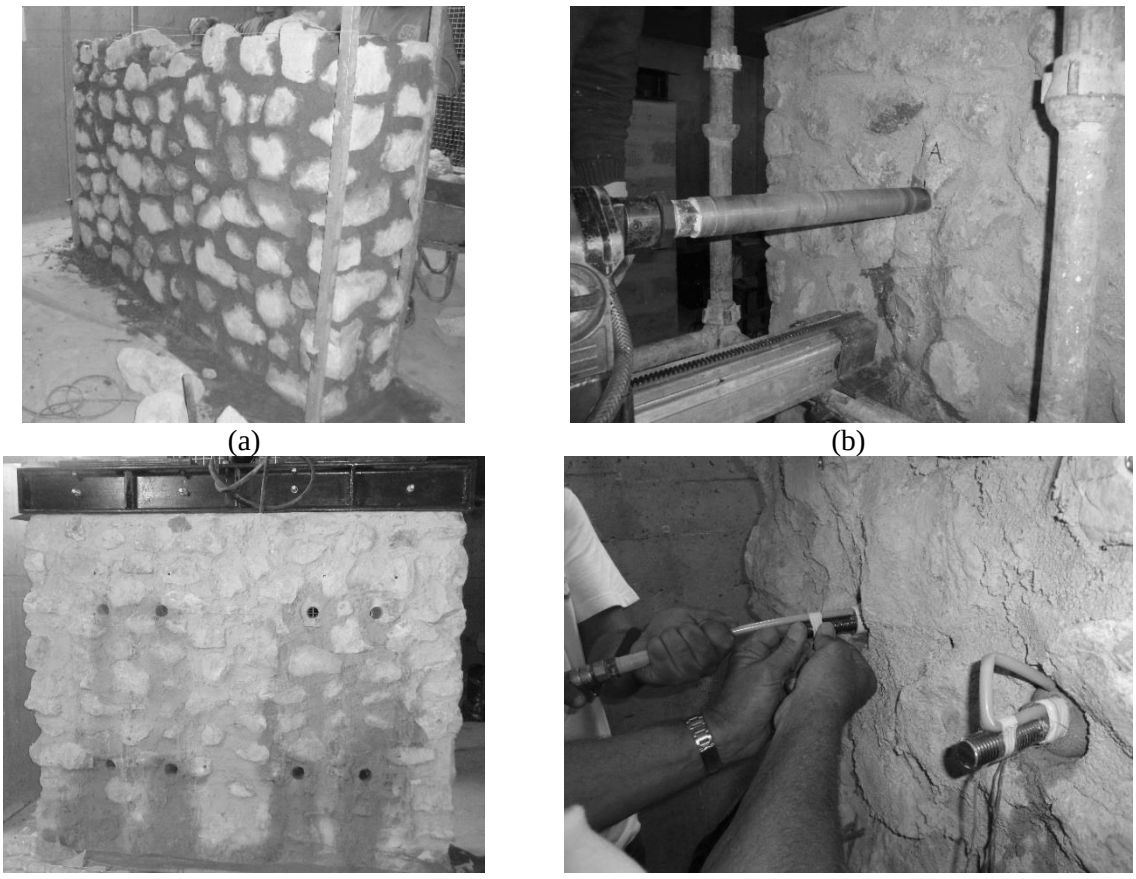

Figure 4.5 Construction of the specimens: (a) construction of the walls; (b) core drilling; (c) specimen with all cores drilled; and (d) installation of the injection anchors.

4.3 TEST SETUP

The test setup developed for this experiment had two main objectives: first to maintain a constant compressive state stress throughout the test, and second to apply the horizontal quasi-static cyclic load, without the use of a reaction wall and with minimum deformation of the steel frame. The first objective was carried out, by placing two HE200B steel profiles on top of the wall to distribute the load provided by four hydraulic actuators compressed against a reaction slab (see Figure 4.4). The distributed vertical load was kept constant during the entire test using a manual control to adjust the level of pressure. Due to the imperfections of the steel profiles and the irregularity of the masonry, the walls' top surface was leveled with mortar and a neoprene layer was placed between the two of them. The second objective, which effectively concerns the application of the pullout load, was enabled by a self-balanced apparatus capable of redirecting the pullout force back to the wall, as shown in Figure 4.6.

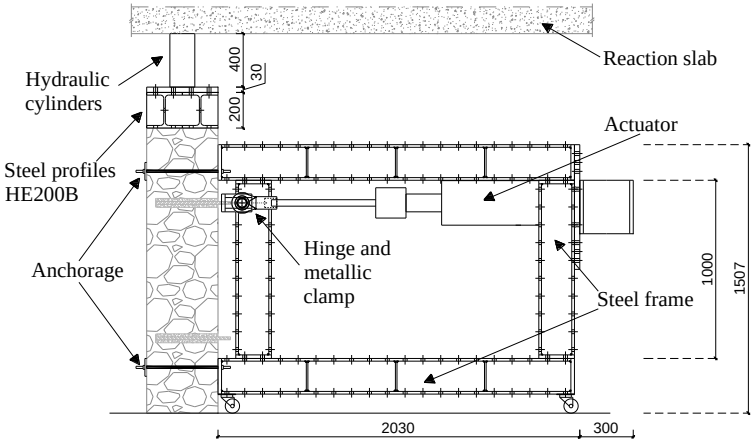

Figure 4.6 Elevation of the test apparatus for monotonic and cyclic pullout tests (dimensions in mm).

As one presented before, there are different types of setups, but the steel frame, developed for these tests, had enough rigidity to apply the cyclic load with negligible deformations. The frame was composed by HE200B steel profiles bolted to each other, and one HE300B profile bolding the actuator, in the way presented in Figure 4.6 and Figure 4.7a. In order to perform cyclic tests the set-up had to be anchored to the masonry wall by using 4 steel bars through the wall and anchor plates. All bars worked in the elastic range during the test. The frame was provided with wheels to facilitate its placement for each specimen.

The pullout load was applied on each pair of anchors at the same time, perpendicular to the wall, using a metallic clamp. The clamp was specially designed for this connection, being rigidly connected to the anchors and hinged on the end connected to the actuator. The hinge allows small deformations in the vertical and horizontal plans (see Figure 4.7b).

Another key aspect of the test setup is the instrumentation, which for these pullout tests was focused on measuring the out-of-plane displacements of wall and injection anchors, using a frame independent from the rest of the setup, as shown in Figure 4.7b,c.

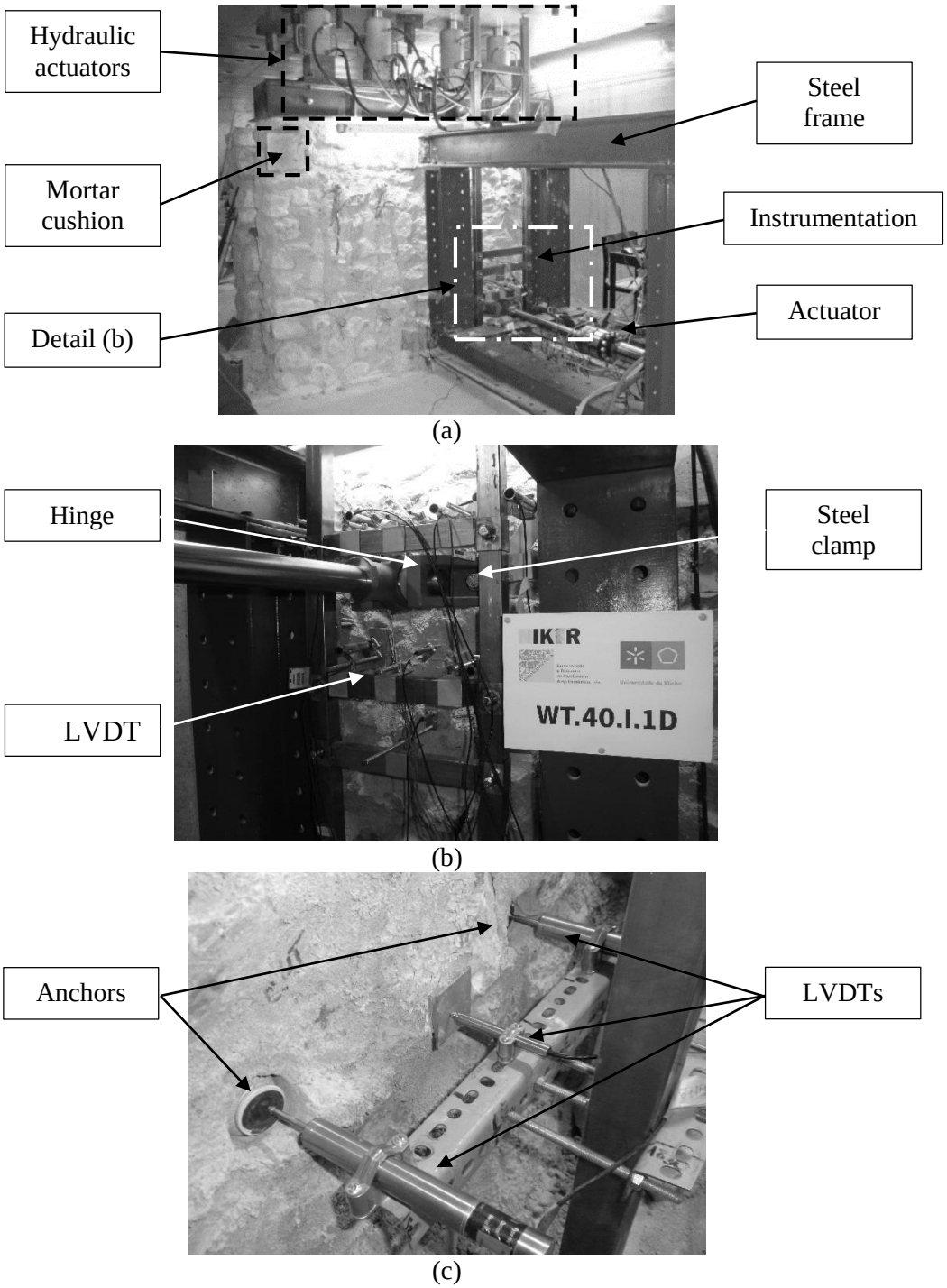

Figure 4.7 Detailed setup: (a) total apparatus; (b) instrumentation at the front of the wall; and (c) instrumentation at the back of wall.

Figure 4.8a shows the displacements needed to be measured in order to characterize the loaded end slip (s_L) and the total slip (s_T). The loaded end slip s_L represents the behavior of the interface grout/masonry, defined as the relative displacement between the loaded end of the

anchors (average of displacements measured at points 6 and 8 of Figure 4.8b) and the front face of the wall (average of displacements measured at points from 2 to 12, except for 6 and 8, of Figure 4.8b, which are inside the expected projected area of the cone). The total displacement is the relative displacement between the loaded end of the anchors (calculated as for s_L) and the back face of the wall measured outside the potential cone failure area (displacement at point 15). Total displacement is related with the global performance, meaning that it includes contributions from the grout/masonry interface and the masonry cone failure.

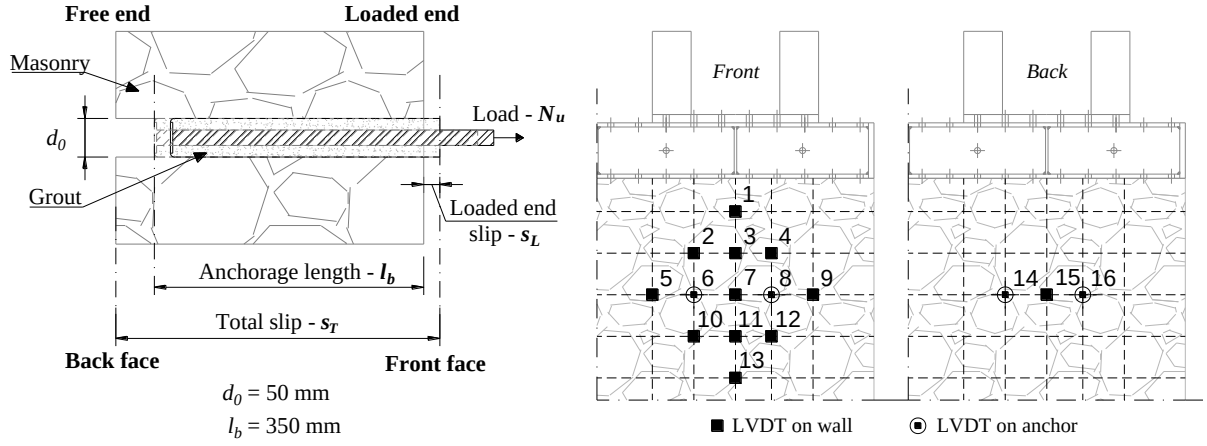

Figure 4.8 Instrumentation: (a) idealized model of the displacements to be measured; (b) detailed look on the LVDTs

A total of 16 Linear Variable Differential Transducers (LVDTs) were distributed on the specimen (see Figure 4.8b), of which 12 were placed on the wall (11 on the front of the wall and 1 on the back) to monitor the out-of-plane displacements, as presented in Figure 4.7. The LVDTs were placed exclusively on stones to avoid premature detachment, as this is known to happen to mortar. Their distribution on the wall followed a quadrangular grid of 150 mm around the two parallel anchors and they were specially concentrated around the anchors. A set of 4 LVDTs were also placed on the loaded and free ends of the injection anchors. The LVDTs placed at the loaded end were carefully located on a portion of the steel rod between the wall and the rigid clamp and hinge in order to avoid interference from the test apparatus on the measurements.

4.4 TEST PROCEDURE

The first monotonic test was carried out on specimen WT.40.I.1C under displacement control at a displacement rate of 5 μm/s, with the purpose of capturing the post-peak behavior and preventing disruptive failures. On the second test (WT.40.I.2C) the displacement rate was

doubled to 10 μm/s, knowing that the later cyclic tests had to be performed at higher velocities or else the tests would have unreasonable durations (around 10 hours). The stopping criteria adopted for the monotonic test were a 50% decrease in maximum load or the propagation of cracks beyond the expected area of damage. From these tests, it was possible to define a cyclic procedure with at least two displacement amplitudes during the elastic phase and a minimum of three for the softening phase. Amplitudes ranged from 2 mm to 18 mm, with each one comprising two equal cycles and never unloading below 0.5 mm. A maximum amplitude of 18 mm was established so that no damage could propagate to areas of surrounding tests (see Figure 4.9). The range of velocities was between 10μm/s to 40 μm/s, respecting always a minimum of 120 s for duration of each loading or unloading branch.

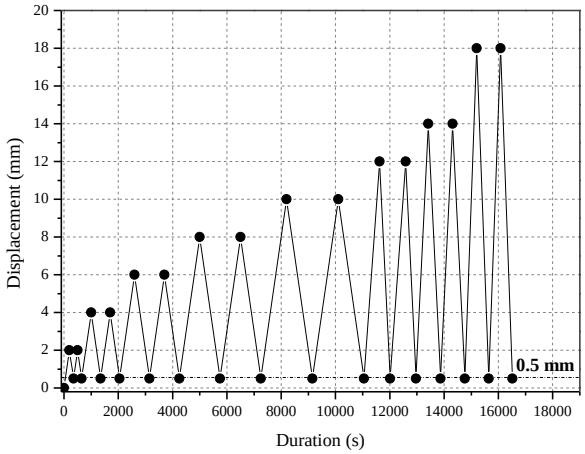

Figure 4.9 Cyclic test procedure

4.5 RESULTS

The main outcomes of the experimental tests are organized in terms of results of tests performed at the bottom and top of the wall, since a clear distinction was detected during the tests and early on in the analyses of the results.

4.5.1 Hysteretic curves and performance parameters

Of the 8 tests prepared initially in the two walls, one test was not carried out successfully, due to an equipment malfunction. A total of 2 monotonic and 5 quasi-static cyclic pullout tests were performed. An immediate observation of the resistance pointed out the difference between tests conducted at top and bottom of the wall (see Table 4.1), with a difference of approximately 30% in ultimate load, which is discussed in section 4.6. At the base of the wall the average maximum pullout force was 107.9 kN, while at the top the same parameter reached 76.8 kN, both with a CoV below 5%. These values correspond to the load required to pullout the pair of anchors, simultaneously.

Displacements and other parameters presented in Table 4.1, also account for the combined behavior of both anchors. The initial stiffness (k_0), the yield displacement (d_y), and the ultimate displacement (d_u), referring to the pair of injection anchors, were estimated based on the total slip (s_T) (see Figure 4.8a), which accounted for the contributions of all possible failure modes. The calculation of k_0 was done with a linear least squares fit on the linear portion of the ascending branch of the first cycle of the 2 mm step. The yield displacement was taken as the displacement when first yielding occurs and the ultimate displacement corresponded to the post-peak displacement when a loss of 20% load carrying capacity happened (Park, 1989). The ratio between d_u and d_y is the displacement ductility factor, μ, which expresses the energy dissipation capacity of the strengthening. The initial stiffness and displacements display great variability, with CoV ranging from 5% to 75%. Still, specimens at the bottom of the wall have in average a smaller ductility factor than the ones at the top.

Table 4.1 Performance parameters of the pullout tests.

Specimen	Type of pullout	Maximum force (kN)	k_0 (kN/mm)	d_y (mm)	d_u (mm)	μ
WT.40.I.1A	Cyclic	111.7	33.3	2.0	6.30	3.2
WT.40.I.2A	Cyclic	107.2	-	-	-	-
WT.40.I.2B	Cyclic	104.9	35.1	2.7	9.53	3.5
Bottom average		107.9	34.2	2.6	8.2	3.4
CoV (%)		3.2	3.7	5.4	23.6	18.3
WT.40.I.1C	Monotonic	76.8	18.2	3.1	16.8	5.4
WT.40.I.1D	Cyclic	81.2	62.0	0.7	12.1	18.6
WT.40.I.2C	Cyclic	75.0	40.9	0.9	6.7	7.4
WT.40.I.2D	Monotonic	74.3	40.2	1.3	7.7	5.9
Top average		76.8	40.3	1.5	10.8	9.4
CoV (%)		4.0	44.4	74.5	42.7	66.7

Specimen WT.40.I.1C presents a completely different force-displacement curve compared to others (see Figure 4.10a) with much lower stiffness (18.2 kN/mm) and a slower decrease in load immediately after the peak followed by an abrupt drop of load (35%) at approximately 13.5 mm. This drop corresponds to a clear detachment of a small portion of the front face of the wall around the anchor that was further from the lateral edge of the wall, which was not consistent with the behavior observed for the remaining tests. Also, the stiffness and ductility factor determined for specimen WT.40.I.1D are very high compared to the other specimens. The difference on the observed behaviors lies on the masonry and on the interface grout/masonry, which is discussed in subsection 4.6.

Figure 4.10 shows the monotonic and envelope curves of the tests performed on both walls, except the one of WT.40.I.2A due to problems with the instrumentation. The envelope curves resulted from connecting the points of maximum force of the first cycle of each step, with linear branches. Force-displacement curves display a long linear branch until 50% to 85% of the peak load, with the higher percentages belonging to the tests performed on Wall 1. The softening branch in all tests tended to an ultimate load interval between 35 kN to 45 kN, even for specimens WT.40.I.1C and WT.40.I.1D. This is most likely related with friction of the interface grout/masonry and the compression state of the walls. The cyclic curves from tests at the top did not show a clear degradation, when compared to the monotonic curves.

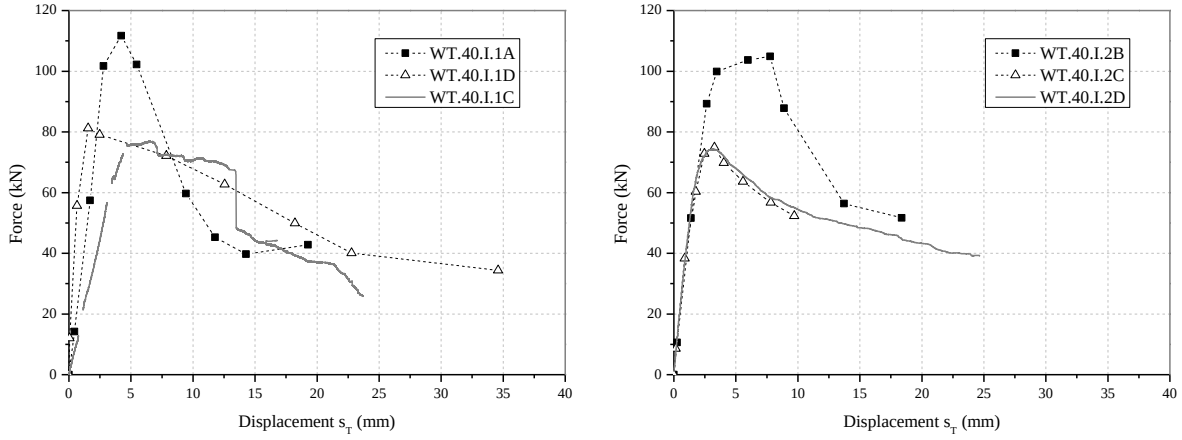

(a) (b)

Figure 4.10 Monotonic and envelope curves based on s_T: (a) Wall 1; (b) Wall 2.

The force-displacement curves of the cyclic tests present similar hysteresis loops, but the ones performed at the top present a smother slope after the post peak than the ones performed at the bottom (see Figure 4.11). Specimen WT.40.I.1D had higher deformations, because one of the anchors presented high relative displacements at the interface grout/masonry. A small fault in the acquisition box caused a loss of data during the second step of the procedure, in specimen WT.40.I.2B, but it did not compromise the analysis of the results. As can be observed, the pinched hysteresis loops show great similarity and are controlled by bond slip phenomena at the grout/masonry interface. The cyclic behavior shows a degradation of force and stiffness with the increasing steps and an accumulation of residual displacements. The descending branches of the cycles pushed the specimen as much as 0.5 mm, which caused the development of compressive forces. The values of this force obtained for top and bottom of the walls were close (21.0 kN and 30 kN), not portraying the clear distinction noticed for tension. Specimen WT.40.I.1D behavior in compression also stood out in comparison with the remaining specimens, since its compression forces reached almost 10 kN more. Residual displacements

and compression forces seem to depend greatly on the composition of the interface grout/masonry and surrounding masonry.

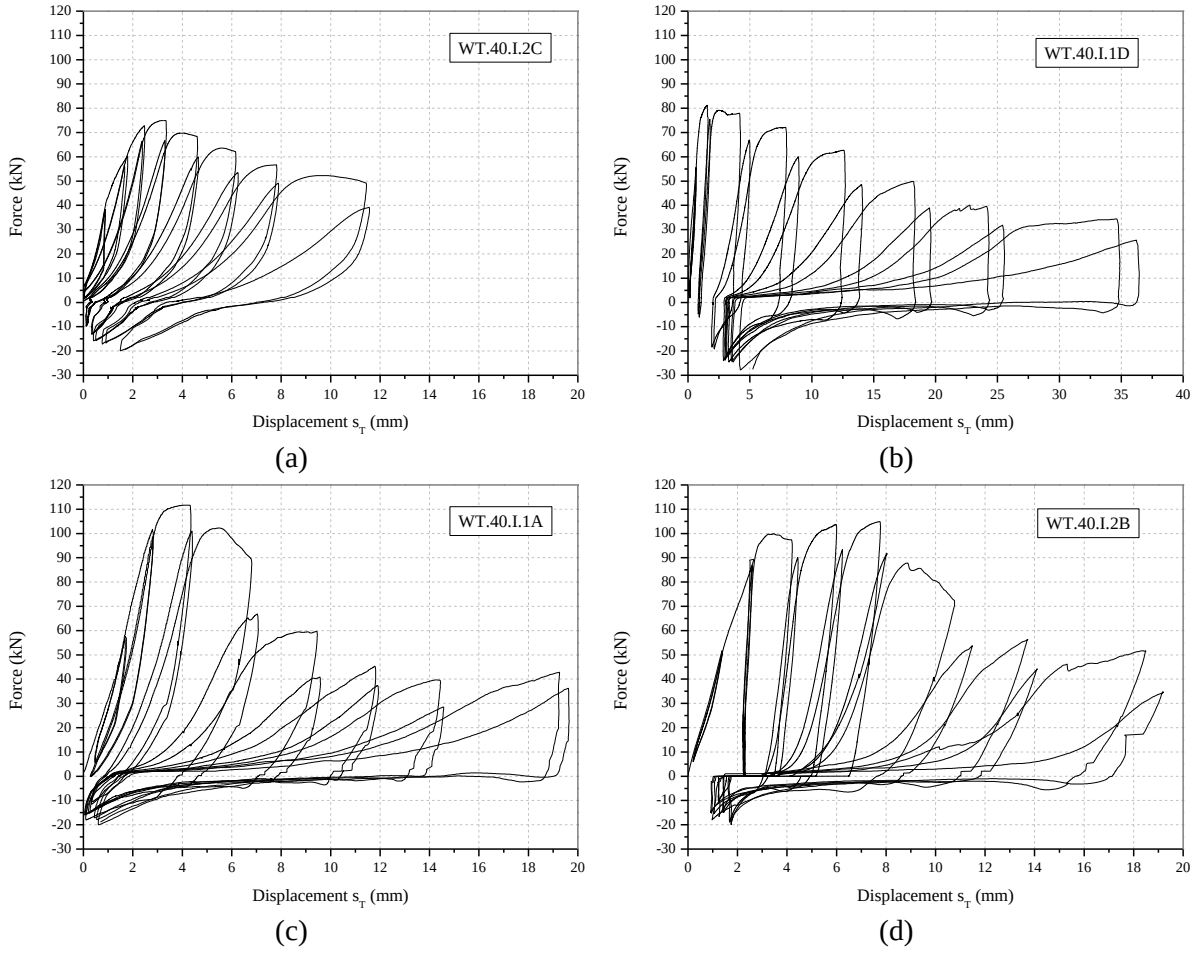

Figure 4.11 Force-displacement curves for cyclic tests, based on s_T: (a) bottom of the wall; (b) top of the wall.

Figure 4.12a presents the force-displacement curves for the front of the wall, considering the average of the displacements from positions 2 to 12 (see Figure 4.8), except numbers 6 and 8, which correspond to the anchors. All tests presented considerable accumulation of residual displacements after the peak load due to the appearance of cracks, which continued to open as the tests progressed. Tests performed at the bottom of the wall and specimen WT.40.I.1D (at the top) do not show increase displacement of the front of the wall towards the end of the last step of the procedure, meaning that the anchor is completely sliding at the interface with the masonry. At the back of the wall a snap-back effect on the curve was clear, after the peak, meaning that the back face of the wall was no longer being engaged in the full response and the masonry cone breakout occurred (see Figure 4.12b). At both front and back faces of the wall, tests performed at the bottom of the wall engaged the wall less than the ones at the top, with much smaller displacements.

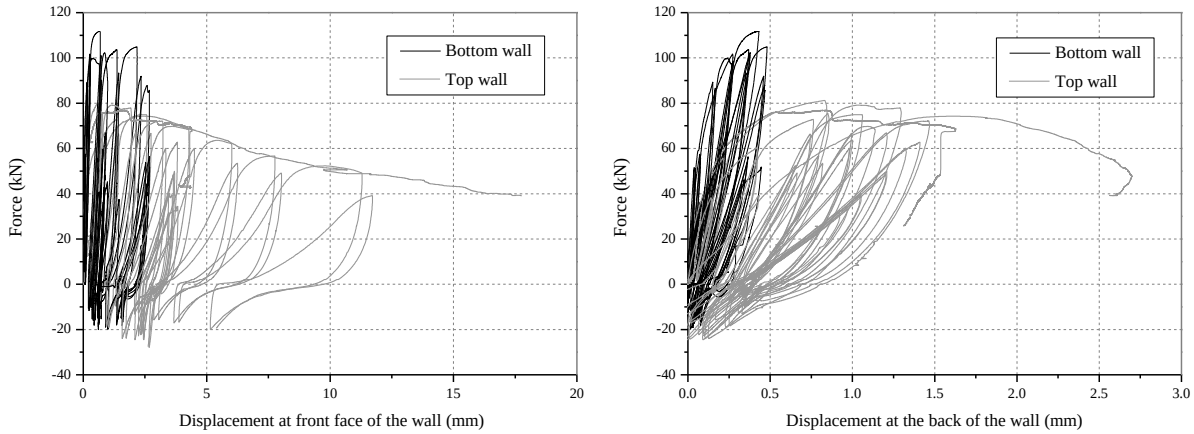

(a) (b)

Figure 4.12 Force-displacement curves of the wall: (a) average of the front face of the wall; (b) back face of the wall.

4.5.1 Crack pattern analysis

After performing the tests, specimens were demolished and carefully surveyed in order to find physical evidences of the failure modes and other aspects that could influence the results. A fully formed masonry cone failure was observed on tests performed on the top of the wall, as shown in Figure 4.13a,b (arrows indicate the direction of the pullout force). These tests evidenced a failure cone angle between 45° and 50°, which confirmed the initial assumption, and results from the energy dissipation analysis. This survey showed an overlap between failure cones, which is a direct result of the proximity between injection anchors. Also, it can be observed that the formation of the cone did not initiate at the free end of the anchor, the cone depth varied between 180 mm and 300 mm. Due to the large difference in resistance between mortar and stone, cracks propagated through mortar – especially through mortar/stone interface (see Figure 4.13c, d). Crack pattern of each specimen is presented in Annex 2. Sliding at the interface grout/masonry was also observed.

Except for specimen WT.40.I.2A, which presented one crack in the masonry radiating from half distance of the anchoring length (no other similar cracks were observed), remaining tests at the bottom showed smaller shallow cones (see Figure 4.14a, b), without cracks crossing the borehole, as shown in Figure 4.14c. During the tests, parts of the shallow cone, containing mortar and stone, detached and fell. For the tests at the bottom, sliding at the interface grout/masonry was more prominent, as shown in Figure 4.14d.

The grout plug of a certain number of the anchors had transversal and longitudinal cracking––a phenomenon also observed by Gigla (2004) —and in some cases a cone-shaped segment of the grout plug detached from the free end of the anchor (see Figure 4.15 and Annex 2, for more details). Longitudinal cracks are probably related with compression along the grout plug, and

the transversal cracks might result from coned-shape micro-cracking radiating from the threads of the steel tie (Ožbolt et al., 1999). Main observations, included in Annex 2, concerned cracks (longitudinal and/or transversal), cone-shaped segment of the grout plug broken at the free end of the anchor, presence of grout bulbs, and position of the tie rod relatively to the grout plug. Visual inspection revealed distinct aspects between the anchors that can contribute for the differences in behavior, but one could not quantitatively relate them to the physical quantities measured.

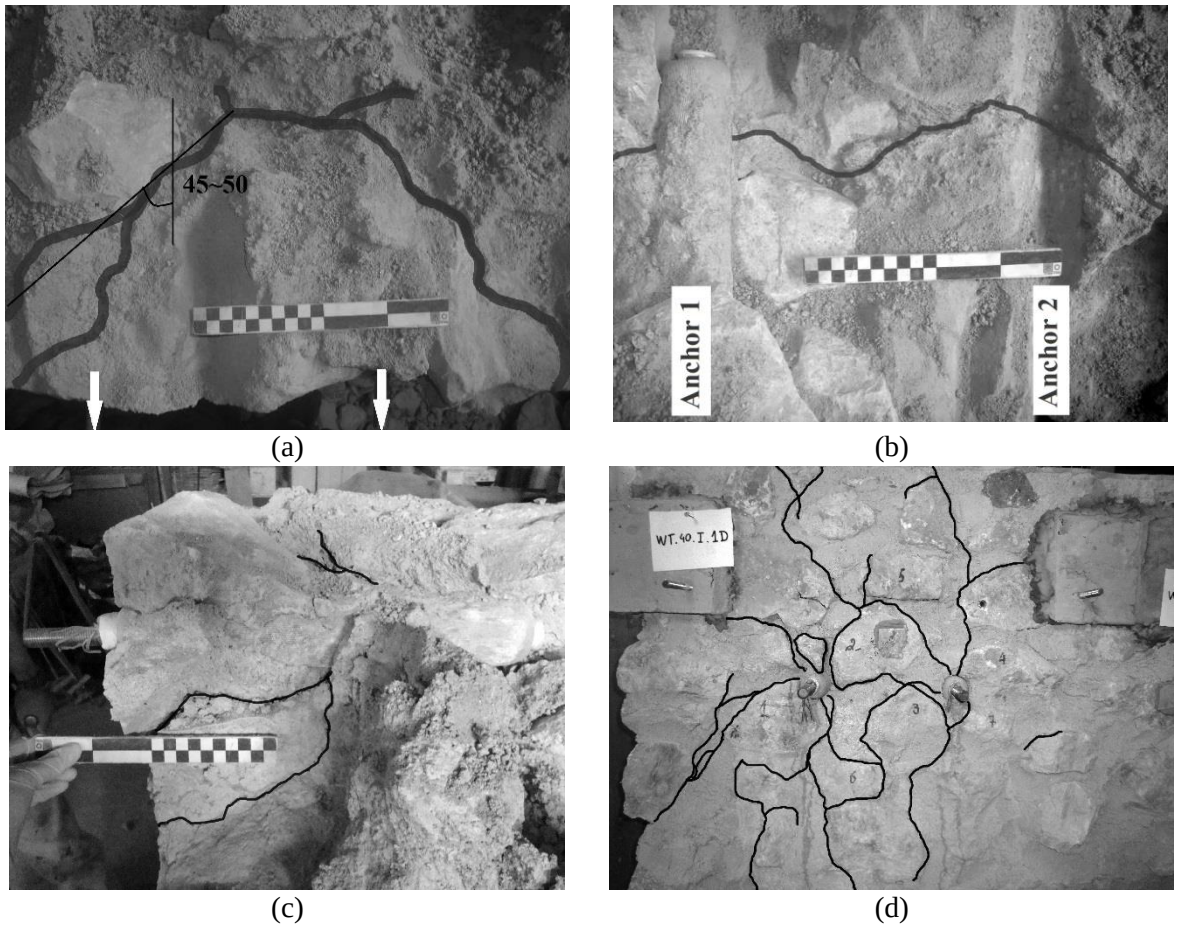

(a) (b)

(c) (d)

Figure 4.13 Observed damage on tests at the top: (a) top view of a fully formed cone (WT.40.I.2C); (b) cone intersecting the anchors (WT.40.I.2C); (c) side view of the masonry cone (WT.40.I.2D); and (d) generalized cracking (WT.40.I.1D).

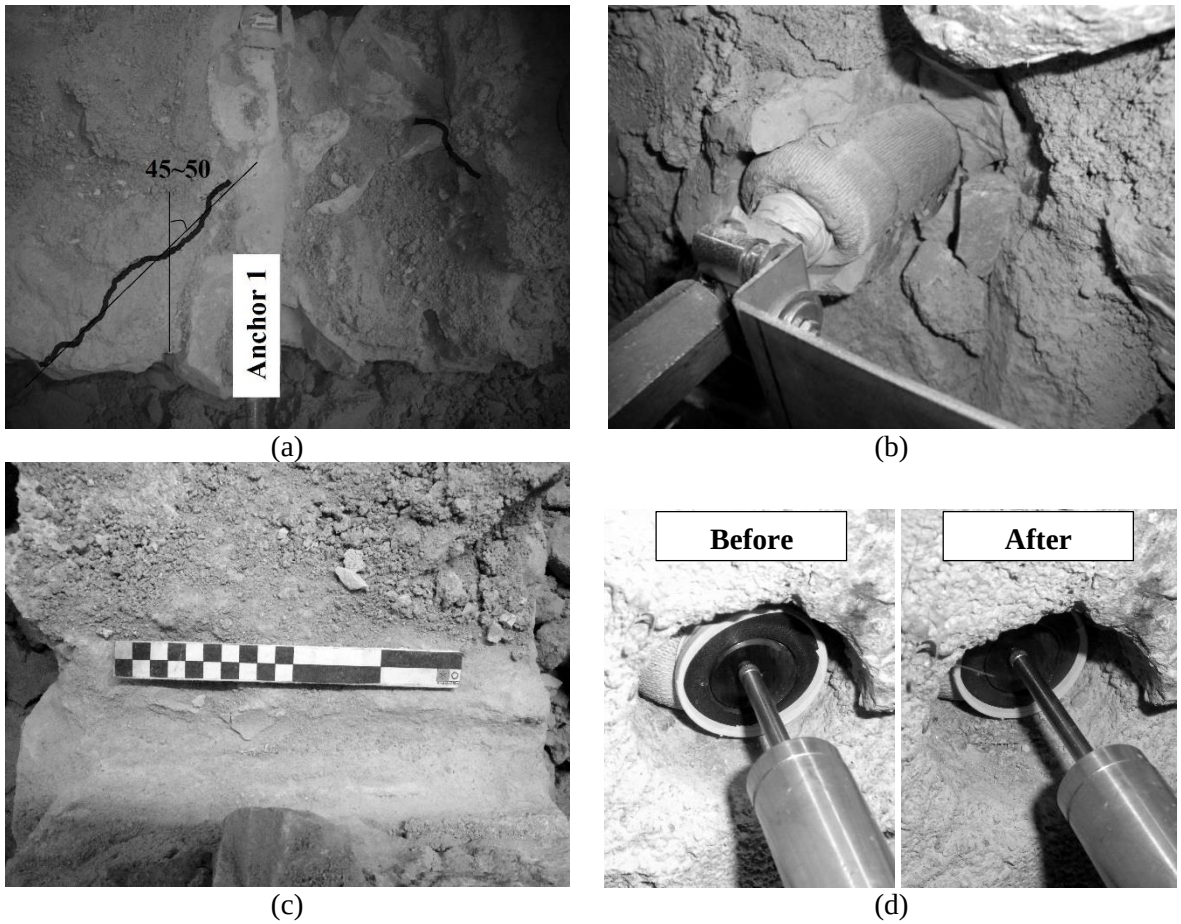

Figure 4.14 Damage observed on tests at the bottom: (a) crack due to masonry cone breakout on specimen (WT.40.I.2A) (b) sliding on the interface grout/masonry with detachment of a shallow masonry cone (WT.40.I.2B); (c) no cracks across the borehole (WT.40.I.1D); and (d) sliding at the free end (WT.40.I.1D).

Figure 4.15 Injection anchors after testing.

All injection anchors were measured after testing and the interfaces grout/masonry were studied. In spite of the theoretical anchorage length being assumed as 350 mm, measurements of the fully expanded anchors showed that not the entire length is in contact with the borehole. Instead, the real h_{ef} is smaller than the theoretical one, as presented in Table 4.2, but there is no great distinction between anchors.

As shown in Figure 4.15, it was possible to observe that anchor's diameter varied with the type of surface existing in the hole and that the sock expanded more when in contact with mortar, generating grout bulbs. While the diameter of the borehole was ϕ50 mm, the anchor diameters ranged from 49.9 mm to 63.6 mm, with an average of 56 mm. The largest anchor diameters were in fact over 10 mm greater than core size. The parameter e_d in Table 4.2 reflects the absolute difference between the diameters measured and the diameter of the borehole. The difference of e_d between anchors of the same pair possibly had an impact on the distribution of forces per anchor, since higher e_d leads to higher interlocking at the interface grout/masonry. In specimen WT.40.I.1A, the higher e_d of Anchor 2 is consistent with the fact that this anchor displayed smaller displacements than Anchor 1. Low values of e_d characterize both anchors of specimen WT.40.I.1C (high percentage of interface grout/masonry in contact with stone), which may explain the lower value of stiffness determined for this test. Searching for a correlation between the proportion of areas of stone and mortar in the interface grout/masonry with the pullout strength, as suggested by Gigla (2004), those areas were determined but no direct correlation was found with the maximum load. Detailed values for each anchor are presented in Table 4.2.

Table 4.2 Mortar and stone surface distribution per anchor

Specimen	Anchor 1				Anchor 2			
	Real l_b	**Mortar (%)**	**Stone (%)**	**e_d (mm)**	**Real l_b**	**Mortar (%)**	**Stone (%)**	**e_d (mm)**
WT.40.I.1A	32.5	53	47	4.75	31.5	70	30	9.33
WT.40.I.2A	34.0	32	68	5.86	34.0	56	44	7.08
WT.40.I.2B	34.0	75	25	7.45	34.5	25	75	4.39
Bottom average	33.5	54	46	6.0	33.3	51	49	6.9
CoV (%)	2.6	40	46	22.5	4.8	46	47	35.6
WT.40.I.1C	33.5	22	78	4.48	32.5	10	90	3.93
WT.40.I.1D	33.5	58	42	6.23	33.5	53	47	6.67
WT.40.I.2C	32.5	56	44	6.52	33.0	76	24	8.15
WT.40.I.2D	33.0	69	31	5.34	33.5	65	35	6.90
Top average	33.1	51	49	5.6	33.1	51	49	6.4
CoV (%)	1.4	40	42	16.4	1.4	56	58	27.7

4.5.2 Cyclic response parameters

From the force-displacement curves based on s_T (see Figure 4.11), it was possible to analyze total energy, energy dissipation, and force degradation over the 8 steps of the cyclic procedure. The total energy accounts for the elastic energy and the dissipated energy, and is determined by taking the integral of the force-displacement curve. In this particular case, it is of great interest to study the energy released in total by the grout/masonry interface and by the masonry cone. Since s_T accounts for both the grout/masonry interface (s_L) and masonry cone displacements, the difference between s_T and s_L gives an estimation of the contribution of the masonry cone alone.

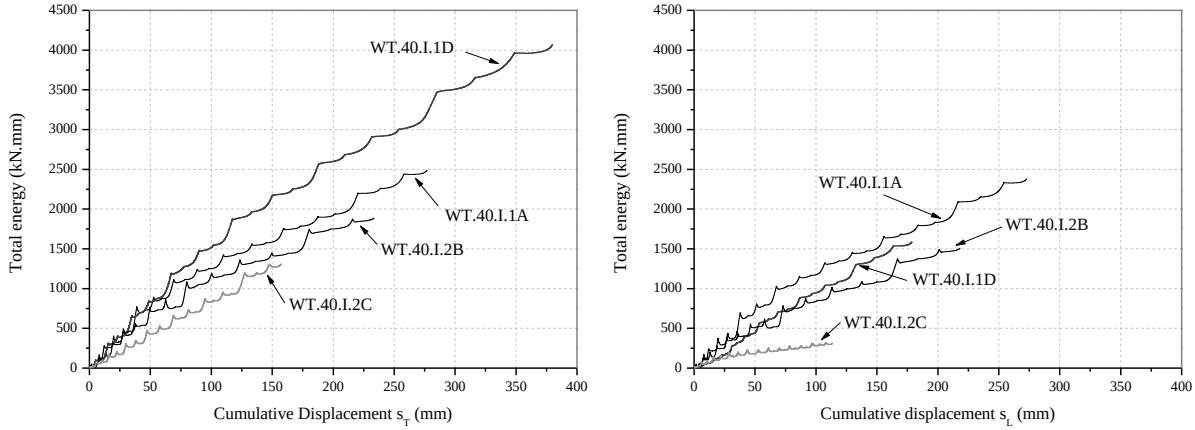

(a) (b)

Figure 4.16 Total energy analysis (a) based on s_T; (b) based on s_L.

The tests performed at the bottom of the wall (WT.40.I.1A and WT.40.I.2B) resulted in energy curves that have a good agreement among them (see Figure 4.16). The curves for the tests performed at the top of the wall (WT.40.I.1D and WT.40.I.2C) show very different ranges of total energy as well as cumulative displacement. The differences between WT.40.I.1D and WT.40.I.2C can be explained mainly by large displacements in the pair of anchors in WT.40.I.1D, rather than a large increase in force (in this case only 8%). As it can be observed in Figure 4.16a, the concavity of the curves has a tendency to weaken with the progression of the test due to the high residual displacements verified at the cracked face of the wall.

The dissipated energy per step and cycle, shown in Figure 4.17, gives better insight of the response through the development of the failure mode. Tests WT.40.I.1A and WT.40.I.2B (bottom of the wall) had peaks at 8 mm and 12 mm steps for the 1st cycle, respectively. This release of energy occurred during the step after the peak load was reached: 6 mm and 10 mm steps, respectively. Tests WT.40.I.1D and WT.40.I.2C presented smoother curves, always with a tendency to increase, as shown in Figure 4.17a. On the other hand, cycle repetition does not have such distinct peaks and less energy is dissipated (see Figure 4.17b**)**.

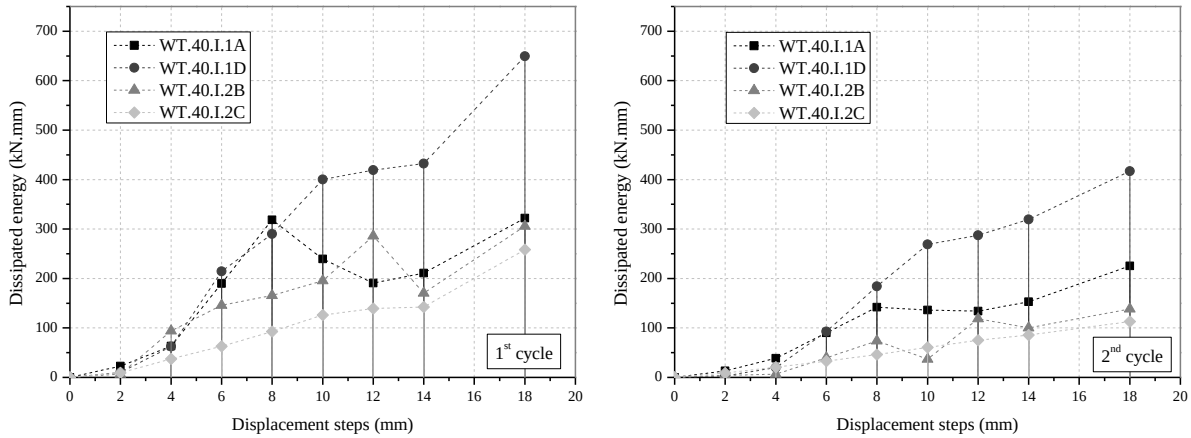

(a) (b)

Figure 4.17 Dissipated energy analysis per cycle: (a) 1st cycle; (b) 2nd cycle.

The dissipated energy per displacement contributions (grout/masonry interface and cone) calculated for each test shows that the tests performed at the bottom of the wall have a higher contribution from the interfaces than the ones performed at the top. Tests WT.40.I.1A and WT.40.I.2B showed little contribution from the masonry cone, with values ranging from 5% to 12%. On the other hand, WT.40.I.1D and WT.40.I.2C relied more on masonry cone failure, but with less extreme contributions of the interface: 38% and 22% (see Figure 4.18a).

Strength degradation between cycles was also determined for each step of the cyclic procedure (see Figure 4.18b) and there is a great deal of variability between tests. Again, tests WT.40.I.1A and WT.40.I.2B showed higher strength loss in the steps after the peak load was reached. This explains why the peaks are barely noticeable on the dissipated energy of the 2nd cycle (see Figure 4.17b). For the tests at the top of the wall (WT.40.I.1D and WT.40.I.2C) higher values of strength degradation were observed for the next 2 to 3 steps after the peak load. At the 18 mm step (last step), each test had the following strength reduction: WT.40.I.2B – 51%, WT.40.I.1A – 62%, WT.40.I.2C – 30%, and WT.40.I.1D – 58%.

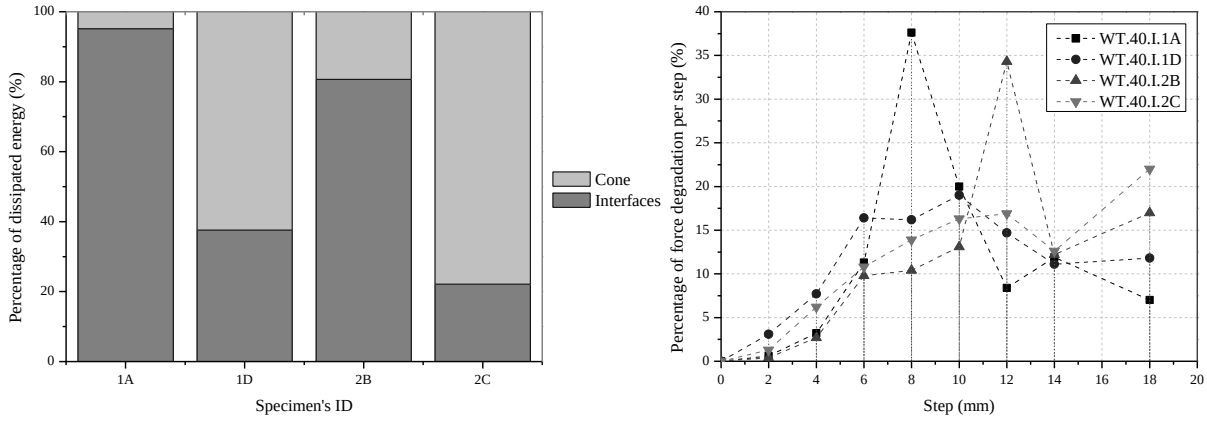

(a) (b)

Figure 4.18 Dissipated energy per displacement contributions (interface and cone); (b) Force degradation between cycles per displacement level.

The unloading stiffness, k_{un}, was determined for each cycle of the displacement levels and its evolution is presented in Figure 4.19. To facilitate comparison, the stiffness k_{un} was calculated as the slope of the line connecting the points corresponding to 40 % and 85 % of the maximum force of the cycle in question, in the unloading branch. Considering the pinched behavior of the hysteretic loop, the 40 % limit corresponds to the transition between unloading stiffnesses, and the 85 % limit was established by the need to exclude the effect of load reversal caused by the actuator.

There is not a clear difference between tests performed at the top and bottom, instead specimen WT.40.I.2C shows a distinct evolution when compared to the remaining tests (see Figure 4.19). The latter presents a clear degradation of stiffness throughout the cyclic loading, starting with high values of k_{un} – 357.9 kN/mm and 379.0 kN/mm – in the first and second cycles of the first displacement level (2 mm) respectively, which decreased abruptly in the second displacement level (4 mm), and continued to decrease steadily until reaching approximately 10 % of k_{un} of the first displacement level. For specimen WT.40.I.2B, k_{un} was not calculated for the second displacement level (4 mm), for the reasons previously presented. Nonetheless, is possible to observe an increase in k_{un} until the displacement level of 6 mm, which also occurs for specimens WT.40.I.1D and WT.40.I.1A. These two last specimens show very high values of stiffness (WT.40.I.1A only for the second cycle curve), towards the end of the cyclic procedure. However, most curves presented in Figure 4.19 show a degradation of stiffness throughout the test and between cycles of the same displacement level. The stiffness values corresponding to the last displacement level of specimen WT.40.I.1D were excluded from Figure 4.19, because they were not considered valid (negative values).

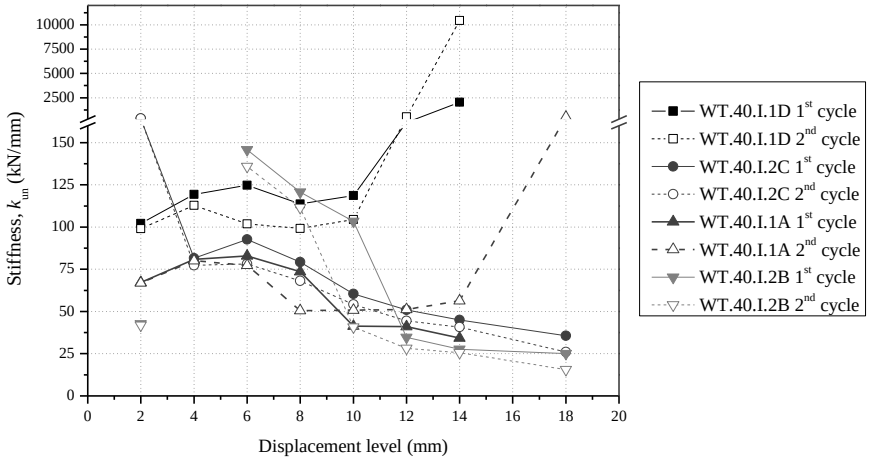

Figure 4.19 Evolution of unloading stiffness throughout the cyclic loading.

4.6 DISCUSSION OF RESULTS

The location of the anchors on the wall was specifically chosen so that the masonry cone failure could fully develop. This was done by keeping the distance to all edges greater than the embedment length. A compromise had to be made when idealizing the test apparatus — the steel supports overlapped 7% of the projected area of the masonry cone. Therefore, there can be a small confinement resultant from this overlap.

The monotonic test, WT.40.I.1C, presented a different force-displacement curve compared to other tests (see Figure 4.10), with lower stiffness and a rough softening branch that could have been related to a different arrangement of the masonry wall or the grout/masonry interface.

All tests showed combined cone-bond failure with sliding at the interface grout/masonry and masonry breakout. Energy dissipation quantification (see Figure 4.18) confirmed what was observed during visual inspection: tests at the top showed a higher influence of the masonry cone while tests at the bottom showed bond failure at the interface grout/masonry as the major contributor for failure. The different behavior in failure is apparently linked to the high discrepancy in tensile capacity between top and bottom anchors.

Tests were carried out from bottom to top, but when large differences in force were observed it was decided to perform test WT.40.I.1C (top anchors) before others. Regardless, the same difference in load was observed. A possible interference between tests sequence was thus discarded as an explanation for the difference in behavior. The source of this 30% difference in load may lie in the different boundary conditions of the wall. The bottom of the wall was supporting directly on the lower concrete slab, while the top of the wall had the steel profiles and the hydraulic cylinders between it and the upper reaction slab. Especially the hydraulic cylinders, constituted much slender elements than the rest, leading to rotation of the upper part. Evidence of this phenomenon, was the continuous need for adjustment of the pressure necessary to keep the compressive state of the wall constant. The hydraulic cylinders loading the wall from above required continuous adjustment to keep the compressive state constant. The pressure slightly increased while pulling and decreased while pushing. Also, tests carried out close to the base of the wall consistently showed smaller displacements, as presented in Figure 4.12. Therefore, it is likely that the test set up created a fixed support at the bottom and a pinned support at the top of the wall. This can explain the different behaviors of the tests in different locations, including the predominance of the failure modes. Further studies of anchors with different boundary conditions are required to answer the distinct behavior observed, but the lower values obtained in the tests can be adopted on the safe side.

Since boundary conditions were the main factor affecting the results, it is difficult to derive any influence of the diameter of the steel rods. The existence of a washer at the free end of the anchors prevented, as expected, occurrence of sliding at the interface steel rod/grout. Also, the high grade of steel class excluded yielding of the rod and kept it within the elastic range. Both factors tend to assure that the diameter of the rod had a small influence on the results.

The envelop force-displacement curves (see Figure 4.10), especially of the tests performed at the bottom, towards the end of the softening branch tend to a force interval between 35 kN to 45 kN, which is an effect of friction at the interface grout/masonry or in the cone region due to the presence of vertical load on the wall. When drilling the holes for installation, installing the injection anchors, and carrying out the test, the walls were always under a compressive state. Therefore, sliding at the interface has the contribution of cohesion (right after the peak) and internal friction, which is the tangent of the friction angle multiplied by the normal stress (tendency for a horizontal plateau). A similar effect can occur at the cone due to crack dilatancy and wall confinement.

In spite of the variability obtained for the ductility factor, one must point out that all specimens presented ductility factors above 3, which is favorable for seismic performance. It means that the connection has the ability to undergo considerable amount of deformation in the plastic range with a reduction in strength up to 20%. The average ductility of the tests at the bottom of the wall (3.4) is lower than the one determined for the top (6.3, if specimen WT.40.I.1D is excluded), which is mainly justified by prolonged linear branches and the abrupt loss of load immediately after the peak, observed for the tests on the bottom.

While tests performed on the bottom of the wall present good agreement in terms of total and dissipated energy, tests at the top show different behaviors. Sliding occurring on the grout/masonry interface is the phenomenon that governs stiffness and force degradation between cycles, the pinching effect observed on the hysteretic loops, and the decrease in energy dissipation between cycles. The different contributions of grout/masonry interface damage and masonry cone breakout to the failure of each specimen might explain the distinctions on the performance parameters quantified.

4.7 CONCLUSIONS

The tests were successfully executed, since many of the initial considerations were confirmed, but also new questions were raised. This research adds critical experimental

information about the behavior of parallel injection anchors for wall-to-timber elements connections or similar applications in stone rubble masonry.

Boundary conditions seem to have provided a distinct behavior between anchors at the top and bottom of the wall in terms of force-displacement curve, maximum pullout force, and failure mode type (bond and/or cone failure). All tests showed combined cone-bond failure, with higher contribution of the bond slip in the tests performed at the bottom and higher participation in failure of the cone breakout in tests performed at the top. The compressive stress of the wall influenced the behavior of the injection anchors, which was especially noted with the contribution of internal friction in the softening branch of the curve.

Chapter 5. Wall-to-floor connections

Highlights

- Four failure modes were hypothesized;
- Unstrengthened connections failed by nails pullout;
- Strengthened connections presented failure of the connection between steel angle and timber joist;
- Other damage mechanisms influenced the response of the connection;
- Strengthening increased the tensile capacity comparatively to the unstrengthened connections;
- Changes on the strengthening solution and compressive state of the wall influence the response of the connection.

5.1 INTRODUCTION

This chapter focuses on the experimental campaign carried out on wall-to-floor connections, in the Laboratory of Structures of University of Minho (LEST). The performed tests concerned the pullout behavior of unstrengthened and strengthened wall-to-floor connections, with the objectives of developing a full functioning test apparatus for this particular type of tests, studying failure modes and quantifying parameters as: maximum pullout force, stiffness and force degradation, displacement ductility, and energy dissipation.

Following sections describe all the levels from the hypothesized behavior, passing through test set-up development, and closing with the discussion of the results.

5.2 EXPERIMENTAL BACKGROUND AND HYPOTHESIZED BEHAVIOR

In spite of their recognized importance, wall-to-floor connections have not been subject of many experimental campaigns with the objective of characterizing their behavior and studying possible retrofit solutions. Only recently, pullout tests have been conducted *in situ*, on original specimens, or in laboratory, with representative specimens.

Lin & LaFave (2012) carried out several pullout tests on strengthened connections (representative specimens), under different conditions, to study their capacity and the influence of parameters like the loading protocol and compressive stress state. Pullout tests were also performed on unstrengthened specimens to assess the friction coefficient, at different compressive load levels. The representative connection belonged to typical pre-50s URM constructions and it was constituted by a brick masonry wall portion and a timber floor joist, supported on approximately 0.1 m of the wall. While the unstrengthened connection relied only on friction to resist to horizontal actions, the strengthened connection was equipped with wall anchors made of a steel strap and a threaded rod, welded together. The steel strap was nailed to the timber floor joist, by two nails, and the threaded rod was anchored on the external face of the masonry wall portion, by means of a washer and a standard hex nut. Its capacity was estimated to be between 5.8 kN and 8.5 kN, and was associated with nails' shear off and pullout. It was also concluded that dynamic loading leads to more conservative displacements, in comparison with monotonic and quasi-static cyclic loadings, which consequently increases brittleness of behavior. At the same time, there was no clear distinction between backbone curves of the specimens tested under monotonic or cyclic loading.

Campbell et al. (2012) discussed failure modes of wall-to-floor connections strengthened with a similar solution as the one studied by Lin & LaFave (2012), observed after the 2011

Christchurch earthquake. The most common failure mode was punching shear failure of masonry, followed by yielding or rupture of the connector rod, rupture at weld between connector rod and joist plate, and splitting of joist or stringer. The failure modes concerning failure of fixing at joist plate, splitting or fracture of the anchor plate, and yielding or rupture at threaded nut were not observed.

As presented in Chapter 1, the wall-to-floor connection's configuration chosen as research focus is commonly observed in *Pombalino Tardio* and *Gaioleiro* types of buildings (timber floor joist resting on a timber wall-plate embedded in the masonry wall), and is also observed in other URM buildings across the world. The high seismic vulnerability of these typologies of buildings reveals the pressing necessity to improve their connections. The unstrengthened connection relies on the nailed joint between the wall-plate and the timber joist and on friction between them, as well as on friction between them and the masonry wall, to resist to any horizontal demand. Consequently, possible failure mechanisms regard shear off of nails, pullout of nails, and pullout of timber elements (sliding at interfaces between timber elements and masonry wall). After failure of the nails, the interface wall-plate/joist can continue sliding with residual force due to friction.

The strengthened wall-to-floor connection under study consists of a reinforced steel angle bolted to the timber joist and anchored to the masonry wall by a tie rod with an anchor plate (see Chapter1). Considering the aforementioned research works, the existent literature on the behavior of steel ties, and specificities of the strengthening solution under study, the following failure modes are hypothesized (see also Figure 5.1):

- Formation of the masonry cone breakout (FM1);
- Crushing of masonry under the anchor plate (FM2);
- Failure of the connection between the steel angle and the timber floor joist (FM3);
- Yielding of the steel tie (FM4).

Due to the limited rotation capabilities of the hinge, one admits that there might be yielding of the steel tie (FM4) due to bending, besides direct tension. FM3 is a very complex failure mode because is the result of combined effects that occur at the bolted connection. This failure mode comprises crushing of the timber floor joist under the bolts and steel angle's reinforcements, bending and shear failure of the bolts, and yielding of the steel angle. The behavior predicted for the unstrengthened connections is also applicable to the strengthened ones, but it is marginal when compared to the contributions described previously. These

damaging mechanisms were expected to occur simultaneously, and failure could result from one clear type of failure or a combined behavior.

FM1 and FM2 are the failure modes related with the masonry, and their contribution to the connections' performance depends mainly on the mechanical properties of the masonry and on the dimensions of the anchor plate. For FM1 there is also the thickness of the wall as a determinant parameter on its capacity. FM4 strength capacity limit is determined by the nominal diameter of the cross-section of the steel tie and by the steel's strength class, but its interaction with the steel angle determines if the tensile stresses come from direct tension or bending. FM3 is mainly governed by the single shear bolted connection between steel angle and timber floor joist, and the connection between the steel angle and tie. The first one depends on the mechanical properties of the steel and timber used, and on the thicknesses of the elements involved, while the second one is conditioned by the stiffness and the tensile capacity of the steel angle. The failure modes described are directly affected by the geometrical and mechanical characteristics of the components involved, but their interaction determines how their capacities are exploited. This matter is further developed in Chapter 6.

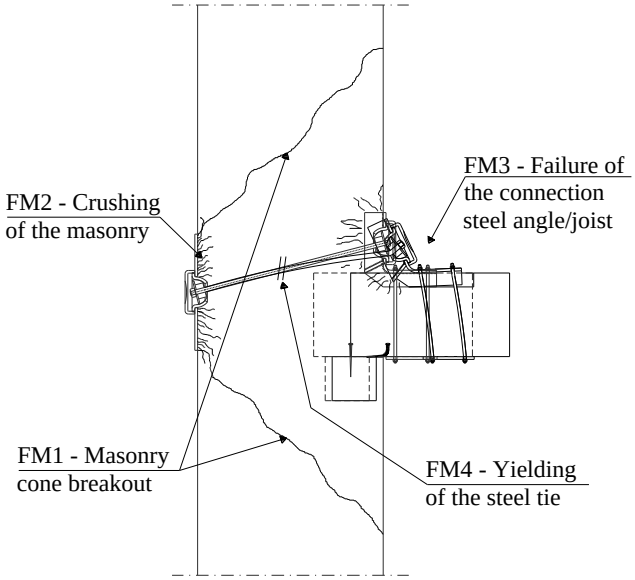

Figure 5.1 Failure modes predicted for the pullout tests of the wall-to-floor connections.

A particularity of this strengthening solution resides on the use of two hinges, one at each end of the steel rod, which enables the steel tie to be placed at an angle, rather than placed horizontally. The hinge consists of a ring notched in a half-sphere placed in a fitting cup, with all components in stainless steel, and it was developed by the company Monuments Lda. to facilitate the application of the strengthening (see Figure 5.2). In addition to improved

workability, it is possible that the presence of the hinges decreases the bending moments transmitted to the steel tie, whose validity is discussed in section 5.9.

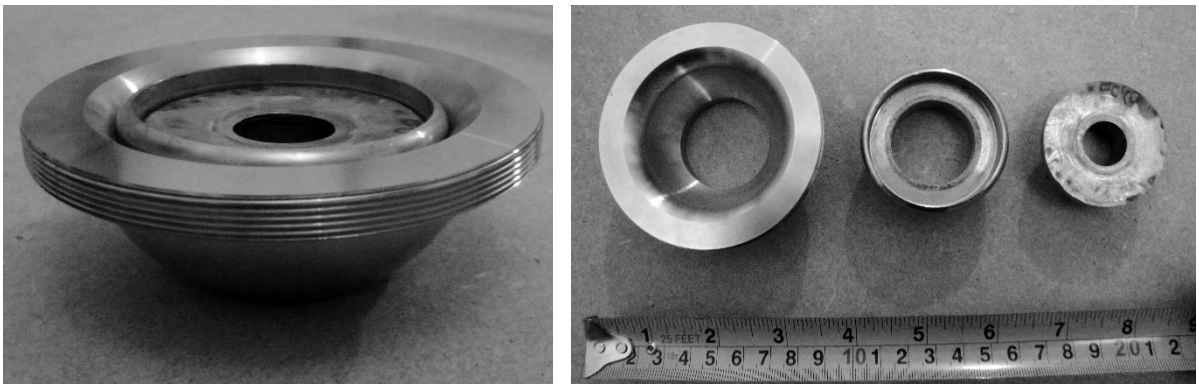

Figure 5.2 The hinge and its components.

5.3 SPECIMENS

Two types of specimens were prepared: unstrengthened and strengthened. The unstrengthened specimens consisted of an irregular masonry wall, as the ones described in Chapter 4, with timber wall-plates and floor joists. The dimensions of the specimens, masonry wall and timber elements, were defined considering the existent literature, the laboratory limitations, the test setup to be used, and especially, the failure modes expected for the strengthened specimens. Space limitations constrained in particular the length of the wall, which would have great impact on the formation of the masonry cone breakout. It was established that interference with the formation of the failure modes should be minimized by balancing the dimensions of the specimens with the test apparatus.

Two different wall thicknesses, 0.4 m and 0.6 m, were chosen in order to represent an upper floor (4^{th} floor) and a ground floor, respectively. Thus, two distinct levels of compressive stress caused by quasi-permanent service loads were applied during the tests. Those two levels were 0.2 MPa (0.4 m) and 0.4 MPa (0.6 m), and were calculated considering a quasi-permanent combination of vertical loads. The length and height defined for the specimens are the same for both thicknesses: 2.0 m and 1.6 m, respectively (see Figure 5.3). Irregular masonry walls were hand constructed by professional masons, using limestone with a maximum dimension of 0.2 m, and at most 0.05 m joints. In each wall two connections were built. Each connection had a timber wall-plate of 0.095 × 0.095 × 1.000 m^3 embedded in the masonry wall, at 0.03 m of its front face, and three timber floor joists, with a cross-section of 0.13 × 0.18 m^2, nailed perpendicularly to the wall-plate. Only the central floor joist was extended beyond the front face of the wall (0.5 m) and pulled during the test (see Figure 5.3). The timber floor joist is

0.15 m inside the wall and the nails are located at approximately 0.08 m from the end of the joist. Nails shank was 0.07 m long and were placed as showed in Figure 5.3b.

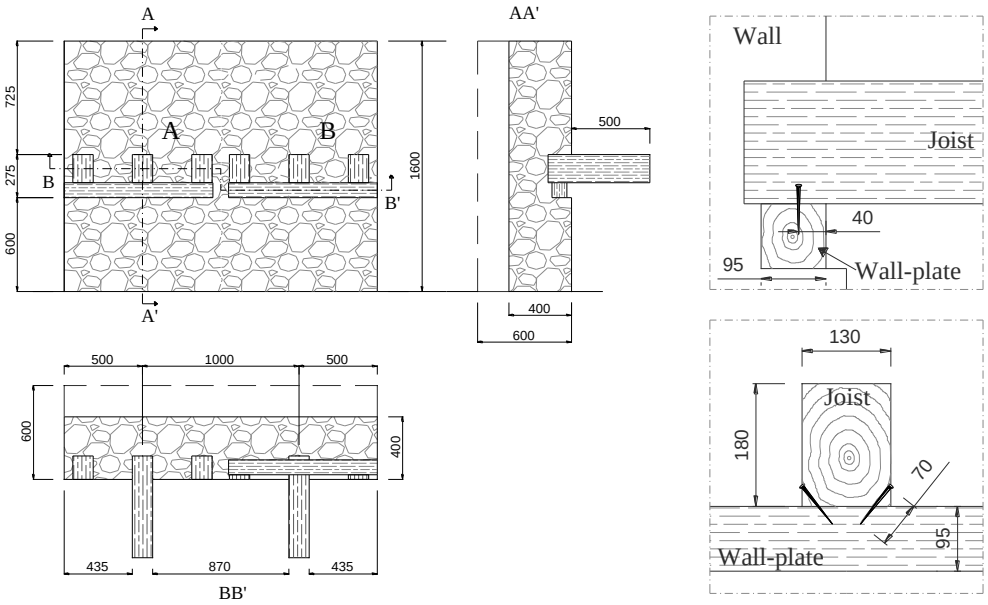

(a) (b)

Figure 5.3 Sketch of the unstrengthened specimens (dimensions in mm): (a) general configuration; and (b) detail of the nailed connection.

As presented in Figure 5.4, the masonry walls were constructed without the use of formwork, only using four vertical posts connected by threads to keep the correct thickness and verticality. The distribution of stones was as random as possible (see Figure 5.4), always assuring bond stones and discontinuous vertical joints. In order not to collapse under their own weight, the walls were built in three phases, spaced of at least 12 hours: until 0.6 m, between 0.6 m and 1.2 m, and finally from 1.2 m to 1.6 m. When the walls were raised up to 0.6 m (1st phase), the timber wall-plates were positioned according to Figure 5.3. Then, the timber floor joists were nailed to the wall-plate, and mortar and stones started to be fitted around the timber elements, as seen in Figure 5.4a, b. To prevent rotation of the joists due to their own weight, during the curing process, they were supported with small vertical posts.

The strengthening solution developed in collaboration with the company Monumenta, Ltd. consists of a steel angle bolted to the timber joist that is anchored to the masonry wall by a steel rod with an anchor plate system, as shown in Figure 5.5. The same strengthening solution is applied to both thicknesses of the walls, and the configuration of the connection is the exact same one as for the unstrengthened connections (see Figure 5.6). In addition, as part of the strengthening solution, the timber beam was wrapped with a GFRP sheet. Since the steel angle was placed while the epoxy resin was still fresh, it got glued to the timber joist.

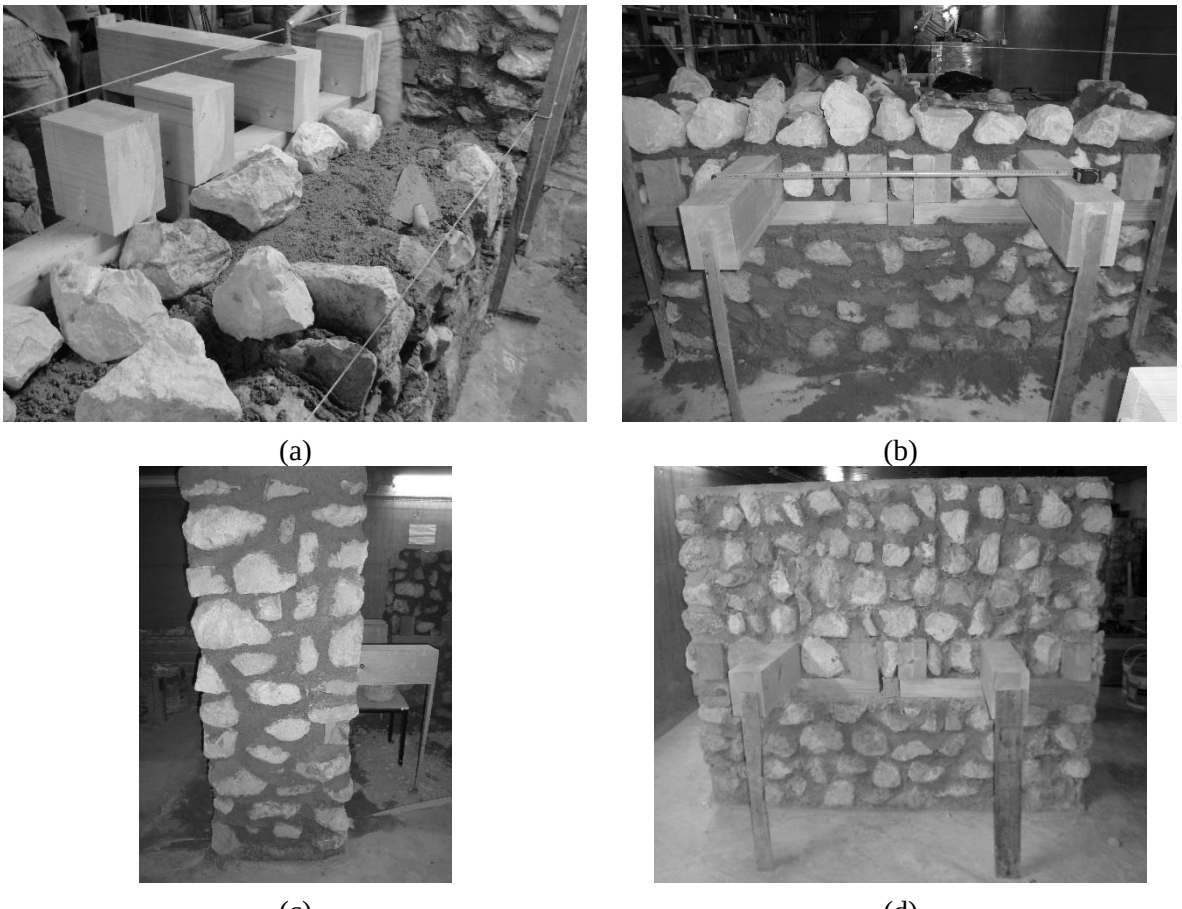

(a) (b)

(c) (d)

Figure 5.4 Construction of the specimens: (a) placement of the timber wall-plate and joists; (b) construction of the wall above the timber elements; (c) elevation of a finished wall; (d) complete specimen.

As explained, due to the presence of the two hinges, one in each extremity, the tie rod was installed with an angle of 15° angle with the horizontal plane, which was suggested by the construction company as common angle of application. As a result, an eccentricity arose relatively to the horizontal middle plan of the floor joist, being approximately 0.049 m (upwards) for the 0.4 m thick walls, and 0.007 m (downwards) for the 0.60 m thick wall (see Figure 5.5). The anchor plate applied on the 0.40 m walls had a squared shape and the dimensions of 0.175 × 0.175 × 0.006 m^3. After conducting the cyclic tests on the 0.40 m walls, it was decided to increase the thickness of the anchor plate to 0.020 m, to prevent its bending. The bolted connection between the steel angle and the timber joist consisted of a single shear connection, with four A2 stainless steel (304) bolts of ϕ10 mm. The estimated capacity is discussed in Chapter 6. To prevent premature yielding and failure of the steel tie, ϕ16 mm diameter bars of high-grade steel (class 8.8) were applied. For the same reason, reinforcements were welded to the steel angle, and an AISI 304 stainless steel grade was used. The dimensions of all the components of the strengthening solution are presented in Annex 3.

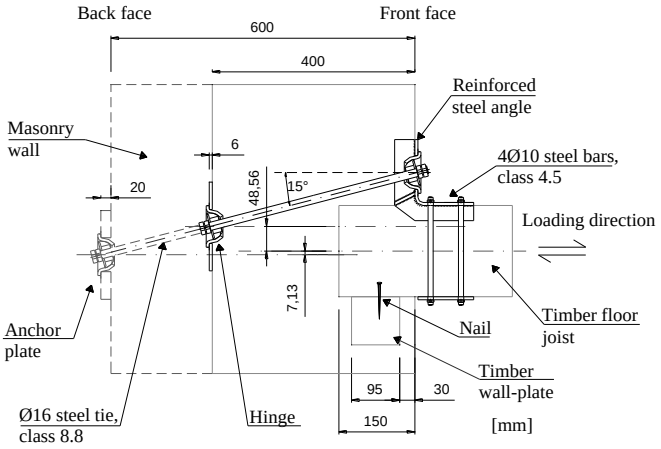

Figure 5.5 Retrofit solution for wall-to-floor connections (dimensions in mm).

A total of ten walls was built, five for each thickness – 0.4 m and 0.6 m. This is equivalent to 10 specimens per wall thickness, adding up to a total of 20 specimens. Of these, four specimens were unstrengthened, while the remaining 16 were strengthened. Following the criteria established in Chapter 4, the specimens' denomination aimed at identifying in all contexts the singularities of each specimen. Therefore, their name comprises: the type of connection (wall-to-floor connection – WF), the thickness of the masonry wall (40 cm or 60 cm), if strengthened (A from anchor plate) or unstrengthened (U), the number of the wall (goes from 1 to 5), and finally the position of the specimen on the wall (A or B, as in Figure 5.6). As an example specimen WF.40.A.1B refers to the wall-to-floor strengthened specimen, in wall number 1, which is 0.4 m thick, in position B.

The installation of the strengthening on the connection followed the levels showed in Figure 5.7. First, one would place a frame of the steel angle, in order to mark on the joist the location of the pre-drilled holes for the bolts and the reinforcement of the steel angle, and also to mark the location of the coring (for the steel tie) on the wall. Then, the holes and the slot were performed. Inside a perimeter of 0.1 m from the location of the steel tie, the masonry wall was broken, on the front and back faces, to accommodate the steel angle reinforcements and anchor plate, respectively. The next level was the application of the GFRP layer, and the placement of the steel angle while the epoxy was still fresh. After positioning the remaining metallic components, the area previously opened on the wall was filled with fast curing cement mortar, completing the installation process (see Figure 5.7). After hardening of the mortar, the entire system was manually tighten. For the tests, this step was carried out after the instrumentation of the steel tie with strain gauges.

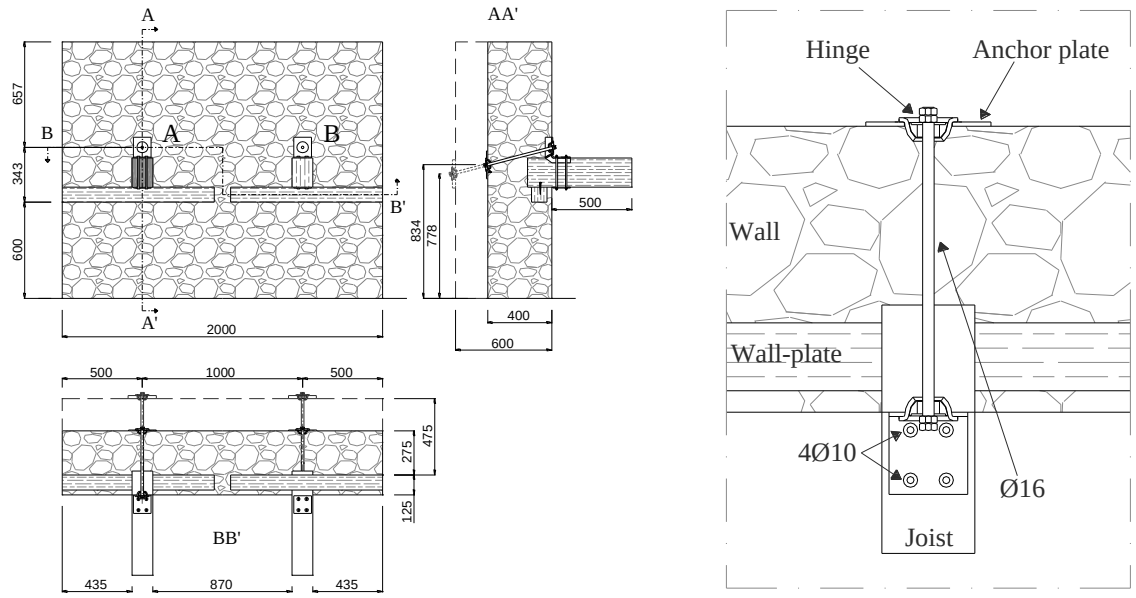

(a) (b)

Figure 5.6 Sketch of the strengthened connection (dimensions in mm): (a) general configuration; and (b) plan view of detail of the strengthening.

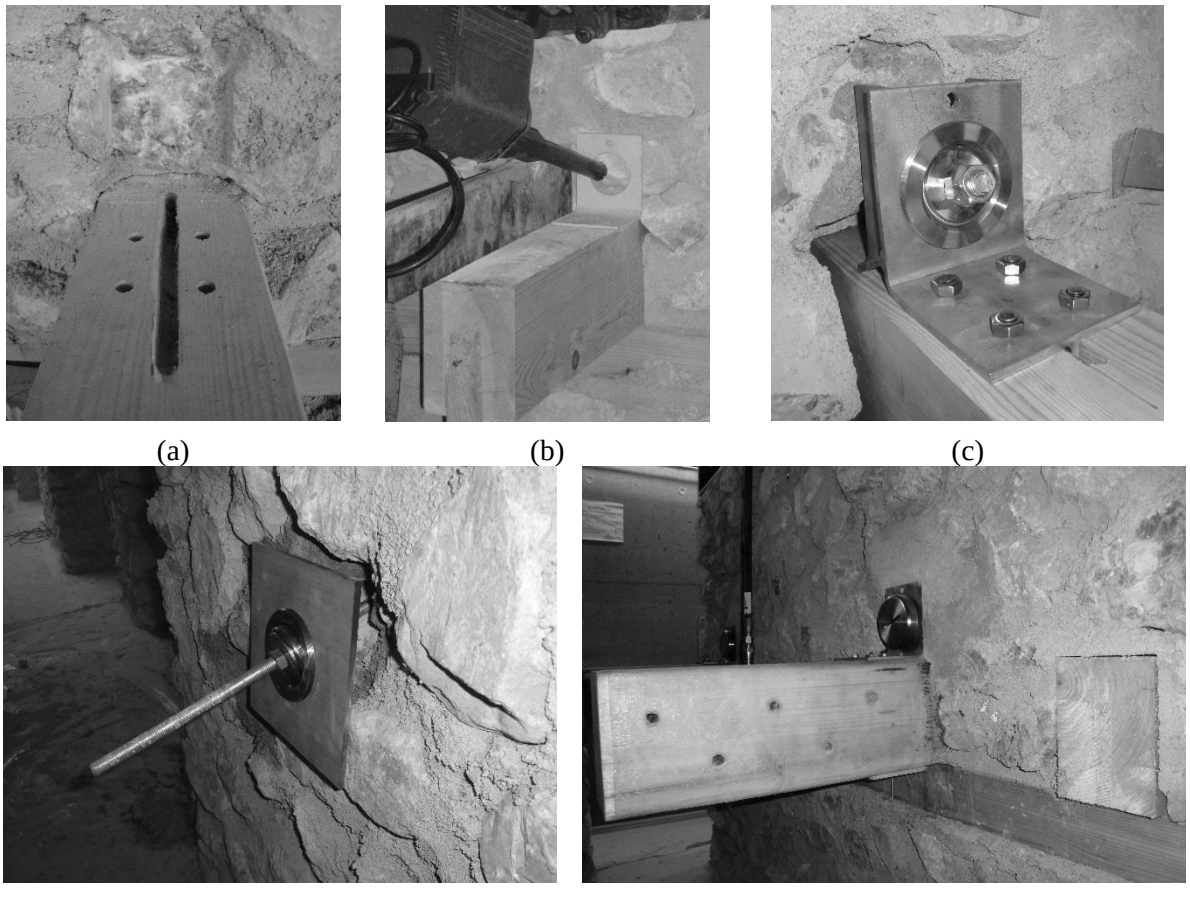

(a) (b) (c)

(d) (e)

Figure 5.7 Application of the strengthening: (a) coring of the hole for the steel tie; (b) execution of the drilled holes and slot to install the steel angle; (c) positioning of the steel angle, half-sphere and cup; (d) positioning of the anchor plate; and (e) completed strengthened connection.

5.4 TEST SETUP

The test setup is, in a lot of aspects, similar to the one used for the pullout tests of the injection anchors, previously described in Chapter 4 (see Figure 5.8). The metallic frame, the anchoring system, the steel profiles and hydraulic cylinders to distribute the vertical load, and actuator were kept from the previous set-up, but adaptations had to be made to pullout the timber joist. Adapting the test setup used for the injection anchors to the strengthened wall-to-floor connections, while trying to interfere the least with the possible failure modes, was the biggest concern. The dimensions of the specimens encompassed the total projected area of a masonry cone breakout, for the 0.4 m thick specimens, but in the case of the 0.6 m thick specimens, this projected area would be partially outside the wall and overlapping with the area of the neighboring connection. To minimize this decrease in capacity, the counter force coming from the test frame had to be partially applied inside the projected cone area. The extent of interference will be discussed in section 5.9.

Initially, the test apparatus had the configuration presented in Figure 5.8, at the left, which was the one used for the monotonic tests, on unstrengthened and strengthened specimens. Later on, features like the anchorage, the vertical support, and the acrow prop were added to enable quasi-static cyclic tests and to prevent excessive rotation of the timber joist (see Figure 5.8, at the right).

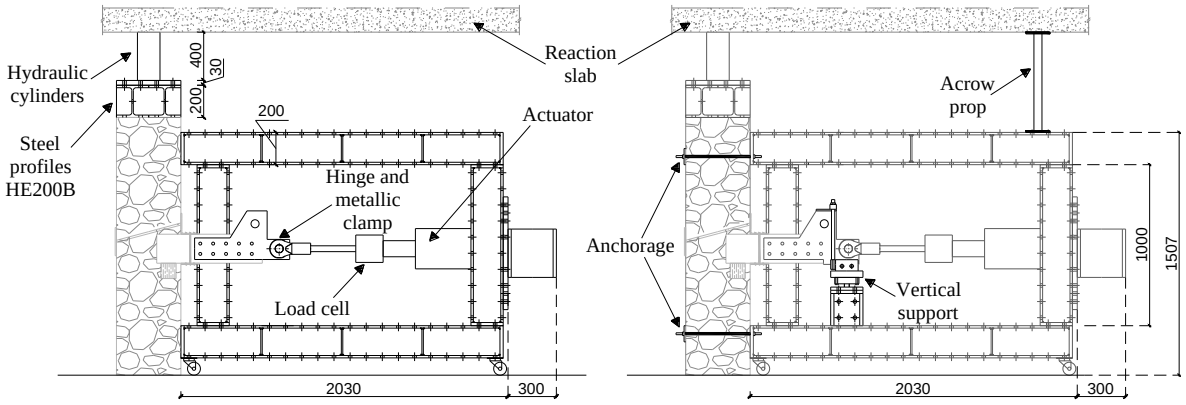

Figure 5.8 Test apparatus of the pullout tests of wall-to-floor connections.

The complete test set-up used during the experimental campaign is presented in Figure 5.9a, where one can see the complex conjugation of all parts of it. To apply the horizontal force, a metallic clamp was designed to be mechanically attached to the timber floor joist, in each test, by means of four pairs of ϕ16 threaded bars, of steel class 8.8, working as a double shear connection (see Figure 5.9b). As a consequence of the load reversal, the frame had to be

anchored to the back face of the masonry, as it was already explained for the pullout of injection anchors (see Chapter 4).

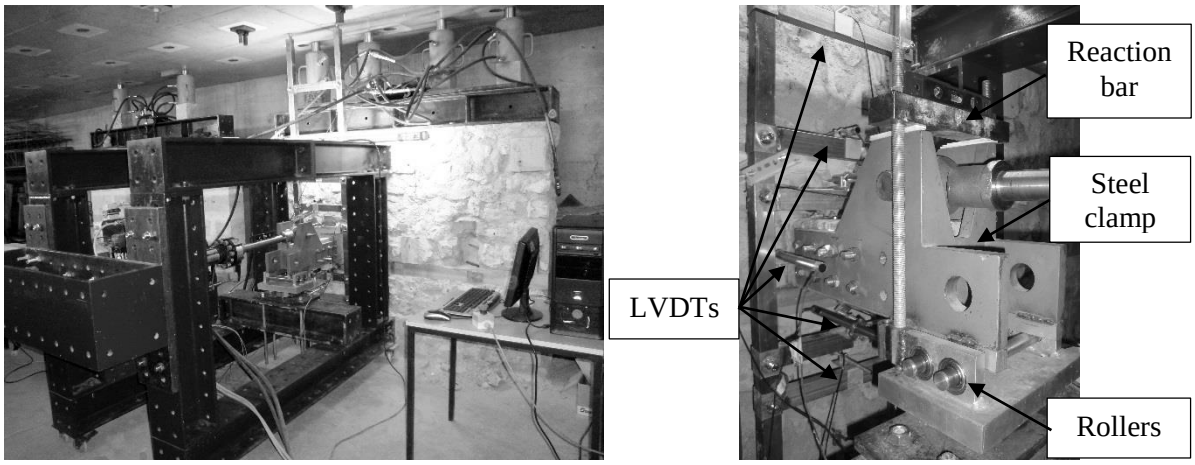

(a) (b)

Figure 5.9 Test set-up: (a) entire set; and (b) detail of the vertical support and instrumentation at the front of the wall.

When trying the initial test apparatus with a cyclic procedure, the timber joist suffered large vertical rotations, resultant of the rigid connection between the actuator and the steel frame, which led to cracking of the joist along the bolted connection with the clamp. To exclude this type of failure, a vertical support was developed for the timber joist. The support works as a roller, restraining both ways of the vertical direction and allowing the joist to slide horizontally, as shown in Figure 5.9b. It is also equipped with a load cell, so that the vertical reaction can be monitored. To counter balance the upward reaction, two acrow props were added between the frame and the reaction slab (see Figure 5.8b).

The vertical load was distributed along the wall with four hydraulic cylinders, on top of HE200B steel profiles, two or three depending on the thickness of the wall being 0.4 m or 0.6 m, respectively. The pressure throughout the test was manually controlled. The procedure to improve contact between the top of the walls and the steel profiles was the same as previously described for in Chapter 4.

As for the pullout tests of injection anchors, out-of-plane displacements of different key points of the specimens are very important to follow the occurrence of damage and ultimately failure. Instrumentation of the tests focused on acquiring out-of-plane displacements and strains in the steel tie rod inside the wall (only for the strengthened specimens), with Linear Variable Differential Transformers (LVDTs) and strain gauges, respectively. For unstrengthened specimens, six LVDTs were distributed on the wall (positions 2, 4', 6, 7', 11, and 13), one on the joist (position 9), and one on the wall-plate (position 10). For strengthened connections, a similar configuration was applied, with a set of fifteen LVDTs distributed on the wall, joist,

wall-plate, steel rod, and anchor plate (see Figure 5.10a). Of these, nine monitored the out-of-plane displacements of the wall: eight at the front (see Figure 5.9b) and one at the back (see Figure 5.10b), with some of the positions coinciding with the ones assumed for the unstrengthened specimens. Two LVDTs were placed on the two ends of the tie rod (positions 6 and 15 of Figure 5.10a) and the remaining measured the relative displacement between joist and wall (number 5), and the displacements of the joist (position 9), wall-plate (number 10), and anchor plate (number 14). In Figure 5.10b, one can see the disposition of the LVDTs on the back of the wall. Two strain gauges were applied at mid-length of the steel tie rod to assess the actual load transmitted to the anchorage, during the test (see Figure 5.10a).

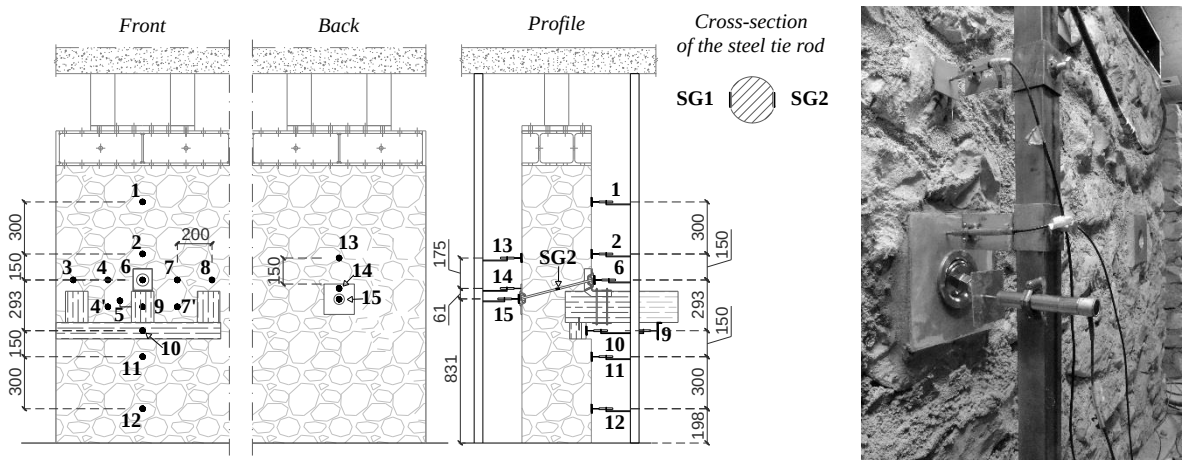

(a) (b)

Figure 5.10 Test set-up (dimensions in mm): (a) location of the LVDTs; and (b) detail of the instrumentation at the back.

The relative displacements between structural elements that constitute the connection, as idealized in Figure 5.11, are considered to be most descriptive of its performance. With the exception of the relative displacement anchor plate/back wall, all displacements can be determined for both unstrengthened and strengthened connections, and consequently allow comparison between behaviors. These displacements result from the difference between displacements measured by the LVDTs, with the exception of the joist/front wall slip, $s_{\text{j-fw}}$, which is measured directly by LVDT in position 5. Considering that the index n, in d_{n}, refers to the LVDT's location in Figure 5.10, the relative displacements were calculated as follows:

- Joist/back wall slip, $s_{\text{j-bw}}$: d_9-d_{13};
- Joist/wall-plate slip, $s_{\text{j-wp}}$: d_9-d_{10};
- Wall-plate/front wall slip, $s_{\text{wp-fw}}$: d_{10}-d_{11};
- Anchor plate/back wall displacement, $d_{\text{ap-bw}}$: d_{15}-d_{13}.

The slip $s_{j\text{-}bw}$ accounts for the contribution of different kinds of damage that occur in all structural elements, during the test, while the slip $s_{j\text{-}fw}$ describes the one between the masonry wall and the timber joist, singling out the "link" between them. The other two important displacements regard the slip of the joist relatively to the wall-plate, $s_{j\text{-}wp}$, and of the latter to the front of the wall, $s_{wp\text{-}fw}$, which highlight the contribution of the wall-plate in the total slip of the connection. The displacement $d_{ap\text{-}bw}$ encompasses the displacements due to crushing of the masonry under the anchor plate (FM2), and bending of the anchor plate.

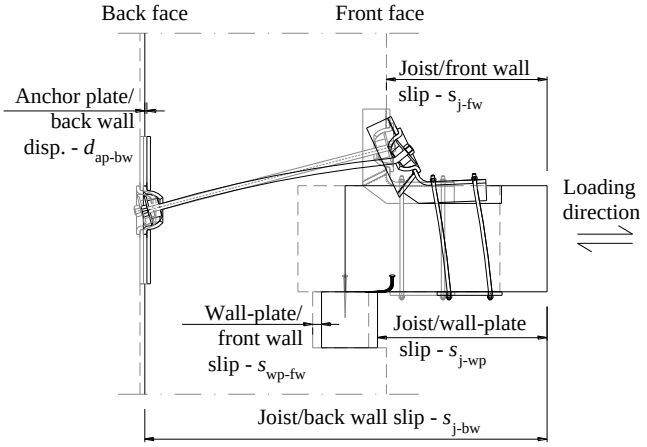

Figure 5.11 Idealization of relative displacements.

5.5 TEST PROCEDURE AND SUMMARY

The monotonic tests on unstrengthened and strengthened connections were carried out under displacement control at a rate of 10 μm/s, so that the different stages of the behavior could be captured. From these tests, it was possible to define a cyclic procedure with 10 levels, from 10 mm up to 100 mm (see Figure 5.12). A maximum amplitude of 100 mm was established so that no damage could propagate to areas of surrounding tests. At first, a minimum displacement of 5 mm was applied, to ensure that the connection would start the test already in tension and to prevent some of the instability experienced with the actuator and acquisition system for lower values of force and displacement in the monotonic tests of unstrengthened connections.

Since no pounding effect of the wood joists on the wall was being studied, the unloading branches stopped at different displacements to prevent the development of high compressive forces on the specimen. The procedure applied on the tests also included a monotonic branch at the end of the cycles, which was carried out to obtain failure on the WF.60.A tests. The range of velocities varied between 25 μm/s and 150 μm/s, respecting always a minimum of 120 s for duration of each loading or unloading branch. The stopping criteria adopted were: completion

of the procedure, propagation of cracks beyond the expected area of damage, or compromise of the test apparatus.

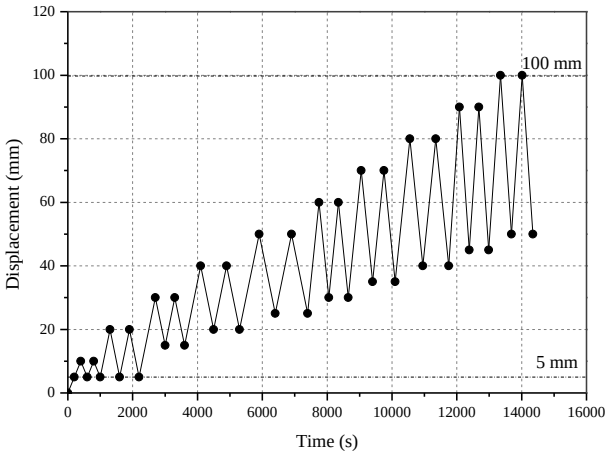

Figure 5.12 Cyclic procedure for strengthened wall-to-floor connections.

The summary of the tests performed is presented in Table 5.1, according to the thickness of the wall, the type of connection, and the test procedure. A total of twenty quasi-static tests was carried out, but in two of those tests the failure modes were a direct consequence of the test setup, excluding them from analysis. Of the remaining eighteen tests, in five tests the strengthening components did not comply with the specifications described in section 5.3 and in one test the vertical load was half of the value defined, nonetheless their results are presented ahead since some relevant questions were brought to light by them. Thus, twelve tests were carried out with the exact characteristics of the strengthening solution described in section 5.3, and their failure modes were considered valid.

Table 5.1 Summary of the pullout tests performed

Thickness of the wall	Type of connection	Procedure		Total
		Monotonic	Cyclic	
0.4 m	Unstrengthened	2	-	2
	Strengthened	3	5	8
0.6 m	Unstrengthened	2	-	2
	Strengthened	2	6	8
	Total	9	11	20

5.6 RESULTS OF UNSTRENGTHENED CONNECTIONS

5.6.1 Hysteretic curves and performance parameters

Four pullout tests were performed on unstrengthened connections, being two per thickness. The tests were monotonic, following the procedure and conditions mentioned in the previous

sections. Specimen WF.40.U.1A displayed considerable rotation during the test, therefore a vertical support under the timber joist was used to limit rotation of the following specimen to test, WF.40.U.1B. Since at the time load cells were not available, the reaction force was not recorded. Specimens with 0.6 m thick walls did not require the use of a support, since rotation was minimal.

As explained before, possible failure modes contemplated shear off the nails, pullout of the nails or pullout of the wall-plate, but all four specimens failed by pullout of the nails. Maximum pullout force (F_{max}), yielding displacement (d_y), displacement at F_{max} (d_{Fmax}), ultimate displacement (d_u), initial stiffness (k_0), and displacement ductility (μ) are presented in Table 5.2 and the displacements were taken from $s_{j\text{-}fw}$. The displacement d_y was defined as the limit of the initial linear branch (see in Figure 5.13a) and d_u was determined for a small reduction in load carrying capacity of 20 % (Park, 1989). Initial stiffness, k_0, was defined as the secant stiffness at the yielding limit defined by d_y and ductility resulted from the ratio between the displacements d_u and d_y.

Specimen WF.40.U.1A shows approximately two times more capacity than the average of the other three tests, 4.70 kN (CoV of 13 %), and it reaches a first peak at 8.69 kN, followed by a plateau around 8.20 kN, and then hardening until the maximum force of 9.57 kN, as one can see in Figure 5.13. The $s_{j\text{-}fw}$ plateau extends for approximately 6.5 mm, but it is also observed in the curves relative to the wall-plate (see Figure 5.14a). When comparing the force-displacement curves of the joist alone (see Figure 5.13b), and relatively to the wall, one can observe that the rotation of the joist creates an "artificial" higher slip of this last one. For the remaining specimens both force-displacement curves are very close, being almost equal. Considering the joist slip as more descriptive of the actual slip, in the case of specimen WF.40.U.1A, the displacement ductility value, as a ratio of displacements, would not suffer much of a change, but the initial stiffness would increase to 9.7 kN/mm. This behavior related to the rotation of the joist in the wall pocket, is later discussed in section 5.9.

Table 5.2 Experimental results of tested unstrengthened specimens

Specimen	F_{max} (kN)	d_y (mm)	d_{Fmax}	d_u (mm)	k_0 (kN/mm)	μ
WF.40.U.1A	9.57	2.20	22.86	33.79	2.74	15.4
WF.40.U.1B	5.49	1.18	21.58	37.89	2.09	32.1
WF.60.U.1A	4.43	0.86	12.85	26.63	2.38	31.0
WF.60.U.1B	4.12	-	32.14	41.42	-	-

Specimen WF.40.U.1B displays similar behavior to the two tests performed on the 0.6 m thick wall, especially with specimen WF.60.U.1A, in terms of initial stiffness and ductility. For

specimen WF.60.U.1B, the acquisition system recorded only "noise" until a force of 2 kN was reached, possibly related with the small values measured (see Figure 5.13 and Figure 5.14). As a consequence, d_y, k_0 and μ could not be determined. In spite of the small initial displacements, this particular specimen presented high maximum and ultimate displacements.

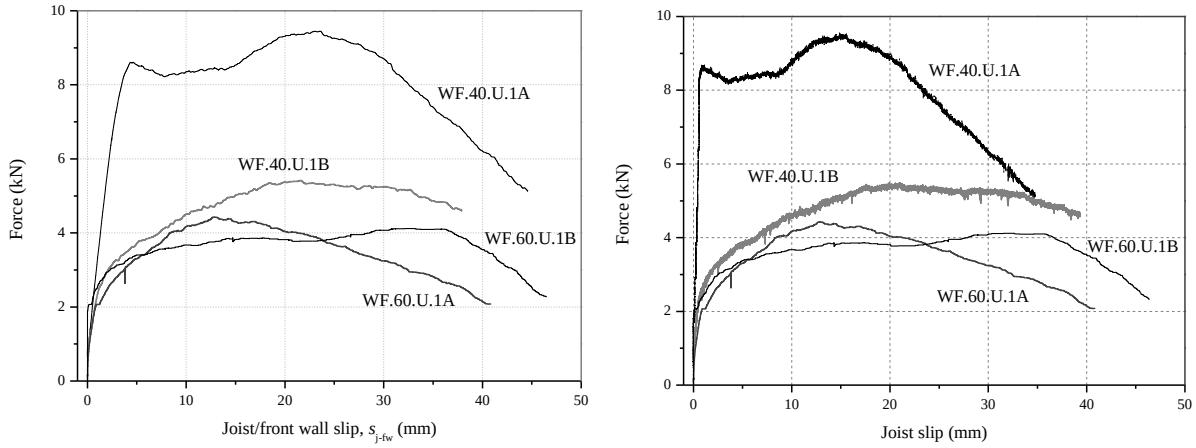

(a) (b)

Figure 5.13 Force-displacement curves: (a) $s_{j\text{-}fw}$; (b) joist.

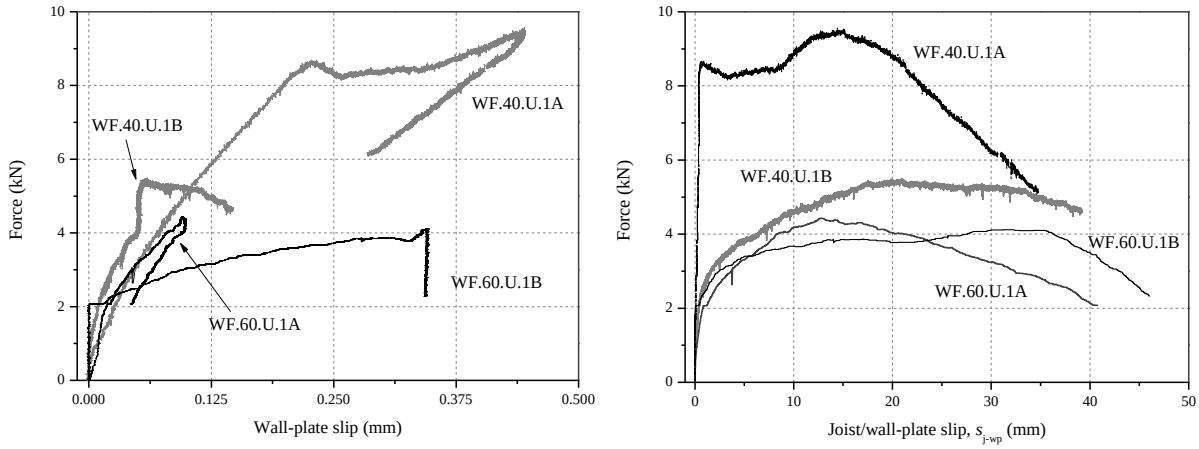

(a) (b)

Figure 5.14. Force-displacements curves of timber elements: (a) wall-plate; and (b) $s_{j\text{-}wp}$.

The out-of-plane displacements of the wall were always below 0.03 mm throughout the four tests, which can be considered within the error of the LVDTs. Consequently, no relative displacements to the wall were calculated. As one can see in Figure 5.14a, the displacements of the wall-plate are equally small, but still higher than the ones of the wall. In all specimens, it appears to occur a sharp increase of the slope of the curve right before the peak. Specimens WF.40.U1A and WF.60.U.1A showed a clear snap-back after the peak, in their force-displacement curve of the wall-plate, consistent with complete pullout of the two nails and with the wall-plate not being engaged anymore by the joist. In the case of WF.60.U.1B, the wall-plate is no longer engaged by the joist, but there is no displacement recovery. For specimen

WF.40.U.1B, there is a post- peak softening branch, meaning the wall-plate is still contributing for the capacity of the connection. As expected, the joist/wall-plate slip force-displacement curve, presented in Figure 5.14b, is very similar to the one from the joist, since the contribution of the wall-plate is clearly small.

5.6.2 Damage survey

Figure 5.15 presents two positions of the joist relatively to the wall, in the beginning and conclusion of the test. The progression of the joist out of the pocket is very clear if one follows the 1st reference line drawn on the joist, which is aligned with the front face of the wall. The 2nd reference line was marked in alignment with the visible face of the wall-plate and it can be seen in Figure 5.15b.

As all unstrengthened specimens failed by pullout of the nails between the timber joist and wall-plate, Figure 5.16a shows how the nails got bent and the timber was slightly crushed in the process. The nails were fully pulled out from the wall-plate in all specimens. After removing the setup from the specimens, one could remove the joists from the pocket, since they were completely loose. The contact surface of the wall-plate was lightly scratched, drag marks from the nails could be seen, and there was a little bit of mortar debris in the slot between wall-plate and wall (see Figure 5.16b).

(a) (b)

Figure 5.15 Sliding of the joist: (a) Initial position; and (b) final position.

(a) (b)

Figure 5.16 Pullout of the nails: (a) view of the slot in the wall and damage on the wall-plate; (b) bended nails with slight crush of the joist.

5.7 RESULTS OF STRENGTHENED SPECIMENS

5.7.1 Hysteretic curves and performance parameters

In total, eight pullout tests were performed on strengthened wall-to-floor specimens, with the characteristics previously described. For each wall thickness, four tests were carried out, being one monotonic and three quasi-static cyclic tests, whose main outcomes are presented in Table 5.3. To facilitate the explanation of the results, from this point on, the cyclic tests on 0.4 m thick walls are addressed as WF.40 tests and the ones on 0.6 m thick walls, as WF.60 tests.

As for the unstrengthened specimens, all displacements and related parameters were determined from the slip between joist and front wall, $s_{j\text{-}fw}$, except for specimen WF.40.A.1A. A malfunction of the acquisition system during the test of the last mentioned specimen corrupted the data obtained from the LVDTs, consequently all parameters listed in Table 5.3 were determined from the internal transducer of the actuator. This displacement tends to be higher than the displacements measured on the specimen, since they include the gaps between components of the testing apparatus (hinge, clamp and others), consequently being misleading. For comparison purposes, the experimental parameters based on the internal transducer were also calculated for specimen WF.60.A.1A and remaining WF.40 specimens (in brackets in Table 5.3).

For the monotonic tests, d_y was determined as the displacement corresponding to the load peak before the sudden drop, as shown in Figure 5.17, which agrees with the end of linearity. For the cyclic tests, it was adopted that d_y would correspond to the displacement measured at the end of the 1st cycle of the 1st level, since after that there is a clear change of stiffness for

most specimens, and comparison between tests is facilitated. When possible, d_u was determined with the same criterion as the one applied for the unstrengthened specimens (see subsection 5.6.1), otherwise d_u corresponded to the maximum measured displacement. The elastic stiffness, k_0, was defined as the secant connecting the origin to the point of corresponding displacement d_y. Displacement ductility, μ, was calculated as in subsection 5.6.1.

The specimens of the monotonic tests presented different failure modes, with specimen WF.40.A.1A failing primordially by masonry cone breakout (FM1) and specimen WF.60.A.1A by ripping of the timber wall-plate. Different failure modes translated into distinct F_{max} and displacement parameters, if one compares within the values obtained from the internal transducer. FM1 is associated with lower pullout forces, and less stiff and ductile behavior, as expected. The failure mode that occurred in specimen WF.60.A.1A was not one of the possible modes presented in section 5.2, obviously because the excessive rotation of the joist was not taken into consideration when studying the mechanical behavior of the strengthened connection. Nonetheless the stiffness and ductility calculated are in good agreement with the ones determined for the specimens of cyclic tests. As explained previously, since both monotonic tests were performed without a vertical support on the joist, this might explain the differences observed in the failure modes and respective forces and displacements.

Table 5.3 Experimental parameters determined from the tests.

Specimen	**Failure Mode**	F_{max} **(kN)**	d_y **(mm)**	d_u **(mm)**	k_0 **(kN/mm)**	μ
Monotonic:						
WF.40.A.1A(1)	FM1	85.20	7.89	61.70	3.68	7.82
WF.60.A.1A	Wall-plate ripping(2)	108.62	2.02 (6.60)	37.45 (67.55)	27.02 (7.84)	18.50 (10.23)
WF.40.A.3A	FM3 (+FM1)	93.09	4.22 (9.91)	91.47 (99.53)	13.90 (5.92)	21.69 (10.04)
WF.40.A.4A	FM3 (+FM1)	94.50	3.78 (9.91)	84.32 (97.42)	10.39 (3.96)	22.31 (9.83)
WF.40.A.4B	FM3 (+FM1)	94.07	3.87 (9.91)	88.04 (99.60)	12.30 (4.80)	22.76 (10.05)
Average		93.9	4.0	87.9	12.2	22.3
CoV (%)		1	6	4	14	2
WF.60.A.2B	FM3	92.42	2.97	74.59	13.37	25.11
WF.60.A.3A	FM3 (bending)	82.67	2.61	41.18	12.63	15.76
WF.60.A.3B	FM3	102.44	4.59	107.78	5.67	23.47
Average		92.5	3.4	74.5	10.6	21.4
CoV (%)		11	31	45	40	23

(1) Values obtained from the internal transducer of the actuator.
(2) Not predicted initially.

The force-displacement curves regarding the internal transducers of the monotonic tests (see Figure 5.17) present a similar shape, in spite of being associated with different failure modes. The abrupt drop of load, caused by detachment of the steel angle from the joist, marks the beginning of the pre-peak nonlinear phase, which is characterized by damage of the bolted connection. The values of the load drop are around 55 % for both specimens. As shown in Figure 5.17b, this phenomenon is present in all force-displacement curves, therefore propagated throughout all the elements of the specimen. It is clear that for specimen WF.60.A.1A failure is associated with the behavior of the wall-plate. Up until failure, there was barely any movement of the wall-plate, and the displacements of the joist and joist/wall-plate were practically equal, but after the peak, there was extensive damage of the wall-plate and it started to govern the behavior of the joist. As expected, force-displacement curve based on the actuator internal transducer is very similar to the one of the joist (position where the pullout load was applied).

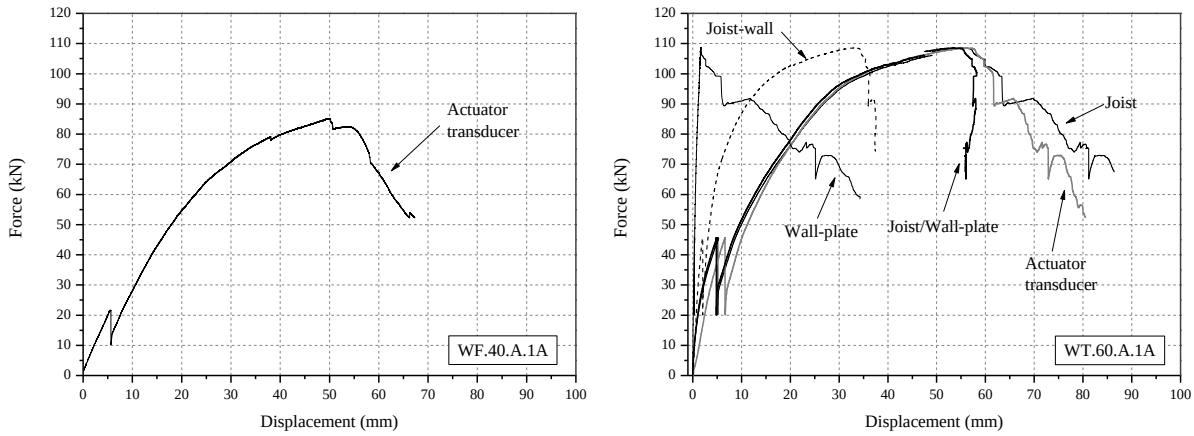

(a) (b)

Figure 5.17 Force-displacement curves of monotonic tests: (a) WF.40.A.1A; and (B) WF.60.A.1.

Both sets of specimens, WF.40.A and WF.60.A, presented failure of the connection between the steel angle and the timber joist, FM3 (see Figure 5.1). However, for WF.40 specimens cracks were also observed on the front and back face of the masonry wall, related with FM1 and FM2. All elements (masonry wall, timber elements and strengthening components) and their interactions contributed for the final outcome of the tests, but the failure mode singled out was considered to be the predominant one. Especially for the WF.40 tests, the intricate behavior of the connections hampered the isolation of the failure modes.

Specimen WF.40.A.4A continuously increased force until the end of the cyclic procedure, but its performance is very similar to the other specimens. To ensure that failure was registered, a monotonic loading branch was added to the cyclic procedure for the WF.60.A tests, which was only applied to specimen WF.60.A.3B.

While WF.40 tests presented low CoVs for all calculated parameters in Table 5.3, WF.60 tests have their lower CoV associated with F_{max}, 10.7 %, being the remaining ones between 23.3 % and 44.7 %. The average value of F_{max} for the 0.4 m thick walls' tests (93.9 kN) was slightly higher than the one obtained for the 0.6 m thick walls (92.5 kN), but if one excludes specimen WF.60.A.3A of the latter average, F_{max} increases for 97.4 kN. Specimen WF.60.A.3A failed by bending of the joist at the bolted connection, contrary to the shear failure observed on the other tests.

Since both WF.40 and WF.60 tests are largely influenced by the performance of the bolted connection and interaction between steel angle and tie rod, similarities can be observed among their hysteretic loops, particularly in the pre-peak phase (see Figure 5.18). The hysteretic behavior of all specimens is characterized by force and stiffness degradation, and pinching, making the second cycle loops much different from the ones of the first cycle. In the post-peak phase, curves are governed by the dominant failure mode, which dictates if the behavior is brittle or if gradual softening takes place. Only in specimen WF.60.A.3A, the abrupt loss of strength occurred, which is related with the joist breaking at the bolted connection by bending. Since damage was concentrated on the flexure crack, this might explain the fact that compression forces (negative value) were small (approximately -4.3 kN), when unloading occurred.

The WT.40 tests presented higher compression forces than the WT.60 tests, an interval of -18.0 kN to -35.2 kN, against an interval of -13.0 kN to -20.0 kN (see Figure 5.18), which is consistent with the higher pullout forces. As for the monotonic curves in Figure 5.17, these cyclic curves also display an abrupt drop of load that occurred during the first cycle of the second level (20 mm) in all cases, with the exception of specimen WF.60.A.2B, for which happened during the first cycle of the first level. The average values of force and displacement at drop, for the WF.40 tests were 59.8 kN and 7.1 mm, respectively, while for the WF.60 tests these values were 43.1 kN and 5.5 mm.

The envelope curves are an approximation to the virgin loading branches of the specimens, reassembling monotonic curves, and enable a better understanding of the upper boundary performance of the tests (see Figure 5.19). They were constructed by connecting with linear branches the maximums of the first cycle of each level, for both WF.40.A and WF.60.A tests. The first symbols in the envelopes result from the minimum displacement applied, of 5 mm (see Figure 5.12), and not from a maximum of a cycle. One can observe more distinctly the change in stiffness after the first cycle of the first level, which is coincident with the detachment of the steel angle from the joist and limited the elastic phase, consequently enabled the

definition of d_y and k_0. With the exception of specimen WF.60.A.3B, all specimens present similar k_0 (see Table 5.3), with an average of 12.52 kN/mm with a CoV of 10.7 %.

The envelope curves of the WF.60.A tests present a rounder shape when compared to the ones of the WF.40.A tests. On the other hand, these last tests showed a tendency to form a plateau around their maximum force, while WF.60.A tests present a clearer softening/brittle branch.

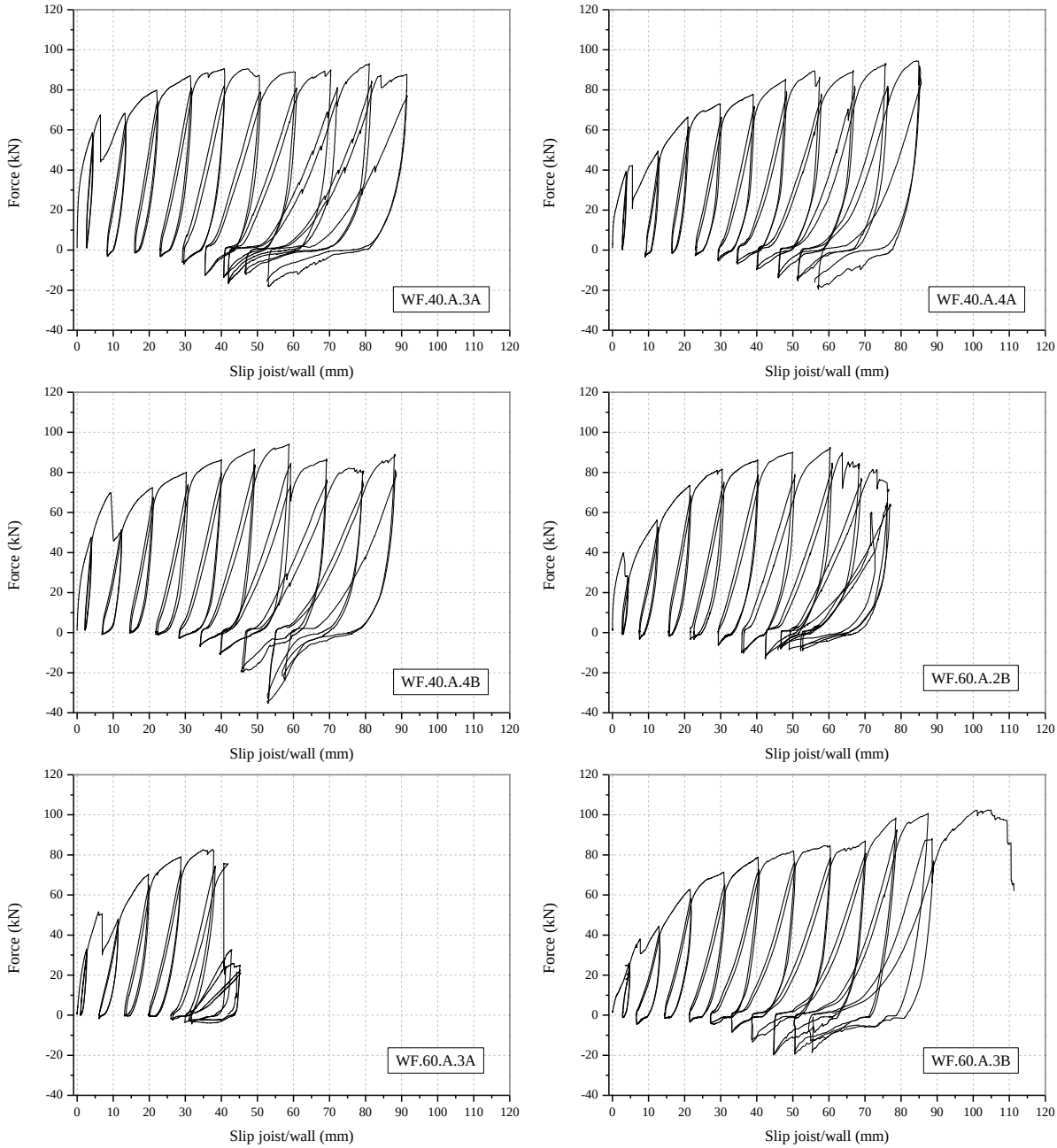

Figure 5.18 Force-displacement curves of joist/front wall slip of all cyclic tests.

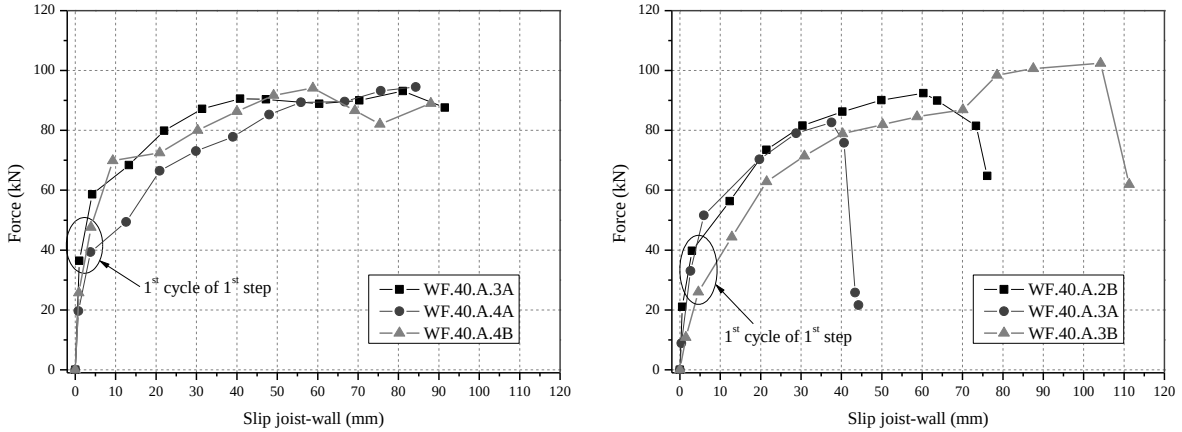

Figure 5.19 Envelopes of the 1st cycle: (a) WF.40 tests; and (b) WF.60 tests.

For both the WF.40.A and WF.60.A tests, wall out-of-plane displacements were very small, but in the second case were below the sensitivity range of the LVDTs. Consequently, for the WF.60.A tests these displacements were considered zero, and all relative displacements to the wall were considered equivalent to the ones of the other element involved. The exception stands for the $s_{\text{j-fw}}$, which was measured directly. Therefore $s_{\text{j-bw}}$ and $s_{\text{j-wp}}$ are assumed to be the joist displacement, $s_{\text{wp-fw}}$ corresponds to the wall-plate displacement, and $d_{\text{ap-bw}}$ is equivalent to the displacement of the anchor plate. The force-displacement curves relative to the joist, the anchor plate, and the back wall displacements of WF.40.A specimens are presented in Annex 3, since they were used to assess relative displacements.

Since back wall displacements were very small, with a maximum of 1.75 mm, in specimen WF.40.A.4A, and the highest contribution to the response of the connection came from the steel angle and bolted connection, the force-displacement curves relative to $s_{\text{j-bw}}$ (see Figure 5.20a) are very similar to the ones of $s_{\text{j-fw}}$ but with slightly higher displacements. The same applies to the WF.60.A specimens presented in Figure 5.20b. Due to the similarity between force-displacement curves of $s_{\text{j-bw}}$ and $s_{\text{j-wp}}$, these last ones were placed in Annex A2. In both curves of specimen WF.40.A.4A, the displacements regarding the last level of the procedure were not measured, since the LVDT placed on the joist was removed.

The force-displacements curves that describe the $s_{\text{wp-fw}}$, and allow a better understanding of the participation of the wall-plate in the response of the connection are presented in Figure 5.21. The $s_{\text{wp-fw}}$ is below 1 mm for the WF.40.A specimens and below 0.3 mm for the only WF.60.A test, where this movement was perceptible by the acquisition system (WF.60.A.3A). In all specimens, the plastic deformations at the end of the cycles were small, being the highest recorded for specimen WF.40.A.4A.

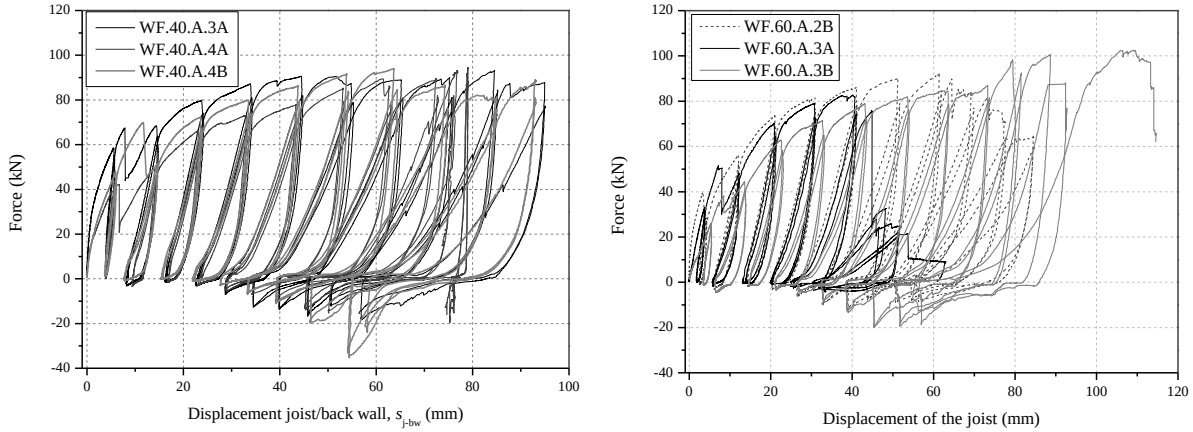

(a) (b)

Figure 5.20 Force-displacement curves relative to $s_{j\text{-}bw}$: (a) WF.40 tests; and (b) WF.60 tests.

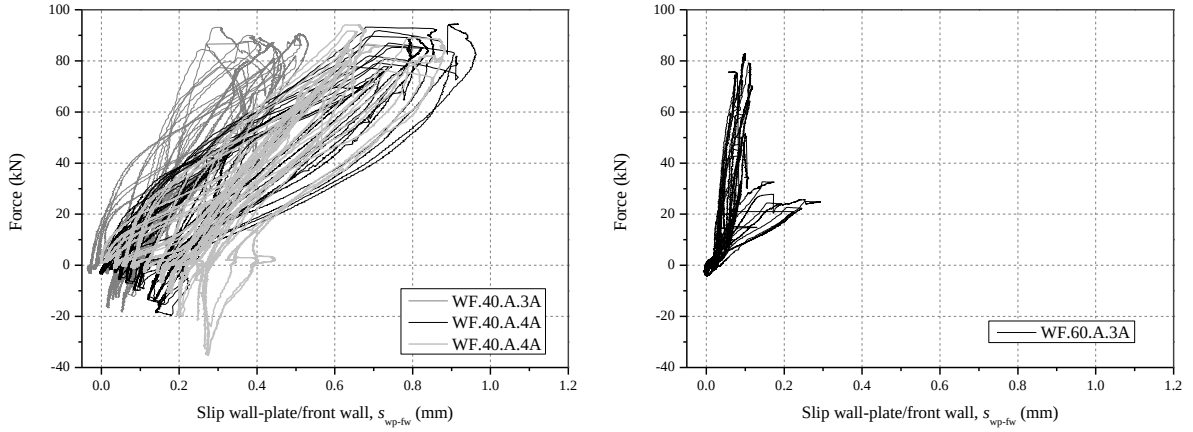

(a) (b)

Figure 5.21 Force-displacement curve relative to $s_{wp\text{-}fw}$: (a) WF.40 tests; and (b) WF.60 tests.

The displacement, $d_{ap\text{-}bw}$, which is related with crushing of the masonry under the anchor plate is represented in Figure 5.22. As expected, the displacements measured on the WF.40.A specimens were higher than the ones of the WF.60.A specimens, by a factor of approximately 3. In both test sets, there are higher settlements of the anchor plates during the first three levels of the cyclic procedure. For the WF.40.A specimens and specimen WF.60.A.3B, the anchor plate continued to be engaged after the peak, while for specimens WF.60.A.2B and WF.60.A.3A, the displacements recovered to the ones measured in the immediate cycle after the peak. While the envelope curves of WF.40.A specimens present a rounder shape, WF.60.A specimens' envelopes show a distinct shift on stiffness, at the beginning of the first level of the cyclic procedure (see Figure 5.22b).

The abrupt loss of load caused by detachment of the steel angle from the floor joist was only noted in the $d_{ap\text{-}bw}$ of specimens WF.40.A.3A, WF.40.A.4A, and WF.60.A.3B. For higher

negative forces, the $d_{ap\text{-}bw}$ of specimens WF.40.A.3A and WF.40.A.4A concentrated around 0.6 mm and 1.3 mm, respectively (see Figure 5.22a).

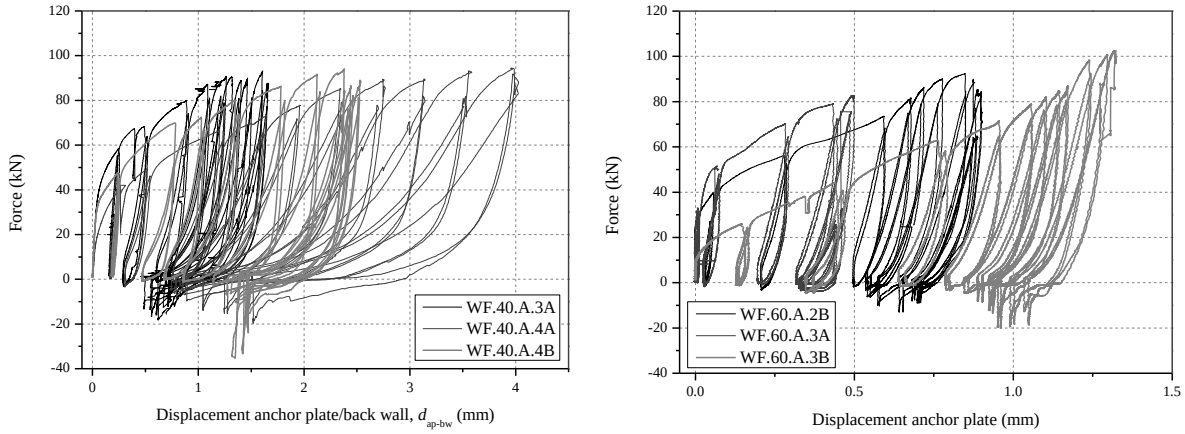

Figure 5.22 Force-displacement curve relative to $d_{ap\text{-}bw}$: (a) WF.40 tests; and (b) WF.60 tests.

The progressions of the average value of the two strain gauges, ε_m, placed diametrically opposed at mid anchorage length of the steel ties, as described in section 5.4, are presented in Figure 5.23. Due to damage caused to the strain gauges when inserting the steel tie in the pre-cored hole or during the tests, the load transmission to the steel tie could only be assessed for four tests (WF.40.A.3A and all WF.60.A). As one can observed, the strain gauges captured the cyclic response, with a clear distinction between loading and unloading and between cycles. During unloading, negative strains were measured on the ties, with the minimum of -0.93 ‰ belonging to specimen WF.60.A.3A, and being approximately zero for specimen WF.60.A.3B. With the exception of WF.60.A.3A, the positive strain measured reached values above the proportional limit of 2 ‰, meaning that plastic deformation occurred. The maximum strain measured was 4.51 ‰ and corresponds to the F_{max} of specimen WF.60.A.3B, as expected.

Since the measured values of the pullout force were inferior to the yield strength of the steel ties, an estimated strain was determined, in order to understand the transmission of stresses to the steel tie, throughout the test. The estimated strain was determined using Hookes' Law where the elastic modulus of steel, E, was assumed equal to 200 GPa and the nominal area of the tie, A, was considered as 157 mm^2. The strain error, e, resulted from the difference between the measured strain, ε_m, and ε_e, and is plotted against time in Figure 5.23, alongside with ε_m.

All specimens initiated with a negative error, meaning ε_m is smaller than ε_e, and only later in the test reached positive differences. Specimen WF.60.A.3B presented higher error at the maximum values of strain, while for the remaining tests, the error was higher when estimating the minimum strain (considering the absolute values). Specimens WF.60.A.2B and WF.60.A.3A had the best approximations, with error falling in the interval from 0.3 ‰ to 0.9

‰ throughout the test, which constituted at most 30 % of their maximum ε_m. The highest error agreed with the F_{max} of specimen WF.60.A.3B, which was approximately 60 % of its maximum ε_m. With the exception of specimen WF.60.A.2B, there was an increment in error towards the end of the test.

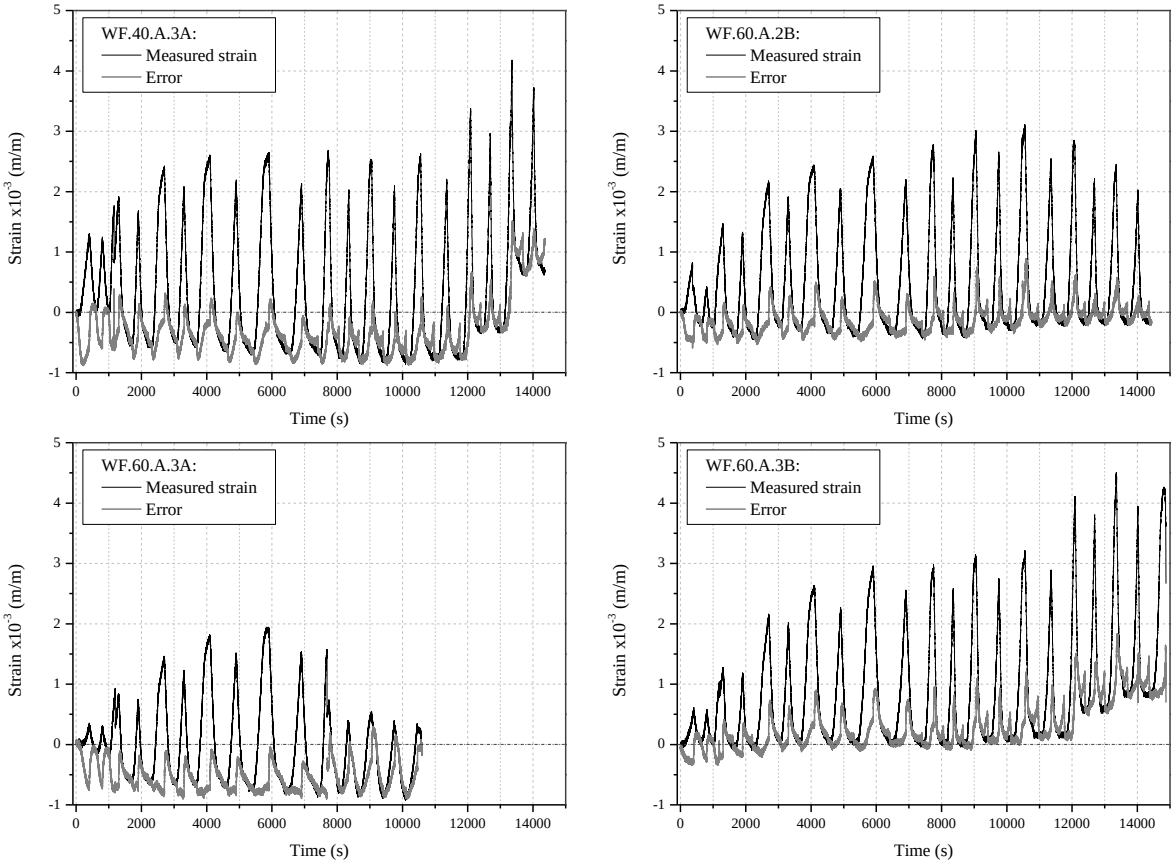

Figure 5.23 Progression of strain in the tie and displacements at the back of the wall.

Based on the out-of-plane displacements of the front face of the wall measured at F_{max}, the deformed shapes of the three WF.40.A specimens and of specimen WF.60.A.3A were built and are presented in Figure 5.24. From the WF.60.A specimens, only the last one mentioned was included, because of its small yet measureable out-of-plane displacement of the wall-plate. This was probably due to the rotation of the joist (since it broke by bending), which pressed its inner end against the wall-plate, forcing it to move.

To build the deformed shapes, zero displacement was assumed at the bottom of the wall but no condition was taken for the top, since it is not clear what kind of boundary condition prevails during the test. The displacements were connected by linear branches, with the exception of the joist displacement. All 0.4 m thick specimens presented higher displacements at the top of the wall rather than at the bottom, and the shape seems to be consistent with a fixed base and a pinned or roller top (see Figure 5.24). From these deformed shapes, it is very clear that the large displacements are carried out by the timber elements, especially by sliding of the joist.

Specimen WF.40.A.4A presented approximately 2 times higher displacements than the other specimens.

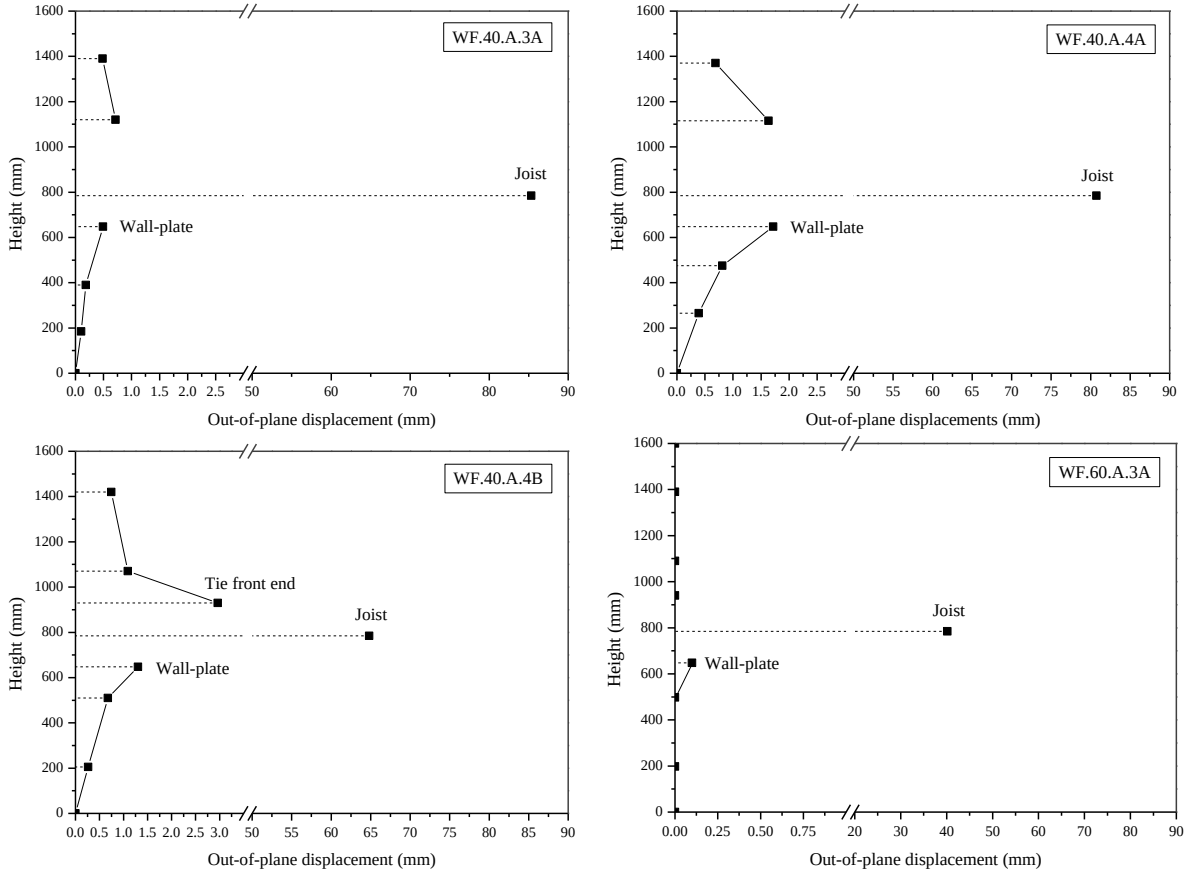

Figure 5.24 Out-of-plane displacements at the front face.

In an effort to understand the out-of-plane displacement of the wall immediate to the floor joist, the difference between the displacement of the joist and the displacement joist/wall was determined. For specimens WF.40.A3A and WF.40.A.4B, these displacements were practically 5 times higher than the average of displacements measured in positions 2, 4, and 7 (see Figure 5.10), while for specimen WF.40.A4B was by a factor of 2.5, as shown in Figure 5.25a. WF.60.A specimens also showed an even higher difference, since displacements were practically zero in other positions of the wall, but were very sensitive to local deformations (see Figure 5.25b.

When the timber joist was being pulled (loading), the joist rotated downwards, increasing the upwards vertical reaction, as seen in Figure 5.26, while during unloading the opposite occurred, but less pronounced. For WF.40.A.3A and WF.40.A.4B, the maximum vertical reaction occurred in the first cycle, of the first level of the procedure, followed by a continued descent, while for the remaining tests, the shapes of the reaction-displacement curves have similarities with the pullout force-displacement ones, presented in Figure 5.18. For WF.60.A

tests, positive reactions are in the same range of the values of reactions of the WF.40.A tests, but no negative reactions generate during these tests. This last phenomena is possibly related with the eccentricity between load application position and location of the anchor plate, which is discussed ahead, in section 5.9.

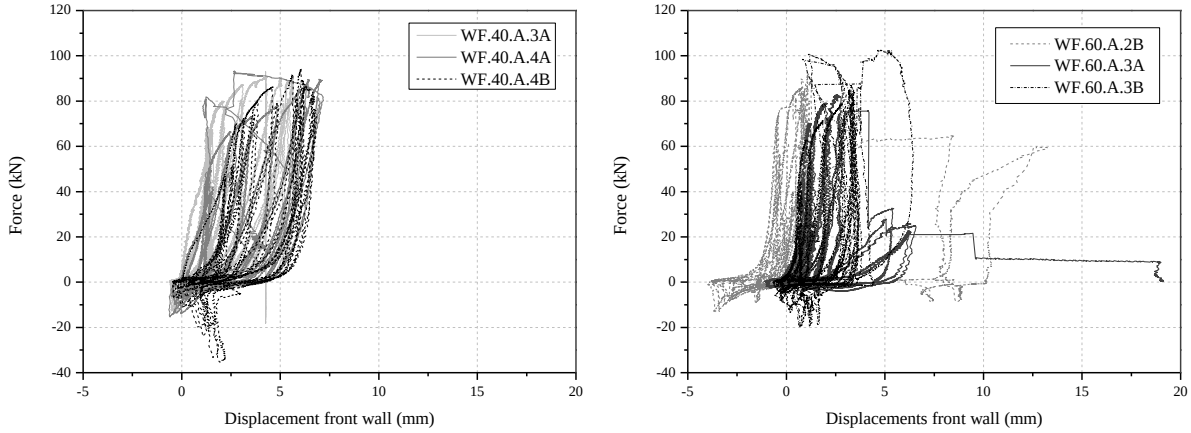

Figure 5.25 Force-displacement curves of the wall immediate next to the joist: (a) WF.40 tests; and (b) WF.60 tests.

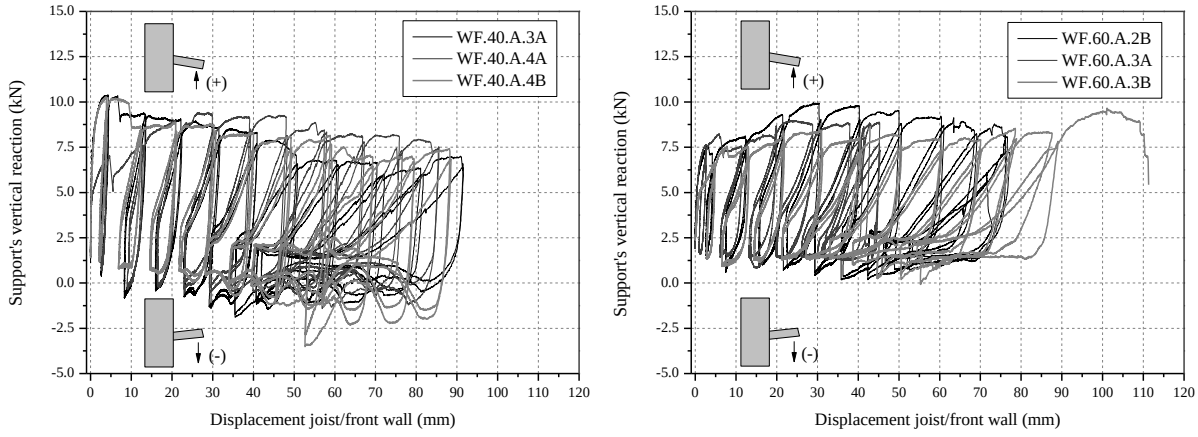

(a) (b)

Figure 5.26 Support's vertical reaction vs. displacement joist/front wall: (a) WF.40 tests; and (b) WF.60 tests.

5.7.2 Damage survey

During each test and disassembly of the specimens for demolition, the damage observed was documented to better interpret what was measured by the instrumentation. In all tests, the nails between timber joist and wall-plate were completely pulled out of the latter, similarly to what happened to the unstrengthened specimens (see Figure 5.16).

An important phenomenon, common to all specimens, was the detachment of the steel angle from the joist, since they were glued together with epoxi. Figure 5.27 presents the moments before and after the detachment, where the gap formed between the steel angle and the joist is

clear. After the occurrence of the detachment, it was visible a gap between the nuts and the bolts of the row closer to the vertical leg of the steel angle.

One of the objectives stated in section 5.2 was to assess the effectiveness of the hinge during the tests. Despite no exact measurement was made, it was possible to observe that there was relative rotation between the half-sphere and the cup holding it. In all specimens, there was a 15° angle between the axis of the cup and the one of the half-sphere, due to the application angle of the steel tie (see Figure 5.28a). For most specimens this rotation allowed these axis to align, as shown in Figure 5.28b, except for WF.40.A.4B and WF.60.A.3B. Their rotation was more pronounced, and there was an inversion of the position they had relative to one another (see Figure 5.28c).

While most tests presented similar damage that relates directly with the hypothesized failure modes, established in Figure 5.1, specimens WF.60.A.1A and WF.60.A.3A had particular failures. In the first one, excessive rotation of the joist engaged the timber wall-plate, and shearing across the grain occurred in the last, as shown in Figure 5.29a. Nonetheless, the response of the specimen was influenced by the failure modes expected initially. The failure of specimen WF.60.A.3A can be categorized as FM4, since it occurred in the bolted connection (see Figure 5.29b), but it was a clean break extending through the cross-section of the joist, caused by bending moments on the joist. Contrary to other specimens, the steel angle did not open (yield) much, which forced the joist to follow the rotation of the steel angle, and consequently broke. Joist rotation caused higher out-of-plane deformations of the wall-plate.

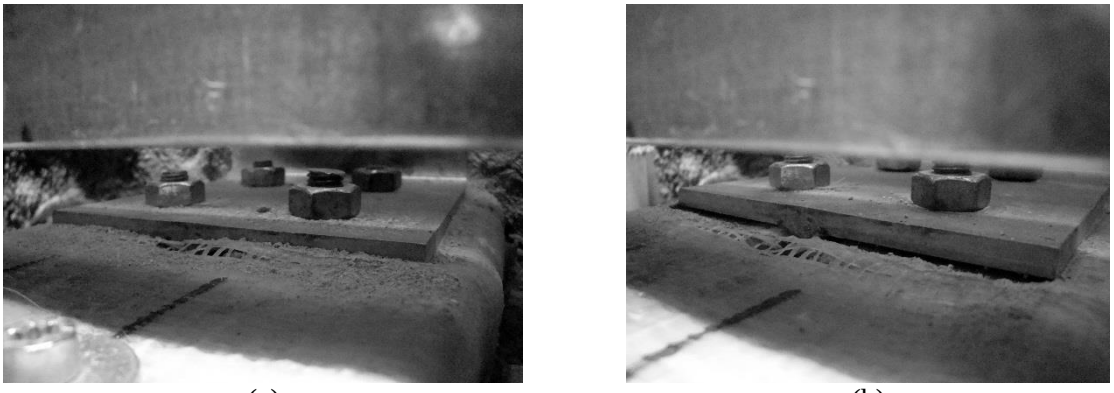

(a) (b)

Figure 5.27 Detachment of the steel angle: (a) before; and (b) after.

(a) (b) (c)

Figure 5.28 Evidence of rotation of the hinge: (a) initial position; (b) aligned axis position; and (c) reversed position.

(a) (b)

Figure 5.29 Failure modes: (a) WF.60.A.1B; and (b) WF.60.A.3A.

FM1 occurred only in the WF.40.A tests, where generalized cracking occurred, radiating from the steel angle, anchor plate, and wall-plate (see Figure 5.30a, b). Cracks appear and propagate in the mortar and in the interface between mortar and stone, at early stages of the tests, commonly during the 2nd or 3rd displacement level of the procedure. Clear evidence of the cone breakout are the cracks formed in the mortar, at an angle between 35° and 55°. They were particularly visible in mortar "cushions" between timber elements and stones, like the ones under the wall-plate or on top of the joists (see Figure 5.30c, d). The most distinct formation of the cone was observed in specimen WF.40.A.1A (see Figure 5.30e), where continuous cracks were traced throughout the entire cross-section of the specimen, from the anchor plate to the cracked face (front face). The kind of cracks observed in Figure 5.30a radiating from the steel angle can also be caused by splitting of the masonry, since there is one crack that propagates mainly vertically at the center of the tensioned face of the wall.

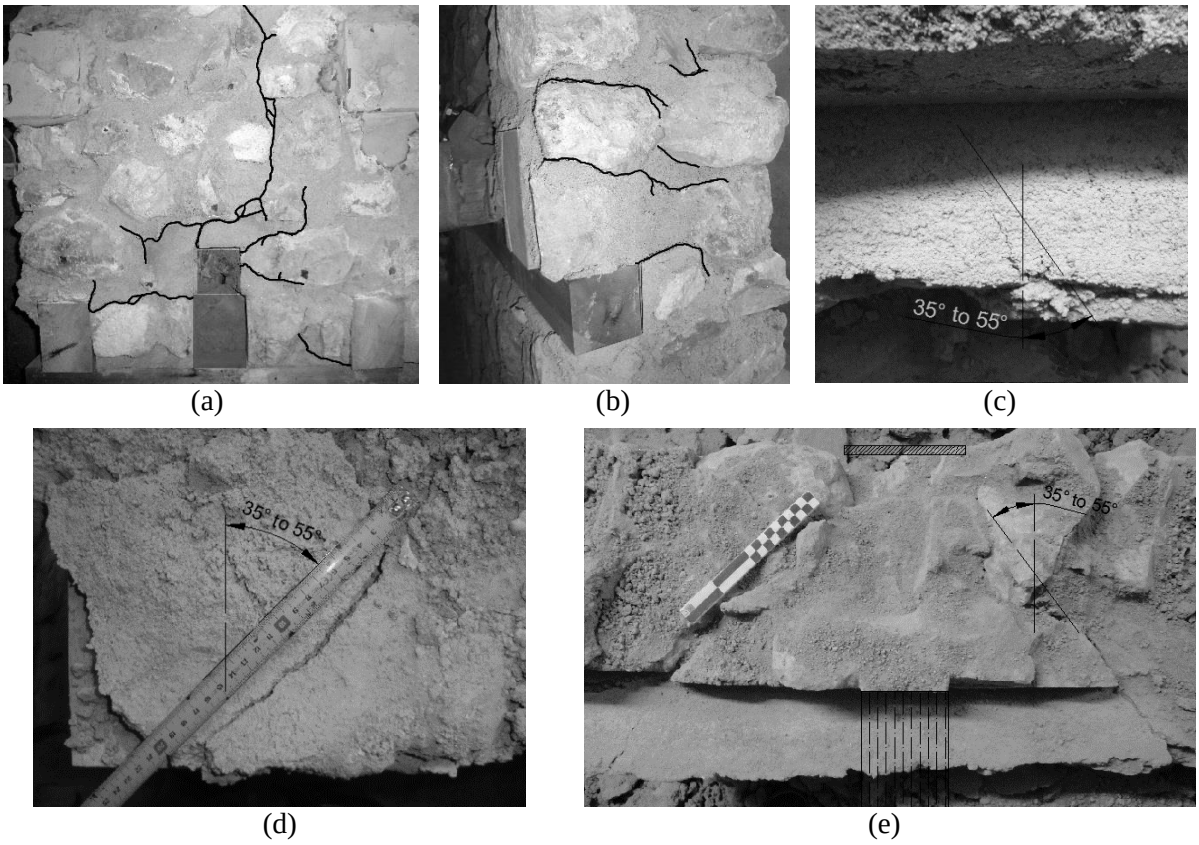

(a) (b) (c)

(d) (e)

Figure 5.30 Damage observed descriptive of FM1: (a) cracked face; (b) cracked lateral; (c) cracks under the wall-plate; (d) cracks above the joists; and (e) complete cone breakout (WF.40.A.1A).

Crushing of the mortar under the anchor plate (FM2) occurred in both WF.40.A (see Figure 5.31a) and WF.60.A tests (see Figure 5.31b), and cracks were visible in the new mortar layer (fast curing mortar placed to better accommodate the metallic elements to the existing masonry wall), surrounding the plate and under it. In addition, the anchor plates used in the WF.40.A.3A and WF.40.A.4B specimens presented a curved shape, with maximum deformation where the compression load was applied (the hinge location). The anchor plates of specimens WF.40.A.1A and WF.40.A.4A did not bend, but the latter moved upward, from the 4th level on.

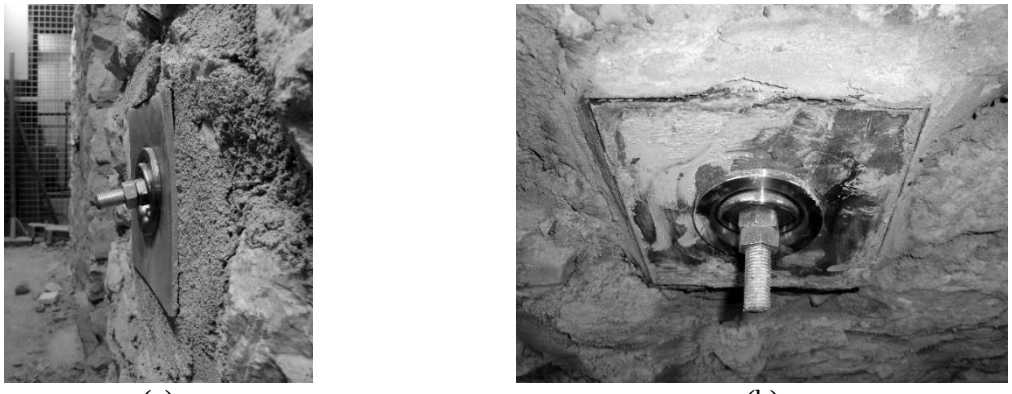

(a) (b)

Figure 5.31 Damage observed descriptive of FM2: (a) WF.40.A tests; and (b) WF.60.A tests.

In all specimens, the damage related with FM4 was concentrated at the end of the steel tie bolted to the steel angle (Figure 5.32). In particular, the reduced section in the steel tie rod, due to bending, corresponds to the end of the steel cup that is part of the hinge. The other end of the steel rod that is bolted to the anchor plate remained straight throughout the test. A number of ties presented a slight curvature resultant from fitting them in holes with small deflections. Specimen WF.60.A.3A presents a very small curvature, when compared to what is showed in Figure 5.32.

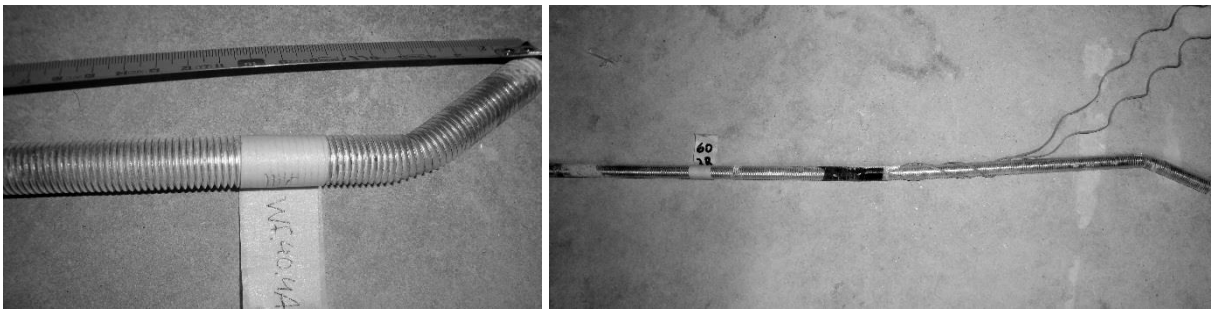

(a) (b)

Figure 5.32 Damage observed descriptive of FM4: (a) WF.40.A tests; and (b) WF.60.A tests

Failure mode, FM3, concerns the damage in the connection between the steel angle and the joist, and it was present is all specimens. It encompasses a variety of contributions, interacting among themselves. Damage on the timber joist was related with crushing against the bolts and the horizontal reinforcement of the steel angle, and shearing parallel to the grain, due to the vertical reinforcements, as shown in Figure 5.33a, b. Regarding the steel components, there was yielding of the bolts, the steel angle, and the cup of the hinge. The shear stress bent the bolts, particularly the row closer to the vertical leg (see Figure 5.33c). Since the horizontal leg of the steel angle was being pulled, and the vertical one was anchored to the wall, the steel angle opened and its reinforcements buckled, due to compression against the timber joist (see Figure 5.33d, e). In specimen WF.60.A.3A, there was not any buckling of the reinforcements. The vertical leg of the steel angle was deformed by the compression applied by the hinge's cup, while the last presents a wavy shape due to buckling.

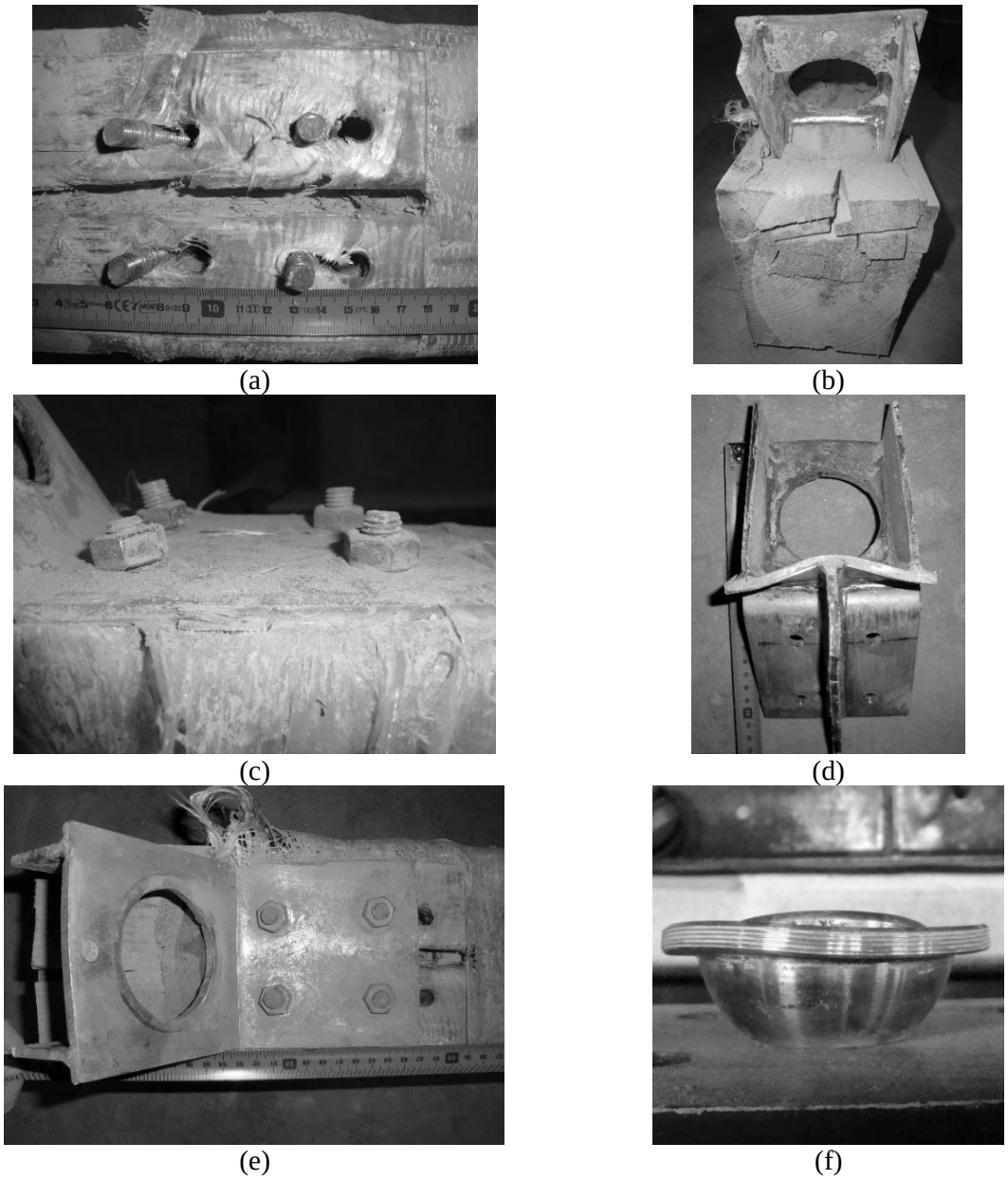

Figure 5.33 Different types of damage within FM3 category: (a) crushing of the timber under the bolts; (b) shearing of the timber; (c) bending of the bolts; (d) yielding of the steel angle's reinforcements; (e) opening of the steel angle; and (f) yielding of the hinge's cup.

The slip that occurred at the bolted connection and the opening of the steel angle were measure for each test, and are presented in Table 5.4. Again, the WF.40.A tests present low variability, which is consistent with the low CoVs obtained for the other experimental parameters (see Table 5.3). The variability of the slip and opening in the WF.60.A tests is a result of the distinct post-peak responses. On the other hand, there is a high linear correlation between slip and opening, F_{max} and slip, and F_{max} and opening, for the three WF.60.A specimens (see in Annex 3).

Table 5.4 Parameters related with FM3

Specimen	Slip (mm)	Opening angle (degrees)
40.3A	23	118
40.4A	23	113
40.4B	22	113
Average	23	115
CoV (%)	3	3
60.2B	28	105
60.3A	17	91
60.3B	50	118
Average	32	105
CoV (%)	53	13

5.7.3 Cyclic response parameters

From the hysteretic curves, it was possible to determine some important seismic parameters like the total energy, the dissipated energy, and strength degradation. Displacement ductility was already presented in the previous section, in Table 5.3. The total energy was calculated from $s_{j\text{-}fw}$, which is associated with damage occurring in the connection between the steel angle and the joist, and concentrates most of the deformations. The dissipated energy is calculated for $s_{j\text{-}fw}$, as well as, for d_{cone} (difference between $s_{j\text{-}bw}$ and $s_{j\text{-}fw}$) and $d_{ap\text{-}bw}$, in order to assess the contributions of other failure modes, FM1 and FM2, respectively. Since FM1 did not occur for the WF.60.A specimens, the dissipated energy relative to d_{cone} cannot be calculated. The contribution of FM4 (yielding of the steel tie) is not clear in terms of displacements, therefore is not considered for analysis.

The total energy encompasses the elastic strain energy and the dissipated energy through hysteresis, which is deeply connected with the displacement ductility and was examined in detail. From the total energy curves, one can distinguish pairs of consecutive peaks correspondent to the two cycles per level (see Figure 5.34). As the curves progress there is a lagging between peaks, which is due to the slip at the bolted connection. Both sets of tests share similar progressions, within the same range of values. Specimen WF.60.A.3A presents lower values of total energy, due to its fragile failure by bending, and specimen WF.60.A.3B shows a final increase, as a consequence of the additional monotonic loading till failure.

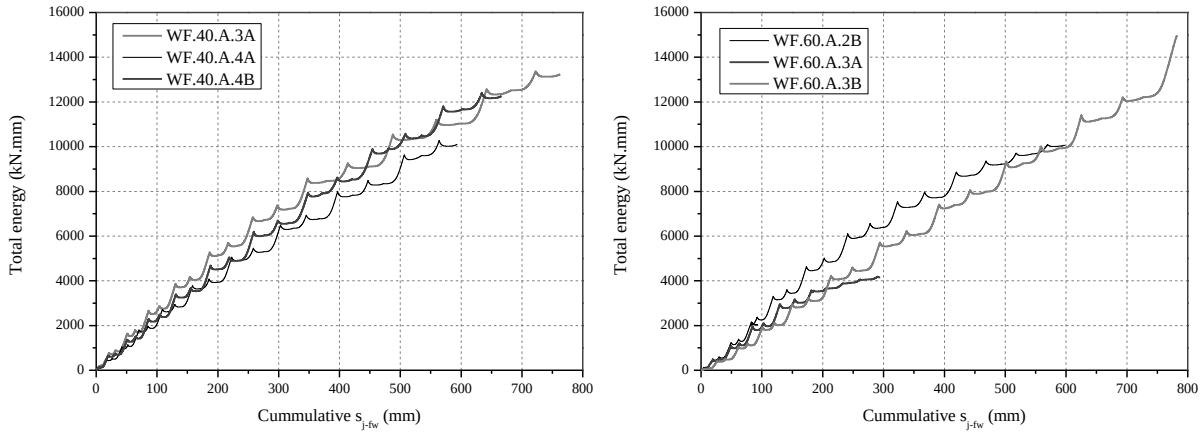

(a) (b)

Figure 5.34 Total energy based on $s_{j\text{-}fw}$: (a) WF.40 tests; and (b) WF.60 tests.

WF.40.A specimens have continuous increase in the dissipated energy per level, with exception of specimen WF.40.A.4B, which decreased after F_{max} was reached. Between the 20 mm and 60 mm levels, this growth is practically constant (see Figure 5.35a). Coincidently, in the same interval there is an ascending branch of the dissipated energy quantified from d_{cone} (see Figure 5.36a). For WF.60.A specimens, the sudden loss or increase of dissipated energy between consecutive levels is related to the fluctuations of pullout forces observed in Figure 5.18. Failure of specimens WF.60.A.2B and WF.60.A.3A is clearly characterized by a loss of dissipated energy. This is not observed for specimen WF.60.A.3B because the monotonic increase of displacement applied after the cyclic procedure was completed, was not followed by unloading of the specimen (see Figure 5.35).

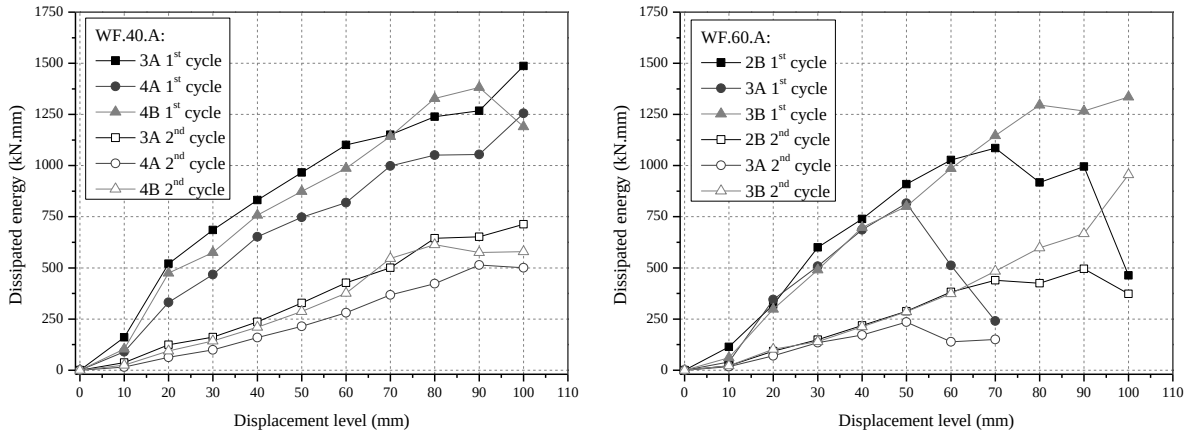

(a) (b)

Figure 5.35 Dissipated energy per level based on $s_{j\text{-}fw}$: (a) WF.40.A tests; and (b) WF.60.A tests.

The dissipated energy relative to d_{cone} and $d_{ap\text{-}bw}$, for the WF.40.A specimens, are presented in Figure 5.36. The dissipated energy of the 1st cycle calculated with d_{cone} follows the same trend for all specimens, presenting a peak at the 1st level (10 mm), followed by a significant

drop at the 2nd level (20 mm), and continuously increasing until the 5th or 6th level, finally dropping until zero. The 2nd level drop in energy, is not present on the 2nd cycle curves, meaning that is possible related to the drop in load, caused by detachment of the steel angle from the timber joist. The highest contribution of FM1 to the response of the connections occurs during the 5th (WF.40.A.3A) and 6th levels (WF.40.A.4A and WF.40.A.4B), being WF.40.A.4A the one with lowest values (see Figure 5.36a). Curves of specimen WF.40.A.4A are cut off at the 8th level, because the LVDT positioned at the joist was removed.

The contribution of FM2 seems to vary among the WF.40.A specimens. While specimens WF.40.A.4A and WF.40.A.3A have a small peak in energy, at the 3rd level, specimen evidences that peak earlier, at the 2nd level. Both specimens WF.40.A.3A and WF.40.A.4B reach the 10th level with a decreasing dissipated energy tendency, while specimen WF.40.A.4A shows opposite behavior, as shown in Figure 5.36. Nonetheless, the dissipated energy based on $d_{\text{ap-bw}}$ is higher for the WF.40.A specimens than for the WF.60.A specimens (see Figure 5.37), as expected, since the anchor plate was less engaged in these tests. All WF.60.A specimens had an accentuated peak, during the 1st cycle of the procedure, at the 3rd level, with minor fluctuations until the last cyclic level. In both sets of tests, the 2nd cycle is not as sensitive as the 1st one, to changes in dissipated energy.

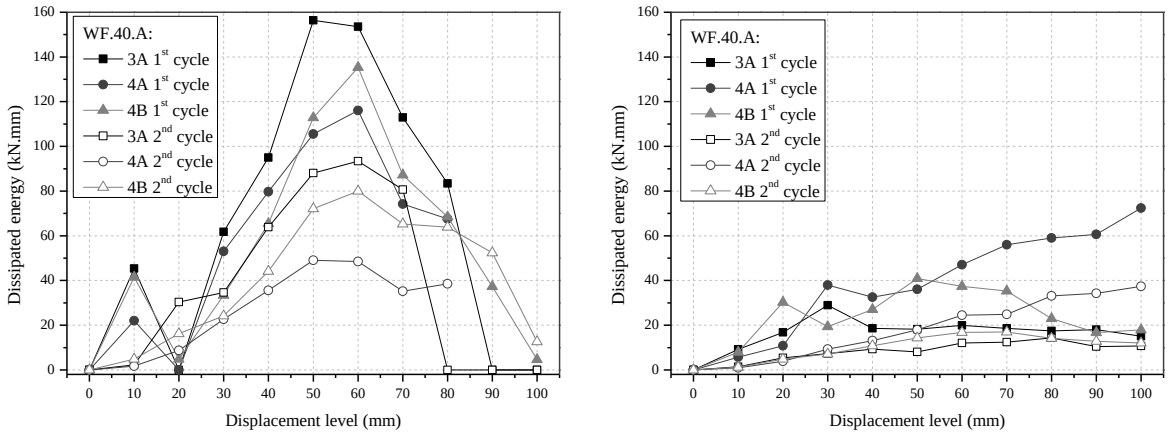

Figure 5.36 Dissipated energy per level for WF.40.A tests: (a) based on d_{cone}; and (b) based on $d_{\text{ap-bw}}$.

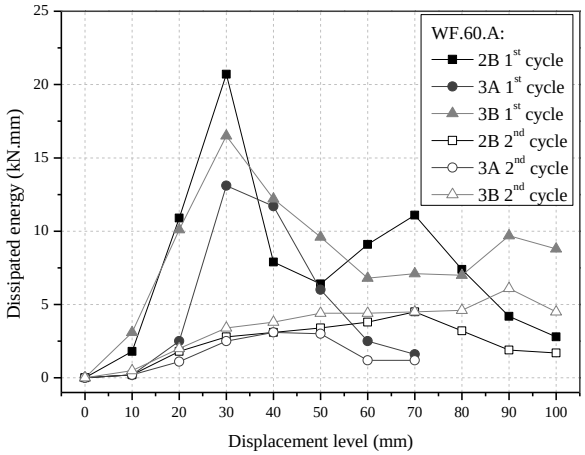

Figure 5.37 Dissipated energy per level based on $d_{ap\text{-}bw}$ for WF.60.A tests.

Considering the summation of the cumulative dissipated energy of the 1st cycle, at the 10th level, of each failure mode, one quantified their contribution, in %, to the global response (see Figure 5.38). For specimen WF.60.A.3A, this quantification was made with the cumulative dissipated energy of its last level. As expected, FM3 has the higher participation in the hysteretic behavior, reaching the averages of 89.7 % (CoV 3 %) and 98.9 % (CoV 0.15 %) for the WF.40.A and WF.60.A specimens, respectively. The second highest participation, for WF.40.A specimens, corresponds to FM1 and is 8.7 % of the total. The small differences pointed out on the hysteretic curves and dissipated energy of specimen WF.40.A.4A sum up into higher contribution of FM1 and FM2 than in any other test. FM2 contribution for the response of WF.60.A specimens was marginal, and no difference between specimens stands out that could explain the distinctions in behavior.

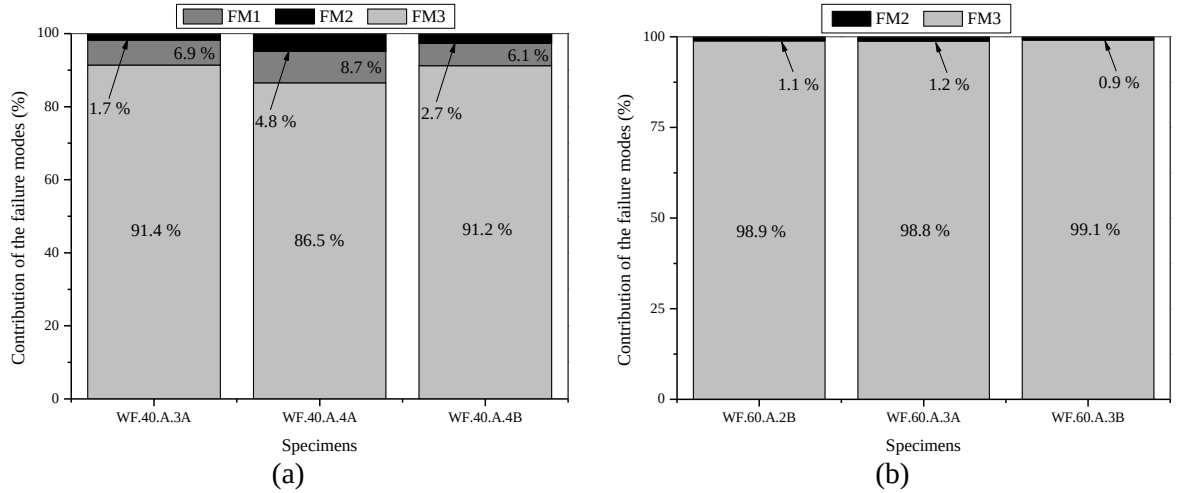

Figure 5.38 Contribution of failure modes to the dissipated energy.

Force degradation refers to the loss of strength between cycles of the same level. For comparison purposes, each test was normalized to the maximum difference determined for each

set of specimens (WF.40.A and WF.60.A), and then plotted against the displacements levels, as presented in Figure 5.39. In spite of the fluctuations in force degradation, in all specimens there is a tendency for increased force degradation throughout the test.

For the WF.40.A specimens, the highest loss of strength occurred at the 2nd level of displacement of specimen WF.40.A.4B. The absolute value of the loss was 18.6 kN, and corresponds to the detachment of the steel angle from the joist. The same phenomenon was responsible for the peak in force degradation, at the 1st level of displacement of specimen WF.60.A.2B. For both WF.40.A.3A and WF.40.A.4A, their maximum loss in absolute values was 11.5 kN, and in the first is related to an intermediate peak in force at the 6th level of displacement.

For the WF.60.A specimens, the maximum force degradation occurred at the 6th level of displacement of specimen WF.60.A.3A, and corresponds to the level after F_{max} was reached. In absolute values, it was a 48.0 kN drop, due to the brittleness of the failure mode. The higher peaks on the remaining specimens correspond to absolute the values of 17.2 kN and 12.5 kN, for specimens WF.60.A.2B and WF.60.A.3B, respectively.

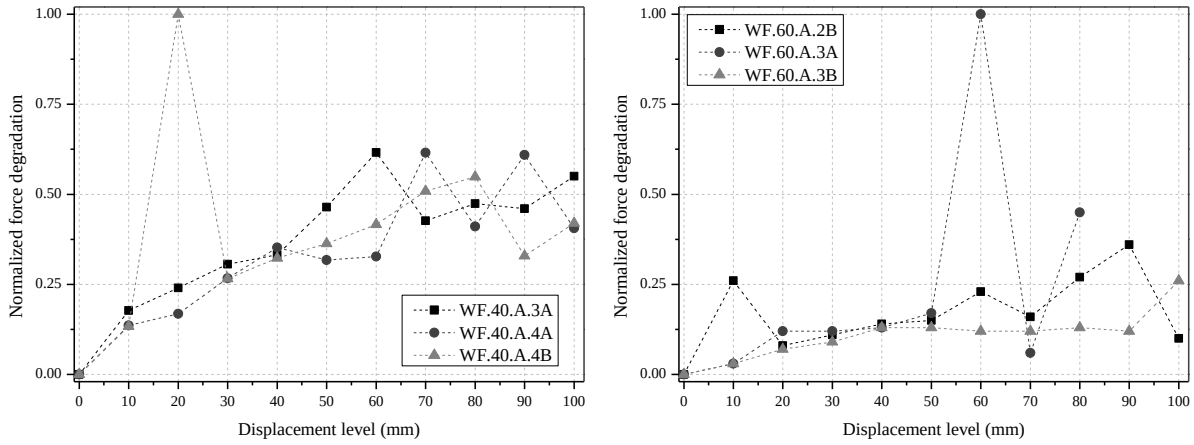

Figure 5.39 Normalized force degradation per displacement level: (a) WF.40 tests; and (b) WF.60 tests.

For the WF.40.A and WF.60.A specimens, the unloading stiffness per cycle was calculated in the same way applied to the injection anchor's specimens, but the lower force limit was 30 % of F_{max} of each cycle. This limit attempts to reflect the pinching effect observed on the unloading branch of the hysteretic curves. With the exception of specimens WF.60.A.2B and WF.60.A.3A, all specimens display significant losses of k_{un} in the first and second displacement levels (10 and 20 mm respectively), and smaller and steadier losses for the remaining displacement levels, for both cycles (see Figure 5.40). This is probably related with the detachment of the steel angle from the timber joist during the second displacement level. For

specimen WF.60.A.2B, the detachment occurred during the first displacement level, which might explain the abrupt loss of k_{un} from the first to the second cycles, and the steady decrease until the last displacement level. The value of k_{un} determined for the second cycle of the last displacement level of specimen WF.60.A.2B is higher than the one of the remaining specimens because the measurement of the displacements of that last cycle was possibly affected by the damage on the wall surrounding the joist, distorting the shape of the loop (see Figure 5.18).

Specimen WF.60.A.3A displayed increased k_{un} after failure, as shown in Figure 5.40, possibly due to distortions of the hysteretic loops caused by damage related to its particular failure mode, but not as significant as the increase observed on the tests of the injection anchors. With the exception of the latter, specimens from both sets of tests present close values of k_{un} per displacement level and cycle (single values, averages and CoVs are presented in Annex 3) and seem to follow a similar trend. In the last displacement level, the average k_{un} is 36 % and 45 % of k_{un} corresponding to the first displacement level (initial), for the WF.40.A and WF.60.A specimens.

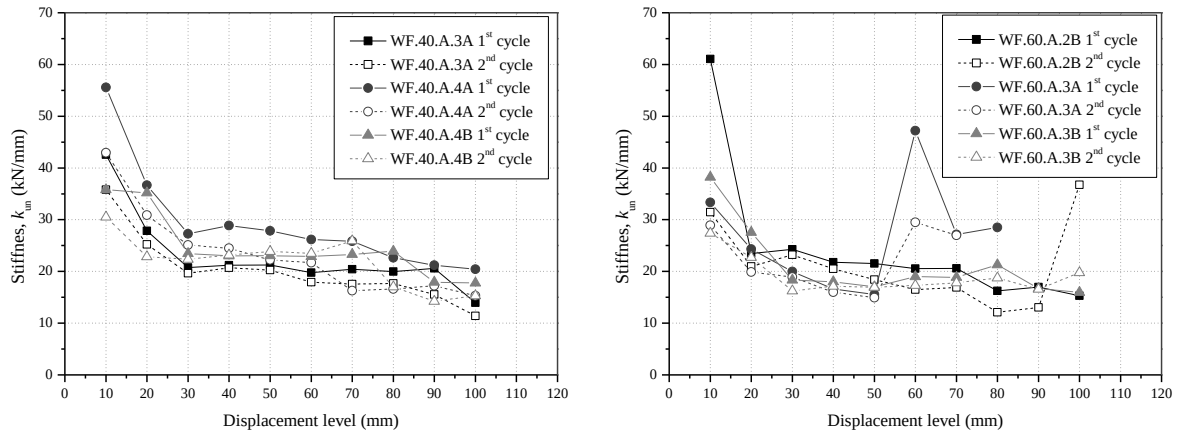

(a) (b)

Figure 5.40 Evolution of unloading stiffness throughout cyclic loading.

5.8 NONCONFORMITIES ASSOCIATED TO STRENGTHENED SPECIMENS

5.8.1 Hysteretic curves and cyclic parameters

This section focused on the analysis of the results of four specimens with nonconformities but tested with the same test setup and procedure applied on specimens of previous section 5.7, from now on referred to as regular specimens. These tests are presented in order to highlight the impact that the variability of certain parameters, like the dimensions of the metallic components or vertical compression of the specimens, might bring to the response of the strengthened connection. The performance parameters of these tests are presented in Table 5.5 and they were determined using the same criteria stated for the regular strengthened specimens

(see subsection 5.7.1), with the exception of d_y for the specimens with the steel angle not glued to the joist. All displacement dependent parameters were determined from the $s_{j\text{-}fw}$.

Table 5.5 Performance parameters of the tests with nonconformities

Specimen	Failure Mode	F_{max} (kN)	d_y (mm)	d_u (mm)	k_0 (kN/mm)	μ
40.2B	FM4	110.90	31.40	93.42	2.33	2.98
60.2A	FM3	77.29	5.93	92.11	6.99	15.54
60.4A	FM3	91.25	6.93	109.97	4.74	15.87
60.4B	FM4	90.02	6.25	59.19	5.50	9.47

One of the specimens, WF.60.A.4A, was tested and during the post-test survey, it was observed that the steel angle reinforcements were not according to what was established previously, which resulted in a less rigid steel angle. This faulty type of steel angle had been installed in other two specimens. The steel angles were removed and substituted by correct ones, which were not glued back to the timber joist. Since the specimens had already been through alterations, one decided to proceed with testing, considering a hypothetical scenario where the steel angles were placed on the joist, after the epoxi had dried. Thus, the connection between steel angle and timber joist was only mechanical, through the bolted connection and the interlock resulting from the reinforcements of the angle being inserted in the timber slots. The two specimens tested under these conditions were WF.40.A.2B and WF.60.A.2B. Specimen WF.60.A.2A was tested with half of the vertical compressive stress, 0.2 MPa when it should had been 0.4 MPa, due to an error in adjusting the pressure of the hydraulic jacks before the test.

While specimen WF.40.A.2B presents an increase in strength of 18 % in comparison to the regular WF.40.A tests, the WF.60.A specimens with nonconformities are within minus two standard deviations of the capacity of regular WF.60.A specimens. Both k_0 and μ are only comparable with the minimum values determined for the regular tests (5.67 kN/mm – minimum k_{el} for WF.60.A.3B; 15.76 – minimum μ for WF.60.A.3A), revealing that the presence of the nonconformities had higher impact on the deformations rather than on the capacity.

Specimens WF.40.A.2B and WF.60.A.4B, which did not have the steel angle glued to the joist, had FM4 as the predominant failure mode, and present rounder force-displacement curves until the brittle failure. Specimen WF.40.A.2B showed a very steep first linear branch, as shown in Figure 5.41a, which also denoted in all the other displacements measured on the specimen. Since it occurred for small values of displacement (until 0.44 mm) relatively to the maximum displacement (93.42 mm), this segment was considered an adjustment of the specimen, and d_y

was established at 31.40 mm, when the another change of stiffness occurred. Not to completely dismiss this initial adjustment, k_0 was determined as the secant line between the origin and the point in the curve corresponding to d_y.

Specimen WF.40.A.2B displayed small drops followed by increases in load, between 90 kN and failure, which was consistent with damage of the threads of the steel tie (see in Figure 5.41a). The same phenomenon was not observed for specimen WF.60.A.4B. The higher tensile capacity of specimen WF.40.A2B can result of the test being monotonic, but the force-displacement curve is not near the upper boundary of the envelope curves. On the contrary, specimen WF.60.A.4B is within the boundaries of the envelope area of the regular WF.60.A tests, as presented in Figure 5.41b.

Although specimens, WF.60.A.4A and WF.60.A.4B, had different nonconformities, their predominant failure mode was FM3. Due to a malfunction in the acquisition system, the first two levels of displacement of the procedure were not recorded for specimen WF.60.A.4A, but there was still the record of the internal transducer of the actuator. From this last one, was possible to observe the shape of the curve for these first levels (see Annex 3), and determine that the drop of load caused by the detachment of the steel angle from the joist occurred during the second level of displacement, at 42.8 kN. Taking all these factors into consideration, a quadratic regression was applied to the remaining segment of the first cycle of the third level (R^2 = 0.99), in order to have a conservative estimate of the displacements during the first two levels. The estimation and actual measurement are presented in Figure 5.42a, where the first is represented with a dashed line. Throughout the test, the specimen reached peak values between 60 kN and 75 kN, below the envelope area of regular WF.60.A tests, and failed abruptly in the last step (no softening).

The force-displacement curve of specimen WF.60.A.2A developed close to the lower boundary of the envelope area of the regular WF.60.A specimens, and had a well-defined linear branch until the detachment of the steel angle from the joist occurred, for a yield force, F_y, of 41.4 kN and a d_y of 5.9 mm. After F_{max} is reached, the load decreased in steps, which is characteristic of timber shearing (see Figure 5.42b).

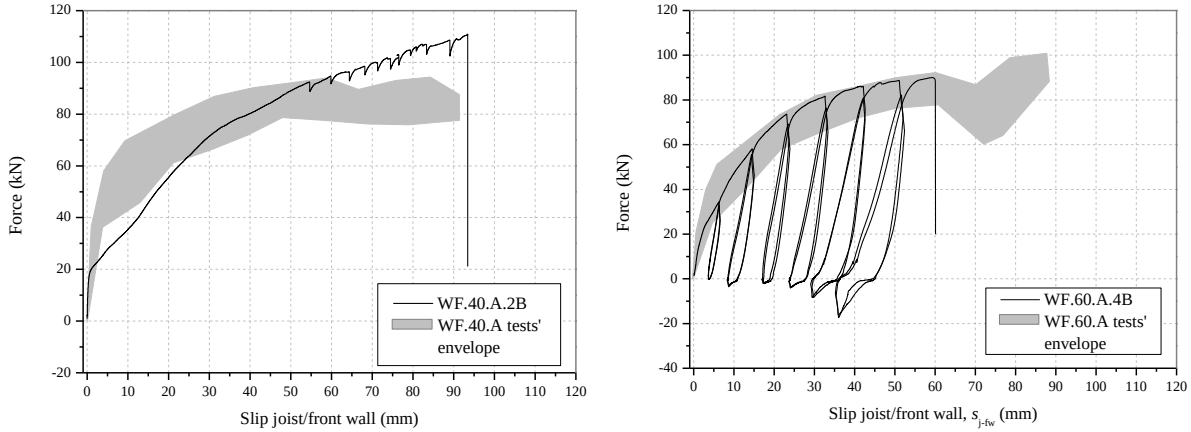

(a) (b)

Figure 5.41 Force-displacement curves of specimens w/o the steel angle being glued: (a) WF.40.A.2B; and (b) WF.60.A.4B.

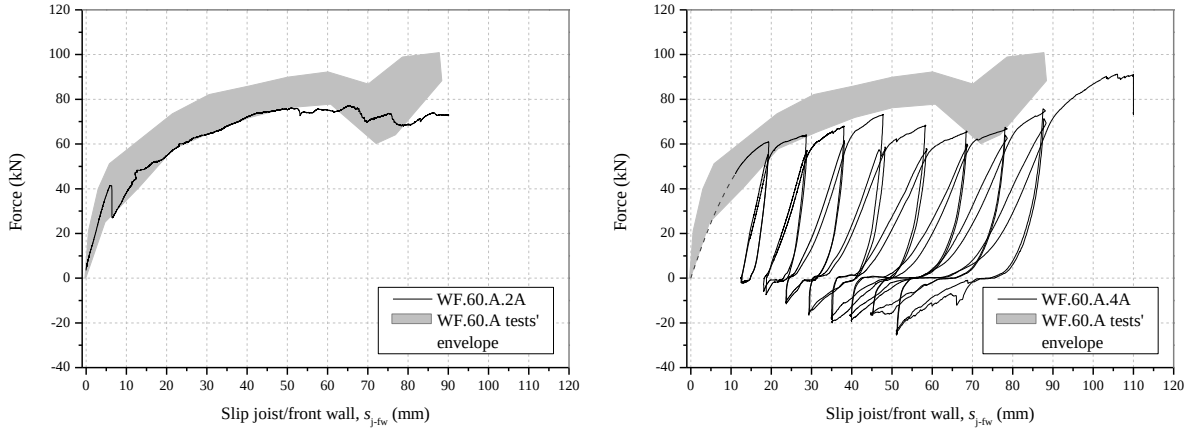

(a) (b)

Figure 5.42 Force-displacement curves of specimens with nonconformities: (a) half of the vertical stress; and (b) less rigid steel angle.

In all the WF.60.A specimens with nonconformities the contribution of the wall was negligible, since no significant out-of-plane displacements were measured on the front and back of the wall. Specimen WF.40.A.2A presented a maximum average displacement of 1.19 mm, for the three LVDTs in the positions around the steel angle (2, 4, and 7), in the front face of the wall, and a maximum displacement at the back of 1.61 mm. In Figure 5.43a are presented the force-displacement curves based on $d_{\text{ap-bw}}$, for specimen WF.40.A.2B, and on the anchor plate displacements for the WF.60.A specimens with nonconformities. As expected, the contribution of FM2 for the response of the WF.60.A specimens, which is associated with these displacements, is lower than the one of the regular specimens. The contribution to WF.40.A.2B specimen's response is in the same order of specimen WF.40.A.3A.

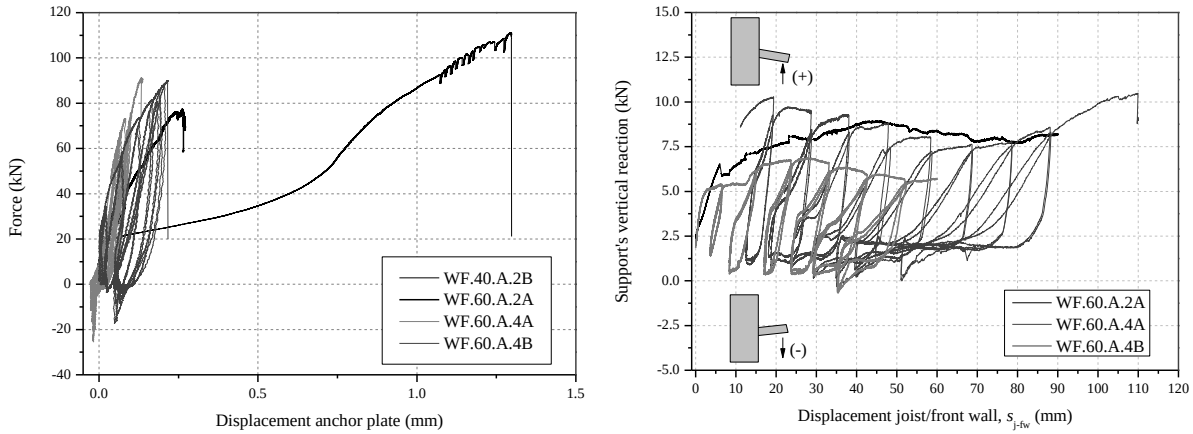

Figure 5.43 Force-displacement curves relative to: (a) the anchor plate; and (b) the supports' vertical reaction.

The vertical support's reaction followed the cyclic procedure, and there is a significant difference between loading and unloading, with a much higher downward rotation of the joist, when being loaded (see Figure 5.43b). The reaction values are in same range of the values measured for the regular WF.60.A specimens, with a maximum of approximately 10.0 kN and a minimum around 0.5 kN. For specimen WF.40.A.2B, the test was carried out with the vertical support, but the load cell was not yet calibrated, therefore there is no data available.

For the two specimens with cyclic hysteresis curves, the dissipated energy per displacement level was calculated, as well as the normalized force degradation, and both are presented in Figure 5.44. The dissipated energy of specimen WF.60.A.4A was determined from the level of displacement, where displacements were recorded. Both specimens show increasing dissipated energy until the last level of displacement, and the values determined are in the range of the ones calculated for the regular WF.60.A specimens. One must point out that for specimen WF.60.A.4A the loss of dissipated energy between cycles is practically constant (curves running in parallel), while for specimen WF.60.A.4B the loss increased throughout the test (see Figure 5.44a).

As performed for the regular specimens, force degradation was normalized to the maximum loss of force between the two cycles of the same level of both specimens. The maximum loss of strength occurred for specimen WF.60.A.4A, at 60 mm, which in absolute values was equivalent to a loss of 14.6 kN, and corresponds to a peak of force before F_{max} (see Figure 5.42b). The minimum loss happened for the first level of both specimens, being equivalent to a loss of 1.7 kN. For specimen, WF.60.A.4B, force degradation increased until failure, while for specimen WF.60.A.4A decreased considerably after an intermediate peak at 60 mm level.

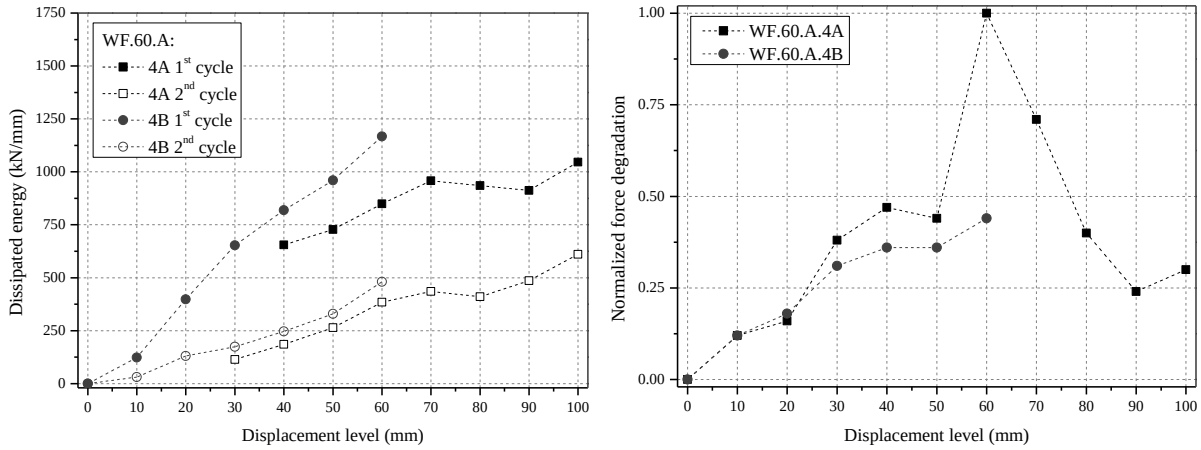

(a) (b)

Figure 5.44 Cyclic parameters for specimens WF.60.A.4A and WF.60.A.4B: (a) dissipated energy; and (b) force degradation.

5.8.2 Damage survey

The damage observed on the specimens is similar to the one described before for the regular specimens, in subsection 5.7.2. This section describes the aspects of the damage that are particular of these specimens.

During the tests, when the abrupt fracture of the steel tie (FM4) occurred for specimens WF.40.A.2B and WF.60.A.4B (see Figure 5.45a), the hinge components fitted in the steel angle were projected forward (see Figure 5.45b), and the release of tension caused a detachment of the anchor plate and of the new mortar layer placed between the plate and the masonry wall (see Figure 5.45c). Both specimens displayed damage of the bolted connection between the joist and the steel angle, and yielding of the latter. The slip of the bolted connection was 15 mm for both specimens (see Table 5.6), which is the lowest value measured in all specimens, including the regular ones. No generalized cracking was observed on the wall, front and back, of specimen WF.60.A.4B. On the other hand, specimen WF.40.A.2B presented cracks propagating from the steel angle to the edges of the specimen (particularly one that propagated to the top of the wall, presented in Annex 3), one single crack radiating from the corner of the wall-plate until half of the thickness of the wall (see in Annex 3), and hairline cracks around the anchor plate. There also bending of the latter, as shown for regular WF.40.A specimens, in Figure 5.31a.

The two remaining specimens, WF.60.A.2A and WF.60.A.4A, which failed by FM3 displayed similar damage to the one observed on the regular WF.60.A specimens, characterized by crushing of the timber against the bolts, yielding of the steel angle and consequent buckling of its reinforcements, and shearing of the timber joist behind the steel angle (see Figure 5.46).

The lesser rigid steel angle had a final opening angle higher than the remaining specimens, accompanied by a high value of slip at the bolted connection, as presented in Table 5.6.

(a) (b) (c)

Figure 5.45 Damage related to FM4: (a) broken steel tie; (b) projection forward of the hinge components; and (c) detachment of layer of mortar and anchor plate.

(a) (b) (c)

Figure 5.46 Damage related to FM3: (a) sliding of the steel angle relatively to the joist; (b) yielding of the steel angle reinforcements; and (c) shearing of the timber.

Table 5.6 Parameters related with FM3

Specimen	Slip (mm)	Opening angle (degrees)
40.2B	15	112
60.2A	26	109
60.4A	35	133
60.4B	15	105

5.9 DISCUSSION OF RESULTS

From the twenty tests carried out, sixteen were considered valid and presented in the previous sections. The remaining four tests were used to adjust components of the strengthening or to try out alterations to the setup.

In all unstrengthened specimens the failure occurred by pulling out of the two nails connecting the joist to the wall-plate, but the capacity was influenced by the rotation of the joist, especially for the specimens with 0.4 m thick walls. Along the test without support, as the joist was being pulled out from the wall, its weight shifted away from the wall, causing a downwards' rotation (see Figure 5.47). By doing so, the top edge of the back end of the joist that was inside the masonry pocket started being pressed against the wall, generating an uplift reaction equivalent to the self-weight that affects the component of the shear force due to friction. For specimen WF.40.U.1A, this component became higher than the one due to the compressive state of the wall (approximately 0.2 MPa), increasing the capacity of the connection. For the WF.60.U specimens this feature did not happen, since the compressive state of the wall was higher (approximately 0.4 MPa), approximating their behavior to a connection with a vertical support, as provided for specimen WF.40.U.1B. The vertical support introduces a reaction to the self-weight, eliminating the uplift force. The interface that contributes the most is the one between the joist and wall-plate, because relies on friction and the nails. The average capacity of the latter and the WF.60.U specimens was 4.68 kN (CoV of 15%), which was very close to the value of 5 kN obtained by Cóias e Silva (2007), for in-situ pullout of timber members from *Pombalino* buildings. Since the results of the pullout tests performed by Lin & LaFave (2012), had pullout and shear off at head of the nails as main failure modes, as briefly introduced in section 5.2, is worth to mention that the capacity obtained for the unstrengthened specimens was a little below their lower interval value (5.8 kN).

The test apparatus had impact on the results of the unstrengthened and strengthened connections, particularly on the rotation of the joist. This aspect was aggravated by the cyclic procedure, which was observed on discarded tests, leading to the introduction of the vertical support (roller) of the joist, in the test setup. One minimized the effect of the rotation, isolating the tensile capacity and deformation of the connection. The contribution of the masonry wall to the resistant capacity of the connection was very low, for all sets of tests, consequently one considered that there was no interference of the test frame on the projected area of the cone.

The observed damage and failure modes were according to the hypothesized mechanical failures of the connection, except for specimens WF.60.A.1A and WF.60.A.3A. The first failed

by shearing of the timber wall-plate, while the second failed by bending at the connection between joist and steel angle. In both tests there was a high influence of the rotation of joist. Since the pullout force was applied along the longitudinal axis of the joist, a bending moment resulted from the eccentricity between this axis and the one of the hinge placed in the steel angle. The eccentricity was in average of 0.16 m. For WF.60.A.1A, this movement was not restrained by a vertical support, therefore the joist rotated upwards applying a force perpendicular to the grain of the wall-plate, which led to failure. In the case of WF.60.A.3A, the vertical support was present, but the small deformation of the steel angle, caused the formation of a short beam spanning between the latter and the vertical support, which broke by bending, where the section was reduced (the bolted connection). No physical evidence was observed that could suggest this failure mechanism. Both specimens had higher out-of-plane displacement of the wall-plate, which resulted from the joist pressing against the wall-plate. The above mentioned bending moment was also responsible for the detachment of the steel angle from the joist, but the amount of force associated with the pull-off depended on the contact area with epoxi.

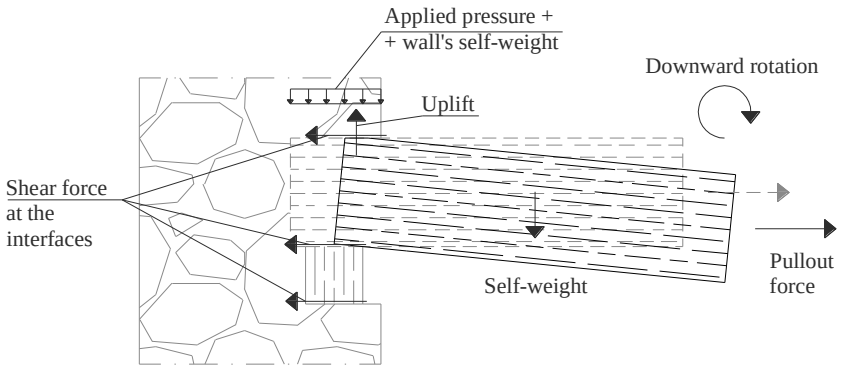

Figure 5.47 Forces generated for pullout of an unstrengthened specimen without support.

Specimen WF.40.A.1A was the only specimen to fail primordially by FM1. Nonetheless it also had damage related with the other failure modes hypothesized initially, especially FM2. One cannot attribute this type of failure to the lack of vertical support of the joist, based on only one specimen. It can also be related with the quality of the masonry, since the tensile capacity obtained for FM1 was below what would be expected. From the photographic record presented, it was possible to observe a complete masonry cone breakout (see Figure 5.30e) and generalized cracking, more than what was observed for other WF.40.A specimens. As a consequence of this type of failure, ductility was the lowest of all specimens.

The quantification of contributions to the response of the specimens based on the dissipated energy, confirmed what was observed during the tests and on the survey performed at

demolition, the predominant failure mode of strengthened connections was FM3, failure of the connection between steel angle and the timber joist. Especially, WF.40.A specimens present great results consistency, with a CoV of all parameters below 14 %. Both sets of specimens, WF.40.A and WF.60.A, share similarities on the hysteresis loops, and consequently tensile capacity, ductility, and dissipated energy, supporting that their failure mode was similar. The difference between the two sets of sets resides on the post-peak behavior of the WF.60.A specimen, and on the contributions of the masonry cone breakout and crushing of masonry under the anchor plate, as well as bending of the latter. These two types of damage were more prominent on the WF.40.A specimens, which could explain the slight increase in tensile capacity and difference in post-peak behavior. As described in 5.7.2, besides the formation of cracks characteristic of the cone breakout, there were also vertical cracks radiating from the steel angle that could be related to splitting of the masonry. In particular, bending and dislocation of the anchor plate for the WF.40.A specimens affected the capacity to engage the masonry cone, which could explain why its contribution was not higher. Dissipated energy contributions, presented in Figure 5.38a, showed that contributions of FM1 and FM2 were higher for specimen WF.40.A.4A, which coincidently did not have the anchor plate bent, but instead it moved slightly. For the WF.60.A specimens, the higher thickness and vertical stress discouraged the formation of FM1, and the increase in thickness of the anchor plate prevented it from bending, and there was a better distribution of the load on the back face of the wall. The contribution of the yielding of the steel tie is rather complicated to quantify, since it could not be isolated from the remaining failure modes.

The pullout capacity of the strengthened connections is approximately 19 times the one of the unstrengthened ones, but the ductility decreased around 30 %. Although the ultimate displacements are much higher (110 %), the elastic limit was also extended, decreasing the ductility. Nonetheless the ductility of the strengthened specimens is approximately 23 (CoV of 6%), if specimen WF.60.A.3A is excluded, which is a considerably high value, and the dissipated energy is higher than before. Both WF.40.A and WF.60.A specimens have approximately 60 % loss in dissipated energy between cycles, which is explained by the slip that occurs at the bolted connection with force practically zero, until it regains strength. While the virgin branch of first cycle has a negative concavity, increasing the area below it, the second cycle branch has always a positive one. Force and stiffness between cycles degraded throughout the test, and this degradation is deeply related with damage accumulation.

The incapacity to measure the small displacements of the wall on the WF.60.A specimens suggests that LVDTs with higher resolution should be used. It was also noted that if LVDTs

start the test compressed, they are more sensitivity to displacement changes than starting opened, which enabled better data acquisition at the back of the wall. The deformed shapes of the specimens, provided in Figure 5.24, seem to confirm what was already observed for the injection anchors, in Chapter 4, that the out-of-plane displacements are smaller close to the base of the wall and it might be considered fixed. The displacements measured suggested that the top of the wall can be assumed as a roller. When it comes to the vertical support, all specimens had closer values of positive reactions (during loading), but WF.40.A specimens also developed negative reactions, meaning there was an uplift of the joist, during unloading. Therefore WF.40.A specimens were more susceptible to joist rotations than the WF.60.A specimens, which did not registered any negative vertical reactions.

Strain was only possible to measure in four specimens, therefore the method of protection of the strain gauges from damage has to be improved or rethought. However, from the data gathered (see Figure 5.23), it seems the ties were bent and yielded inside the wall. This was confirmed by the permanent deformation observed along the steel ties, after being removed from the walls. Together with the fact that the tie is bent by the hinge and steel angle, at one of its extremities, failure by bending becomes much more concerning that direct tensile failure. In addition, it affects load transmission to the anchor plate, which is expressed in the error determined between ε_m and ε_e. One must point out that this difference, exists since the beginning of the test, being at first negative ($\varepsilon_m < \varepsilon_e$), and then evolving towards a positive difference ($\varepsilon_m > \varepsilon_e$), possibly due to the permanent deformation of the tie.

Figure 5.48 presents a representation of a final configuration of a tested strengthened connection, based on the damage that was observed and on the data obtained from the instrumentation. It is an interpretation of the contribution of all failure modes to the response of the connection and how they interacted with each other. As the joist was being pulled out of the wall, it mobilized the timber against the four steel bolts and reinforcement of the steel angle, and the single shear connection with the latter. Then the steel angle transmitted the stresses to the tie anchored to the anchor plate, which mobilized the capacity of the masonry wall. The eccentricity between the longitudinal axis of the hinge placed in the steel angle and the joist, where the demand was applied, created a bending moment that led to the detachment of between those two elements. As expected, the weakest link was the junction of these two elements, concentrating most of the damage and limiting the contribution of the failure modes related with masonry.

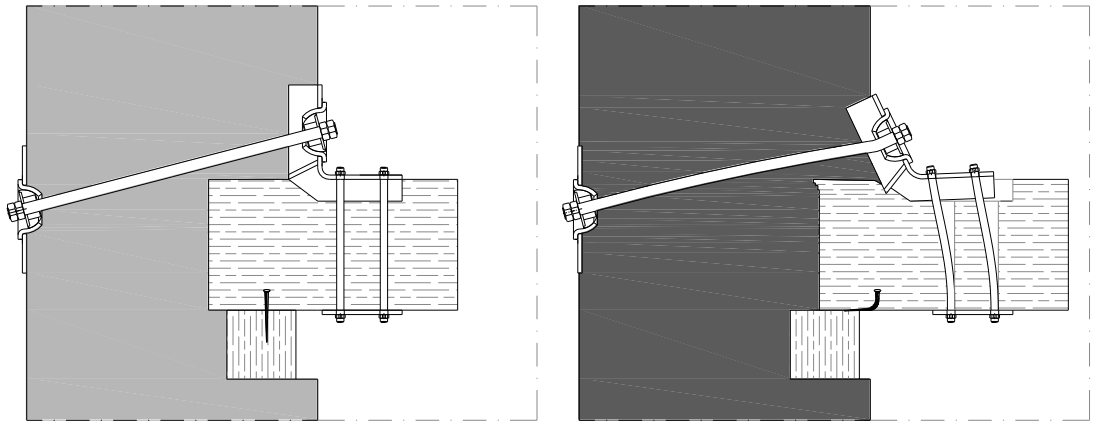

Figure 5.48 Sketch of the strengthened connection before and after testing (deformation in the same scale as the dimensions)

The tests performed on specimens with nonconformities proved that changes to the strengthening solution or to the compressive state of the wall have impact on the response of the connection. In particular, the two specimens without the steel angle glued to the timber joist with epoxi (WF.40.A.2A and WF.60.A.4B) failed by FM4, which is a different failure mode than the one observed for the regular specimens and more concerning, a brittle one. Further investigation of the matter needs to be carried out, but is possible that the drop of load associated with the detachment between steel angle and joist enables a more ductile configuration of the connection.

The specimen with a less rigid steel angle, WF.60.A.4A presented similar tensile capacity to the regular specimens, higher deformation, but decreased ductility and stiffness. These two values were calculated based on a conservative estimation of d_y, therefore they are possibly even lower. Nonetheless, it confirms that much of the ductility and stiffness of the strengthened specimens comes from the steel angle, and changing it has a direct impact on the response of the connection. In fact, the values of these two parameters decreased in all specimens with nonconformities. In addition, specimen WF.60.A.2A, which had half of the prescribed compressive stress applied on the wall, also showed decreased tensile capacity, suggesting that the compressive state of the wall has indeed impact on the performance of the connection.

5.10 CONCLUSIONS

From the pullout tests performed on the unstrengthened and strengthened connections, it was possible to better understand the development and contribution of each damage mechanism to the global response.

The failure of unstrengthened specimens was characterized by pullout of the two nails connecting the timber elements that conferred high ductility to the connections, but low tensile capacity (4.7 kN).

The predominant failure mode for both WF.40.A and WF.60.A strengthened specimens was failure of the connection between the steel angle and the timber joist, consequently they shared similarities on the hysteretic curves, tensile capacity, ductility, and dissipated energy. As previously mentioned, tensile capacity is 19 times higher than the one of the unstrengthened specimens. Although ductility was reduced, it still maintained a high value of approximately 23.

The response of the strengthened connection resulted from the interaction between the different elements that are comprised in it, and changes on the strengthening components or compressive state of the masonry wall seem to influence the tensile and deformation capacities.

Chapter 6. Analytical development

Highlights:

- Global behavior of the connections can be better understood through failure analysis of its components;
- Existing prediction formulae provide good approximations to the experimental results;
- The strengthened connections studied can be classified as deformation-controlled actions, due to their high ductility;
- Comparison between idealized curves obtained from ASCE/SEI 41-06 and Frumento et al. (2009) show that the first method is very conservative;
- Alterations to the definition of backbone curves and acceptance criteria in ASCE/SEI 41-13 bring it closer to what is established by EC8-Part 3;
- Performance criteria were proposed for displacement and force, while the design procedure only focused on the latter;
- Retrofit design should comprise design of the strengthening connection, and verification of the global response of the building, after the intervention.

6.1 INTRODUCTION

This chapter focus on analyzing in detail the results obtained experimentally for the injection anchors and for the wall-to-floor connections, as well as developing tools that enable the use of the data collected on the analysis or design of seismic strengthening. The procedures applied in this chapter intend to guide the way to further experimental, analytical, and numerical developments.

Existing literature, as well as EC8-Part 3 (CEN/TC250, 2004) and ASCE/SEI 41-06 (ASCE, 2006), suggest performance-based design as the most appropriate path towards assessment and design of seismic retrofit, since it establishes a direct relationship between design and expected structural system or component performance. The component should be classified as "brittle" or "ductile", which dictates the use of force-based or displacement-based design criteria, respectively. Nonetheless, force-based design is widely applied by practitioners, especially when linear analysis procedures are used. Therefore, one first focused on the applicability and development of the existing strength prediction formulas to the two types of strengthening tested and how they can be used in a design context. Then, an idealization of the force-displacement curves descriptive of the two types of strengthening is presented, and acceptance criteria are proposed, as well as design recommendations.

6.2 STRENGTH PREDICTION FORMULAE

6.2.1 Injection anchors

The mechanism associated with the wall-to-timber elements connections with injection anchors is assumed to work in series, being the load transmitted first from the timber elements to the steel tie, secondly to the interface tie/grout, in third place to the grout, then to the interface grout/masonry, and finally to the masonry. Depending on the properties of the masonry and interfaces, isolated or combined cone-bond failures can occur. Since masonry and concrete are quasi-brittle materials and the installation and design of anchors in concrete has been widely studied, one can explore some similarities in behavior to study the behavior of anchors in masonry.

Anchors are usually divided in two main groups: cast-in-place and post-installed. Cast-in-place anchors are installed before the concrete is placed while post-installed are applied in existing concrete. Within these two groups there are sub-categories, but this study will focus on post-installed bonded anchors with cementitious grout (Cook et al., 2003). Post-installed anchors (bonded or mechanical) are a viable option to strengthen historical structures because

they allow for minimum intervention and architectural impact on the structure. As previously mentioned, bonded anchors can be adhesive or grouted. Adhesive anchors are usually applied in situations that require fast setting times and have predrilled holes with small dimensions — up to 10 to 25 % larger than the diameter of the steel anchor rod (Cook et al., 1998). Grouted anchors usually apply cementitious or polymer based grouts with predrilled holes typically 50 to 200 % larger than the diameter of the steel anchor (Cook et al., 2003). The grout used can be a polymer, cementitious, or lime based, being the first one applied when dry conditions of the hole are required. The steel rod can be unthreaded or threaded with a nut and a headed bolt, or can even be a deformed reinforcing bar with or without end anchorage (Cook et al., 1998).

Bonded anchors mainly take advantage of bond and mechanical interlock (CEB, 1994; Cook et al., 2003). The presence of a head on the anchor changes the load transfer mechanism and has direct consequences on the failure modes. The most common failure modes for unheaded anchors are bond failure at rod/grout interface and bond failure at grout/substrate (concrete or masonry) interface. The existence of the head prevents the failure at the rod/grout interface and adds two more possible failure modes: substrate cone breakout and combined cone-bond failure (Cook et al., 2003), as shown in Figure 6.1. Headed or not, bonded anchors can also fail by yielding of the steel rod, which can be controlled by properly choosing the steel grade and diameter. These failure modes are confirmed extensively in literature, mainly with the works of (Zamora et al., 2003) and Cheok & Phan (1998) citing Eligehausen et al. (1984a, 1984b).

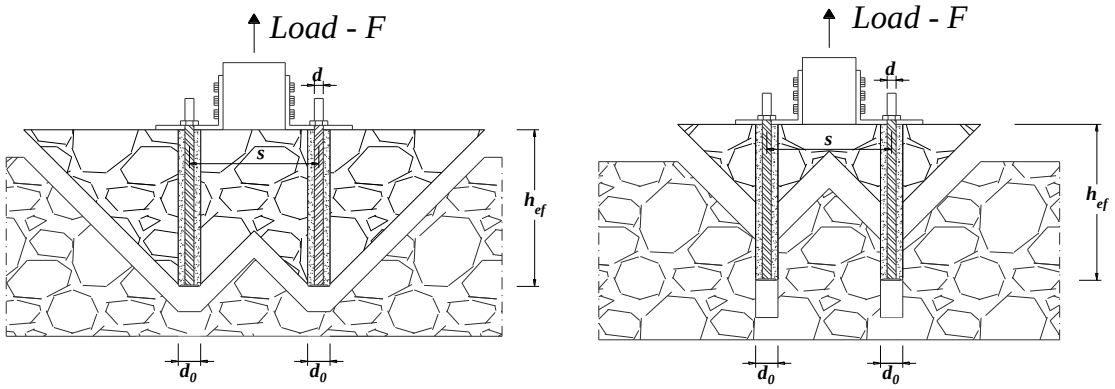

Figure 6.1 Failure modes: (a) substrate cone failure; and (b) combined cone-bond failure (adapted from (Zamora et al., 2003)).

With injection anchors in masonry, CEB (1994) states that they are mainly used for low compressive strength (lightweight and aerated concrete) and in perforated brick or hollow block masonry, which is consistent with the base material considered in the ETAG 029 (EOTA, 2010). Load transfer mechanisms for these particular anchors can involve mechanical interlocking between injection anchor and masonry substrate, local mechanical interlocking

between injection mortar and voids, and bond and friction between sleeve-grout and surface of the drilled hole. The use of an expandable sleeve around the anchor rod is commonly used to control the flow of mortar into voids. This effect of the sleeve, combined with the fact that the bearing walls are continuously under compression may introduce pre-compression to the grout––allowing for load transfer through friction between sleeve-grout interface and the surface of the drilled hole (and to adjust to possible internal voids, which increases the pull out strength capacity). The tests discussed in this paper used an expandable sleeve on walls that were in compression for the installation and testing of the anchors to best represent *in situ* conditions.

6.2.1.1 Steel tie failure

In reality, the steel tie is subjected to shear and bending stresses that might precipitate failure, but since the force was applied in the direction of the longitudinal axis of the steel tie and from its total length, only 17 % was outside the wall, one considers that the tensile stresses on the tie came mostly from direct tension. Therefore, Equation (6.1) can be used for the prediction of the nominal tensile strength by steel failure, N_{sa}.

$$N_{sa} = nA_s f_u \tag{6.1}$$

where n is the number of anchors, A_s is the stressed cross-section of steel, and f_u is the steel ultimate tensile strength (nominal value). Considering n equal to 2, the diameters of the tie rods used experimentally, ϕ16 and ϕ20, and the average f_u obtained experimentally, 870 MPa, the respective tensile strengths associated with steel failure would be 350 kN and 547 kN. For design purposes, the ACI 530 (ACI 530, 2005) proposes the use of the yield strength, f_y, rather than the ultimate one, and the application of a design reduction factor, ϕ, of 0.90. On the other hand, the ACI 318 (ACI 318, 2005) recommends the use of the tensile strength, but it should not be taken greater than the smaller of $1.9f_y$ and 860 MPa. It suggests a lower reduction factor (0.75), which is consistent with the use of a higher value for f_y.

6.2.1.2 Masonry cone breakout (FM1)

Since the mid-1970s, different design methods have been developed for anchorage to concrete, based mainly on plasticity models (modified Coulomb failure condition) and on linear elastic fracture mechanics (LEFM) (Zamora et al., 2003; Fuchs et al., 1995). Zamora et al. (2003) stated that headed grouted anchors are expected to behave similarly both with cast-in-place headed anchors and post-installed headed adhesive anchors. The significant behavioral models have only been developed for concrete cone failure, observed in both types of anchors, and bond stress models, only seen in adhesive anchors.

The equations listed in Table 6.1 allow the prediction of the nominal (commonly defined at the 5th percentile) tensile strength of a group of anchors, in uncracked concrete or masonry, N_c. Equations presented in Table 6.1 are expressed in SI units (N, mm) and the ones regarding concrete are in terms of nominal concrete compressive strength of 200 mm cubes, $\sqrt{f'_{cc,200}}$ (for comparison purposes), except for Eq. (6.6). Parameters that reflect common concepts across equations have the same denomination. Since no equivalent expression was found defined using $\sqrt{f'_{cc,200}}$, Eq. (6.6) in Table 6.1 is presented in terms of f'_c as in the nominal concrete cylinder compressive strength on 150 mm by 300 mm cylinders.

Table 6.1 Summary of methods to determine the nominal tensile load conical concrete/masonry breakout

Method	Type of anchor	Conical failure - N_c (N)	
ACI 349-90	CIP headed anchors for concrete	$\frac{A_{Nc}}{A_{Nco}}\ 0.96\sqrt{f'_{cc,200}}\ h_{ef}\ [h_{ef} + \mathrm{d}]$	(6.2)
VAC method (1995)	CIP headed anchors for concrete	$\frac{A_{Nc}}{A_{Nco}} 0.96\sqrt{f'_{cc,200}}\left(\frac{h_{ef}}{\tan\theta}\right)\left[\frac{h_{ef}}{\tan\theta} + d\right]$	(6.3)
Eligehausen et al. (1984)	Adhesive anchors for concrete	$\frac{A_{Nc}}{A_{Nco}} 0.85\ h_e^2\sqrt{f'_{cc,200}}\,, if\ h_{ef} \le 9d$	(6.4)
CCD method (1995)	CIP headed anchors for concrete	$\frac{A_{Nc}}{A_{Nco}}\psi_{s,N}\ \psi_{ec,N}\ 15.5\sqrt{f'_{cc,200}}\ h_{ef}^{1.5}$	(6.5)
Zamora et al. (2003)	CIP headed anchors for concrete (5th percentile)	$\frac{A_{Nc}}{A_{Nco}}\psi_{s,N}\ \psi_{ec,N}\ 12.6\sqrt{f'_c}\ h_{ef}^{1.5}$	(6.6)
ACI 530-05	Headed anchors for masonry	$0.33\ A_{Nc}\sqrt{f'_m}$	(6.7)
Allen et al. (2000) "5-X" framework	Headed anchors for masonry	$\frac{A_{Nc}}{A_{Nco}}\ 0.418 \cdot \mathrm{k}\sqrt{f'_m}\ h_{ef}^{1.5}$	(6.8)

The first models were developed for headed anchors using plasticity type models as per ACI 349 (1990) (see Eq. (6.2) in Table 6.1), which idealizes a maximum tensile stress of $f_t = 4\sqrt{f'_c} = 0.96\sqrt{f'_{cc,200}}$, distributed uniformly on the projected area of a 45° angle stress cone radiating from the free end of the anchor towards the loaded end (Farrow & Klingner, 1995). When the anchor is located near a free edge or is included in a group of anchors where the cone intersects the edge or overlaps another cone, the reduction in tensile capacity is accounted for with the introduction of the geometric factor $\frac{A_{Nc}}{A_{Nco}}$. This ratio between the actual projected area of anchor or anchor group (A_{Nc}) and the projected area of one anchor not limited by edge or spacing influences (A_{Nco}) is present in all formulations developed over the years (see Table 6.1). The variable angle cone method (VAC method) is similar to the method proposed by the ACI

349 (1990), with the exception that the maximum tensile stress is distributed uniformly on the projected area of a variable cone angle θ. Both methods consider the dependence of the tensile capacity on the effective embedment length — measured from the free end of the anchor to the loaded end (h_{ef}) — and on the diameter of anchor head, taken as anchor diameter (d) (Farrow & Klingner, 1995). Cheok & Phan (1998) mentioned that Eligehausen et al. (1984a, 1984b), after performing several pullout tests on resin anchors, developed a similar expression for cone failure of adhesive anchors, only applicable for embedment lengths equal or smaller than $9d$ (see Eq. (6.4) in Table 6.1).

Several authors compared the previous design models with experimental data and demonstrated that they predict non-conservative estimates of the capacity for typical embedment lengths due to the assumption that the failure area increases with d^2 (Ballarini et al., 1986; Eligehausen & Sawade, 1989; Fuchs et al., 1995; Piccinin et al., 2010). Same authors denoted the importance of the size effect and consequently, developed prediction equations for the failure load using linear elastic fracture mechanics (LEFM). With the application of LEFM, the nominal stress at failure decreases in proportion to $1/\sqrt{h_{ef}}$ and failure load increases with $h_{ef}^{1.5}$. Fuchs et al. (1995) introduced this methodology through the concrete capacity design (CCD) method and determined experimentally the value of k_c for different types of anchors, which relates fracture toughness with the tensile strength, see Eq. (6.9).

$$N_{n,c} = k_c \sqrt{f_c}\, h_e^{1.5} \tag{6.9}$$

The value of k_c is obtained empirically, thus varying with units, with the type of anchor used, substrate, and other characteristics of the specimen that can affect failure. For cast-in-place headed anchors in concrete, the recommended k_c is 15.5 (for calculations in SI units and also for $f'_{cc,200}$), as seen in Eq. (6.5)). The CCD idealizes the failure cone as being a pyramid at 35° radiating from the free end of the anchor to the loaded end. Consequently, the projected area is a square instead of a circle, as adopted for ACI 349 (1990), which facilitates the calculation of overlapping areas and reduced areas due to free edge effects. The CCD method combines the physical visualization of the cone failure with the accuracy of the ψ-method, which reflects the influence of certain parameters by applying factors to the strength of a single anchor. These factors account for geometric alterations on the projection area (free edge, spacing between anchors, etc.), the influence of edges of the concrete member on the distribution of stresses in the concrete ($\psi_{s,N}$), and for the group effect when different tension loads are imposed to the individual anchors of a group — eccentricity ($\psi_{ec,N}$), see Eq. (6.5) in Table 6.1 for a summary. Zamora et al. (2003) determined experimentally the most suitable k_c

(as 12.6) for headed grouted anchors, as presented in Eq. (6.6) in Table 6.1. This method is adopted by *fib* Bulletin No. 58 (CEB, 2011), EOTA-TR 029 (2007), and ACI 318 (ACI 318, 2005), to determine the design value of the concrete conical failure, including for bonded anchors.

Design methods for masonry anchors are far less developed compared to design of concrete anchors, but there are guidelines in ACI 530 (ACI 530, 2005), Allen et al. (2000), and Arifovic & Nielsen (2004), to compute the nominal strength corresponding to brick masonry breakout of headed anchors. Eq. (6.7) in Table 6.1 is based on the plasticity theory and idealizes a maximum tensile stress of $f_t = 0.33\sqrt{f'_m}$ (f'_m is the nominal compressive strength in MPa for masonry), distributed uniformly on the projected area of a 45° angle stress cone radiating from the free end of the anchor towards the loaded end. The issue related to overlapped areas of adjacent anchors is accounted for in A_{Nc}, by subtracting one-half of the overlapping area in the projected area of each anchor, A_{pt}. The approach is conservative when accounting for the influence of the edges of the masonry member, since it considers for A_{pt} the minimum of the two areas: $\pi\, h_{ef}^2$ (calculated from the effective embedment length) and $\pi\, c_a^2$ (calculated from the minor edge distance, c_a).

Tomaževič (1999), considering past experimental campaigns to assess existing stone masonry mechanical properties, proposes the following two ranges of characteristic values or the tensile strength, f_{tk}, and the compressive strength, f_{mk}, respectively: 0.08 MPa – 0.21 MPa and 0.3 MPa – 0.9 MPa (average values can be estimated, by multiplying f_{tk} and f_{mk} by 1.2). In order to maintain the philosophy of all formulations, with respect to the estimation of f_t through f_m, one used the previous intervals and estimated one interval, $[0.08; 0.33]\sqrt{f_m}$, which reflects that relationship. The upper boundary of the interval coincides with the value present in Eq. (6.7) in Table 6.1, which indicates that the expression might lead to overestimation of the tensile capacity of anchors installed in historical masonry. In addition, the latter mentioned equation should take into account overlapping areas of adjacent anchors and distances to the edge of the masonry element similarly to the concrete expressions, in order to better quantify the projected area. These recommendations are reflected in Eq. (6.10).

$$\frac{A_{Nc}}{A_{Nco}} A_{Nco} \cdot f_t = \frac{A_{Nc}}{A_{Nco}}\, k_1 A_{Nco} \sqrt{f'_m} \qquad \text{with} \qquad 0.08 \leq k_1 \leq 0.33 \tag{6.10}$$

From pullout tests of bonded anchors installed in clay brick masonry, Arifovic & Nielsen (2004) calibrated an equation, also based on the plasticity theory, that turned out to be equal to the expression proposed in the ACI 349-90, but with f_m instead of $f'_{cc,200}$. Allen et al. (2000) discuss the provisions for the calculation of the design tensile strength of headed anchors, noting

the well-established plasticity approach presented previously, but also introducing a LEFM approach, similar to the one already adopted for the design of anchorage in concrete, as shown in Eq. (6.8) in Table 6.1. The factor k_c has an equivalent $0.418k$, and k can take values from 10 to 24, depending if it is a cast-in-plane or post-installed anchor and the type of masonry (clay bricks or concrete blocks). When used for design, the previous equations are multiplied by a strength reduction factor, ϕ, of 0.5, which is specific for masonry breakout, as suggested by ACI 530 (ACI 530, 2005). All the formulations presented concern uncracked concrete and masonry. Design for cracked concrete requires the application of an additional reduction factor. On the contrary, ACI 318 (ACI 318, 2005) provides expressions that determine the basic concrete breakout strength in cracked concrete, which can be affected by a factor reflecting uncracked state. Cracks affect anchor-to-concrete load transfer, so typical force-displacement curves in cracked concrete present lower strength and stiffness. The reduction of concrete failure cone load varies with the type of anchor, ranging from 25% (headed and undercut anchors) to 35% (torque-controlled expansion anchors) when located in or close to cracks with a width from 0.3 to 0.4 mm (Eligehausen & Balogh, 1995). Since the transfer load mechanism is similar for anchors in masonry, a reduction in load and stiffness is also expected. When designing anchors for seismic loads, concrete or masonry should always be considered cracked, see fib Bulletin No.58 (CEB, 2011). Several studies mentioned by Cheok & Phan (1998) suggest that the tensile capacity of anchors is reduced from 10 % to 20 %, when subjected to a cyclic or dynamic action.

6.2.1.3 Bond failure mode (FM3)

There are two types of bond stress models: the elastic bond stress models and the uniform bond stress models. The latter is more appropriate for strength design methods and suitable for shallow embedments (prone to cone failure) as well as deeper embedments (prone to combined cone/bond failure). It also has the advantage of being more user friendly (Cook et al., 1998). Therefore, is also recommended by the *fib* Bulletin No.58 (CEB, 2011) and EOTA-TR 029 (2007).

The uniform bond stress model is used to describe the behavior of the interfaces steel rod/grout (see Eq. (6.11) in Table 6.2) and grout/concrete (see Eq.(6.12) in Table 6.2). Both depend on the embedment length, h_e, but take into consideration different diameters — d and d_0 — and bond strengths — τ' and τ'_0 — where d is the steel rod diameter (mm), d_0 the hole diameter (mm), τ' the nominal value for the uniform bond stress (MPa) at the interface steel rod/grout and τ'_0 the nominal value for the uniform bond stress (MPa) at the grout/concrete.

Eq. (6.11) in Table 6.2, related to interface for adhesive anchors, already takes into consideration the factor Ψ_c, which reflects the influence of the concrete strength on the adhesive properties. Zamora et al. (2003) confirmed that for headed grouted anchors, the use of the hole diameter with the corresponding bonding stress is more appropriate than the steel rod diameter, since d_0 is usually 50% or more larger than d. For injection anchors in masonry this would be the case, thus the consideration of the hypothesis of applying this formulation to the current study. The disadvantage of this method is the lack of information regarding the bond strength of the interface, which needs to be available in the product approval standard. Cook & Konz (2001) stated that bond strength is affected by internal factors (chemical formulation, manufacturing processes, and packaging) that are beyond the control of the designer and external factors within the control of the designer, such as the condition of the drilled hole during installation: (1) cleaned, damp, or wet; (2) the strength and type of coarse aggregate of the concrete base material; (3) short-term adhesive curing; and (4) loading at an elevated temperature. The condition of the drilled hole during installation, curing of the grout, and typology of masonry also have influence on the performance of injected anchors. To take this into account, during design the previous equations are multiplied by a strength reduction factor, ϕ, of 0.65, which is specific for pullout failure, as suggested by ACI 530 (ACI 530, 2005).

Algeri et al. (2010) performed a series of monotonic pullout tests on injection anchors with sleeves (similar to the ones used in the pullout tests described in Chapter 4), installed in different types of masonry walls. The tests varied the bulb shape of the anchor, embedment length, and grout type (cement or lime based). The nominal bond strength of the interface grout/masonry was characterized and the following values were obtained for different substrates: 1.34 MPa for solid limestone; 0.53 MPa for Credaro limestone; and 1.64 MPa for Zorzino limestone. These values are considerably lower, when compared to bond strength values at the (cementitious) grout/concrete interface found by Zamora et al. (2003).

Table 6.2 Summary of methods to determine the nominal tensile load for bond failure

Method	**Type of anchors**	**Bond failure - N_b (N)**	
Cook et al. (1998)	Single adhesive anchor in concrete	$\Psi_c \, \tau' \pi \, d \, h_{ef}$	(6.11)
Zamora et al. (2003)	Single grouted anchor in concrete	$\tau_0' \, \pi \, d_0 \, h_{ef}$	(6.12)

6.2.1.4 Combined cone-bond failure mode (FM1+FM3)

The combined cone-bond failure model results from the necessity to express analytically what was observed in experimental tests with adhesive anchors (Cook et al., 1998), which was the formation of a masonry cone close to the loaded end of the anchor combined with sliding of the remaining anchorage length not covered by the cone. Its complexity relies on the determination of the transition point between failure models. Cook et al. (1998) proposed combining the two contributions, masonry cone breakout and bond failure, in a two terms equation, with the cone depth, h_c, corresponding to the minimum load to produce failure, see Eq. (6.13) in Table 6.3 for a single anchor. This method combines Eq. (6.4) in Table 6.1 developed by Eligehausen et al. (1984a, 1984b) for concrete cone failure, with the uniform bond stress model described by Eq. (6.11) in Table 6.2. The depth h_c depends on the diameter of the anchor, the bond strength at the interface, and the compressive strength of the masonry, and the balance between these variables determines if there is only the formation of the masonry cone ($h_{ef} \leq h_c$) or a combined failure ($h_{ef} > h_c$). For situations, where the cone depth h_c is very small, one can assume that there is only bond failure.

Table 6.3 Summary of methods to determine the nominal tensile load for combined cone-bond failure, N_{cb}

Method	Type of anchor	Combined cone-bond failure - N_{cb} (N)	
Cook et al. (1998)	Adhesive anchors for concrete – Single anchor	$0.85\, h_c^2 \sqrt{f_{cc,200}} + \pi\, \tau\, d\, (h_{ef} - h_c)$ $, if\ h_{ef} > h_c\ and\ h_c = \frac{\tau \pi d}{1.7\sqrt{f_{cc,200}}}$	(6.13)
Proposal	Grouted anchors for historic masonry – Two parallel anchors	$A_{Nc}(h_c) \cdot \mathrm{k}\sqrt{f_m} + 2\pi \cdot d_0 \cdot \tau_0 \cdot (h_{ef} - h_c)$ $, if\ 0 \leq h_c \leq h_{ef}\ , s \leq 2h_c\ and\ with$ $h_c = \frac{\pi \cdot d_0 \cdot \tau_0 - s \cdot k\sqrt{f_m}}{4 \cdot k\sqrt{f_m}}$	(6.14)

Since this was the failure mode observed experimentally, one decided to propose an equation that could express this combined effect for a pair of parallel anchors. Following the same principles, the difficult challenge is to calculate h_c, considering that it can be overlapping between projected areas. Determining the cone depth, h_c, is not straightforward and involves elaborate derivatives, if the combined expression takes into account circular projected areas. For design purposes, one proposes the estimation of h_c considering projected quadrangular areas, resultant from a pyramidal masonry failure at 45°. Then, for the calculation of the masonry cone capacity one can use A_{Nc}, resulting from circular projection areas. The expressions for the calculation of the latter is in Annex 3. The cone depth h_c continues to depend on the parameters mentioned previously, but now it also varies with the distance *s*

between anchors. In fact, the inequality $s \leq 2h_c$ has to be verified, so that there is overlapping of projection areas. Mathematically, h_c can result negative or larger than the effective embedment length h_{ef}, but physically h_c has to respect the condition $0 \leq h_c \leq h_{ef}$. If negative, h_c takes the value zero and only bond failure occurs. If h_c is higher than h_{ef}, h_c takes the value of h_{ef} and only masonry breakout failure occurs. When used for design, each term of Eqs. (6.13) and (6.14) in Table 6.3 should be multiplied by the appropriate strength reduction factor, ϕ, which would be 0.5 for the masonry breakout contribution and 0.65 for the bond failure one, as suggested by ACI 530 (ACI 530, 2005).

6.2.1.5 Application to the experimental results

A comparison between the experimental results and the most appropriate existing strength prediction formulas for pullout capacity was performed, which is evidenced in Table 6.4 and Figure 6.2. The tensile strength of the masonry, if calculated from $0.33\sqrt{f'_m}$ is in this case equal to 0.44 MPa (f'_m = 1.8 MPa). This value is 3.14 times higher than the average value obtained from the diagonal compression tests performed on masonry wallets representative of the walls' masonry, 0.14 MPa. This confirms what was already discussed previously in subsection 6.2.1.2 that k_1 equal to 0.33 is excessive and a lower value is required for a more realistic approach. For this particular case, a tensile strength of 0.14 MPa corresponds approximately to k_1 equal to 0.1 ($0.1\sqrt{f_m}$), which falls within the proposed range, closer to the lower bound.

For comparison purposes, the estimation using Eq. (6.7) (ACI 530 (2005b)) was applied using $0.33\sqrt{f'_m}$ for the tensile strength. When applying the updated version of the latter equation, which is Eq. (6.10), a value equal to 0.14 MPa ($0.1\sqrt{f_m}$) was then applied. The full embedment length was assumed as effective and the value used for calculation was the average of embedment lengths measured on the specimens (see Chapter 4), equal to 333 mm. Remaining two geometric characteristics took the following values: d_0 = 50 mm and s = 300 mm. In the bond models, pullout strength was determined from three values of τ_0, two of them proposed by Algeri et al. (2010) – 0.53 MPa (minimum) and 1.64 MPa (maximum) – and a third one equal to 0.90 MPa, estimated from the pullout tests carried out at the top of the wall. Following the experimental evidences, the cone breakout models were used to predict the tensile capacity obtained on the tests performed at the top of the wall, N_{exp}^{T} and the bond failure models were used to estimate the tensile capacity for the tests at the bottom of the wall, N_{exp}^{B}. The combined cone-bond model proposed previously should provide the better approximation to the experimental results, consequently its validity against the both experimental values is discussed.

The Eq. (6.14) of the proposed combined cone-bond model and the value of N_{exp}^{T}, 76.8 kN were used, to estimate h_c and respective τ_0. These parameters allowed a better understanding of the validity of the model, by assessing if they are within reasonable intervals and by comparing them to the ones observed experimentally. The values obtained were, respectively, 177.4 mm and 0.90 MPa. The first corresponds to 53% of h_{ef}, which is close to the minimum cone depth obtained experimentally (approximately 180 mm), and the second is within the values determined by Algeri et al. (2010), indicating that the proposed combined cone-bond model for parallel pairs of injection anchors in historical masonry performed adequately for the tests at the top of wall. Using the newly estimated τ_0 and assuming a minimum shallow cone depth of approximately 50 mm (as observed in a number of specimens), the proposed model predicted a pullout capacity equal to 88.9 kN (error of 18 % to N_{exp}^{B}, 107.9 kN), if a factor of 2 was applied to f_t, reflecting the confinement at the base of the wall. Further analysis is needed, to understand if the confinement effect at the base of the masonry wall or the compressive state of the wall can affect the f_t of the masonry.

Table 6.4 Comparison between predicted tensile capacities and experimental values.

Prediction Equation	**Masonry cone breakout**		**Bond failure**		**Combined cone-bond failure**	
	N_c	N_c/N_{exp}^{T}	N_b	N_b/N_{exp}^{B}	N_{cb}	N_{cb}/N_{exp}
ACI 530-05	268.8	3.5	-	-	-	-
Allen et al. (2000)/ Zamora et al. (2003)	51.8 (k = 14)	0.7	55.4 (τ = 0.53)	0.5	-	-
	88.9 (k = 24)	1.2	94.2 (τ = 0.90)	0.9	-	-
	-	-	171.6 (τ = 1.64)	1.6	-	-
Arifovic & Nielsen (2004)	248.9	3.2	-	-	-	-
Proposal	85.0	1.1	-	-	91.1 (Bot.) 76.7 (Top)	0.8 1.0

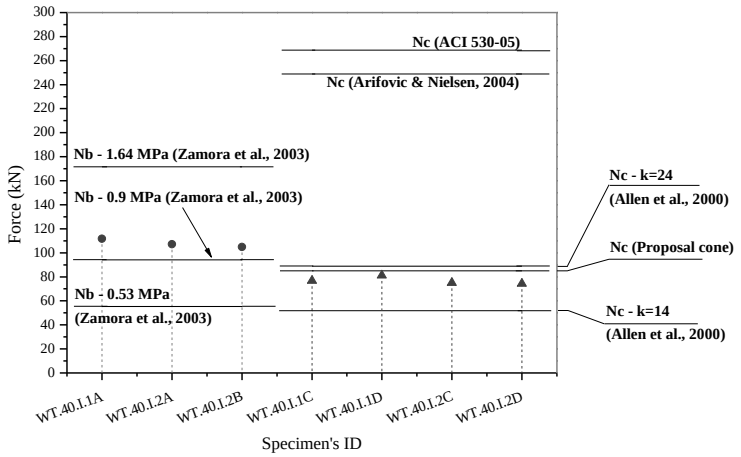

Figure 6.2 Comparison between experimental results and behavioral models.

Since the tests at the bottom of the wall had a contribution of the interface grout/masonry much higher than the one of the masonry cone breakout (see Chapter 4), one used Eq. (6.12) of Zamora et al. (2003) for uniform bond model and a value of τ_0 equal to 0.9 MPa to predict the pullout capacity, resulting a value with an error of 13 % relative to N_{exp}^{B} (see Table 6.4). It is a good approximation that clearly evidences that bond failure at the grout/masonry interface played a primordial role on the failure of the tests at the bottom part of the wall. The two other values of τ_0 proposed by Algeri et al. (2010), 0.53 MPa and 1.64 MPa, underestimate and overestimate, respectively, the pullout capacity associated with bond failure, as shown in Figure 6.2.

For the application of CCD related methods like the ones proposed by Zamora et al. (2003) and Allen et al. (2000), the values 14 and 24 were assumed for *k* in Eq. (6.8). They refer to cast-in-place headed bolts in concrete and clay masonry, respectively. The first provides the lowest value for the tensile capacity of all models, being very conservative, while the second provides a good approximation to N_{exp}^{T}, which had a higher contribution of the masonry cone breakout (see Table 6.4). Since this type of model is considered the most appropriate approach for estimating the tensile capacity related to concrete or masonry breakout (CEB, 1994; Zamora et al., 2003), greater effort, experimental or numerical, needs to be done to correctly estimate the coefficient *k*.

The tensile capacity for cone failure calculated with the ACI 530 (2005b) equation is overestimating N_{exp}^{T} by a factor of 3.5, which is considerably high and confirms the necessity to adequate the value of k_1 to the type of masonry. Arifovic & Nielsen (2004), Eq. (6.2), also predicts a high value for N_{exp}^{T}, close to the one of ACI 530 (2005b), possibly because it was also calibrated for new clay brick masonry. On the other hand, the adapted Eq. (6.10) predicts a pullout force equal to 85 kN, which slightly overestimates N_{exp}^{T} (error = 11%),

probably because is considering the entire embedment length as effective (see Table 6.4 and Figure 6.2).

In general, one can conclude that if the empirical coefficients k, k_1 and k_c affecting the pullout capacities are not appropriate, the predictions will not express the experimental values. Studies have proven that significant amount of tests allow good calibrations of these coefficients (Farrow & Klingner, 1995; Cook et al., 1998). Especially for CCD related approaches, assuming a pyramid with an opening angle of 55° (90°-35°), increases significantly the critical edge distance ($c_a = 1.5h_{ef}$), which consequently affects greatly the ratio A_{Nc}/A_{Nco} when edge distance is below that value. For the case of parallel pairs of anchors, there is also the influence of distance s. Figure 6.3 reflects the impact of distance s and edge distance c_a on the ratio A_{Nc}/A_{Nco}, which accounts for the effective number of anchors. The two variables were introduced in the calculation of the areas, as functions of h_{ef} affected by coefficients C_s and C_c, respectively. The situation where critical edge distance is respected is represented by the line with a C_c value of 1.5. One can confirm that for no intersecting projected areas ($C_s = 3$), the value of A_{Nc}/A_{Nco} is equal to 2 anchors, while for C_s values tending to zero, the A_{Nc}/A_{Nco} ratio tends to one, which suggests that for certain distances s, no longer compensates to have two anchors. This situation only gets aggravated with decreasing edge distance (decreasing C_c). In extreme cases, in spite of having two anchors installed, the effective capacity is equivalent to less than one anchor (see Figure 6.3).

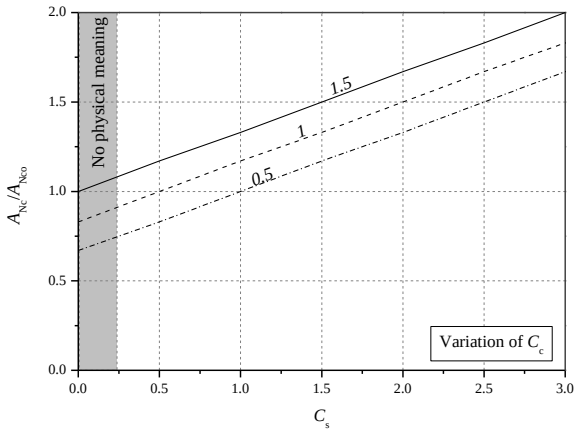

Figure 6.3 Influence of edge distance and pair effect in the effective number of anchors, according to the CCD approach.

Considering the proposed combined cone-bond failure model, expressed by Eq. (6.14), a parametric sensitivity to analyze h_c was performed to better understand the influence of d_0, f_t, τ_0 and s. Figure 6.4a represents the variability of h_c to different values of f_t and d_0, with constants s and τ_0, clearly showing that for high values of f_t the formation of the cone is less prone to happen. Injection anchors with the same geometric characteristics, installed in different parts

of the wall or subjected to different boundary conditions or other factors that might affect the tensile strength, can present different cone depths, and consequently different failure modes and tensile capacities, as verified for tests performed at the top and bottom of the walls. The relation expressed in Figure 6.4a, is also valid for variation of τ_0 instead of d_0. Figure 6.4b represents the variability of h_c to different values of f_t and s, with constants d_0 and τ_0, demonstrating that s has an impact on h_c lower than the other parameters. In fact, for lower values of f_t, the contribution of s to h_c is practically negligible.

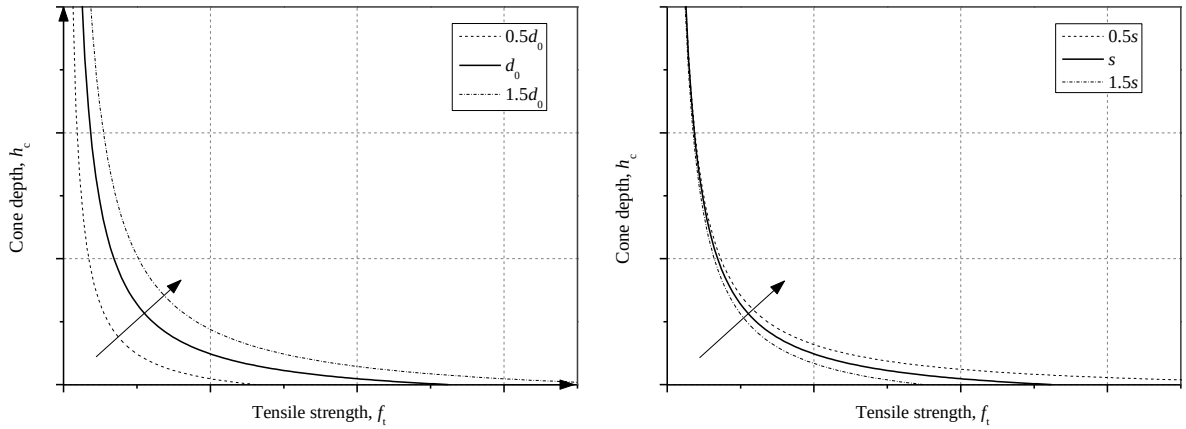

(a)

Figure 6.4 Parametric sensitivity of h_c: (a) to f_t and d_0 (also valid for τ_0); and (b) to f_t and s.

6.2.2 Wall-to-floor connections

The mechanism associated with the wall-to-floor connections is assumed to work basically in series, from the timber joist to the masonry wall. Minimum capacities need to be assured, so that the chain of effects is not interrupted. If that happens, failure occurs. Taking into consideration the failure modes observed experimentally for the wall-to-floor connections, one suggests a number of approaches that allows the estimation of the measured pullout forces. These expressions were also applied to the experimental results allowing a better understanding on why certain failure mechanisms were more prominent than others. For the calculations, mean values of material properties were used (see Chapter 3).

6.2.2.1 Failure of the nailed connection between joist and wall-plate

The strength capacity of the nailed connection between joist and wall-plate in all wall-to-floor specimens was determined according to Johansen's theory (Johansen, 1949), which is the base of the EC5 method (CEN/TC 250/SC5, 2004) for design of connections with metal fasteners. The load-carrying capacity of the connection is the minimum capacity of all failure modes possible. Since it is a timber-to-timber single shear connection, the possible failure modes are six, and they depend on the following variables: (1) diameter of the nail;

(2) penetration depth; (3) embedment strength in timber; (4) nail yield moment; (5) axial withdrawal capacity of the nail; and (6) position and distance between nails.

The configuration of the connection is presented in Chapter 5, and the nails used were typical of flooring in existent buildings. This type of nail is round and smooth, and has a shank diameter of 3.4 mm for a length of 75 mm. The mean capacity estimated, using EC5 – Section 8 (CEN/TC 250/SC5, 2004), was approximately 3.5 kN and corresponds to failure type *f* in section 8.2.2 of EC5 (CEN/TC 250/SC5, 2004)), which is consistent with the plasticity of the nails observed experimentally.

6.2.2.2 Masonry cone breakout

The principles expressed in subsection 6.2.1.2 for the masonry cone breakout of headed anchors are valid for tie rods with anchor plates. Therefore Eq. (6.10) also applies to this case. Since the anchor plate is quadrangular, the singular projected area was estimated (see Equation (6.15)) based on considerations commonly made for punching shear in concrete (see Figure 6.5).

$$A_{Nc} = b^2 + 4 \cdot b \cdot t_w \cdot \tan\alpha + \pi(t_w \cdot \tan\alpha)^2 \tag{6.15}$$

where b is the anchor plate width, t_w is the thickness of the wall, and θ is the opening angle. For the 400 mm walls, A_{Nc} was completely inside the wall, while for the 600 mm walls, A_{Nc} was limited horizontally to one side by edge distance and to the other by the neighboring testing specimen. Thus, A_{Nc} of the latter was decreased by 27%. To balance this effect, part of the reaction of the self-balanced frame was redirected to A_{Nc}. Considering an angle of 45°, the pullout masonry breakout capacity for each thickness of the wall, 400 mm and 600 mm is respectively, 113.9 kN and 167.6 kN. For design purposes, this value should be affected by a reduction factor of 0.5, as suggested by ACI 530 (ACI 530, 2005).

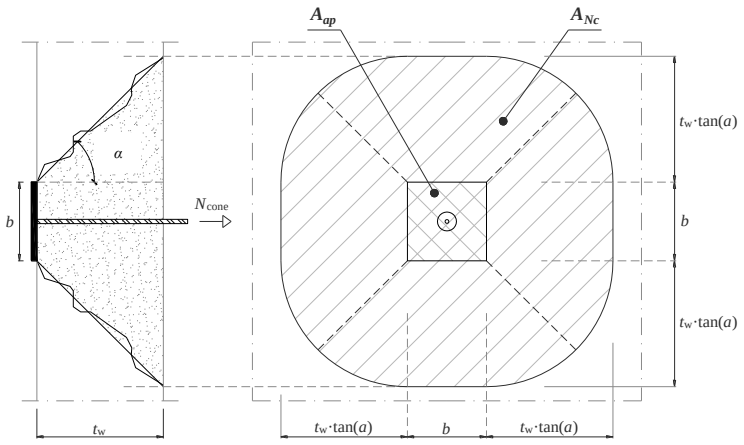

Figure 6.5 Projection of masonry cone breakout area.

6.2.2.3 Crushing of masonry under the anchor plate (FM2)

From the damage survey, no cracks were observed on the back face of masonry wall, but permanent displacements were measured at the anchor plate and there were small cracks on the layer of fast-curing mortar, placed between the anchor plate and the masonry wall. This new layer of mortar has a compressive strength higher than the masonry itself, 4 MPa (> 1.8 MPa), and it distributes the stresses to the wall through an area larger than the surface of the anchor plate, which leads to the absence of cracks on the masonry wall. Therefore, Equation (6.16) allows the estimation of the nominal strength associated with crushing of the new layer of mortar under the anchor plate.

$$N_{cap} = A_{ap} \times f_{cm} = b^2 \times f_{cm} \tag{6.16}$$

In current applications, the fast-curing mortar can be substituted by a reinforced layer of mortar, as long as its area is wide enough to distribute stresses to the wall without causing permanent damage. One can assume the same design reduction factor as for masonry cone breakout, which is 0.5.

6.2.2.4 Failure of the bolted connection between steel angle and joist (FM3)

Again the most widely used method to estimate the load-carrying capacity of bolted connections between timber and steel is the Johansen's theory (Johansen, 1949) adopted in EC5 – Section 8 (CEN/TC 250/SC5, 2004). The minimum load-carrying capacity corresponds to the minimum one associated with different failure modes, which are dependent on the same variables stated for the nailed connection, in subsection 6.2.2.1 but now for bolts.

The single shear timber-to-steel connection is ensured by four AISI 304 (A2) bolts ϕ10 mm, running throughout the entire height of the cross-section of the joist, 180 mm. The steel angle's leg is 6 mm thick, which is in the interval between a half and a whole diameter of the bolts, therefore the load-carrying capacity of the connection has to be interpolated from values obtained for connections with thin (equal to or less than half diameter) and thick (equal to or greater than whole diameter) steel plates.

In this particular case, the shear behavior of the bolted connection has the beneficial contribution of a "lever" effect on the bolts caused by rotation of the steel angle. EC5 – Section 8 (CEN/TC 250/SC5, 2004) considers a similar effect in the quantification of the shear stress – the rope effect – which in this case does not reflect the phenomenon observed experimentally. Thus, the shear capacity was estimated without this effect, excluding the F_{ax} contribution, obtaining the value of 10.1 kN per bolt, per row. It results from the interpolation of failure

modes *b* and *d*, being closer to *b*, which is according to what was observed experimentally (formation of a plastic hinge on the bolt and partial crushing of the timber). To this value, an addend should be summed to represent the "lever" effect, F_{lev}, which was not quantified. This contribution to capacity should reflect the tensile strength of the bolts and the bearing strength of the timber under the plate, on the opposite side of the timber element. The summation can be then multiplied by the effective number of bolts in a row (approximately 1.6) and the number of rows (2). The total load-carrying capacity of the connection should be 32.8 kN + F_{lev} (multiplied by the two factors previously mentioned).

6.2.2.5 Yielding of the steel angle (FM3)

The experimental value of the pullout force of the strengthened connections resulted from failure at the bolted connection between steel angle and timber joist, with the steel angle and tie already yielding. It means that the bending moment at this section of the connection is high enough to cause yielding of the steel components but not enough to take them to failure. From the measurements of the LVDT placed in position 6 (see Figure 4.8b), at the front end of the steel tie, it was possible to estimate when the opening of the steel angle started. This moment was established as the point when displacement at position 6 reverts, equivalent to a snap-back effect. For WF.40.A and WF.60.A specimens, the value of the force corresponding to the described moment was 73.9 kN (CoV of 5%) and 71.7 kN (CoV of 5%), respectively. Since the theoretical value is dependent solely on the geometry of the steel angle and the steel mechanical properties, the proximity between the two determined values is considered a good indication that they can be used to estimate the yield capacity of the steel angle. Therefore, the yield limit of the steel angle should be close to the average of all specimens, 72.8 kN (CoV of 5%). The failure capacity is not only above this limit, as it is superior to the minimum F_{max} (93.1 kN) obtained experimentally.

6.2.2.6 Failure of the steel tie (FM4)

From the damage observed on tested steel ties, it was possible to detect that it was concentrated on the section in contact with the half-spherical hinge, placed on the steel angle (see Figure 6.6). That section in particular is subjected to an axial force and a bending moment transmitted by the steel angle, which decreases the maximum pullout force to be sustained by the steel tie. Based on the experimental results, one verified that there is rotation of the hinge to a certain extent, but towards the end of the test, the contact between steel tie and the cup of the hinge forces the first to bend. The axial force at that section is the projection at 15° of the

pullout force at the joist, but the bending moment is particularly difficult to quantify. The tensile capacity value for the tie used (ϕ16 mm, steel grade of 8.8) is equal to 160.8 kN, if only the axial load is considered. If bending moment is included, this value decreases.

6.2.2.7 Comparison to the experimental pullout capacity

All the load-carrying capacities estimated allowed the establishment of the boundaries of each possible failure mode and they are presented in Figure 6.6. For the unstrengthened wall-to-floor connections, pullout of the nails was the failure mode observed in all tests. It also occurs for the strengthened wall-to-floor connections at very early stages of the tests. The mean capacity estimated for the load-carrying capacity of the nailed connections was approximately 3.5 kN, which is 75 % of the pullout capacity determined experimentally for the unstrengthened connections. In spite of being a conservative estimate, the failure mode correspondent to the load-carrying capacity estimated — failure *f* in section 8.2.2 of EC5 (CEN/TC 250/SC5, 2004) — is consistent with the plasticity of the nails observed experimentally.

Regarding the strengthened connections, the different load estimations suggest that the lowest one is associated with failure of the bolted connection, as observed experimentally. However, the estimated load-carrying capacity of the bolted connection is dependent on the correct quantification of F_{lev}. Considering the experimental results, this contribution should be responsible for the remaining 62.8 kN, necessary to reach an average value of 95.7 kN (average load-carrying capacity of both WF.40.A and WF.60.A specimens), which constitutes a significant portion, approximately 65 %.

One should refer that possibly due to the redistribution of stresses as the connection plasticizes and the contribution of shear strengths due to friction in the interfaces between timber elements, and these and the wall, the overall analytical capacity should increase. The cumulative damage occurring throughout the test on the different elements of the connection has an impact on the load-carrying capacity that is not reflected on the isolated analysis of the contribution of each component.

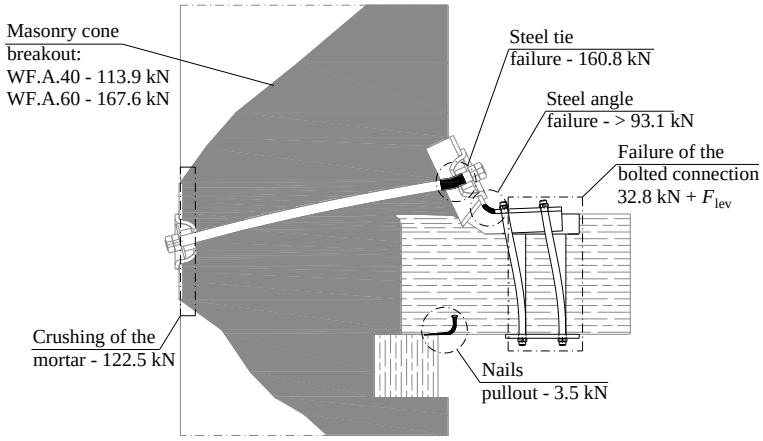

Figure 6.6 Estimated load-carrying capacities for different types of failure modes.

6.3 IDEALIZED FORCE-DISPLACEMENT CURVES

On the base of application of simplified theoretical approaches and numerical analysis is the idealization of elements' behavior models. They can be defined in terms of stress-strain, force-displacement, moment-curvature or bond slip relationships and be expressed by simple analytical functions. In this particular case, the force-displacement curves were expressed by analytical functions obtained empirically. The first step towards the development of an element behavior model is the definition of its idealized envelope curve, and a second step is to express the hysteretic rules, describing its post-elastic loading-unloading cycles and, consequently, its energy dissipation capabilities.

The idealized curves were developed for all sets of tests: the wall-to-timber framed connections strengthened with injection anchors, and the unstrengthened and strengthened wall-to-floor connections. The hysteretic rules will be a part to be developed in future work. Choosing an adequate mechanical model depends mainly on how the stress-strain relationship develops between these three limits states: yield; maximum stress; and ultimate strain (fracture). There is a variety of behaviors, but the stress-strain relationship is commonly considered linear elastic, until yielding. This limit also marks the start of permanent deformation. For most elements, stress keeps increasing as deformation continues, until the maximum stress is reached, being this phenomenon called strain-hardening. After the maximum stress and before fracture, the element can evidence strain-softening with or without a residual stress branch. A linear elastic model can be sufficient, if permanent strain is small. If not, and if one wants to express strain-hardening or softening, the most common approach is to use a power function. The idealized curves can have several branches, usually four at most, being two the minimum required for a nonlinear analysis – bilinear curves. Trilinear curves are recommended, when

pre- and post-cracking stiffnesses are necessary to better describe the intended behavior (CEN/TC250, 2004). Backbone curves and respective idealizations are presented next.

6.3.1 Backbone curves

The initial step towards idealized force-displacement curves is the definition of multi-linear envelopes based on the experimental curves – backbone curves. These can be determined according to the methodology suggested by ASCE/SEI 41-06 (ASCE, 2006) or the one proposed by Frumento et al. (2009), but both incorporate strength degradation due to cyclic loading. According to ASCE/SEI 41-06 (ASCE, 2006), the backbone curve of each specimen shall be defined by connecting with linear segments the intersections between the first cycle curve for the *i*-th deformation level with the second cycle curve of the $(i-1)^{th}$ deformation level, for all *i* levels. Each backbone curve shall be approximated to a multi-segmented curve, conforming to one of the types of curves provided by the standard for the definition of deformation or force-controlled actions, as shown in Figure 6.7. The final step is to average all the multi-segmented curves of all specimens, within a certain test sets, into a single multi-linear idealization. The approximation to the types of curves presented in Figure 6.7 enables simplified implementation in nonlinear procedures, and also classification of the governing actions into force or deformation-controlled. Points 1, 2 and 3 regard limits of distinct phases of the behavior of the connection. The elastic phase goes from 0 to 1, the strain hardening is comprehended between 1 and 2, and the strength degradation phase develops between 2 and 3. Curves fitting type 1 or 2, with the strain-hardening range characterized by $e \geq 2g$, correspond to ductile behavior and are deformation-controlled actions. Curves matching type 3 represent brittle or non-ductile behavior, therefore are always classified as force-controlled actions. For the deformation-controlled actions is possible to establish acceptance criteria, according to performance levels to use in nonlinear procedures.

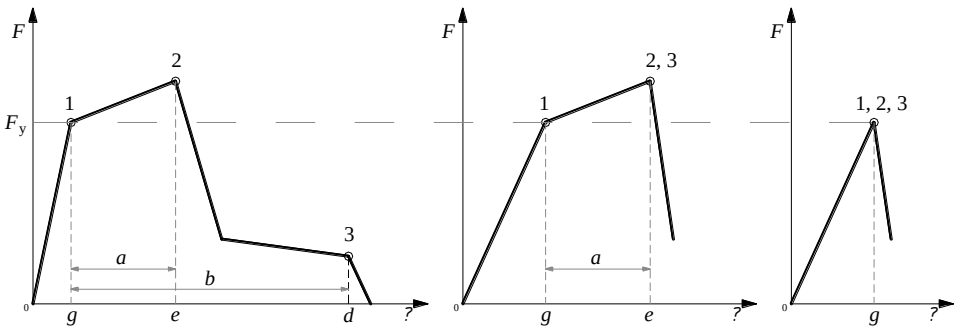

Type 1 curve *Type 2 curve* *Type 3 curve*

Figure 6.7 Component force versus deformation curves [adapted from ASCE/SEI 41-06 (ASCE, 2006)].

Frumento et al. (2009) applied a different method to determine backbone curves from experimental cyclic envelopes. The backbone curves result from connecting, with linear segments, the points of maximum force per cycle, meaning there will be a backbone curve per cycle. If the test procedure is composed by two or three cycles per displacement level, two or three backbone curves are drawn per specimen, respectively. Then, an idealized curve (simplified) is determined for each backbone, and later all the curves are "averaged" into a single equivalent curve.

The backbone curves, obtained through both methodologies, relative to the WT.40.I, WF.40.A, and WF.60.A specimens are presented in Annex 4. The idealization of these curves was achieved through the application of the balance between the total energies of the experimental and idealized curves (see Figure 6.8a). The total energy results from the integral of the force over the displacement. Some changes were made to the trilinear method, to improve its adequacy to the experimental results, but one believes that the principles applied can have a wider range of application.

The backbone curves defined according to ASCE/SEI 41-06 (ASCE, 2006) method are much more conservative, in force and in maximum displacement, than the ones defined with Frumento et al. (2009) method. With the latter method, maximum forces and displacements present decreases below 6% regarding the envelope corresponding to the first cycle, while using the ASCE/SEI 41-06 (ASCE, 2006) method that loss is in the interval of 1% to 32%. The values of force defined according to ASCE/SEI 41-06 (ASCE, 2006) method are smaller because the intersection between cycles occurs at most for the maximum level of forces attained during the second cycle, while the Frumento et al. (2009) method calculates averages forces of the two cycles. Although, the intersecting displacements for each i^{th} deformation level are higher than the ones obtained with the Frumento et al. (2009) method, the maximum displacement is smaller, since the displacement of the last displacement level is disregarded in the ASCE/SEI 41-06 (ASCE, 2006) method.

6.3.2 Multilinear idealizations

As previously mentioned, the idealized curves rely on the determination of critical limit states from the experimental data and on the definition of theoretical limits, needed for analysis simplification. The following five limits are commonly defined, three experimental and two theoretical (Tomaževič, 1999):

- Crack limit – found on the experimental envelope, when small cracks start appearing on the masonry wall and minor damage begins on the timber joist, leading to a change of stiffness in the envelope curve. It is defined by the displacement d_{cr} and the force F_{cr};
- Maximum force – found on the experimental envelope, when the maximum resistant capacity, F_{max}, is reached. The corresponding displacement is d_{Fmax};
- Maximum displacement – found on the experimental envelope, when the maximum displacement is attained during the test, d_{max}, and its corresponding capacity is, F_{dmax};
- Idealized elastic limit – found on the idealized curve and corresponds to the idealized elastic limit, obtained through total energy balance between curves. It is defined by the idealized ultimate force, F_u, and the idealized elastic displacement, d_e;
- Idealized ultimate limit – found on the idealized curve and corresponds to the idealized fracture point. It is defined by the idealized ultimate force, F_u, and the idealized ultimate displacement, d_u.

Depending on the idealization used, bilinear or trilinear, these limits can be points of the idealized curve or variables in the determination of the curve.

6.3.2.1 Bilinear curves

The bilinear curves presented approximate the experimental behavior to an elastic-perfectly plastic mechanical model, which is expressed by two linear branches, connecting the origin (zero displacement and zero force) to an idealized elastic limit, and the latter to an idealized ultimate limit (see Figure 6.8a). These two idealized limits are determined by equalizing the total energy of the experimental envelope curve, A_{env}, to the bilinear one, A_{bil}, and by the definition of three limit states — crack limit, maximum force, and maximum displacement — on the experimental force-displacement envelope (Tomaževič, 1999). As for calculation of ductility, the definition of d_e and d_u are debatable and different approaches can be applied (Park, 1989), which can have a direct impact on the values obtained for the parameters determined. The criteria chosen for these specimens are the ones considered most suitable and in agreement with suggestions gathered from existent literature (Magenes & Calvi, 1997; Tomaževič, 1999).

The definition of the crack limit should be based on mathematical models and/or on physical evidence, and it should reflect stiffness changes beyond the initial stiffness, k_0, besides enabling a good approximation between experimental and idealized curves. EC8 recommends that the first branch of the bilinear idealizations should reflect cracked stiffness, taking the denomination of effective stiffness, k_e. For bilinear capacity curves of whole buildings and shear

walls, the crack limit is commonly determined by applying a reducing factor, C_{cr}, of 60 % or 70 % to F_{max}. Following the same reason, the value of C_{cr} was determined by establishing the following three conditions: k_e should be lower than k_0; d_{cr} should be higher than d_y; and the calculated force F_u should always be lower or at most equal to F_{max}. For strengthened wall-to-floor connections, after the first clear change of stiffness in the experimental curves, the detachment of the steel angle from the timber joist, leads to an abrupt change of stiffness that should also be reflected by k_e. This can be achieved by imposing a displacement d_{cr} higher than the displacement corresponding to the detachment of the steel angle from the timber joist, d_{det}.

Force F_u is determined by Equation (6.17) and displacement, d_u, corresponding to F_u, is calculated by intersecting the experimental envelope with a function defined by $F = C_{sd} \cdot F_{max}$, where C_{sd} is a reduction coefficient that reflects a small level of capacity loss after the peak (Tomaževič, 1999). For this application, this factor takes the value of 0.8 (Park, 1989; Frumento et al., 2009). Then, the idealized bilinear curve can be expressed as presented in Equation (6.18), applied singularly to the tensile behavior (first quadrant).

$$F_u = k_e \cdot \left[d_{max} - \sqrt{d_{max}^2 - \frac{2 \cdot A_{env}}{k_e}} \right] \tag{6.17}$$

$$F(d) = \begin{cases} k_e \cdot d & for \quad 0 \le d \le d_e \\ F_u & for \quad d_e \le d \le d_u \end{cases} \tag{6.18}$$

The bilinear idealization was applied to the two types of backbone curves defined previously in section 6.3.1. For the ASCE/SEI 41-06 backbone curves, the idealization procedure is more straightforward, since there is only one curve to be determined. On the other hand, for the backbone curves determined according to Frumento et al. (2009), the bilinear idealization had to be applied to the backbone curve of each cycle per displacement level, per specimen, and an equivalent bilinear was determined, assuming d_u as the lowest of all cycles and the remaining parameters as the average of all cycles, as shown in Figure 6.8b. Thus, including a direct contribution of cyclic degradation on the idealized curve, similarly to what ASCE/SEI 41-06 (ASCE, 2006) recommends by intersecting the curves of the first and second cycle of consecutive steps. One needs to bear in mind that force and stiffness degradation, due to repetitive cyclic demand, already has an indirect impact on the envelope curve of the first cycle. For tests with several cycles per displacement level, and for specimens with high degradation, the "averaging" of several envelopes might become unrealistic. An alternative option is to stop

averaging the curves after a certain number of cycles or to introduce a weighting factor to the average, decreasing importance from the first cycle to the last one.

This type of curves was not developed for the wall-to-timber elements connections strengthened with injection anchors, because the shape of the experimental envelopes, particularly the ones from the tests performed at the bottom, would not allow a good approximation to the idealized curve. Therefore, was only applied to the backbone curves of wall-to-floor connections.

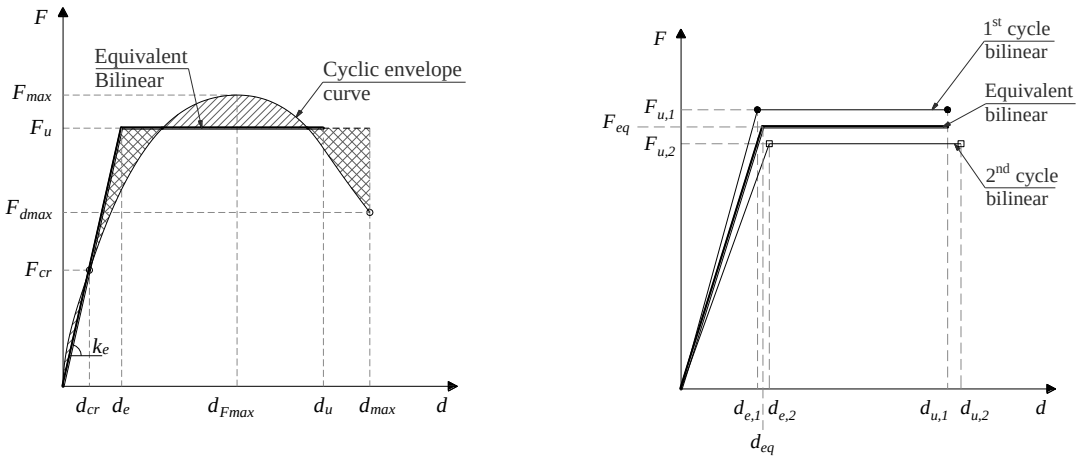

(a) (b)

Figure 6.8 (a) Bilinear idealization; and (b) Definition of the equivalent (adapted from Frumento et al., 2009).

6.3.2.2 Trilinear curves

As the name suggests, this type of curve is defined by three linear branches, and is commonly applied when there is a need to improve the pre- and post-peak behavior of the idealizations. Tomaževič (1999) suggests a simpler approach to the trilinear curve that does not require energy balance, being the great challenge the determination of k_e, as for the bilinear curves. The trilinear curve is defined by linear segments connecting four consecutive points that belong to the experimental backbone curve: the origin; the crack limit; the maximum force limit; and the maximum displacement limit. However, the last branch as the slope defined by the latter two limits, but it is finishes at the idealized ultimate point. Thus, the trilinear approach suggested by Tomaževič (1999) can lead to significant differences in total energy between the backbone curve and the idealized curve. Consequently, a new proposal was developed, which combines criteria established for the bilinear curve like the idealized elastic limit and the energy balance, with conditions applied to the existing trilinear procedure, such as incorporating the maximum load point for the determination of the post-peak branch.

For trilinear curves, there are two pre-peak stiffnesses, one referring to pre-cracking and the other one to post-cracking. Therefore, k_e does not need to reflect a "cracked" stiffness and can

take the values estimated for k_0, determined in Chapters 4 and 5. However, the value taken needs to be ponder to each specimen in order to enable a good approximation between experimental and idealized curves. Then, the backbone curve is divided in two parts, before and after the maximum load, originating two integrals - $A_{env}^{pre-peak}$ and $A_{env}^{post-peak}$ (see Figure 6.9a). The energy balance is made for each part of the backbone curve, resulting on two idealized points: the elastic limit and the maximum displacement limit. The first one, is part of the trilinear curve, while the second is an auxiliary point to determine the idealized ultimate point, as shown in Figure 6.9b.

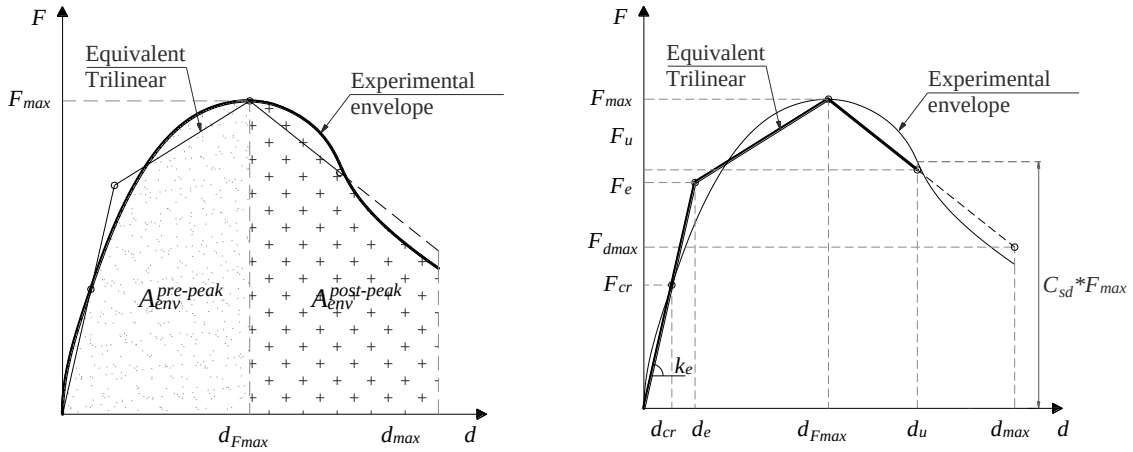

Figure 6.9 Trilinear idealization: (a) backbone curves' areas; and (b) defining points.

For the tests carried out, it was considered that the crack limit would correspond to the yield limit directly established from the experimental curves, in Chapters 4 and 5. The general procedure for the determination of the points that constitute limits of the trilinear idealization is as follows:

1. From the experimental envelope determine the maximum force limit → (d_{Fmax}, F_{max});
2. Estimate initial C_{cr};
3. Calculate F_{cr} and determine the corresponding displacement d_{cr} on the experimental envelope curve:

$$F_{cr} = C_{cr} \times F_{max} \tag{6.19}$$

4. Calculate k_{e}:

$$k_e = \frac{F_{cr}}{d_{cr}} \tag{6.20}$$

5. Calculate the two areas below the experimental envelope, before and after the peak, $A_{env}^{pre-peak}$ and $A_{env}^{post-peak}$, respectively (see Figure 6.9a);
6. Solve $A_{env}^{pre-peak} = A_{tri}^{pre-peak}$ in order to get d_{e}:

$$d_e = \frac{2A_{envv}^{pre-peak} - F_{max} \times d_{Fmax}}{(d_{Fmax} \times k_e - F_{max})} \quad (6.21)$$

7. Calculate F_e:

$$F_e = k_e \times d_e \quad (6.22)$$

8. Determine d_{max} from the backbone curve;
9. Solve $A_{env}^{post-peak} = A_{tri}^{post-peak}$ in order to get F_{dmax}:

$$F_{dmax} = \frac{2A_{env}^{post-peak}}{(d_{max} - d_{Fmax})} - F_{max} \quad (6.23)$$

10. Estimate the displacement d_u from the experimental envelope, corresponding to a force degradation of $(1 - C_{sd}) \cdot F_{max}$;
11. Calculate the ultimate force, F_u, corresponding to d_u:

$$F_u = F_{max} + \frac{(F_{max} - F_{dmax}) \times (d_{Fmax} - d_u)}{d_{Fmax} - d_{max}} \quad (6.24)$$

12. Construct the trilinear curve as represented in Figure 6.9b.

Through Eq. (6.25), the different branches of the trilinear curve can be expressed analytically. The last two linear branches have their stiffness defined by multiplying k_e by coefficients α and β. These coefficients, together with forces F_2 and F_3 were determined for each specimen and equivalent curve of the sets (see Annex 4).

$$F(d) = \begin{cases} k_e \cdot d & for \quad 0 \le d \le d_e \quad (1) \\ \alpha \cdot k_e + F_2 & for \quad d_y \le d \le d_{Fmax} \quad (2) \\ \beta \cdot k_e + F_3 & for \quad d_{Fmax} \le d \le d_u \quad (3) \end{cases} \quad (6.25)$$

For the tests of wall-to-timber elements with injection anchors performed at the bottom of the wall, there was a considerable residual strength towards the end of the test that could not be ignored and prevented a good trilinear idealization. Consequently, one decided to reformulate the procedure presented previously and divide the post-peak branch in two segments: one for softening and another one to represent the residual capacity (see Figure 6.10). By observing the backbone curves, one considered that the two last points would be used to define the residual force, F_{res}. The next step consisted of calculating an idealized residual displacement limit, d_{res}, which would correspond to the beginning of the residual linear segment, by balancing $A_{env}^{post-peak}$ with the area below the two post-peak linear branches. The first three branches of these curves can be expressed by Eq. (6.25), but in expression (3) the segment is defined until d_{res} instead of d_u. The residual force branch (4) is defined by $F(d) = F_{res} \ \ for \ d_{res} \le d \le d_{max}$.

For ductility calculations, the displacement d_u was also calculated for these specimens following the same criteria applied for the remaining tests.

6.3.3 Comparison between approaches

This subsection was divided according to the set of tests performed – injection anchors for connections, unstrengthened and strengthened wall-to-floor connections.

6.3.3.1 Injection anchors for connections

As previously mentioned, the experimental curves of these connections were approximated by trilinear curves only (see Figure 6.10). In order to get the best approximation possible to the experimental backbone curve, the criteria for the determination of C_{cr} was pondered for each and every tests. The backbone curves based on ASCE/SEI 41-06 (ASCE, 2006) of specimens WT.40.I.1A and WT.40.I.1D have only two branches before the peak, therefore no pre-peak energy balance was needed, and the two segments are part of the trilinear curve. For the latter specimen, the same occurred for the trilinear curve idealized from the backbone curve based on Frumento et al. (2009). This specimen presents a considerable increase of stiffness, approximately 30 %, regarding the value determined from the cyclic curve, due to initial stiffening of the cyclic force-displacement curve not being captured by the method used to estimate k_0. As one recalls, the latter parameter was determined using a linear least squares fit on the linear portion of the virgin ascending branch of the first cycle, while k_e was determined by the secant line connecting the origin to the crack limit.

Coefficient C_{cr} for the remaining trilinear curves was found by approximating stiffnesses k_e to k_0, and respecting the overall shape of the backbone curves. Average C_{cr} is slightly higher for the bottom specimens than for the top ones, taking the values of 0.65 and 0.60, respectively, independently of the backbone method. A greater variability of the parameters associated with the trilinear idealization is observed for the specimens at the top, as a direct consequence of the experimental results (see Table 6.5). Both backbone methods provide similar values of μ and k_e for the tests at the bottom of the wall. For the tests at the top of the wall, the stiffness k_e is practically the same for both methods, but μ determined from Frumento et al. (2009) is 1.5 times higher than the one calculated from ASCE/SEI 41-06 (ASCE, 2006). The trilinear curves obtained from the latter method present in general lower displacements, especially post-elastic, and lower forces, resulting in curves with similar shape to the ones obtained from Frumento et al. (2009) but smaller (see Figure 6.10). The forces F_{max} obtained with ASCE/SEI 41-06 (ASCE, 2006) are approximately 85 % of the F_{max} obtained with Frumento et al. (2009).

However, ASCE/SEI 41-06 (ASCE, 2006) trilinear curves had lower CoVs for the main variables, which is visible in Figure 6.10. The values of the variables needed to analytically express (see Eqs. (6.18) and (6.25)) the curves presented in Figure 6.10 can be found in Annex 4, as well as k_e and μ concerning each specimen. The definition of points 1, 2 and 3 on the equivalent trilinear curves obtained from ASCE/SEI 41-06 (ASCE, 2006) backbone curves, as seen in Figure 6.10, resulted on the classification of the tested specimens (top and bottom ones) as ductile, belonging to type 1, since their post-peak behavior can be considered for analysis. The same criteria applied to the trilinear curves obtained from Frumento et al. (2009) type of backbone curves confirms the tested connections as ductile. As a consequence, the displacement acceptance criteria shown in Figure 6.10 can be established, being latter discussed in subsection 6.4.1.

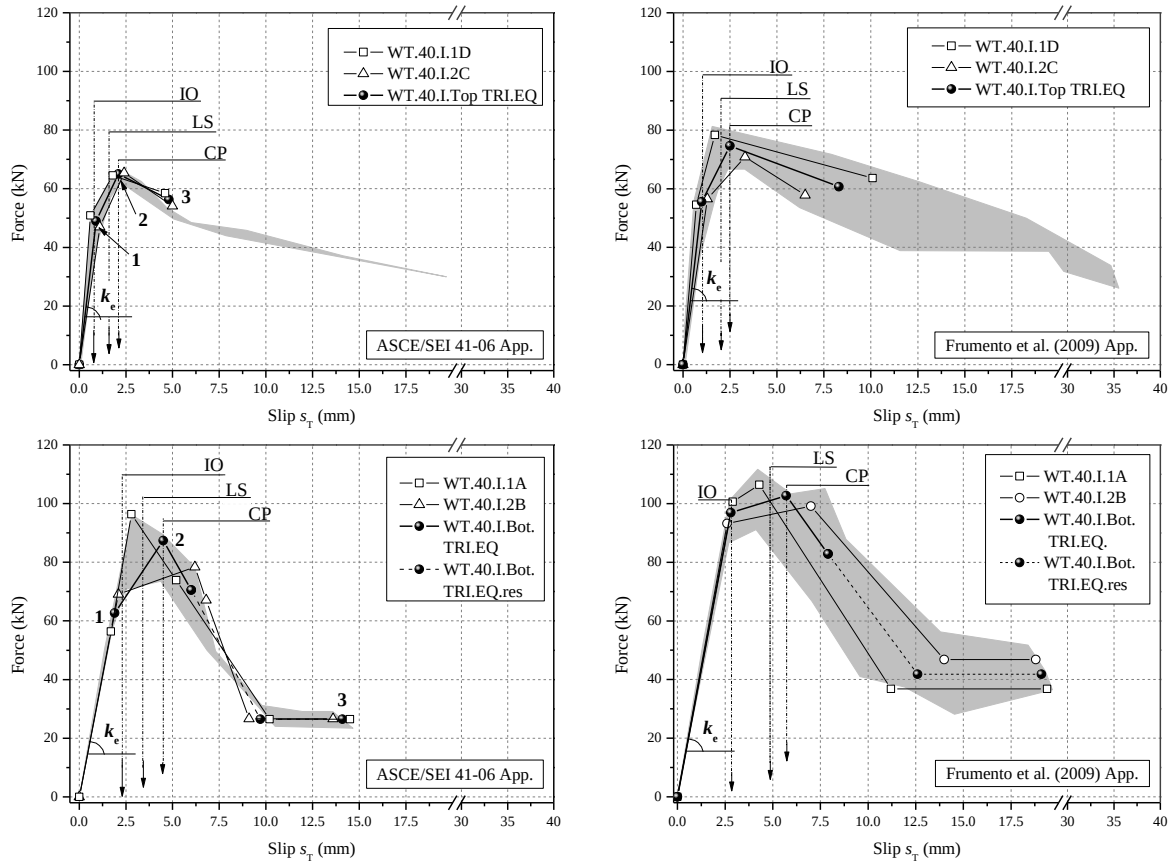

Figure 6.10 Equivalent trilinear curves for the injection anchors specimens.

Table 6.5 Main parameters concerning trilinear idealizations for injection anchors for connections (CoV in parentheses).

Specimens	Parameters	Frumento et al. (2009)	ASCE/SEI 41-06
Top	k_e (kN/mm)	56.1 (42%)	57.5 (42%)
	μ	8.4 (69%)	5.6 (32%)
	F_{max} (kN)	74.6 (7%)	65.0 (1%)
	R^2	122	118
Bottom	k_e (kN/mm)	35.0 (1%)	33.6 (1%)
	μ	2.9(35%)	3.2 (4%)
	F_{max} (kN)	102.7 (5%)	87.4 (15%)
	R^2	98	131

6.3.3.2 Unstrengthened wall-to-floor connections

When assessing the contribution of connections to the global seismic behavior of the structure, prior to retrofit, the inclusion of the nonlinear response of the unstrengthened connection can enable a more accurate analysis, and consequently better judgment on the extent of seismic retrofit needed. Therefore, bilinear and trilinear idealizations were performed for the force-displacement curves obtained from the monotonic tests on unstrengthened wall-to-floor connections, as presented in Figure 6.11. The WF.U equivalent bilinear and trilinear curves were determined solely from the curves of specimens WF.40.U.1B and WF.60.U.B, due to the proximity of response, already analyzed in Chapter 5.

To determine the most appropriate bilinear approximations, one considered the conditions previously stated, which led to C_{cr} values of 0.6 to 0.85. The equivalent bilinear (EQ. Bilinear WF.U) shows decreases in stiffness and ductility of 55% and 75% respectively, clearly depicting a cracked condition (see Table 6.6). Figure 6.11 shows the bilinear curves completely out of the experimental envelope area. However, a decrease on k_e enables an increase on F_u, in order to balance the total energy, resulting on the latter being 86 % of F_{max} (average of the two specimens considered), for the EQ. Bilinear WF.U. By comparison with the trilinear curves, the bilinear curves have a higher associated error, R^2, as expected (see Table 6.6). The coefficient R^2 was calculated as the sum of the squares of the vertical deviations between experimental and idealized curves. Displacement ductility μ of the equivalent trilinear curve (EQ. Trilinear WF.U) is 28% lower than the one determined from the experimental curves, because the present μ is calculated with d_e, which is higher than d_y (equal to d_{cr}). Nonetheless, both approaches maintain low CoVs, previously determined directly from the experimental curves. The values of the variables needed to analytically express the curves (see Eqs. (6.18) and (6.25)) presented in Figure 6.11 can be found in Annex 4.

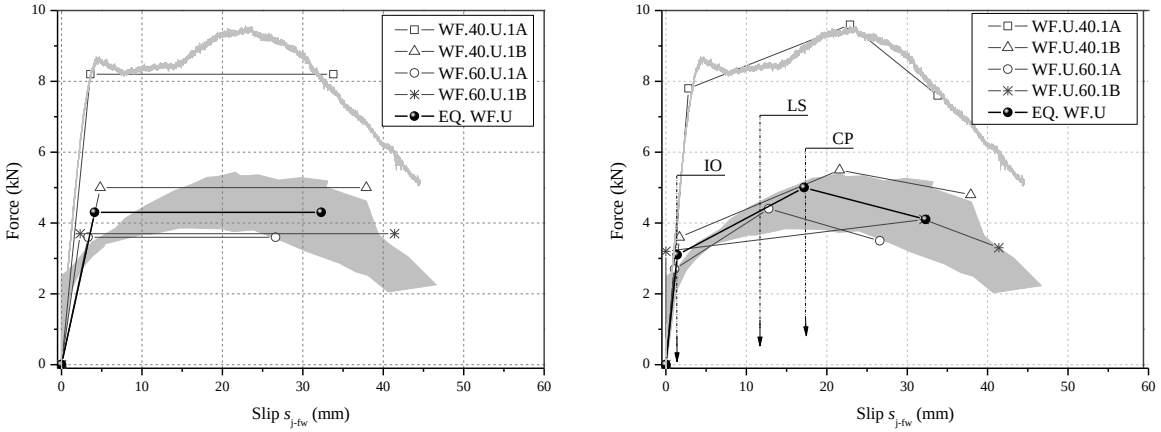

(a) (b)

Figure 6.11 Idealized unstrengthened wall-to-floor connections: (a) Bilinear curves; and (b) Trilinear curves.

Table 6.6 Main parameters concerning unstrengthened wall-to-floor connections idealizations (CoV in parentheses).

Type of backbone	F_{max} (kN)	k_e (kN/mm)	μ	R^2
Bilinear	4.3 (23%)	1.0 (3%)	7.9 (1%)	3999
Trilinear	5 (15%)	2.2 (9%)	22.6 (3%)	429

6.3.3.3 Strengthened wall-to-floor connections

As a direct result from the criteria established for each method used for the determination of the backbone curves, ASCE/SEI 41-06 (ASCE, 2006) curves inherently have lower forces and post-peak displacements than the ones from Frumento et al. (2009) (see Figure 6.12 and Figure 6.13). As a consequence, k_e and μ are slightly higher for the latter and closer to the values estimated directly from the experimental values, as shown in Table 6.7. The k_e of the bilinear curves is approximately 50% of the one of the trilinear ones for the WF.40.A specimens, and 70% for the WF.60.A specimens, independently of the type of backbone curve. In Figure 6.12, are presented the bilinear curves for the WF.40.A and WF.60.A specimens (cyclic tests only), and it can be observed how their first branch is placed outside the envelope area. As it was discussed in Chapter 5, it is clear that specimen WF.60.A.3A shows a very distinct behavior of the remaining two WF.60.A specimens, consequently it was excluded from the equivalent WF.60.A curve.

The force F_{cr} for bilinear curves based on ASCE/SEI 41-06 (ASCE, 2006) is 65% and 55% of F_{max}, for WF.40.A and WF.60.A specimens, respectively. While for bilinear curves based on Frumento et al. (2009), the percentages are slightly lower, taking the values of 60% and 44%, respectively. It means that to fulfill the conditions expressed in section 6.3.2.1, the crack limit had to be extended for the ASCE/SEI 41-06 (ASCE, 2006) approach. On the other hand and as

expected, the bilinear curves based on Frumento et al. (2009) backbone curves allow a higher estimation of F_u, approximately 87% of F_{max} for the WF.40.A specimens, and 82% of F_{max} for the WF.60.A specimens, against the 74% and 72% obtained from ASCE/SEI 41-06 (ASCE, 2006) curves, respectively.

Table 6.7 Main parameters concerning strengthened wall-to-floor connections idealizations (CoV in parentheses).

Approach	Type of backbone	Set of specimens	F_u (bil.) or F_{max} (tril.) (kN)	k_e (kN/mm)	μ	R^2
Bilinear	Frumento et al. (2009)	WF.40.A	81.6 (4%)	5.9 (18%)	6.1 (18%)	1359
		Equivalent				
		WF.60.A	79.3 (2%)	4.6 (22%)	4.6 (12%)	1382
		Equivalent				
	ASCE/SEI 41-06	WF.40.A	69.7 (6%)	5.2 (25%)	5.7 (22%)	762
		Equivalent				
		WF.60.A	69.9 (4%)	3.2 (23%)	3.3 (21%)	367
		Equivalent				
Trilinear	Frumento et al. (2009)	WF.40.A	89.6 (1%)	11.6 (15%)	15.8 (27%)	347
		Equivalent				
		WF.60.A	93.0 (7%)	6.3 (19%)	9.3 (11%)	460
		Equivalent				
	ASCE/SEI 41-06	WF.40.A	74.0 (3%)	10.7 (17%)	15.9 (7%)	67
		Equivalent				
		WF.60.A	77.4 (5%)	4.8 (9%)	6.7 (25%)	214
		Equivalent				

The most penalized parameter is μ, decreasing considerably for both sets of specimens and both types of backbone curves, mostly due to the increase in the displacement d_e. Decreases were around 74 % for WF.40.A specimens and 83 % for WF.60.A specimens, independently of the type of backbone curve.

Figure 6.13 shows the first branches of the trilinear curves within the boundaries of the envelope area, being the k_e of the equivalent trilinear curves lower than the one determined in Chapter 5, since it includes the contribution of the backbone curve of the second cycle. For WF.40.A specimens this decrease is 5% and 12%, for Frumento et al. (2009) and ASCE/SEI 41-06 (ASCE, 2006), respectively, while for the WF.60.A specimens equivalent quantities are much higher, taking values of 34% and 50%, respectively. This results from a considerable decrease in initial stiffness from first to second cycle backbone curves, penalizing the equivalent stiffness of the specimen. The same effect also had a very high impact on the ductility of WF.60.A specimens, decreasing 62% and 72%, for Frumento et al. (2009) and ASCE/SEI 41-06 (ASCE, 2006) types of backbone curves, respectively. For WF.40.A specimens, μ decreased around 30 % in comparison to the value determined in Chapter 5.

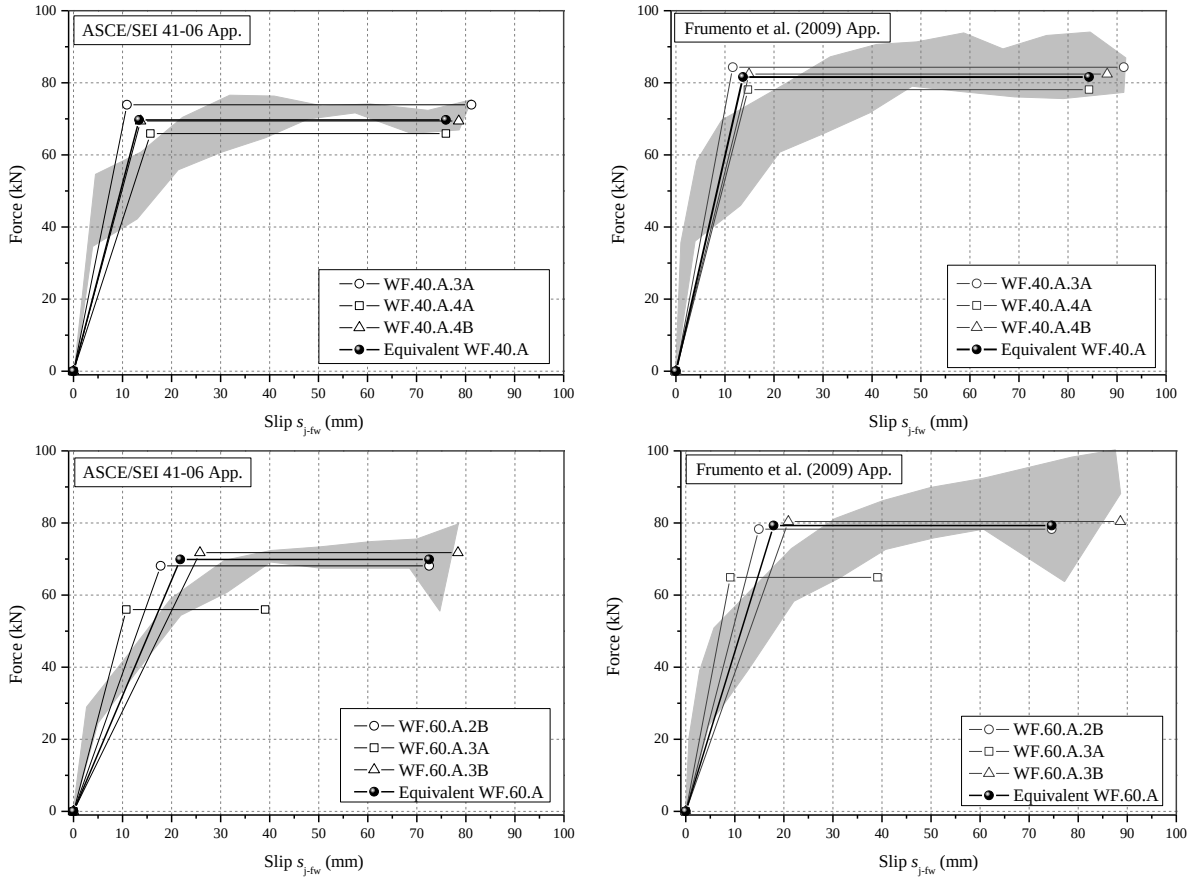

Figure 6.12 Equivalent bilinear curves for strengthened wall-to-floor specimens.

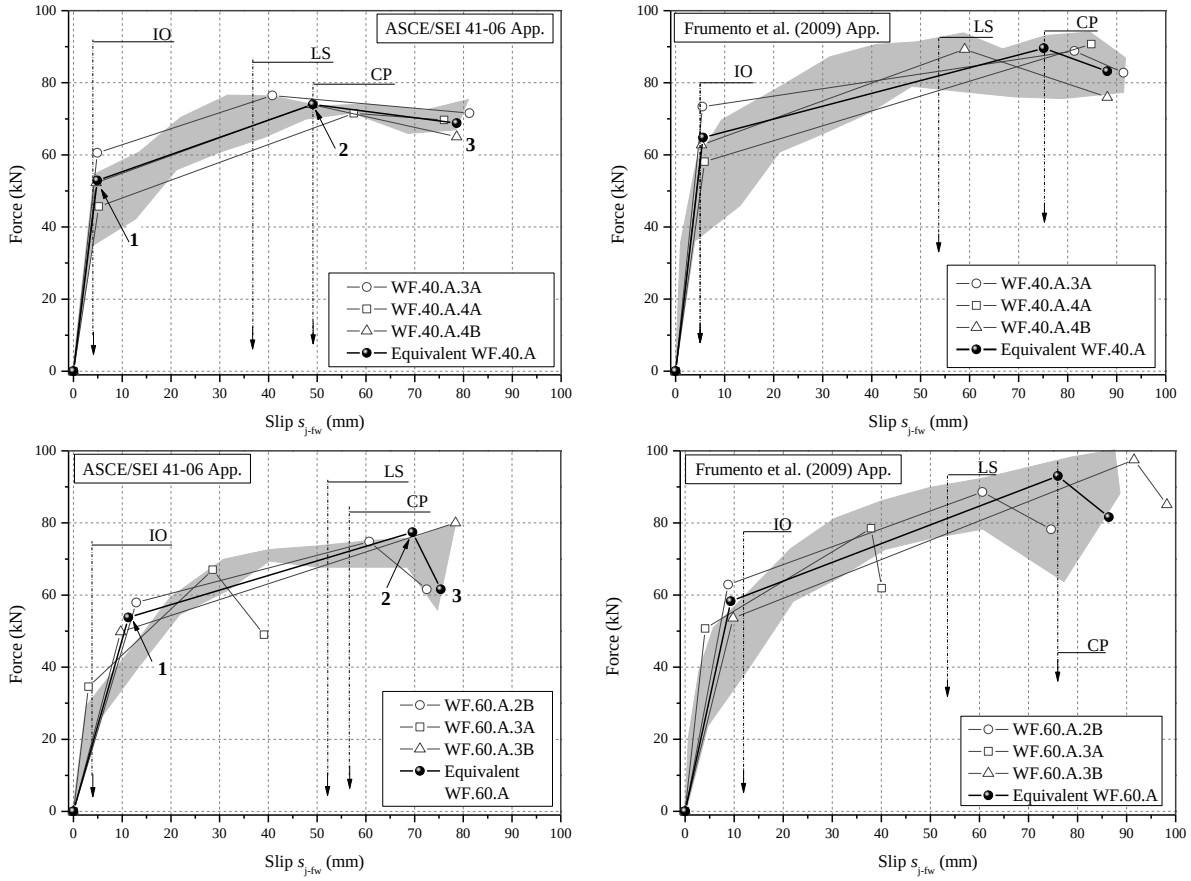

Figure 6.13 Equivalent trilinear curves for strengthened wall-to-floor specimens.

As expected, the trilinear curves provided better approximations than the bilinear curves, with smaller R^2 values. In Annex 4 are presented all the parameters necessary to analytically express the curves shown in Figure 6.12 and Figure 6.13. The definition of points 1, 2 and 3 on the equivalent trilinear curves obtained from ASCE/SEI 41-06 (ASCE, 2006) backbone curves, as seen in Figure 6.13, resulted on the classification of the tested specimens (WF.40.A and WF.60.A) as ductile, belonging to type 1 (see Figure 6.7), since their post-peak behavior can be considered for analysis. The same criteria applied to the trilinear curves obtained from Frumento et al. (2009) type of backbone curves confirmed the tested connections as ductile. As a consequence, the displacement acceptance criteria shown in Figure 6.13 can be proposed and they are latter discussed in subsection 6.4.1.

6.4 RETROFIT DESIGN

6.4.1 Acceptance criteria

Since one is developing seismic retrofit solutions for existing structures, this research falls within the scope of the EC8-Part 3 (CEN/TC250, 2004) and the ASCE/SEI 41-06 (ASCE, 2006). Provisions of this standard are based on performance-based design methodology, specifically developed for existing buildings, to minimize or eliminate unnecessary seismic rehabilitation.

Performance-based design, as the name suggests, relies on the definition of performance levels to be achieved when designing the new structure or the rehabilitation measures. Prior to undertake the rehabilitation process, one needs to assess if the present condition of the structure is sufficient to achieve the desired performance level. If the building is indeed in need of seismic rehabilitation, the first step is to carry out an exhaustive survey of the structural characteristics, the site seismic hazards, the historic and social importance, among other considerations. Then the Rehabilitation Objectives should be established, defining suitable target Building Performance Levels and Earthquake Hazard Levels combinations, for each goal, and the amount of goals to be accomplished. In ASCE/SEI 41-06 (ASCE, 2006), there is a total of sixteen possible goals combinations (among four performance levels and four hazard levels), corresponding to limited, basic safety, and enhanced objectives. EC8 (CEN/TC250, 2004) addresses the rehabilitation goals as Limit States, and establishes three limits, each one corresponding to a certain return period, defined by each National Annex. The number of Limit States to be checked is defined in the same Annex. The performance levels/limit states besides reflecting the extent of damage that would be sustained by the building, also account for the

safety level to its occupants during and after the seismic event, the cost and time of repair, among others. EC8 (CEN/TC250, 2004) establishes three discrete levels, while ASCE/SEI 41-06 (ASCE, 2006) defines four. The additional level is the Operational (O) performance level, which accounts for negligible damage on structural and nonstructural components, meaning extremely low risk to life safety, and ensures that all important systems for normal operation shall function. The costs associated with this performance level are very high, decreasing its feasibility. The remaining three levels can be compared with the ones established by EC8 (CEN/TC250, 2004) (second designation), and they are characterized as follows:

- Immediate Occupancy (IO) or Damage Limitation (DL) – Minor cracking on structural components and nonstructural ones are secure; all systems important for normal operation are functioning, but there might be disruptions of nonessential services; risk of life-threatening injury is very low; in general, no repair is required prior to reoccupancy;
- Life Safety (LS) or Significant Damage (SD)– moderate to extensive damage to both structural and nonstructural components; building may be beyond economical repair; most systems are damaged;
- Collapse Prevention (CP) or Near Collapse (NC) – severe damage to both structural and nonstructural components; building is near collapse; life safety is at risk.

For each level, the limiting design parameters are established to achieve the desired performance for a known earthquake demand. Since the gap between some performance levels seems to be large or small, two intermediate levels were created (Priestley, 2000). These two intermediate levels, Damage Control Range and Limited Safety Range, can be interpolated between the acceptance criteria for the IO and LS levels, and between LS and CP levels, respectively.

For EC8 (CEN/TC250, 2004), the limit states DL, SD, and NC correspond respectively to the following Earthquake Hazard Levels, defined by their return periods (respective probabilities of exceedance in 50 years, in parentheses): 225 years (20%), 475 years (10%), and 2475 years (2%). Similar Earthquake Hazard Levels are established in ASCE/SEI 41-06 (ASCE, 2006), but they can be combined with all the performance levels, as already mentioned. The Basic Safety Objective (BSO), considered a reasonable and commonly applied requirement for buildings retrofit in the United States, consists of two goals: Life Safety performance level for a probability of exceedance of 10% in 50 years, and Collapse Prevention for a probability of exceedance of 2% in 50 years. By comparison, these goals would be the equivalent of

retrofitting the building to limit states of Significant Damage and Near Collapse, according to EC8 (CEN/TC250, 2004). In particular, for heritage buildings and key facilities for society, there is an especial interest in limiting the damage caused by frequent seismic events. Therefore, another goal concerning the Damage Limitation limit state or Immediate Occupancy for a probability of exceedance of 20% in 50 years (when added to the two goals of BSO, the rehabilitation objective is considered enhanced) should be checked.

One must stress that the performance criteria proposed are valid for the specimens tested and for the failure modes obtained, and they intend to demonstrate how to transfer the experimental output into practical knowledge. Further experimental or numerical effort has to be done in order to study the influence of other failure modes, mechanical properties, and geometric characteristics (height to thickness ratio of the wall, anchorage length of the joist, number of bolts, etc.). Based on the experimental results from strengthened connections, performance criteria can be proposed, in order to adequate the retrofit design to the rehabilitation objectives established for the component. Masonry-to-timber connections are primary components, which are needed to create effective load paths for the seismic demand. Then, the first step is to classify the type of action controlling the mechanism of the component, meaning the connection can be classified as force or deformation-controlled. Here lies the difference between brittle and ductile components, respectively, and how their design becomes distinct. ASCE/SEI 41-06 (ASCE, 2006) states very clearly the difference between the two types of actions, as explained in section 6.3.1., while EC8 (CEN/TC250, 2004) is not as clearer. Nonetheless, following the criteria specified in ASCE/SEI 41-06 (ASCE, 2006), the trilinear curves of both connections strengthened with injection anchors and with tie rods with anchor plates complied with the requirements for deformation-controlled actions. Consequently, is possible to establish performance criteria based on displacements, to be used in nonlinear procedures, as well as criteria in force to apply in simplified linear procedures. Since the trilinear curves obtained from the backbone curves based on Frumento et al. (2009) are more commonly applied in Europe, it was chosen to determine the compliance criteria with EC8 (CEN/TC250, 2004) recommendations, while the criteria established from the trilinear curves based on ASCE/SEI 41-06 (ASCE, 2006) shall follow the same standard.

Deformations, *m*-factors and expected strengths (Q_{CE}) for each level — IO, LS, and CP — were calculated and are presented in Table 6.8. They are also represented in Figure 6.10 and Figure 6.13, together with the trilinear curves. The IO limit, Δ_{IO}, is defined by the deformation at which visible damage occurred but it cannot be greater than 0.67 the deformation limit for LS, Δ_{LS}. The latter displacement is defined by 0.75 times the deformation at point 2 on the

curves (see Figure 6.10a and Figure 6.13a), placing this limit before the peak load is achieved. Finally, the CP limit displacement, Δ_{CP}, corresponds to the displacement at point 2 but not greater than 0.75 displacement at point 3, taking advantage of the capacity of the component to still carry seismic loads after the peak load but before complete fracture (d_u). The displacement criteria for each level are displayed in Figure 6.10a and Figure 6.13a., and can be then used in nonlinear analysis. For simplified linear procedures, based on the equal displacement rule (it considers a bilinear idealization of the backbone curve, where elastic and inelastic displacements are the same for structures beyond a given period range), and applied at component level, the resistant capacity of the connection should result from the product between the expected strength, Q_{CE}, the *m*-factor, and the appropriate knowledge factor. The first two are determined from the displacement for each performance level, while the second reflects the degree of information regarding the existing connection. For the present context, this value is taken as 1 and for new materials this factor is not applicable. Q_{CE} is the mean resistant capacity at the considered performance level and the *m*-factor is a modification factor that accounts for the expected ductility associated with the action at the deformation level under consideration. The latter is determined by the quotient of the intended displacement level by the yield displacement (at point 1), multiplied by 0.75.

Table 6.8 Proposed acceptance criteria for deformation-controlled actions [based on ASCE/SEI 41-06 (ASCE, 2006)].

Set of tests	IO			LS			CP		
	Δ_{IO} (mm)	Q_{CE} (kN)	*m*	Δ_{LS} (mm)	Q_{CE} (kN)	*m*	Δ_{CP} (mm)	Q_{CE} (kN)	*m*
WT.I.Top	0.8	46.0	0.7	1.6	58.2	1.4	2.1	65.0	1.8
WT.I.Bottom	2.3	66.4	0.9	3.4	76.8	1.4	4.5	87.4	1.8
WF.40.A	4.0	42.4	0.6	36.8	68.1	5.6	49.1	74.0	7.4
WF.60.A	3.8	18.0	0.3	52.2	70.4	3.5	56.6	72.2	3.7

The *m*-factors for the IO limit are very conservative, because of the difference in displacements between the cracking limit and the idealized elastic limit. The high values obtained for *m*-factors for LS and CP performance levels of the wall-to-floor connections reflect the high ductility observed experimentally.

EC8-Part 3 (CEN/TC250, 2004) recommends that for ductile elements, compliance with the requirements of each performance level should be made through verification of deformations, except when using the *q*-factor approach, which is done in terms of strength. The latter method is an elastic procedure that uses a design response spectrum reduced by factor *q*, which intends to account for the cyclic deformation and energy dissipation effects. *q*-factors can be determined

from experimental and numerical campaigns at the component level to be applied in verification and design of retrofit, as well as to assess the global behavior factor (Magenes et al., 2009), similarly to the *m*-factor introduced in ASCE/SEI 41-06 (ASCE, 2006). Mean values of the mechanical properties, divided by the appropriate confidence factor should be taken for ductile elements. For NC and SD limit states, the capacity of the ductile component should be determined from the deformations, instead of strength. On the other hand, capacity relative to the DL limit state should be based on strength for both ductile and brittle components. In order to determine the displacements correspondent to each limit state from capacity curves, the EC8-Part 3 (CEN/TC250, 2004) advises criteria to be applied on global systems and on singular elements subjected to a specific action. For system capacity curves it suggests that Δ_{NC}, Δ_{SD}, and Δ_{DL} should be taken as d_u, 0.75 of d_u, and d_y, respectively, which is less conservative than the limits established in ASCE/SEI 41-06 (ASCE, 2006). The notation, regarding the average force per limit state, is referred as *F*, with the appropriate index, as presented in Table 6.9, and is the equivalent of Q_{CE} in ASCE/SEI 41-06 (ASCE, 2006).

Similarly to what was already performed for the ASCE/SEI 41-06 (ASCE, 2006) approach, deformations, and expected strengths (*F*) were proposed for each state limit — DL, SD, and NC (see Table 6.9). The q^0-factor (basic behavior factor) was derived for the wall-to-floor connections from the bilinear curves (see Table 6.9), and is defined as the ratio between the force the connection would experience if the if its response was completely elastic, $F_{el,max}$, and the yielding force F_y (Tomaževič, 1999; Frumento et al., 2009). Since the specimens regarding the injection anchors (WT.I.Top and WT.I.Bottom) were not approximated by bilinear curves due to their shape, the first branch of the trilinear curves was used to estimate q^0.

As it was already discussed in section 6.3.2, the trilinear curves inspired by Frumento et al. (2009) backbone curves lead to higher values of displacements and forces, resulting on less conservative acceptance criteria than the ones established based on the ASCE/SEI 41-06 backbone curves. The values of q^0 proposed for the WT.I.Top and WT.I.Bottom specimens are within the interval commonly considered for the behavior factor of unreinforced masonry buildings, from 1.5 to 2.5 (CEN/TC250, 2004; Paulay & Priestley, 1992). Since the behavior of the wall-to-floor connections is a combination between the unreinforced masonry wall, the timber elements, and the steel strengthening solution, the behavior factor q^0 is higher than the one obtained for the injection anchors. In fact, the values obtained for the connections tested are close to the interval suggested by EC 8-Part 1 (CEN/TC250, 2004) for timber structures (1.5 to 5), as it would be expected, since failure occurred at the bolted connection.

Table 6.9 Proposed acceptance criteria for deformation-controlled actions [based on EC8 (CEN/TC250, 2004)].

Set of tests	DL		SD		NC		
	Δ_{DL} (mm)	F_{DL} (kN)	Δ_{SD} (mm)	F_{SD} (kN)	Δ_{NC} (mm)	F_{NC} (kN)	q^0
WT.I.Top	1.0	55.5	6.2	65.6	8.3	60.7	1.9
WT.I.Bottom	2.8	96.9	14.3	41.8	19.1	41.8	1.9
WF.40.A	5.6	64.8	66.1	86.4	88.1	83.2	5.5
WF.60.A	9.3	58.3	64.8	87.2	86.4	81.6	4.4

6.4.2 Design procedure proposals and recommendations

As already mentioned, before engaging in any retrofit intervention, it is necessary to assess the present condition of the structure. If an intervention is required, one should then consider the technical criteria to take into account. Even if planning an intervention at component level, such as strengthening masonry-to-timber connections, the global perspective of the building always needs to be taken into consideration. This means that the intervention should not decrease the overall available ductility and if clear deficiencies are detected, they should be corrected or improved as much as possible.

Common retrofit design methodologies encompass the following stages: conceptual design; analysis; and verifications (CEN/TC250, 2004). In the first step, there is the selection of the details of the intervention, the preliminary design of the strengthening solution, and a preliminary estimation of the modified stiffness of the retrofitted component. Particularly for historic constructions, the compatibility between existing and new materials, the reversibility of the intervention, or the limitations in terms of its execution demand a well-thought plan. The second step assesses the global response of the building, after the intervention, using linear or nonlinear analysis procedures. The final step consists of safety verifications. Retrofit design is then an iterative process conditioned by these three steps.

Considering all the information presented in the previous sections, and bearing in mind the three steps mentioned, design procedures were proposed to both studied retrofit solutions. There are several approaches to the design of the retrofit solutions (Paganoni & D'Ayala, 2014), but the procedures proposed are considered to be easier to implement. A basic retrofit goal is to design a connection for Significant Damage limit state, in order to maintain the primordial function of load transmission and still be able to explore some of its ductility. In addition, for historic structures it is important to keep damage under control, therefore the Controlled Damage limit state should also be a retrofit goal. Procedures focus on these two steps, which occur at component level. After concluding the procedures, it is recommended to assess the

response of the entire structure and verify if there is no decrease in global ductility or if the interstorey drift limitation is being respected. If not, the retrofit solution should be redesigned. Both the EC8 (CEN/TC250, 2004) and the Italian code (NTC, 2008) introduce this requirement, which the latter has specifically defined for unreinforced masonry structures, as shown in Eq. (6.26).

$$d_r \nu \leq 0.003h \tag{6.26}$$

where d_r is the design interstorey drift, ν is a reduction factor, which takes into account the lower return period of the seismic action associated with the damage limitation requirement and it also depends on the importance class of the buildings (0.4 can be adopted for heritage structures), and h is the storey height.

Since the masonry-to-timber connections demonstrated a ductile behavior, the retrofit design should follow a displacement-based approach. Ideally, the seismic demand should be determined in terms of displacement, which would then be directly checked against the displacement limits corresponding to the performance levels (as the ones defined in Table 6.8 and in Table 6.9), for nonlinear analysis. Since most procedures and codes are organized in terms of force-based design, it is difficult to implement displacement checks for performance. Consequently, it is commonly to carry out the design in terms of force and include towards the end of the process a displacement check (Priestley, 2000). In this case, the values determined for the forces (Q_{CE} and F) and the behavior factors (m and q_0) can be applied as capacity limits.

In this section, the flowcharts proposed for design of the retrofitted connections follow this common practice of force-based design (see Figure 6.14 and Figure 6.15), with displacement/ductility checks regarding the whole building (Paganoni & D'Ayala, 2014). Therefore, design results from checking that the resisting force, F_R, is higher than the design seismic demand per anchor, F_D, calculated for the retrofit goals established previously, Significant Damage and Controlled Damage limit states, according to EC8-Part 3 (CEN/TC250, 2004). These limit states equivalents in ASCE/SEI 41-06 (ASCE, 2006) were explained in section 6.4.1. Considering the failure modes and respective methods to calculate their strength capacity, described in section 6.2, the design of the retrofitted connection must assure that the minimum of the capacities is higher than the seismic demand.

The quantification of the seismic demand is not part of the scope of this section, but it is recommended the use of dynamic methods, nonlinear if possible, as recommended by EC8 (CEN/TC250, 2004) and ASCE/SEI 41-06 (ASCE, 2006).

The flowcharts presented in Figure 6.14 and Figure 6.15 consider the demand per anchor for design of the retrofit solutions, therefore there is a need to establish a minimum number of

anchors per storey (to anchor floors or walls). Tomaževič (1999) suggests that spacing between anchors should be around 1.5 m to 2.0 m, while in older applications of strengthening, as for example with metal straps, this distance was approximately 4 m. Thus one suggests an interval between 1.5 and 4 m, as maximum spacing, which can be pondered by assessing the ductility of the whole building before and after the strengthening application.

For the injection anchors, one opted for the determination of the steel tie diameter, *d*, by ensuring that the steel tie capacity, F_{SD}^{steel} is higher than the demand per anchor, $F_{D,SD}$. From this variable, the diameter d_0 can be defined, considering that it should be between 1.5 and 3 times the diameter *d*. Together with material properties, *s* (distance between anchors dependent on the thickness of the timber element and on the dimensions of the steel gussets), and *c* (minimum wall coverage to the free end of the anchor), these variables determine the value of h_c, which is independent of the h_{ef} to be chosen. One of the key steps of the procedure is the definition of h_{ef}, which can control the expected failure mode of the connection and has to be equal to or lower than the thickness of the wall minus *c*. Existing recommendations for the installation of injection anchors in masonry suggest that h_{ef} should be at most 2/3 of the thickness of the wall or *c* should be at least 50 mm (Algeri et al., 2010). Depending on the relationship between h_c and h_{ef}, the verification is made for the failure mode that is most likely to occur – cone (F_{SD}^{cone}), bond (F_{SD}^{bond}), or combined cone-bond ($F_{SD}^{cone+bond}$) failures (see Figure 6.14).

The design approach applied to the strengthened wall-to-floor connections relies on the capacity of the various parts of the strengthening, which are susceptible to distinct failure modes, to be equal to or higher than the demand per connection (see Figure 6.15). Thus, the minimum capacity corresponds to the prevailing failure mode. Since the strength capacity of the steel angle (F_{SD}^{sa}) is an input in the process, this component of the strengthening is not subjected to design. To fulfill the safety condition, alterations should be made on the demand side, by increasing or decreasing the number of anchors. The remaining components are subjected to design and their capacity is estimated according to the failure mode most likely to occur – failure of the bolted connection (F_{SD}^{bc}), failure of the steel tie (F_{SD}^{st}), and masonry cone breakout (F_{SD}^{cone}). Crushing of the mortar under the anchor plate can be prevented by applying a higher strength mortar or reinforced mortar, which can be introduced as a recommendation for the application of the strengthening, rather than a design step.

Both design procedures, comprise the step regarding the Damage Limitation limit state compliance, which should be verified for the connection. The capacities corresponding to DL

are difficult to quantify, since most formulae is developed for the ultimate state, unless experimental data is available.

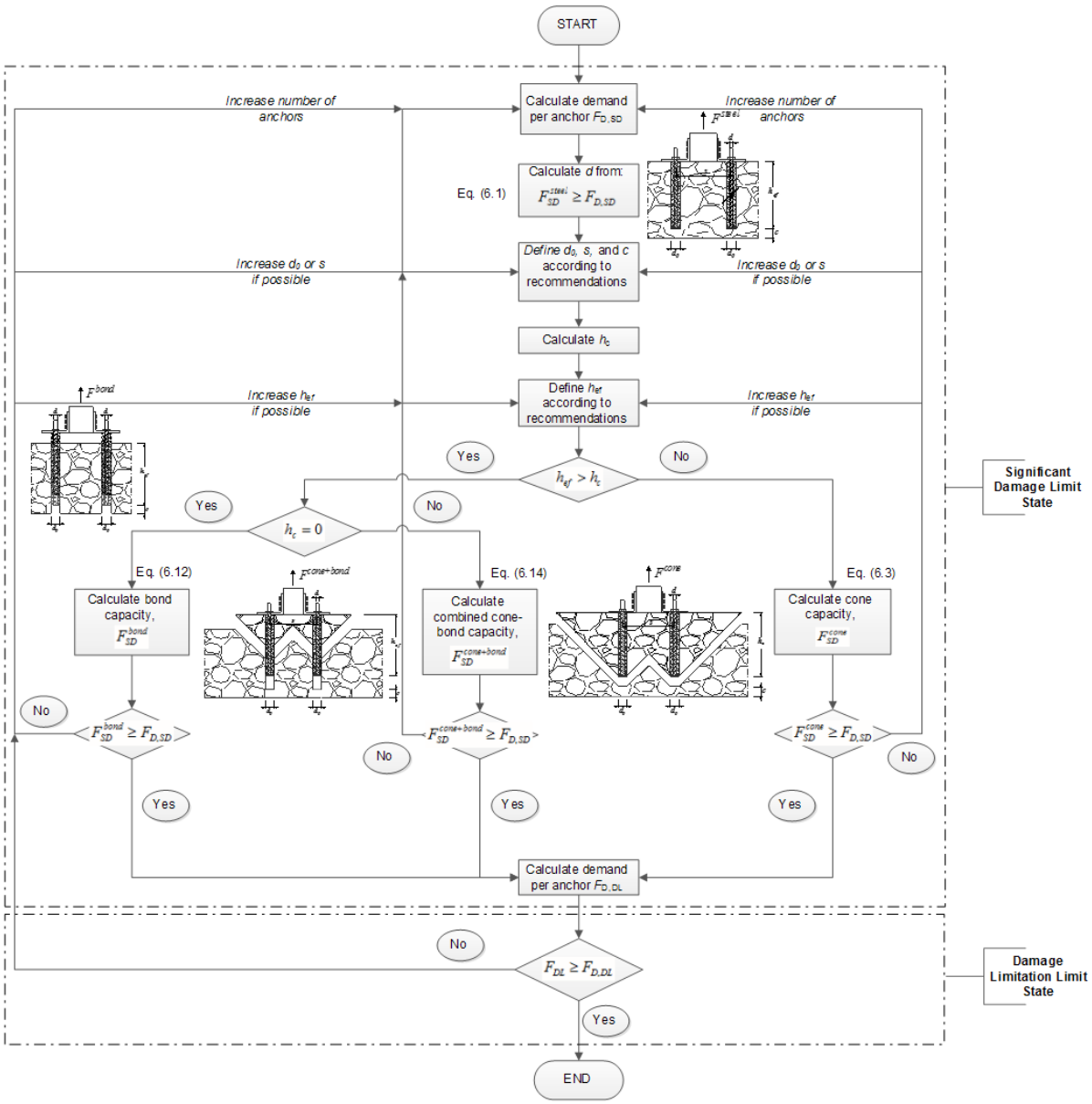

Figure 6.14 Flowchart for the design of injection anchors.

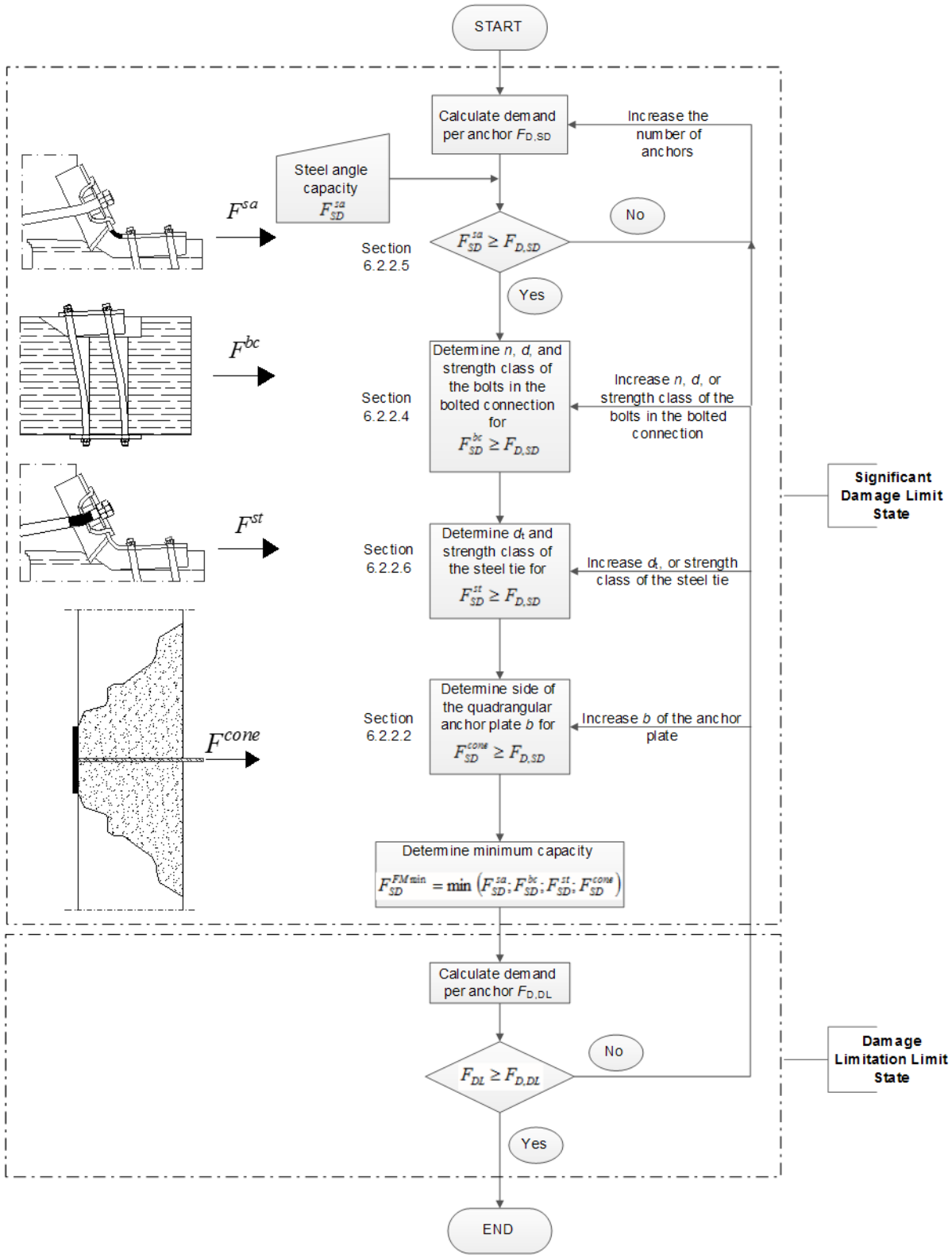

Figure 6.15 Flowchart for the design of strengthened wall-to-floor connections.

Despite not being included in the procedures presented, improvement of the mechanical properties of masonry and timber are an alternative or complementary option to changing the number of anchors or characteristics of the strengthening components. In fact, it can be even

absolutely necessary, if the two connecting elements, the masonry wall and the timber element, are not in fair conditions to sustain static and dynamic actions. In historical constructions, is common to observe decay at the end of the joist supporting on the wall, caused by excessive humidity (see Figure 6.16a). This type of damage can significantly reduce the cross-section and support length of the joist, as well as, affects severely mechanical properties. For the wall-to-floor connections, it can also happen that the width of joist is smaller than the fixed width of the steel angle, creating the necessity of increasing this dimension of the joist. To address these two situations, retrofit of the supporting end of the joist is required.

As referred previously, the pullout tests carried out focused on the tensile behavior of the connection, but in reality the shear and flexure capacity of the connection are also engaged. Therefore, the assessment and the design retrofit of the connection should include the combined effect of these actions, especially shear and tensile stresses.

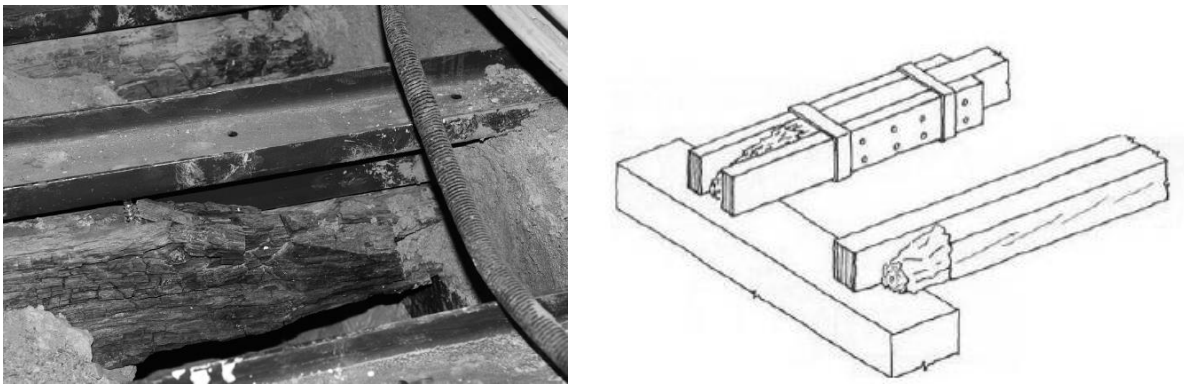

(a) (b)

Figure 6.16 Retrofit of the joist: (a) Strengthening with steel profiles (González-Bravo et al., 2011); (b) strengthening by adding new timber elements to the existing one (Arriaga, 2000).

6.5 IMPLICATIONS OF THE NEW ASCE/SEI 41-13

In 2014, at the end of the thesis development, a new version of ASCE-SEI 41 was made available, which contained some alterations relatively to its previous version, ASCE/SEI 41-06 (ASCE, 2006). This section discusses briefly these alterations and the main implications that they have on the different thesis outputs.

ASCE/SEI 41-13 (ASCE, 2014) addresses the definition of backbone curves and acceptance criteria differently than the previous version, and the aspects with higher impact on the output presented in the previous sections are discussed in the following. While the backbone curves defined according to ASCE/SEI 41-06 (ASCE, 2006) directly include strength and stiffness degradation through the intersection of an unloading branch with the loading curve of the next displacement level, backbone curves according to ASCE/SEI 41-13 (ASCE, 2014) do not account for this effect. The backbone curve of each specimen is defined by connecting with linear segments the points corresponding to the peak displacement of the first cycle, of the different displacement levels. Therefore the backbone curves reflect solely the indirect effect of past cyclic loading history. Defining the points in terms of peak displacement has mainly impact on the displacement levels immediately after the peak force, since it might happen that the force starts degrading before the applied displacement is complete. Thus these backbone curves are practically the same as the ones obtained for the first cycle, according to Frumento et al. (2009).

The other aspect with larger implications is the definition of the acceptance criteria. In fact, small differences are introduced on the typologies of curves, to which the backbone curves should conform (see Figure 6.7), but the criteria for classification of the components as ductile or brittle stands the same for primary components (as connections). Therefore, both types of strengthened specimens continue to be classified as ductile and displacement acceptance criteria for nonlinear procedures can be proposed. To establish the acceptance criteria, ASCE/SEI 41-13 (ASCE, 2014) adopts a letter system, A to E, instead of the numbers previously used (see Figure 6.7). As shown in Figure 6.17 and Figure 6.18, the elastic phase goes from A to B (former 0 to 1), the strain hardening is comprehended between B and C (former 1 to 2), and the strength degradation phase develops between C and E (former 2 to 3). The latter phase can encompass the occurrence of non-negligible residual force between point D and E. After point E, there is a complete loss of load capacity. While ASCE/SEI 41-06 (ASCE, 2006) uses the displacement corresponding to F_{max} (point 2 in Figure 6.7) as threshold for the CP performance level, ASCE/SEI 41-13 (ASCE, 2014) uses the displacement at point E, which is the maximum

displacement for type 1 curves, or the ultimate displacement for type 2 curves. Consequently, the displacement correspondent to the LS performance level, is 0.75 of the CP displacement. Displacement of the IO performance level remains the minimum of the crack limit displacement or 0.67 of the LS displacement. These conditions are similar to the ones suggested in EC8-Part 3 (CEN/TC250, 2004), as mentioned in section 6.4.1, bringing the two codes closer. Parameters for the definition of the new idealized curves are presented in Annex 4.

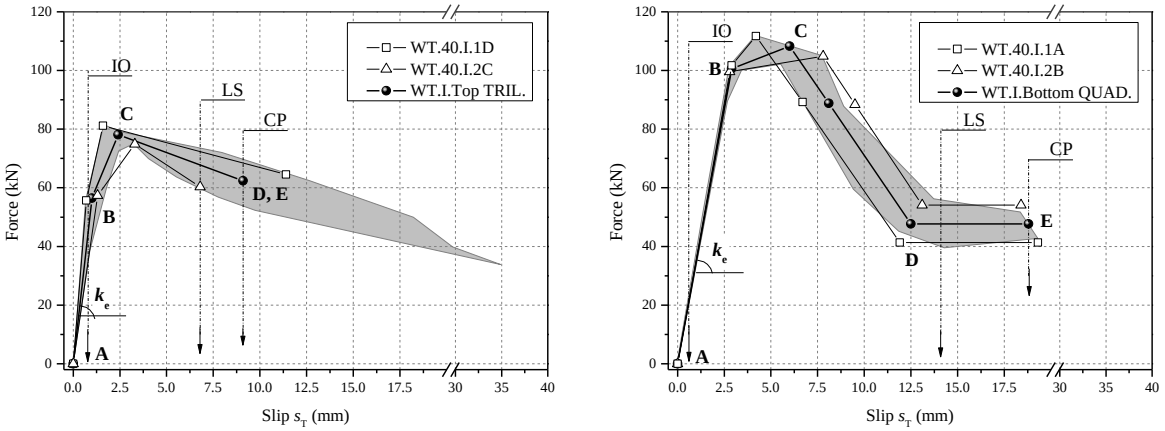

(a) (b)

Figure 6.17 Idealized trilinear and quadrilinear curves for injection anchors' specimens: (a) WT.40.I.Top; and (b) WT.40.I.Bottom

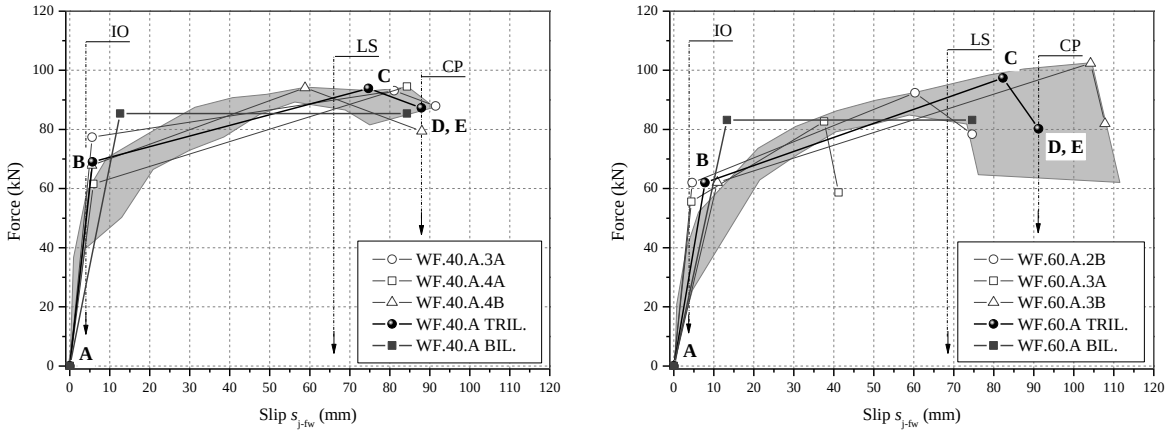

(a) (b)

Figure 6.18 Idealized bilinear and trilinear curves for strengthened wall-to-floor specimens: (a) WF.40.A specimens; and (b) WF.60.A specimens.

As expected, these idealized curves share more similarities with the ones obtained from Frumento et al. (2009) backbone curves rather than with the ASCE/SEI 41-06 (ASCE, 2006) curves. However, the variability of parameters as k_e and μ increased, especially for the WF.40.A specimens. Regarding the acceptance criteria, Δ_{IO} remains the same (it corresponds to the cracking limit) but the other two displacements increase considerably (see Table 6.10). The *m*-factors for the wall-to-timber elements (WT.40.I.Top and WT.40.I. Bottom) show a slight decrease or remain the same, because in spite the increase on the displacements of

performance levels LS and CP, there is an equivalent increase on the displacement of point B (former point 1). On the other hand, for WF.40.A and WF.60.A specimens the values of the *m*-factors increase, due to the substantial increase on all displacements (see Table 6.10). Particularly for the WT.40.I.Bottom specimens the difference in acceptance criteria for the LS and CP performance levels is significant, because they now fall within the residual force branch of the curve (see Figure 6.17b).

Table 6.10 Proposed acceptance criteria for deformation-controlled actions (based on ASCE/SEI 41-13 (ASCE, 2014)

Set of tests	IO			LS			CP		
	Δ_{IO} (mm)	Q_{CE} (kN)	*m*	Δ_{LS} (mm)	Q_{CE} (kN)	*m*	Δ_{CP} (mm)	Q_{CE} (kN)	*m*
WT.I.Top	0.8	44.1	0.6	6.8	67.8	1.3	9.1	62.4	1.8
WT.I.Bottom	2.4	83.9	0.6	14.1	47.7	1.2	18.8	47.7	1.6
WF.40.A	4.0	48.1	0.5	66.0	90.7	7.4	87.9	87.3	8.7
WF.60.A	3.8	60.1	0.4	68.4	90.8	5.9	91.2	80.2	6.6

6.6 CONCLUSIONS

The behavioral models studied for the different types of damage observed enabled a better understanding of the experimental findings and also allowed the development of analytical tools capable of translating the experimental results into design proposals and recommendations.

The behavioral models used for strength prediction of the load-carrying capacity of injection anchors can provide good estimations of the experimental values, considering some modifications to existing formulae. The adopted models for the individual types of damage that can lead wall-to-floor connections to failure provide capacity boundaries that are consistent with the experimental observations. However, further work needs to be developed in order to better estimate the load-carrying capacity resulting from the interaction between different types of damage.

The backbone curves were obtained through two different methods that incorporated cyclic strength degradation — ASCE/SEI 41-06 (ASCE, 2006) and Frumento et al. (2009) — and simplified into bilinear and trilinear curves. The ASCE/SEI 41-06 (ASCE, 2006) approach to the backbone curves proved to be much more conservative than the Frumento et al. (2009), leading to lower values of stiffness, ductility, forces, and consequently acceptance criteria. As already explained, the new version of ASCE/SEI 41-13 (ASCE, 2014) introduced some changes on the method to obtain the backbone curves and the acceptance criteria, bringing it closer

together with the criteria shared by Frumento et al. (2009) and the EC8-Part 3 (CEN/TC250, 2004).

In terms of idealizations, the trilinear curves provided better approximations to the backbone curves, as expected. Both idealized curves rely mostly on the accuracy of the definition of k_e, which can obey to general conditions but needs to be pondered for each test. The specimens regarding the injection anchors and the ones regarding strengthened wall-to-floor connections were both considered to be ductile (deformation-controlled), based on their trilinear curves. The unstrengthened wall-to-floor connections were only tested monotonically but also display a ductile behavior. Consequently, acceptance criteria focused on displacement were proposed for each limit state. Considering that common practice is force-design oriented, force limits and behavior factors were also proposed. The values obtained for the q^0 factors are within reasonable intervals suggested for masonry and timber elements. Design proposals are presented for both injection anchors and strengthened wall-to-floor connections, based on the strength prediction formulae, the performance levels studied, and the recommendations of EC8 (CEN/TC250, 2004).

The key to improvement of the strength prediction formulae and acceptance criteria lies on the need to perform more tests on connections with varying parameters or/and to develop numerical models of the existing tests and then carry out sensitivity analysis. Other important aspects regard the material characterization of all the steel strengthening components and timber, to introduce more accurate inputs into the strength prediction formulae, the study of the pounding effect of timber joist on the wall. Future works will also focus on establishing the hysteretic rules, taking into consideration energy dissipation, strength and stiffness degradation, and pinching. Only by including the loading-unloading curves, it will be possible to fully implement connections in numerical models.

Chapter 7. Conclusions and Future work

7.1 INTRODUCTION

This thesis addressed how to develop seismic retrofit solutions for connections between masonry walls and timber elements, such as floors and timber framed walls. The initial objectives were accomplished and as a consequence, other important questions were raised. Besides the core contributions on the analysis of the tensile behavior of masonry-to-timber connections, a comprehensive literature review on the typologies of existing connections and the critical role that they fulfill in ensuring viable load-paths during seismic excitations. Since conclusions were presented in each chapter, a summary of the main conclusions and suggestions for future works, regarding the experimental and analytical tasks, are presented next.

7.2 CONCLUSIONS

7.2.1 Material characterization

The stone masonry and timber used on the specimens were chosen according to the mechanical properties described in literature, regarding the historical materials that constituted the connections. The material characterization tests carried out enabled a better understanding of the experimental observations taken from the pullout tests with injection anchors and the wall-to-floor connections.

Compression tests were carried out on mortar, limestone, and masonry itself, as well as diagonal compression tests on the latter. The proportions of the mortar were purposely chosen to be slightly higher than what was described historically, so that other failure modes could be observed, besides masonry breakout. The high ratio between the compressive strengths of stone and mortar (f_b/f_{cm}) reflected a clear poor mortar/strong unit behavior, where cracking mainly occurs on mortar and/or on mortar/stone interface. In this kind of irregular stone masonry, the role of mortar is more related to accommodating the randomly distributed stones than actually effectively distributing the stresses.

While the stone masonry was well characterized, timber was not characterized experimentally. When trying to apply behavior models and their strength prediction formulae to the pullout tests on wall-to-floor connections, it became clearly the necessity of performing tests to characterize the mean values of certain mechanical properties like the density, tensile and compressive strengths, parallel and perpendicular to the grain, and properties related with steel bolts interaction as the bearing strength against bolts and withdrawal strength. This necessity was also evident regarding the characterization of the bond strength behavior of the

grout/masonry interface of the injection anchors and the study of the isolated behavior of the steel angle from the retrofit solution for the wall-to-floor connections.

7.2.2 Injection anchors applied to connections

Through quasi-static monotonic and cyclic tests, one was able to characterize the simultaneous response of injection anchors placed in parallel in masonry walls. All tests showed combined cone-bond failure, with observation of generalized cracking and deep cone-shaped detachments of masonry at the tests performed at the top of the wall, and detachment of shallow parts of masonry on the tests carried out at the bottom. Sliding at the interface grout/masonry was visible throughout the tests.

The analysis of energy dissipation distributions confirmed what was observed experimentally, there was a higher contribution to failure of bond slip in the tests performed at the bottom and higher participation of the cone breakout in tests performed at the top. This distinct behavior was most obviously reflected on the 30% difference in maximum pullout forces, but as well, on the shape of the envelope curves. However, hysteretic loops showed similarities in all tests, being mainly characterized by strength degradation between cycles of the same displacement level, stiffness degradation among cycles, and pinching at loading and unloading. This similarity is possibly due to sliding at the interface grout/masonry, which occurs for both tests on top and bottom of the wall.

The distinct behavior was probably due to different boundary conditions of the masonry wall. The top of the wall, which was connected to the reaction slab through more flexible elements like steel profiles and hydraulic actuators, was possibly functioning like a roller support (with limited horizontal movements), while the bottom of the wall was sitting directly on a concrete slab, with only a plastic sheet between them. This boundary possibly acted like a fixed support instead. Therefore, it can be considered that there was a confining effect, acting upon the tensile strength of the masonry and the bond strength of the grout/masonry interface, at the bottom of the wall that led to higher maximum pullout forces, a distinct shape of the curves, and more prominent residual forces. Although, tests performed at the top also evidence a tendency towards a residual strength, which results, on both cases, from the vertical compression stress applied during the tests.

7.2.3 Wall-to-floor connections

The experimental campaign carried out enabled a better understanding of the unstrengthened and strengthened behavior of wall-to-floor connections. The specimens were constructed at the image of existing connections found in the historical buildings under scope.

The unstrengthened wall-to-floor connections had their response characterized by monotonic tests, while for the strengthened ones the focus of study was their cyclic behavior. In all unstrengthened specimens, failure occurred by pulling out of the two nails connecting the joist to the wall-plate. Their capacity was highly influenced by the rotation of the joist, especially for the specimens with 0.4 m thick walls, phenomenon that was mitigated in the cyclic tests of strengthened wall-to-floor connections by adding a vertical roller support on the joist. The contribution of the wall for the unstrengthened connections' response was very small, since no relevant out-of-plane displacements were measured (lower than 0.3 mm).

The tensile capacity of the strengthened connections is approximately 19 times the one of the unstrengthened ones and the ultimate displacements are much higher (110%) by comparison. Due to an increase of the elastic limit, there was a decrease in ductility of 30%, which might be also influenced by the fact that cyclic tests tend to present lower displacements. Nonetheless the ductility of the strengthened specimens is approximately 23 (CoV of 6%), if specimen WF.60.A.3A is excluded, and the dissipated energy is higher than before. Both WF.40.A and WF.60.A specimens have approximately 60% loss in dissipated energy between cycles, which is explained by the slip that occurs at the bolted connection with force practically zero, until it regains strength. Hysteretic loops are similar in both sets of tests and characterized by strength and stiffness degradation, as well as pinching. This behavior is the result of the damage accumulated on the bolted connection between the steel angle and the timber joist. The large joist/front wall displacements measured also result from this phenomenon, in combination with yielding of the steel angle.

For the strengthened connections, the damage observed experimentally was concentrated on the steel angle and one the bolted connection between the latter and the timber joist. Yielding of the steel angle, and crushing and shearing of the timber was observed in all specimens. Minor cracking of the new mortar placed to feel the cavities below the anchor plate and the steel angle, as well as, yielding of the steel tie, were also common to all specimens. For the WF.40.A specimens, cracking on the wall's front face and cone-shaped cracks on the cross-section was also visible. The quantification of contributions to the response of the specimens based on the dissipated energy, confirmed what was observed during the tests and on the survey performed at demolition. In comparison to the other types of damage observed,

failure of the bolted connection between steel angle and the timber joist was definitely predominant (approximately in average 89.7 % and 98.9 % of the dissipated energy of WF.40.A and WF.60.A specimens).

There was some interference of the test apparatus on the projected area of the masonry cone to be formed in case of breakout, but since the contribution of the masonry wall to the resistant capacity of the connection was very low, for all sets of tests, one considered that there was no interference of the test frame on the projected area of the cone.

The incapacity to measure the small displacements of the wall on the unstrengthened and WF.60.A specimens suggests that LVDTs with higher sensitivity should be used. The deformed shapes of the specimens seem to confirm that the bottom of the wall might be acting as fixed, while the top is behaving like a roller support, supporting the observations made for the injection anchors' specimens.

7.2.4 Analytical development

The analytical applications developed for the experimental results allowed a better understanding of the behavior observed experimentally, as well as the analysis of strength prediction formulae and the definition of idealized force-displacement curves that can contribute for more practical uses of the data obtained. One intended at giving the first steps on force- and displacement-based design criteria for masonry-to-timber connections.

Based on theoretical failure modes and the ones observed experimentally, different strength prediction formulae can be applied. The ones used for estimating the load-carrying capacity of injection anchors can provide good estimations of the experimental values, considering some modifications to existing formulae. The correct estimation of material properties is fundamental on determining the most adequate behavioral model, especially the bond strength of the grout/masonry interface and the tensile strength of masonry. For the wall-to-floor connections, by analyzing the individual contributions of each type of possible failure mode, one could established the order of capacities but could not accurately predict the experimental maximum load. Further work needs to be developed in order to better estimate the load-carrying capacity resulting from the interaction between different types of damage.

The backbone curves were obtained through two different methods that incorporate cyclic strength degradation — ASCE/SEI 41-06 and Frumento et al. (2009) — and simplified into bilinear and trilinear curves. The ASCE/SEI 41-06 approach to the backbone curves proved to be much more conservative than the Frumento et al. (2009) one, leading to lower values of stiffness, ductility, forces, and consequently acceptance criteria. As expected, the trilinear

curves provided better approximations to the backbone curves, but both idealized curves rely mostly on the accuracy of the definition of the effective stiffness. This parameter can be estimated based on general conditions, such as the ones used, but it needs to be pondered for each test. Based on their trilinear curves, the injection anchors' specimens and the ones regarding strengthened wall-to-floor connections were both considered ductile. The unstrengthened wall-to-floor connections were only tested monotonically but also display a ductile behavior.

Following a performance-based design approach, acceptance criteria based on displacement were proposed for each limit state (performance level), as suggested by ASCE/SEI 41-06 (ASCE, 2006) and EC8-Part 3 (CEN/TC250, 2004) for ductile components. Considering that common practice is force-design oriented, force limits and behavior factors were also proposed. The values obtained for the q^0 factors are within reasonable intervals suggested for masonry and timber elements. The retrofit design proposals are recommended for design at component level, for both injection anchors and strengthened wall-to-floor connections, using the strength prediction formulae studied but also incorporate conditions checks for the whole structure that can lead to redesign of the retrofit.

The changes introduced by ASCE/SEI 41-13 (ASCE, 2014) on the computing of the backbone curves and the acceptance criteria, brought this code closer together with the criteria proposed by Frumento et al. (2009) and by the EC8-Part 3 (CEN/TC250, 2004).

7.3 FUTURE WORKS

Future works should focus on characterizing experimentally the material properties that are necessary to better understand the role that each element brings to the overall behavior, especially the ones regarding timber, grout, and the steel components that have not yet been targeted. As already explained, it is critical to quantify the mean and characteristic values of the mechanical properties of timber to be used in the prediction behavioral models, as well as properties related to steel components/timber interaction like withdrawal and bearing strengths. Friction coefficients of timber/timber and timber/masonry interfaces should be characterized in order to understand their contribution to the behavior of wall-to-floor connections.

Since the steel angle is a key element of the wall-to-floor retrofit solution and has several reinforcements welded, making its geometry complex, the force necessary to increase the opening angle between legs should be investigated, as well as deformation capabilities.

Further experimental characterization of the masonry should focus on physical properties as porosity and water absorption of stone and mortar, since they can have great impact on mechanical properties such as compressive, tensile and shear strengths of masonry, and bond strength of the interface grout/masonry.

Regarding the injection anchors, in order to study the influence of different parameters, such as anchorage length, borehole diameter, influence of the compressive state of the wall, other quasi-static pullout tests should be performed in order to validate efforts already carried out towards numerical modeling of the tests performed (Araújo, 2014) and the behavioral models described in Chapter 6. If using the same test setup, the test frame and boundary conditions should be rearranged in order to decrease the influence of these aspects on the results, and also load cells should be used on each anchor in order to monitor force distribution. Another suggestion is to place LVDTs on the masonry, before the strengthening installation is done, and use the hydraulic actuators to assess the efficiency of stress distribution on the wall, and if possible the elastic modulus. Ideally non-destructive tests, like flat-jack and dynamic tests, could be used to estimate the compressive strength and elastic modulus of the masonry walls, and later be used as data base for comparison with *in situ* results.

Further work on pullout tests of single injection anchors is recommended, in order to study the influence of boundary conditions and distance between anchors. Since this research studied the anchoring system to the wall — the injection anchors — and disregarded the contribution of the timber elements, future developments should also focus on carrying out quasi-static pullout tests on the complete assembly. These pullout tests should be complemented with shear tests, in order to, study the response of the connection to this action, and later assess their combined behavior.

The bond strength distribution along the grout/masonry interface should be studied, possibly performing pullout tests with failure of this interface as sole failure, and introducing proper instrumentation on the injection anchors (e.g. strain gauges).

Regarding the wall-to-floor connections, from the pullout tests carried out, only the tensile behavior was studied, but the shear response and the pounding effect should be subjected to investigation. Both are key elements on the full characterization of the wall-to-floor connections seismic response. Shear tests and complete reverse cyclic tests should be carried out. The suggestions mentioned for the test setup of the injection anchors and methods to assess mechanical properties of the wall are also valid for this case.

Again, varying parameters related to all the structural components that are part of the connection is essential, and it should be achieved by combining further experimental data with numerical analysis.

In order to improve the strength prediction formula and proposed acceptance criteria, one has to diversify the input parameters by using data from other experimental campaigns or by developing numerical models of the existing tests and then carry out sensitivity analysis, as was already suggested in sections 7.2.2 and 7.2.3.

Future works will also focus on establishing the hysteretic rules, taking into consideration energy dissipation, strength and stiffness degradation, and pinching, and choose an appropriate hysteric model that can reproduce the experimental observations. Then, connections can be implemented as an element in numerical models of whole buildings and their contribution to the overall seismic response can be analyzed.

References

ACI 318. Building Code Requirements for Structural Concrete (ACI 318-05) (2005).

ACI 530. Building Code Requirements for Masonry Structures (ACI 530-05) (2005). Masonry Standars Joint Comittee.

Algeri, C., Poverello, E., Plizzari, G., & Giuriani, E. (2010). Experimental Study on the Injected Anchors Behaviour on Historical Masonry. *Advanced Materials Research*, *133-134*, 423–428. doi:10.4028/www.scientific.net/AMR.133-134.423

Allen, R., Borchelt, J. G., Klingner, R. E., & Zobel, R. (2000). Proposed Provisions for Design of Anchorage to Masonry. *TMS Journal*, *18*(December), 35–60. Retrieved from http://www.masonrysociety.org/journalfiles/10012.pdf

Appleton, J. (2005). *Reabilitação de Edifícios "Gaioleiros"* (1st ed.). Amadora: Edições Orion.

Appleton, J., & Domingos, I. (2009). *Biografia de um Pombalino - Um caso de reabilitação na baixa de Lisboa*. (E. Orion, Ed.) (1st ed.). Alfragide, Lisbon.

Arandigoyen, M., & Alvarez, J. I. (2007). Pore structure and mechanical properties of cement–lime mortars. *Cement and Concrete Research*, *37*(5), 767–775. doi:10.1016/j.cemconres.2007.02.023

Araújo, A. S., Oliveira, D. V., & Lourenço, P. B. (2014). Numerical investigation on the performance of wall-to-wall connections in traditional masonry buildings. *Engineering Structures*, *80*, 1–11. doi:10.1016/j.engstruct.2014.09.027

Arifovic, F., & Nielsen, M. P. (2004). *Strength of anchors in masonry*.

ASCE. Seismic rehabilitation of existing buildings - ASCE/SEI 41-06 (2006). Reston, Va.

ASCE. ASCE/SEI 41-13. Seismic Evaluation and Retrofit of Existing Buildings (2014). USA.

ASTM International. ASTM D7012-10. Standard Test Method for Compressive Strength and Elastic Moduli of Intact Rock Core Specimens under Varying States of Stress and Temperatures (2010). West Conshohocken, PA: ASTM International. doi:10.1520/D7012-10

ASTM International. ASTM E519 / E519M - 10. Standard Test Method for Diagonal Tension (Shear) in Masonry Assemblages (2010). West Conshohocken, PA. doi:10.1520/E0519_E0519M-10

ATC-43 Project. Evaluation of earthquake damaged concrete and masonry wall buildings. Basic procedures manuals (1998). USA.

Ballarini, R., Shah, S. P., & Keer, L. M. (1986). Failure characteristics of short anchor bolts embedded in a brittle material. In *Royal Society of London* (pp. 35–54). London.

Bento, R., Lopes, M., & Cardoso, R. (2005). Seismic evaluation of old masonry buildings. Part II: Analysis of strengthening solutions for a case study. *Engineering Structures*, *27*(14), 2014–2023. doi:10.1016/j.engstruct.2005.06.011

Binda, L., & Saisi, A. (2005). Research on historic structures in seismic areas in Italy. *Progress in Structural Engineering and Materials*, *7*(2), 71–85. doi:10.1002/pse.194

Bothara, J., & Brzev, S. (2011). *A TUTORIAL: Improving the Seismic Performance of Stone Masonry Buildings*. Oakland: EERI.

Brignola, A., Frumento, S., Lagomarsino, S., & Podestà, S. (2008a). Identification of Shear Parameters of Masonry Panels Through the In-Situ Diagonal Compression Test. *International Journal of Architectural Heritage*, *3*(1), 52–73. doi:10.1080/15583050802138634

Brignola, A., Frumento, S., Lagomarsino, S., & Podestà, S. (2008b). Identification of Shear Parameters of Masonry Panels Through the In-Situ Diagonal Compression Test. *International Journal of Architectural Heritage*. doi:10.1080/15583050802138634

Bruneau, M. (1994). State-of-the-art report on seismic performance of unreinforced masonry buildings. *Journal of Structural Engineering*, *120*(1), 230–.

Calderini, C., Cattari, S., & Lagomarsino, S. (2010). The use of the diagonal compression test to identify the shear mechanical parameters of masonry. *Construction and Building Materials*, *24*, 677–685. doi:10.1016/j.conbuildmat.2009.11.001

Campbell, J., Dizhur, D., Hodgson, M., Fergusson, G., & Ingham, J. (2012). Test results for extracted wall-to-diaphragm anchors from Christchurch unreinforced masonry buildings. *SESOC Journal*, *25*(1), 57–67.

Candeias, P. (2008). *Avaliação da vulnerabilidade sísmica de edifícios de alvenaria*. University of Minho.

Cardoso, R. (2003). *Vulnerabilidade sísmica de estruturas antigas de alvenaria - Aplicação a um edifício Pombalino*. UTL/IST.

Cardoso, R., Lopes, M., & Bento, R. (2005). Seismic evaluation of old masonry buildings. Part I: Method description and application to a case-study. *Engineering Structures*, *27*, 2024–2035. doi:10.1016/j.engstruct.2005.06.012

CEB. (1994). *Fastenings to Concrete and Masonry Structures. State-of-the-art report*. London: Thomas Telford.

CEB. Design of anchorages in concrete. fib Bulletin No. 58 (2011).

CEN ISE/NFE/4. EN 10002-1: Metallic materials - Tensile testing - Part 1. Method of test at ambient temperature (2001).

CEN/TC 125. EN 1052-1:1999. Methods of test for masonry - Part 1: Determination of compressive strength (1999). Brussels, Belgium.

CEN/TC 250/SC1. EN 1991-1-1: 2002. Eurocode 1: Actions on structures - Part 1-1: general actions - Densities, self-weight, imposed loads for buildings (2002). Brussels, Belgium.

CEN/TC 250/SC5. EN 1995-1-1:2004. Eurocode 5 - Design of timber structures - Part 1-1: General - Common rules and rules for buildings (2004). Brussels, Belgium.

CEN/TC B/525. EN 338: Structural timber - Strength classes (2003).

CEN/TC250. EN 1998 - 3. Eurocode 8 - Design of structures for earthquake resistance. Part 3 Assessment and retrofitting of buildings (2004).

CEN/TC250. EN 1993-1-4. Eurocode 3: Design of steel structures: Part 1-4 General Rules - Supplementary rules for stainless steels. , Pub. L. No. EN 1993-1-4:2006 (2006). Brussels, Belgium.

Cestari, C. B., & Lucchio, A. Di. (2001). Timber floors of a monumental buildings: historical and technological knowledge, diagnosis and two proposals of intervention. In *Wooden Handwork/Wooden Carpentry: European Restoration Sites* (pp. 235–241). Elsevier Masson SAS.

Cheok, G., & Phan, L. (1998). *Post-installed anchors - A literature review*. Maryland.

Chiostrini, S., Galano, L., & Vignoli, A. (2000). On the Determination of Strength of Ancient Masonry Walls via Experimental Tests. In *12th World Conference on Earthquake Engineering* (pp. 1–8). Retrieved from http://www.iitk.ac.in/nicee/wcee/article/2564.pdf

Cóias e Silva, V. (2001). Viabilidade técnica de execução do "Programa de Redução da Vulnerabilidade Sísmica do Edificado." In SPES & GECoRPA (Ed.), *Redução da Vulnerabilidade Sísmica do Edificado*.

Cóias e Silva, V. (2007). *Reabilitação Estrutural de Edifícios Antigos*. Lisboa: Argumentum.

Cóias e Silva, V., & Soares, I. (1997). Vulnerabilidade sísmica dos edifícios "Gaioleiros" de Lisboa e medidas possíveis para a reduzir. In *3º Encontro sobre Sismologia e Engenharia Sísmica*. Lisbon, Portugal.

Committee, R. T. RILEM TC 76-LUM. Diagonal tensile strength of small walls specimens (1994).

Cook, R. A., Burtz, J. L., & Ansley, M. H. (2003). *Design Guidelines and Specifications for Engineered Grouts*. Gainsville, Florida.

Cook, R. A., & Konz, R. C. (2001). Factors Influencing Bond Strength of Adhesive Anchors. *ACI Structural Journal*, *98*(1), 76–.

Cook, R. A., Kunz, J., Fuchs, W., & Konz, R. C. (1998). Behavior and design of single adhesive anchors under tensile load in uncracked concrete. *ACI Structural Journal*, *95*, 9–26.

Costa, A. a., Arêde, A., Costa, A., & Oliveira, C. S. (2011). Out-of-plane behaviour of existing stone masonry buildings: experimental evaluation. *Bulletin of Earthquake Engineering*, *10*(1), 93–111. doi:10.1007/s10518-011-9332-9

Dizhur, D., Ingham, J., Moon, L., Griffith, M., Schultz, A., Senaldi, I., … Lourenco, P. (2011). Performance of masonry buildings and churches in the 22 February 2011 Christchurch Earthquake. *Bulletin of the New Zealand Society For Earthquake Engineering*, *44*, 279–296.

Dizhur, D., Schultz, A., & Ingham, J. (2013). Performance of adhesive wall-to-diaphragm connections in the canterbury earthquakes and the subsequent experimental pull-out test program. In *12th Canadian Masonry Symposium*.

Doherty, K., Griffith, M. C., Lam, N., & Wilson, J. (2002). Displacement-Based Seismic Analysis for Out-of-Plane Bending of Unreinforced Masonry Walls. *Earthquake Engineering and Structural Dynamics*, *31*, 833–850. doi:10.1002/eqe.126

Eligehause, R., Cook, R. A., & Appl, J. (2006). Behavior and Design of Adhesive Bonded Anchors. *ACI Structural Journal*, *103*, 822–831. doi:10.1002/best.200710107

Eligehausen, R., & Balogh, T. (1995). Behavior of Fasteners Loaded in Tension in Cracked Reinforced Concrete. *ACI Structural Journal*, *92*(3), 365–378.

Eligehausen, R., & Sawade, G. (1989). Fracture mechanics based description of the pull-out behavior of headed studs embedded in concrete. In L. E. Ed. (Ed.), *Fracture Mechanics of Concrete Structures. From Theory to Application* (pp. 263–281). London: Chapman & Hall.

EOTA. ETAG 001. Guideline for European Technical Approval of Metal Anchors for Use in Concrete. Part five: Bonded Anchors (2008). Kunstlann 40 Avenue des Arts, B-1040 Brussels.

EOTA. ETAG 029. Guideline for European Technical Approval of Metal Injection Anchors for Use in Masonry (2010).

EOTA-TR 029. (2007). *Design of Bonded Anchors - TR 029*.

Fajfar, P., & Krawinkler, H. (2005). *Nonlinear Seismic Analysis and Design of Reinforced Concrete Buildings*. Oxon: Taylor & Francis.

Farrow, C. B., & Klingner, R. E. (1995). Tensile Capacity of Anchors with Partial or Overlapping Failure Surfaces: Evaluation of Existing Formulas on an LRFD Basis. *ACI Structural Journal*, *92*(6), 698–709.

FEMA 547. (2006). *Techniques for the Seismic Rehabilitation of Existing Buildings*.

Frocht, M. (1931). Recent advances in photoelasticity. *ASME Trans.*, *55*(September-December), 135–153.

Frumento, S., Magenes, G., Morandi, P., & Calvi, G. M. (2009). *Interpretation of experimental shear tests on clay brick masonry walls and evaluation of q-factors for seismic design*. Pavia: IUSS Press.

Fuchs, W., Eligehausen, R., & Breen, J. E. (1995). Concrete Capacity Design (CCD) Approach for Fastening to Concrete. *Aci Structural Journal*, *92*(1), 73–94.

Gigla, B. (2004). Bond strength of injection anchors as supplementary reinforcement inside historic masonry. In *Proceedings of the 13th International Brick and Block Masonry Conference* (pp. 119–128). Amsterdam.

González-Bravo, C., Arriaga, F., Íñiguez-González, G., & Maldonado, L. (2011). Prótesis metálicas para la reparación de cabezas de vigas de madera degradadas. *Informes de La Construcción*, *63*(521), 37–45. doi:10.3989/ic.10.004

Griffith, M. C., & Ferrata, V. (2003). EVALUATION OF OUT-OF-PLANE STABILITY OF UNREINFORCED MASONRY WALLS SUBJECTED TO SEISMIC EXCITATION. *Journal of Earthquake Engineering*, *7*(1), 141–169.

Hudson, J. A., & Harrison, J. H. (1998). *Engineering rock mechanics, and introduction to the principles*. (Pergamon, Ed.).

ICOMOS. INTERNATIONAL CHARTER FOR THE CONSERVATION AND RESTORATION OF MONUMENTS AND SITES (THE VENICE CHARTER 1964) (1965).

ICOMOS. ICOMOS CHARTER- PRINCIPLES FOR THE ANALYSIS , CONSERVATION AND STRUCTURAL RESTORATION OF ARCHITECTURAL HERITAGE (2003) (2003).

INE. (2012). *Censos 2011 Resultados Definitivos - Região Lisboa*. Lisbon, Portugal.

Johansen, K. W. (1949). Theory of Timber Connections. *International Association of Bridge and Structural Engineering*, *9*, 249–262.

Langenbach, R. (2007). From “Opus Craticium” to the “Chicago Frame”: Earthquake-Resistant Traditional Construction∗. *International Journal of Architectural Heritage*, *1*(1), 29–59. doi:10.1080/15583050601125998

Lin, T. J., & LaFave, J. M. (2012). Experimental structural behavior of wall-diaphragm connections for older masonry buildings. *Construction and Building Materials*, *26*, 180–189. doi:10.1016/j.conbuildmat.2011.06.008

LNEC. (1997). *Ficha M4 - Casquinha*.

Macdonald, E., Moore, J., Connolly, T., & Gardiner, B. (2010). Assessing timber quality of Scots pine (Pinus sylvestris L .). In *The Future of Quality control for wood & wood products. The Final Conference of COST Action E53* (pp. 4–7). Edinburgh.

Magenes, G., & Calvi, G. M. (1997). IN-PLANE SEISMIC RESPONSE OF BRICK MASONRY WALLS. *Earthquake Engineering & Structural Dynamics*, *26*(February), 1091–1112.

Magenes, G., Modena, C., da Porto, F., & Morandi, P. (2009). Seismic Behavior and Design of New Masonry Buildings: Recent Developments and Consequent Effects on Design Codes. In E. Cosenza (Ed.), *Eurocode 8 Perspectives from the Italian Standpoint Workshop* (pp. 199–212). Napoly, Italy.

Mascarenhas, J. (2004). *Sistemas de Construção - V, O Edifício de Rendimento da Baixa Pombalina de Lisboa* (2nd ed.). Lisboa: Livros Horizonte.

Milosevic, J., Gago, A. S., Lopes, M., & Bento, R. (2013). Experimental assessment of shear strength parameters on rubble stone masonry specimens. *Construction and Building Materials*, *47*, 1372–1380. doi:10.1016/j.conbuildmat.2013.06.036

Oliveira, D. V. (2003). *Experimental and numerical analysis of blocky masonry structures under cyclic loading*. University of Minho.

Ožbolt, J., Eligehausen, R., & Reinhardt, H. W. (1999). Size effect on the concrete cone pull-out load, *21*, 391–404.

Paganoni, S., & D'Ayala, D. (2014). Testing and design procedure for corner connections of masonry heritage buildings strengthened by metallic grouted anchors. *Engineering Structures*, *70*, 278–293. doi:10.1016/j.engstruct.2014.03.014

Papanicolaou, C. G., Triantafillou, T. C., Papathanasiou, M., & Karlos, K. (2007). Textile reinforced mortar (TRM) versus FRP as strengthening material of URM walls: out-of-plane cyclic loading. *Materials and Structures*, *41*(1), 143–157. doi:10.1617/s11527-007-9226-0

Paquette, J., & Bruneau, M. (2006). Pseudo-dynamic testing of unreinforced masonry building with flexible diaphragm and comparison with existing procedures. In *Construction and Building Materials* (Vol. 20, pp. 220–228). doi:10.1016/j.conbuildmat.2005.08.025

Parisi, M. A., Chesi, C., Tardini, C., & Piazza, M. (2008). Seismic vulnerability and preservation of timber roof structures. In *Structural analysis of historic construction: preserving safety and significance: proceedings of the Sixth International Conference on Structural Analysis of Historic Construction, 2-4 July 2008, Bath, United Kingdom* (pp. 1253–1260).

Parisi, M. A., Chesi, C., Tardini, C., & Piazza, M. (2009). Traditional timber roof structures: seismic vulnerability assessment and preservation. In *Protection of historical buildings: PROHITECH 09: proceedings of the International Conference on Protection of Historical Buildings, PROHITECH 09, Rome, Italy, 21-24 June 2009* (pp. 391–396).

Park, R. (1989). Evaluation of ductility of structures and structural assemblages from laboratory testing. *Bulletin of the New Zealand Society For Earthquake Engineering*, *22*(2), 155–166.

Paulay, T., & Priestley, M. J. N. (1992). *Seismic Design Of Reinforced Concrete And Masonry Buildings*.

Peralta, D. F., Bracci, J. M., & Hueste, M. B. D. (2004). Seismic Behavior of Wood Diaphragms in Pre-1950s Unreinforced Masonry Buildings. *Journal of Structural Engineering*, *130*(12), 2040–2051. doi:10.1061/(ASCE)0733-9445(2004)130:12(2040))

Pereira de Sousa. (1928). No Title.

Pereira, P., Camões, A., & Lourenço, P. B. (2010). The Portuguese masonry's mechanical characterization. In *8th International Masonry Conference* (pp. 611–622). Dresden.

Piccinin, R., Ballarini, R., Asce, F., & Cattaneo, S. (2010). Linear Elastic Fracture Mechanics Pullout Analyses of Headed Anchors in Stressed Concrete, (June), 761–768.

Pinho, F. (2008). *Paredes de Edifícios Antigos em Portugal* (1st ed.). Lisboa: LNEC.

Priestley, M. J. N. (2000). Performance based seismic design. In *12th World Conference on Earthquake Engineering* (Vol. 1, pp. 1–22).

Public Works and Government Services Canada. Guidelines for The Seismic Upgrading of Stone Masonry Structures (2002). Canada.

Ramos, L. F. (2000). *Análise experimental e numérica de estruturas históricas de alvenaria*. University of Minho.

Ramos, L. F., & Lourenço, P. B. (2004). Modeling and vulnerability of historical city centers in seismic areas: a case study in Lisbon. *Engineering Structures*, *26*(9), 1295–1310. doi:10.1016/j.engstruct.2004.04.008

Senaldi, I., Magenes, G., & Ingram, J. M. (2012). The seismic performance of unreinforced stone masonry building during the 2010-2011 Canterbury earthquake sequence. In *Proceedings of the 15th World Conference on Earthquake Engineering*. Lisbon, Portugal.

Senaldi, I., Magenes, G., Penna, A., Galasco, A., & Rota, M. (2014). The Effect of Stiffened Floor and Roof Diaphragms on the Experimental Seismic Response of a Full-Scale Unreinforced Stone Masonry Building. *Journal of Earthquake Engineering*, *18*(3), 407–443. doi:10.1080/13632469.2013.876946

Tomaževič, M. (1999). *Earthquake-resistant design of masonry buildings*. (A. S. Elnashai & P. J. Dowling, Eds.). Imperial College Press.

University of the West of England. (2009). Evolution of Building Elements. Retrieved from http://fet.uwe.ac.uk/conweb/house_ages/elements/section4.htm

Vasconcelos, G., & Lourenço, P. B. (2009). Experimental characterization of stone masonry in shear and compression. *Construction and Building Materials*. doi:10.1016/j.conbuildmat.2009.06.045

Vintzileou, E. (2008). Effect of Timber Ties on the Behavior of Historic Masonry, (June).

Wilson, A. W., Quenneville, P. J. H., & Ingham, J. M. (2011). Experimental testing of full-scale timber floor diaphragms in unreinforced masonry buildings. In *Ninth Pacific Conference on Earthquake Engineerin Building an Earthquake-Resilient Society* (pp. 1–8). Auckland, New Zealnd.

Yi, T., Moon, F. L., Leon, R. T., & Kahn, L. F. (2006a). Analyses of a Two-Story Unreinforced Masonry Building. *Journal of Structural Engineering*. doi:10.1061/(ASCE)0733-9445(2006)132:5(653)

Yi, T., Moon, F. L., Leon, R. T., & Kahn, L. F. (2006b). Lateral Load Tests on a Two-Story Unreinforced Masonry Building. *Journal of Structural Engineering*, *132*(5), 643–652. doi:10.1061/(ASCE)0733-9445(2006)132:5(643)

Zamora, N. A., Cook, R. A., Konz, R. C., & Consolazio, G. R. (2003). Behavior and Design of Single, Headed and Unheaded, Grouted Anchors under Tensile Load. *ACI Structural Journal*, *100*(2), 222–230. doi:10.14359/12486

http://www.architetturaecosostenibile.it/green-life/curiosita-ecosostenibili/legno-regno-due-sicilie-primo-regolamento-antisismico-556/, 16-01-2015

Annex 1.

Annex of Chapter 2

A1.1 Survey data

Table A1.1 Information regarding the surveyed buildings.

Nº	Type	Ground floor	1	2	3	4	5	6	Mansard roof	Number of storeys
1	*Gaioleiro*	0.80	0.80	0.75	0.70	0.65	-	-	-	5
2	*Gaioleiro*	0.80	0.70	0.65	0.60	0.50	-	-	-	5
3	*Gaioleiro*	0.85	0.85	0.80	0.75	0.65	0.65	-	-	6
6	*Gaioleiro*	0.70	0.60	0.50	0.40	-	-	-	-	4
7	*Late Pombalino*	0.70	0.60	0.60	0.60	-	-	-	1.00	5
8	*Late Pombalino*	0.70	0.60	0.50	-	-	-	-	-	3
9	*Late Pombalino*	0.60	0.50	0.45	0.40	0.35	-	-	-	5
10	*Pombalino*	0.60	0.60	0.60	0.25	-	-	-	-	4
11	*Late Pombalino*	0.60	0.55	0.55	0.40	0.40	-	-	-	5
12	*Pombalino*	1.00	0.90	0.80	0.80	0.80	0.50	-	-	6
13	*Late Pombalino*	0.90	0.90	0.95	0.83	0.61	0.50	-	-	6
14	*Pombalino*	1.00	0.90	0.80	0.80	0.70	0.50	-	-	6
15	*Pombalino*	1.00	1.00	0.80	0.80	0.70	-	-	-	5
16	*Pombalino*	1.10	0.90	0.70	0.70	-	-	-	-	4
17	*Pombalino*	0.70	0.70	0.70	0.70	-	-	-	-	4
18	*Pombalino*	1.00	0.90	0.80	0.70	-	-	-	-	4
19	*Pombalino*	1.10	0.90	0.80	0.80	-	-	-	-	4
21	*Gaioleiro*	0.80	0.75	0.70	0.65	0.60	0.55	0.50	-	7
4	*Gaioleiro*	0.80	1.10	1.10	1.10	1.10	1.10	-	-	6

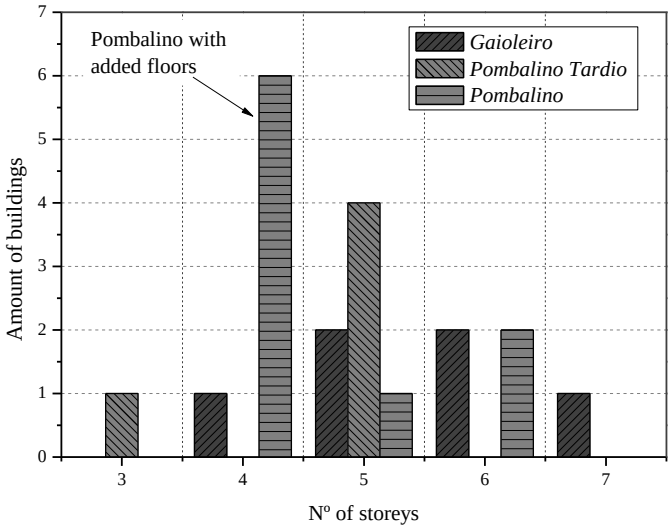

Figure A1.1 Number of storeys per typology of building and number of storeys.

Annex 2.

Annex of Chapter 4

A2.1 Injection anchors' survey

Table A2.1 Observed damage of anchors tested on the top of the wall.

Specimen	Anchors	Free end broken	Cracks	Other obs.
WT.40.I.1A	Anchor 1	-	-	Not centered; Small bulb at the end; Deposit of grout
	Anchor 2	-	-	Centered; Large bulb at 120 mm from the end; Deposit of grout
WT.40.I.2A	Anchor 1	At 45 mm from end	Transversal cracks (at 40 mm and 85 mm from beginning)	Not centered; Central bulb of grout; No deposit of grout
	Anchor 2	From 15 mm to 75 mm from end	Transversal crack (at 45 mm from beginning)	Centered; No deposit of grout
WT.40.I.2B	Anchor 1	-	-	Centered; No deposit of grout
	Anchor 2	At 40 mm from end	Longitudinal and transversal cracks (every 50 mm)	Centered; Central bulb of grout; No deposit of grout

Table A2.2 Observed damage of anchors tested on the bottom of the wall.

Specimen	Anchors	Free end broken	Cracks	Other obs.
WT.40.I.1C	Anchor 1	From 15 mm to 60 mm from end	Transversal cracks (every 40 mm)	Not centered; Bulb of grout at the end; Deposit of grout
	Anchor 2	-	-	Centered; Central bulb of grout; No deposit of grout
WT.40.I.1D	Anchor 1	At 15 mm from end	Transversal crack (at 140 mm from beginning)	Centered; bulb towards the end; No deposit of grout
	Anchor 2	-	-	Centered; Deposit of grout
WT.40.I.2C	Anchor 1	-	-	Centered; Deposit of grout
	Anchor 2	-	-	Centered; No deposit of grout
WT.40.I.2D	Anchor 1	-	-	Centered; Deposit of grout
	Anchor 2	-	-	Centered; Deposit of grout

A2.2 Crack mapping

Figure A2.1 Crack pattern of specimen WT.40.I.1A.

Figure A2.2 Crack pattern of specimen WT.40.I.1C.

Figure A2.3 Crack pattern of specimen WT.40.I.1D.

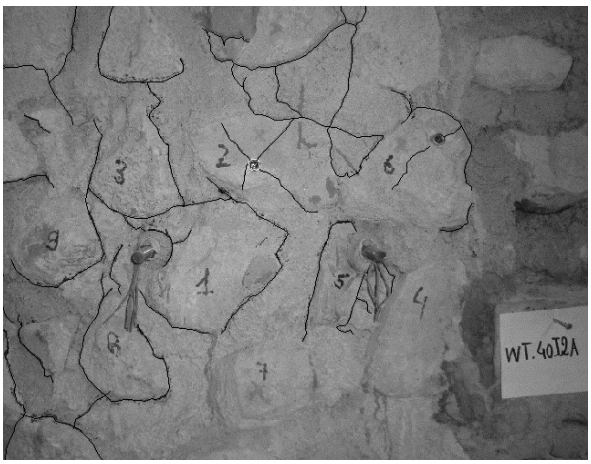

Figure A2.4 Crack pattern of specimen WT.40.I.2A.

Figure A2.5 Crack pattern of specimen WT.40.I.2B.

Figure A2.6 Crack pattern of specimen WT.40.I.2A.

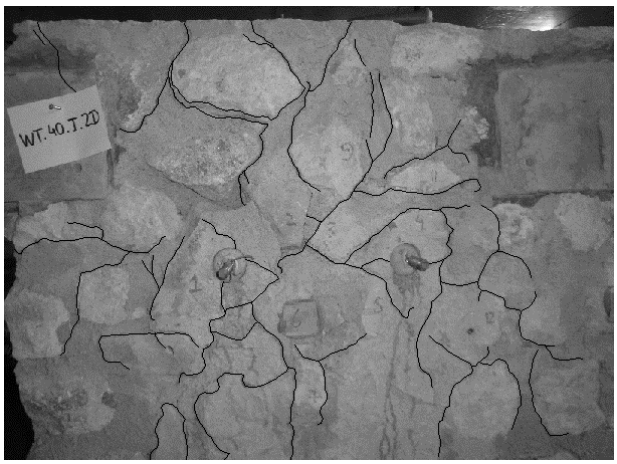

Figure A2.7 Crack pattern of specimen WT.40.I.2D.

Annex 3.

Annex of Chapter 5

A3.1 Force-displacement curves

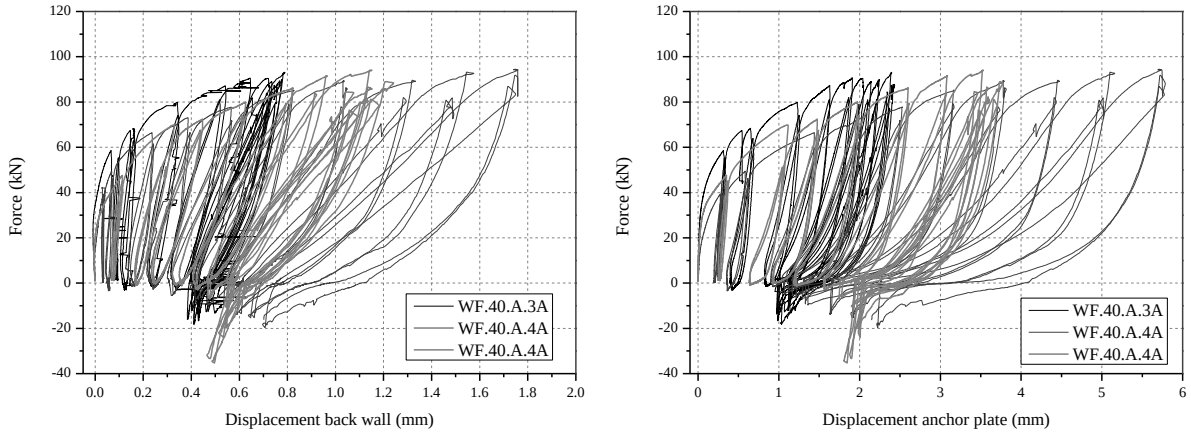

(a) (b)

Figure A3.1 Force-displacement curves of the anchor plates of the WF.40.A tests.

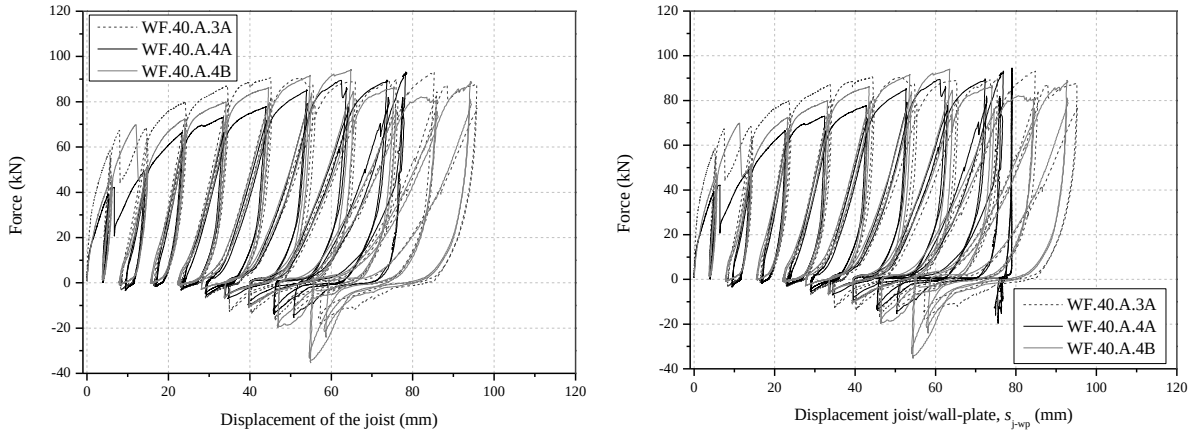

(a) (b)

Figure A3.2 Force-displacement curves relative to WF.40.A specimens: (a) joist; and (b) $s_{j\text{-}wp}$.

A3.2 Relationship between measured variables

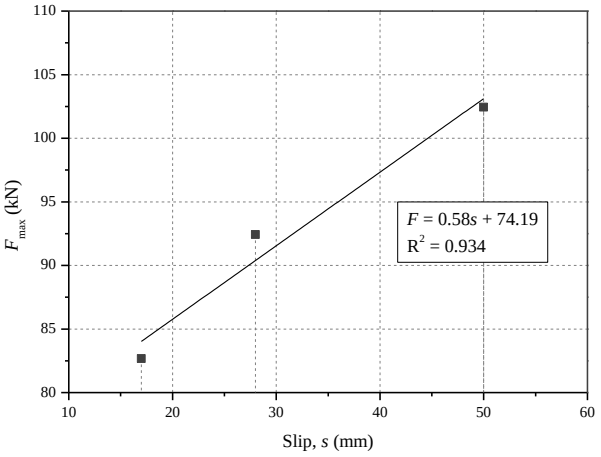

Figure A3.3 Relationship between slip and F_{max}.

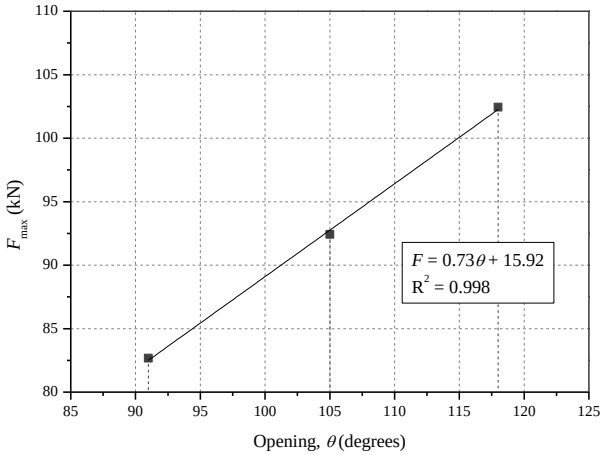

Figure A3.4 Relationship between slip and F_{max}.

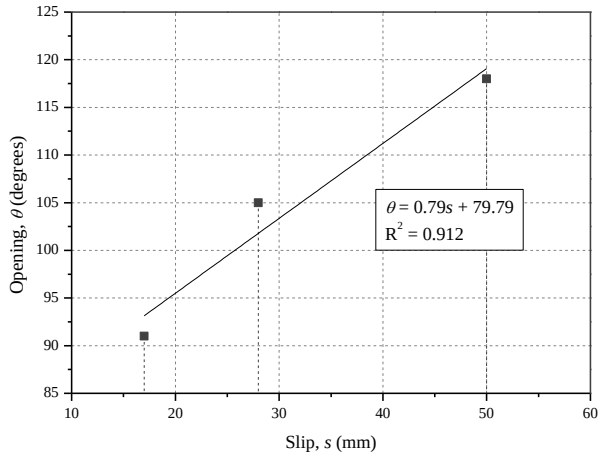

Figure A3.5 Relationship between slip and F_{max}.

A3.3 Specimens with nonconformities

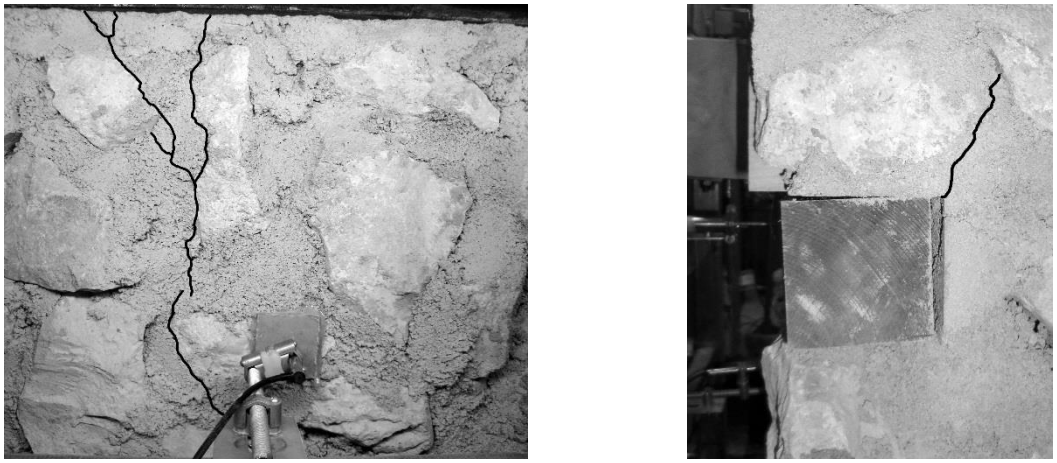

(a) (b)

Figure A3.6 Cracks found on specimen WF.40.A.2B: (a) crack propagating from the steel angle to the top of the wall; and (b) crack radiating from the wall-plate.

Annex 4.

Annex of Chapter 6

A4.1 Strength prediction formulae

A4.1.1 Projected area of parallel injection anchors

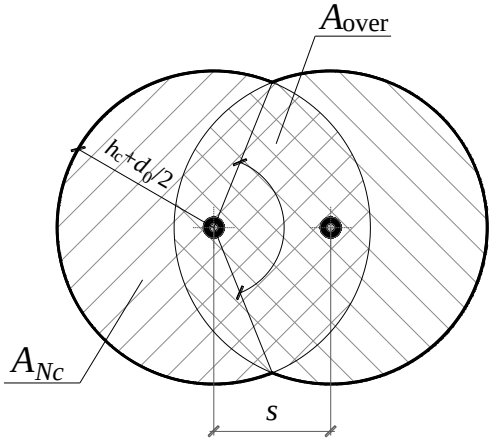

$$r = h_c + \frac{d_0}{2}$$

$$A_{over} = 2 \cdot r \cdot \cos^{-1}\frac{s^2}{2 \cdot s \cdot r} - \frac{1}{2}\sqrt{-s^4 + 4r^2s^2}$$

$$A_{Nc} = 2\pi \cdot r^2 - A_{over}$$

Figure A4.1 Projected area of two parallel injection anchors.

A4.2 Backbone curves

A4.2.1 Injection anchors specimens

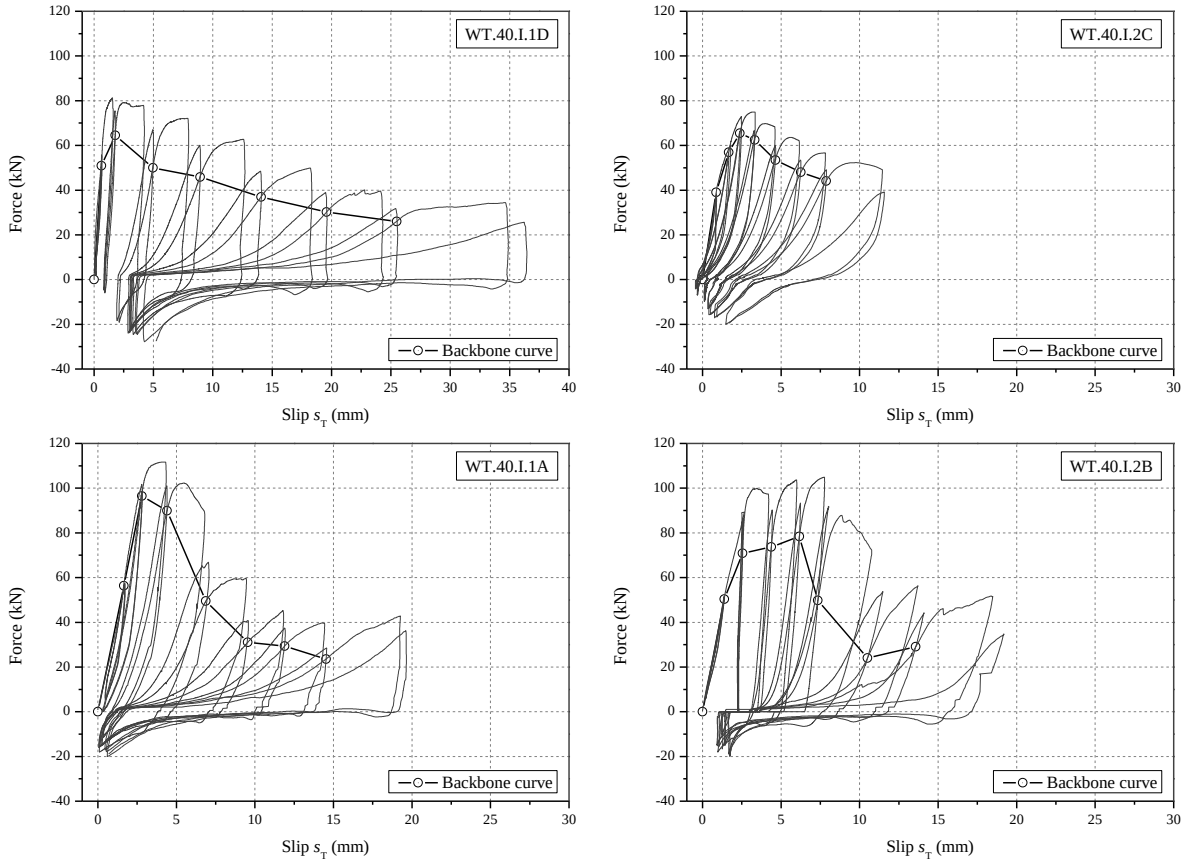

Figure A4.2 Backbone curves of injection anchors' specimens according to ASCE/SEI 41-06.

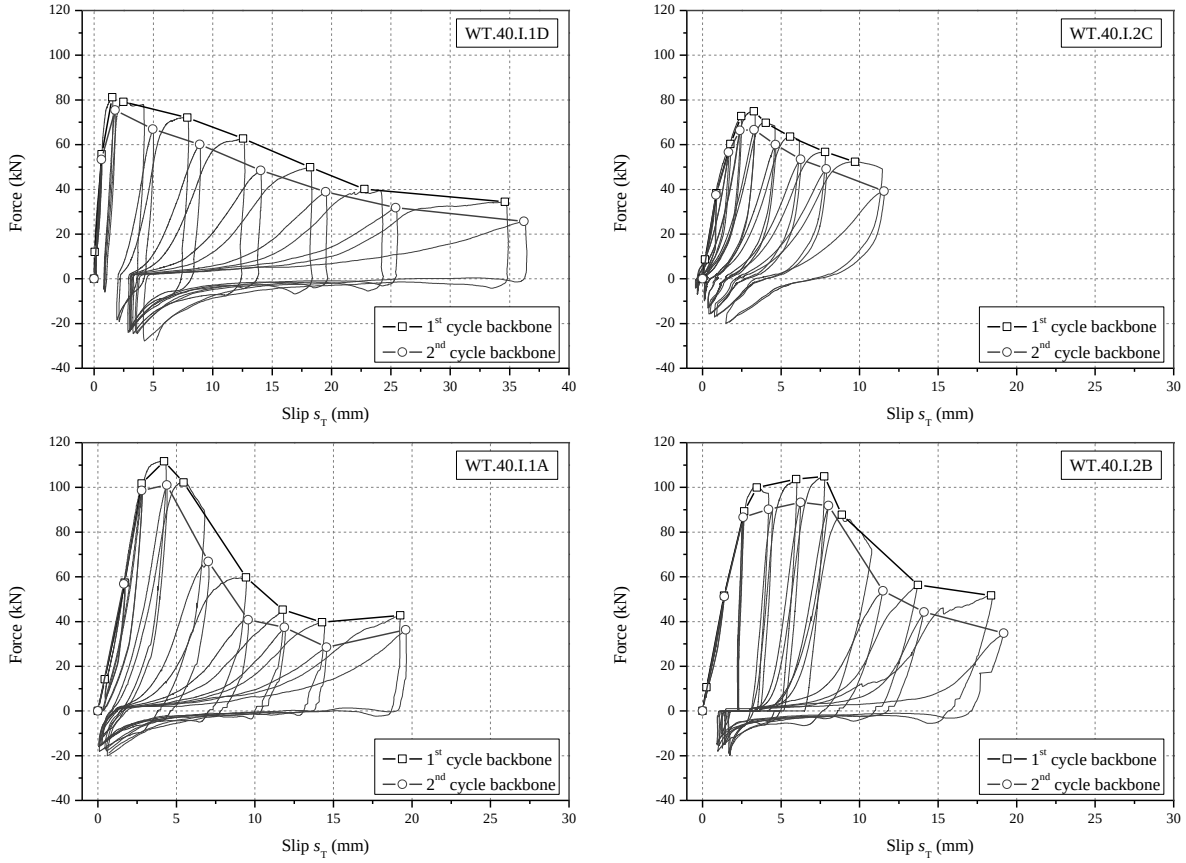

Figure A4.3 Backbone curves of injection anchors' specimens according to Frumento et al. (2009).

A4.2.2 Strengthened wall-to-floor specimens

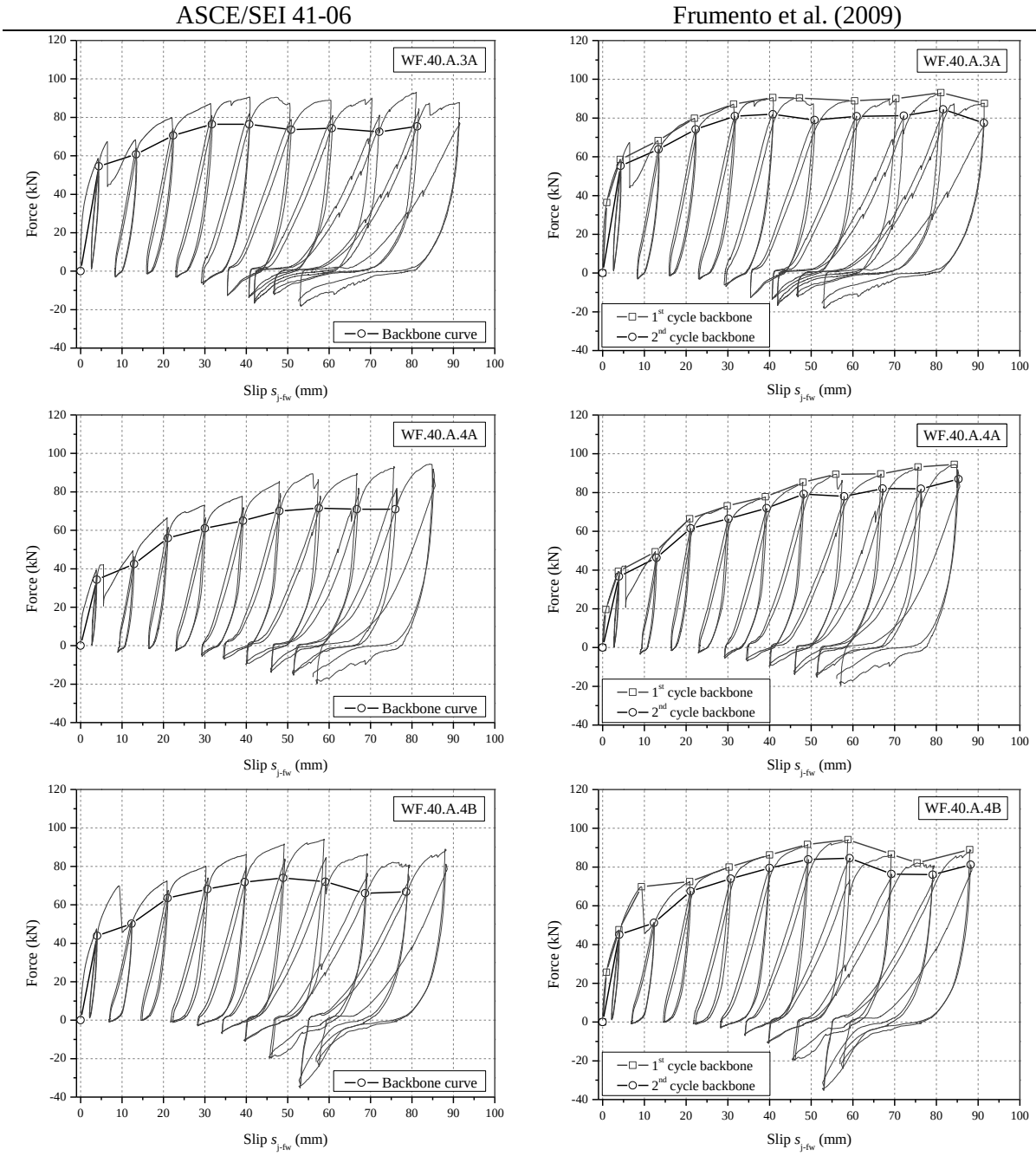

Figure A4.4 Backbone curves of WF.40.A specimens.

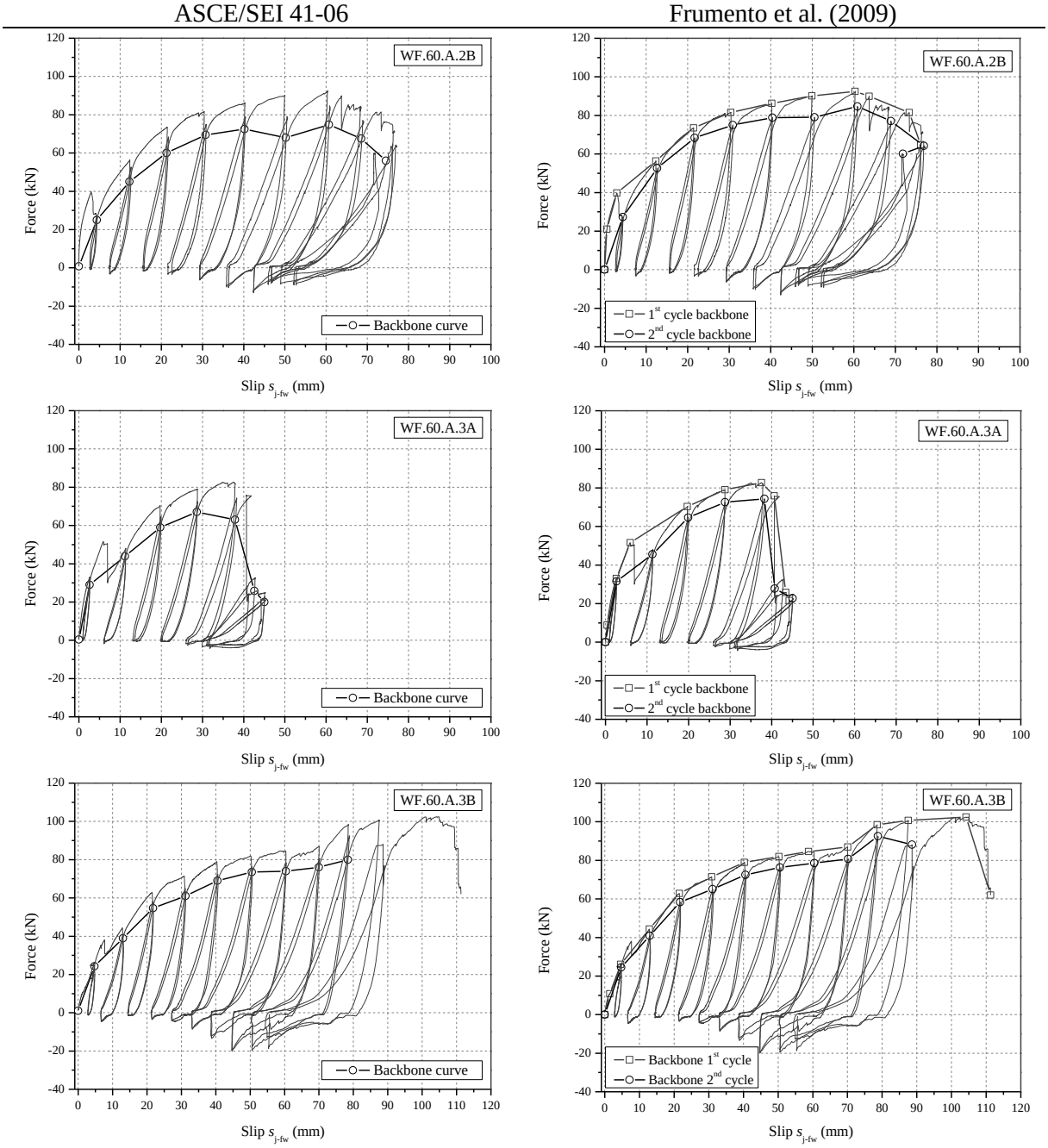

Figure A4.5 Backbone curves of WF.60.A specimens.

A4.3 Bilinear curves parameters

Table A4.1 Parameters for the definition of the bilinear curves of unstrengthened wall-to-floor specimens.

Specimen	d_e (mm)	d_u (mm)	F_u (kN)	k_e (kN/mm)	μ
WF.40.U.1A	3.6	33.8	8.2	2.3	9.4
WF.40.U.1B	4.8	37.9	5.0	1.0	7.8
WF.60.U.1A	3.3	26.6	3.6	1.1	8.0
WF.60.U.1B	-	41.4	3.7	-	-

Table A4.2 Parameters for the definition of the bilinear curves of WF.40.A specimens.

Specimen	d_e (mm)	d_u (mm)	F_u (kN)	k_e (kN/mm)	μ
WF.40.A.3A					
1st cycle	13.1	91.5	89.4	6.8	7.0
2nd cycle	6.1	91.4	77.5	12.7	15.0
Equivalent	11.6	91.4	84.3	7.2	7.9
WF.40.A.4A					
1st cycle	15.3	84.3	82.2	5.4	5.5
2nd cycle	14.1	85.3	74.0	5.2	6.0
Equivalent	14.7	84.3	78.1	5.3	5.7
WF.40.A.4B					
1st cycle	9.6	88.0	84.6	8.8	9.2
2nd cycle	20.2	88.2	80.3	4.0	4.4
Equivalent	14.9	88.0	82.4	5.5	5.9
WF.40.A Equivalent	13.7	84.3	81.6	5.9	6.1
CoV (%)	13	4	4	18	18

Table A4.3 Parameters for the definition of the bilinear curves of WF.60.A specimens.

Specimen	d_e (mm)	d_u (mm)	F_u (kN)	k_e (kN/mm)	μ
WF.60.A.2B					
1st cycle	13.3	74.6	83.2	6.3	5.6
2nd cycle	16.4	74.7	73.3	4.5	4.5
Equivalent	14.9	74.6	78.3	5.3	5.0
WF.60.A.3A					
1st cycle	7.1	41.2	69.3	9.7	5.8
2nd cycle	11.0	39.1	60.4	5.5	3.5
Equivalent	9.1	39.1	64.9	7.2	4.3
WF.60.A.3B					
1st cycle	21.5	107.8	85.5	4.0	5.0
2nd cycle	20.2	88.6	75.3	3.7	4.4
Equivalent	20.9	88.6	80.4	3.9	4.2
WF.60.A Equivalent	17.9	74.6	79.3	4.6	4.6
CoV (%)	24	12	2	22	12

A4.4 Trilinear curves parameters

Table A4.4 Parameters for the definition of trilinear curves of unreinforced wall-to-floors specimens.

Set	Specimen	d_e (mm)	d_{Fmax} (mm)	d_u (mm)	k_e (kN/mm)	α	β	F_2	F_3	μ
WF.40.U + WF.60.U	WF.40.U.1A	2.8	22.9	33.8	2.7	0.03	-0.07	7.5	13.7	11.9
	WF.40.U.1B	1.7	21.6	37.9	2.1	0.05	-0.02	3.4	6.4	22.2
	WF.60.U.1A	1.1	12.8	26.6	2.4	0.06	-0.03	2.6	5.3	23.2
	WF.60.U.1B	-	32.1	41.4	-	-	-	-	-	-
WF.U		1.4	17.2	32.3	2.2	0.05	-0.03	3.0	5.9	22.6
CoV (%)		28	36	25	9	19	23	20	13	3

Table A4.5 Parameters for the definition of trilinear curves for each test from ASCE/SEI 41-06 (ASCE, 2006) backbone curves.

Set	Specimen	d_e (mm)	d_{Fmax} (mm)	d_{res} (mm)	d_u (mm)	k_e (kN/mm)	α	β	F_2	F_3	F_{res} (kN)	μ
WT.40.I.Bottom	WT.40.I.1A	1.7	2.8	10.2	14.5	33.9	1.04	-0.28	-2.3	122.8	26.5	3.1
	WT.40.I.2B	2.1	6.2	9.1	13.6	33.5	0.07	-0.52	64.4	185.9	26.6	3.3
WT.40.I.Top	WT.40.I.2C	1.1	2.4	-	5.0	43.8	0.32	-0.10	31.9	75.9	-	4.6
	WT.40.I.1D	0.6	1.8	-	4.6	80.8	0.14	-0.03	43.6	68.3	-	7.3
WF.40.A	WF.40.A.3A	4.9	40.8	-	81.2	12.4	0.04	-0.01	58.4	81.3	-	16.7
	WF.40.A.4A	5.2	57.5	-	76.0	8.8	0.06	-0.01	43.1	77.2	-	14.6
	WF.40.A.4B	4.7	48.9	-	78.6	11.0	0.04	-0.03	50.0	88.8	-	16.6
WF.60.A	WT.60.A.2B	12.9	60.7	-	72.5	4.5	0.08	-0.25	53.3	142.8	-	5.6
	WT.60.A.3A	3.1	28.6	-	39.1	11.2	0.11	-0.15	30.7	116.1	-	12.6
	WT.60.A.3B	9.7	78.4	-	78.4	5.1	0.09	-	45.5	-	-	8.1

Table A4.6 Parameters for the definition of equivalent trilinear curves for all sets of tests from ASCE/SEI 41-06 (ASCE, 2006) backbone curves.

Specimen	d_e (mm)	d_{Fmax} (mm)	d_{res} (mm)	d_u (mm)	k_e (kN/mm)	α	β	F_2	F_3	F_{res} (kN)	μ
WT.40.I.Bottom	1.9	4.5	9.7	14.1	33.6	0.28	-0.35	45.1	139.9	26.5	3.2
CoV (%)	15	53	8	5	1	124	-43	152	29	0	4
WT.40.I.Top	0.9	2.1	-	4.8	57.5	0.23	-0.06	37.9	71.7	-	5.6
CoV (%)	37	20	-	5	42	54	-83	22	7	-	32
WF.40.A	4.9	49.1	-	78.6	10.7	0.0	0.0	50.5	82.6	-	15.9
CoV (%)	5	17	-	3	17	23	-61	15	7	-	7
WT.60.A	11.3	69.6	-	75.4	4.8	0.1	-0.6	49.3	264.0	-	6.7
CoV (%)	20	18	-	6	9	6	-	11	-	-	25

Table A4.7 Parameters for the definition of equivalent trilinear curves for each test from Frumento et al. (2009) backbone curves.

Set	Specimen	d_e (mm)	d_{Fmax} (mm)	d_{res} (mm)	d_u (mm)	k_e (kN/mm)	α	β	F_2	F_3	F_{res} (kN)	μ
WT.40.I.Bottom	WT.40.I.1A	2.9	4.3	11.2	19.4	34.7	0.12	-0.29	88.7	150.1	36.8	2.2
	WT.40.I.2B	2.6	7.0	14.0	18.8	35.3	0.04	-0.21	89.6	151.3	46.8	3.6
WT.40.I.Top	WT.40.I.2C	1.3	3.3	-	6.5	43.6	0.16	-0.09	47.2	83.8	-	5.0
	WT.40.I.1D	0.7	1.7	-	10.1	79.9	0.31	-0.02	37.9	81.2	-	14.8
WF.40.A	WF.40.A.3A	5.5	81.4	-	91.4	13.3	0.02	-0.05	72.3	137.6	-	24.0
	WF.40.A.4A	5.9	84.8	-	84.8	9.9	0.04	-	55.7	-	-	14.4
	WF.40.A.4B	5.3	59.0	-	88.1	11.8	0.04	-0.04	60.2	116.3	-	16.6
WF.60.A	WT.60.A.2B	8.8	60.6	-	74.6	7.2	0.07	-0.10	58.6	133.4	-	8.5
	WT.60.A.3A	4.1	37.9	-	40.1	12.3	0.07	-0.61	47.3	364.4	-	9.7
	WT.60.A.3B	9.8	91.5	-	98.2	5.4	0.10	-0.34	48.3	267.3	-	10.0

Table A4.8 Parameters for the definition of equivalent trilinear curves for all sets of tests from Frumento et al. (2009) backbone curves.

Specimen	d_e (mm)	d_{Fmax} (mm)	d_{res} (mm)	d_u (mm)	k_e (kN/mm)	α	β	F_2	F_3	F_{res} (kN)	μ
WT.40.I.Bottom	2.8	5.7	12.6	19.1	35.0	0.06	-0.25	91.3	152.5	41.8	2.9
CoV (%)	7	34	16	2	1	72	23	1	1	17	35
WT.40.I.Top	1.0	2.5	-	8.3	56.1	0.23	-0.04	42.8	80.4	-	8.4
CoV (%)	44	46	-	30	42	42	87	16	2	-	69
WF.40.A	5.6	75.1	-	88.1	11.6	0.03	-0.04	62.8	126.7	-	15.8
CoV (%)	5	19	-	4	15	46	11	14	12	-	27
WT.60.A	9.3	76.0	-	86.4	6.3	0.08	-0.18	53.4	176.7	-	9.3
CoV (%)	8	29	-	19	19	23	73	12	45	-	11

A4.5 Curves' parameters according to ASCE/SEI 41-13

Table A4.9 Parameters for the definition of equivalent trilinear curves for each test from ASCE/SEI 41-13 (ASCE, 2014) backbone curves.

Set	Specimen	d_e (mm)	d_{Fmax} (mm)	d_{res} (mm)	d_u (mm)	k_e (kN/mm)	α	β	F_2	F_3	F_{res} (kN)	μ
WT.40.I.Bottom	WT.40.I.1A	2.9	4.2	11.9	6.7	34.8	0.22	-0.27	79.1	150.7	41.3	2.3
	WT.40.I.2B	2.8	7.8	13.1	9.5	35.1	0.03	-0.27	96.5	179.4	54.1	3.3
WT.40.I.Top	WT.40.I.2C	1.3	3.3	-	6.8	43.5	0.21	-0.10	45.5	88.5	-	5.1
	WT.40.I.1D	0.7	1.6	-	11.4	75.8	0.41	-0.02	32.7	83.8	-	15.5
WF.40.A	WF.40.A.3A	5.6	81.1	-	91.5	13.9	0.01	-0.04	76.2	134.0	-	16.4
	WF.40.A.4A	5.9	84.3	-	84.3	10.4	0.04	-	59.2	-	-	14.2
	WF.40.A.4B	5.5	58.8	-	88.0	12.3	0.04	-0.04	65.2	123.5	-	15.9
WF.60.A	WT.60.A.2B	4.6	60.3	-	74.6	13.4	0.00	-0.10	59.4	151.6	-	16.1
	WT.60.A.3A	4.4	37.6	-	41.2	12.6	0.10	-0.50	52.0	331.8	-	9.3
	WT.60.A.3B	10.9	104.2	-	107.8	5.7	0.10	-1.00	57.3	697.3	-	9.8

Table A4.10 Parameters for the definition of equivalent trilinear curves for all sets of tests from ASCE/SEI 41-13 (ASCE, 2014) backbone curves.

Specimen	d_e **(mm)**	d_{Fmax} **(mm)**	d_{res} **(mm)**	d_u **(mm)**	k_e **(kN/mm)**	**α**	**β**	F_2	F_3	F_{res} **(kN)**	**μ**
WT.40.I.Bottom	2.9	6.0	8.1	12.5	35.0	0.07	-0.27	93.5	164.5	47.7	2.8
CoV (%)	2	42	25	7	1	107	-2	14	12	19	27
WT.40.I.Top	1.0	2.4	-	9.1	55.1	0.28	-0.04	40.6	83.7	-	8.9
CoV (%)	40	50	-	36	38	47	-88	23	4	-	71
WF.40.A	5.7	74.7	-	87.9	12.2	0.03	-0.04	66.9	131.3	-	15.5
CoV (%)	4	19	-	4	14	46	-8	13	6	-	8
WT.60.A	7.8	82.3	-	91.2	8.0	0.1	-0.2	58.3	256.2	-	11.7
CoV (%)	57	38	-	26	57	43	-122	3	91	-	34